Subwavelength imaging of optically dense atomic clouds in a quantum gas microscope

Romain Veyron

THÈSE PRÉSENTÉE

POUR OBTENIR LE GRADE DE

DOCTEUR
DE L'UNIVERSITÉ DE BORDEAUX

ÉCOLE DOCTORALE SCIENCES PHYSIQUES DE L'INGÉNIEUR

Spécialité LASERS, MATIÈRES ET NANOSCIENCES

Par **Romain VEYRON**

Subwavelength imaging of optically dense atomic clouds in a quantum gas microscope

Sous la direction de : **Simon BERNON**

Soutenue le 17 décembre 2021

Membres du jury :

Mr. Fabrice GERBIER	DR, LKB, Paris	Rapporteur
Mr. Thierry LAHAYE	CR, LCF, Paris	Rapporteur
Mr. Bruno LABURTHE-TOLRA	DR, LPL, Villetaneuse	Président
Mr. Robin KAISER	DR, INPHYNI, Nice	Examinateur
Mr. Trey PORTO	Pr. adjoint, JQI, Maryland	Examinateur
Mr. Jean-Philippe BRANTUT	Pr. assistant, EPFL, Lausanne	Examinateur
Mr. Philippe BOUYER	DR, LP2N, Talence	Examinateur
Mr. Simon BERNON	Pr. assistant, LP2N, Talence	Directeur de thèse

Contents

Acknowledgments

First I would like to thank the University of Bordeaux for funding my PhD work at Laboratoire Photonique Numérique et Nanosciences (LP2N) in Talence.

Many thanks to my PhD advisor Simon Bernon who taught me a lot about all technical aspects of a cold atom experiment. Scientific discussions were always very interesting. I enjoyed the freedom that you gave me on the experiment. I thank Philippe Bouyer for giving me the opportunity to start working on the experiment AUFRONS as a pre-doctoral student, a period where I have learned a lot.

I am grateful to the two reporters of my manuscript for taking the time to read my manuscript: Thierry Lahaye, and especially to Fabrice Gerbier, who gave me many fruitful corrections to my manuscript. All the comments were very instructive. Thanks to the examiners, Robin Kaiser, Trey Porto, Jean-Philippe Brantut, Philippe Bouyer, and to the president Bruno Laburthe-Tolra. The questions during the defense were very stimulating.

Many thanks to all PhDs, post-docs, and permanents in the Cold Atom in Bordeaux group: Grigor, Max, Devang, Hodei, Geovan, Andrea on BIARO, Luisa on CRYST3, Chen-hao, Paul on ALCALINF, Laura, Martin, Gabriel, Romain, Vincent, Célia and Baptiste on ICE, Laure, Grégoire, Dylan, Joseph, Xinhao, Benjamin on MIGA, Brynle, Pierrick, Simon, Quentin on iXAtom, and on AUFRONS, Caroline, Maxime, Adèle, Guillaume, Vincent and finally Jean-Baptiste, who I enjoyed working with the last year of my PhD. I won't say that it has been paradise everytime as I also got some frustrations due to some people. The atmosphere and respect are essential in a laboratory. But I keep in mind plenty of good memories as weekly Jazz concerts of local groups at Cancan with Grégoire, Grigor, Devang, Hodei, Élise, etc, the list is very long and I thank you all. Special thanks to Devang, I enjoyed Jam sessions at Quartier Libre on Wednesday nights and all the other places.

Also, I acknowledge Philippe from the mechanical workshop and the electronics workshop members, Jean-Hugues and Arnaud, for your time and sympathy in helping design our systems. Thanks to the administrative staff, Stéphanie, Laurent, Fabien. I thank the pedagogical team at Institut d'Optique for giving me the opportunity of lab and class monitoring during my years of PhD. Thanks to the other group members for the nice discussions and for making the laboratory life more fun.

Last but not least, I thank my friends and family for their support. Especially, Dorian for making me forget lab problems. Life-long friends Nathan, Marina, Abderrahim, and others for being present and supportive. I finish by dedicating this PhD to my nephew, who, at the time I am writing this, is already 1-month-old!

Introduction (EN/FR)

English version

The theory of quantum mechanics developed at the beginning of the 20th has revolutionized the understanding of microscopic phenomena. In contrast to classical physics where an object is pointlike and described by a trajectory, quantum mechanics attributes wavelike properties to particles. Nowadays, the applications of such theory are usually classified into four categories (O'Brien, Furusawa, and Vučković, 2009): secure communication through quantum cryptography (Gisin et al., 2002), quantum information for quantum computers (Ladd et al., 2010; Slussarenko and Pryde, 2019), metrology for high sensitivity sensors (Degen, Reinhard, and Cappellaro, 2017) and quantum simulations for modeling new materials (Altman et al., 2021; Georgescu, Ashhab, and Nori, 2014).

Different experimental platforms are foreseen as well adapted to address these applications. These platforms have been developed on parallel tracks like superconducting circuits (Stassi, Cirio, and Nori, 2020), quantum dots (Barthelemy and Vandersypen, 2013), photonic circuits (O'Brien, Furusawa, and Vučković, 2009), trapped ions (Bruzewicz et al., 2019), polar molecules (DeMille, 2002) or cold atoms (Schäfer et al., 2020). Each of them has its assets and drawbacks. The main common source of improvement for those systems is to maximize the coherence time (Wang et al., 2021; Bernon et al., 2013; Rigetti et al., 2012) by limiting the coupling to the environment which is responsible for decoherence. This can be due to residuals couplings with any electromagnetic field, phonons, collisional dephazing in dense ensembles, etc.

Dilute gases of cold atoms have the advantage of being well-isolated from the EM field environment. In addition, a large toolbox of laser trapping and cooling have been developed in 1980s for neutral alkaline atoms (Phillips, Prodan, and Metcalf, 1985). Starting with an atomic gas at room temperature (300 K), laser and evaporative cooling techniques lead to the observation of the Bose-Einstein Condensation (Anderson et al., 1995). It is a macroscopic manifestation of the wave feature of bosonic particles that appears at very low temperatures, below 200 nK. As for electromagnetic waves, it is possible to associate a characteristic wavelength to particles, known as the de Broglie wavelength. It defines the typical coherence length in an atomic ensemble that inversely evolves with the temperature. When this coherence length is larger than the mean inter-particle distance, constructive interferences of atomic wavepackets (bunching) lead to a macroscopic wave well-described by a single wavefunction. It has been predicted by Einstein in 1925 (Einstein, 1924) based on Bose's work on photons (Bose, 1924) and first observed with Rubidium atoms in 1995 (Anderson et al., 1995).

Since then, ultra-cold atoms have been a benchmark for studying many phenomena and

developing new applications. For instance, cold atoms are very sensitive probes. They are used in atomic clocks (Campbell and Phillips, 2011) or inertial sensors (Debs et al., 2011) using atom interferometry. BEC-based experiments have been proposed to explore the quantum theory of gravity (Howl, Penrose, and Fuentes, 2019; Howl et al., 2021).

When particles are interacting with each other via two-body collisions, a mean-field theory describes well the dynamics of a BEC (Dalfovo et al., 1999). This contact interaction can be tuned to be attractive or repulsive using Feshbach resonances (Inouye et al., 1998). Theoretical beyond mean-field corrections due to quantum fluctuations (Pitaevskii and Stringari, 1998) are experimentally measured. For instance, dipolar quantum gases provide an experimental situation to observe droplet crystals (Kadau et al., 2016). In such crystals, an attractive magnetic dipole-dipole force can be exactly compensated by the sum of the usual repulsive contact interaction and a repulsive Lee-Huang-Yang type force from beyond mean-field corrections.

For the case of fermionic atoms, governed by the Pauli exclusion principle, degenerate Fermi gases can be also produced through evaporative cooling techniques (DeMarco and Jin, 1999). They are characterized by a single many-body wavefunction and all eigenstates below the Fermi temperature are occupied. Bose-Einstein condensates and degenerate Fermi gases are routinely produced in laboratories as it is an ideal macroscopic quantum object well-described by a single wavefunction. It is therefore a starting point to deviate towards correlated many-body quantum systems.

For instance, quantum phase transitions have been observed as the Mott-superfluid transition (Greiner et al., 2002) with ultra-cold bosonic atoms in a 3D optical lattice. An antiferromagnet has been realized with ultra-cold fermionic atoms in a 2D optical lattice (Mazurenko et al., 2017). Ultra-cold atoms in reduced dimensions lead to the observation of the Berezinskii-Kosterlitz-Thouless crossover of a 2D gas (Hadzibabic et al., 2006) where superfluid properties are observable without Bose-Einstein Condensation at finite temperature. Another example can be reached by tuning the contact interaction in an ultra-cold fermionic atomic gas leading to the observation of a crossover between a Bardeen-Cooper-Schrieffer superfluid with delocalized atom pairs to a BEC of bounded atom pairs (Greiner, Regal, and Jin, 2003). All these examples show that ultra-cold atoms are used to simulate complex materials. Lots of them use optical lattices which are well-suited for controlling both kinetic and interaction energies.

Many-body features can be measured via interference effects between lattice sites (Greiner et al., 2002) observed in time-of-flight experiments, where atoms, initially trapped in a lattice, are released and subjected to free fall before they interfere. A second method is to measure in situ the atomic density with quantum gas microscopes (Schäfer et al., 2020) to compute spin-correlators and characterize the order in the lattice (Mazurenko et al., 2017). The dynamics of these materials cannot be numerically computed with standard computers due to the very large number of particles. Optical lattice experiments are then operated as quantum simulators (Schäfer et al., 2020). They are real experimental platforms that mimic with high controllability the behavior of electrons in solid state systems.

One of the challenges of condensed matter physics is realize strongly correlated systems. For instance, the origin of high critical temperature cuprate superconductors could be found by studying the Fermi-Hubbard model at temperatures much lower than the Fermi temperature $T/T_F \ll 1$ (Moriya and Ueda, 2003; Lee, Nagaosa, and Wen, 2006). De-

creasing the temperature means here to decrease the entropy per particle S/N to go into new quantum phase transitions (McKay and DeMarco, 2011). Indeed decreasing T down to about 500 pK has already been done but at constant S/N (Leanhardt et al., 2003). The required temperature is at the picokelvin level for which many-body thermalization times are on the order of tens of seconds. This is not compatible with cold atoms systems having a finite lifetime due to vacuum losses (Lee, Nagaosa, and Wen, 2006), heating sources in deep lattice depths (Gerbier and Castin, 2010; McKay and DeMarco, 2011) and three-body losses (Söding et al., 1999; Yoshida et al., 2018).

The other route towards strongly correlated systems is to increase all energy scales to increase the Fermi temperature. It can be achieved in optical lattices by decreasing optical lattice periodicities. Standard optical lattices in far-field are limited by diffraction to 'large' periodicities preventing from entering into those regimes. Therefore, near-field lattices offer a path to reduce the lattice spacing by beating the diffraction limit. Subwavelength lattices can be realized by interfacing atoms with a nanostructured surface generating subwavelength periodic trapping potentials. This is the long-term project of this PhD thesis which aims at realizing such potentials based on a theoretical study (Bellouvet et al., 2018) that proposed to use doubly dressed state traps. This will be discussed in Chapter A. Such a system could also be useful to study different lattice geometry (square, triangular etc.), transport properties in the presence of defects, and long-range interactions mediated by light through the surface.

This PhD thesis aims at studying experimentally these doubly dressed states in free space. In particular, we will use them to realize in situ measurements of atomic densities with subwavelength resolutions. Subwavelength resolutions are indeed necessary for quantum gas microscopes to image atoms in subwavelength trapping potentials. This PhD is divided into the 6 following Chapters:

Chapter A which is theoretical. It gives a toolbox for the understanding of ultra-cold atoms and optical lattice physics. First, we describe the theory of evaporative cooling of a thermal atomic ensemble that leads to Bose-Einstein Condensation that we describe in the mean-field theory. Then, we discuss the physics of standard optical lattices, especially the band structure coming from a 1D periodic trapping potential. Finally, we will give the long-term motivation of this PhD based on a theoretical study (Bellouvet et al., 2018) to create subwavelength lattices by interfacing a nanostructured surface with ultra-cold atoms. One of the ingredients of the technique in (Bellouvet et al., 2018) is to drive many atomic transitions of ^{87}Rb using optical laser fields to engineer new dressed states with subwavelength periodic structures. We will discuss in detail such dressed states.

Chapter B focuses on the experimental setup which enables us to routinely reach Bose-Einstein Condensation in free space with ^{87}Rb atoms. We give a description of the existing experimental apparatus and its modifications to reach BEC. We also describe and characterize the three imaging axis of the experiment for time-of-flight and in situ imaging. The characterization of the BEC is performed through a quantitative analysis of the evolution of the phase-space density. The BEC can be manipulated via microwave magnetic fields that we will describe.

Chapter C reminds the theory of the interaction between a single multi-level quantum system and electric and magnetic fields using the formalism of master equations. Coherent, incoherent, and total scattering rates are computed using the evolution of the density matrix. We will deeply study the modifications of these scattering rates under perturbed

conditions in any saturation regime: under probe polarization changes, magnetic field offsets, and background incoherent fields. This leads to the definition of an effective two-level system (Veyron et al., 2021a) in the presence of all these effects that is the starting point to describe the response of a single quantum system to a coherent probe under perturbed conditions in the next chapter.

Chapter D focuses on the interaction of a coherent probe with an ensemble of single quantum systems using the coherent scattering rate of the effective two-level system. Particularly, through a series of measurements, we study quantitatively the transmission of a coherent probe through an atomic ensemble. We show that the single quantum system response is not sufficient to quantitatively explain the modification of the scattering atomic cross-section even for moderate optical densities (Veyron et al., 2021b). We propose an interpretation of the experimental results when probing an optically dense ensemble of two-level systems by standard saturating absorption imaging techniques, based on multiple scattering.

Chapter E presents the subwavelength imaging method that uses dressed excited states. The method uses a dipole force to dress the first excited state of ^{87}Rb atoms with an optical lattice creating a strong spatial variation of the excited state to get subwavelength resolutions of the ground state. The implemented experimental setup to generate such a light shift in the excited state is presented with its characterization. Finally, a quantitative analysis of the spatial resolution is performed using in situ absorption imaging with a homogeneous cold atom cloud in the ground state, for open and closed optical transitions.

Chapter F is an application of the subwavelength imaging method to a standard 1D optical trapping lattice. The setup consists of a double lattice of different periodicities with global commensurability. It enables us to resolve ground state lattice sites with a standard high numerical aperture diffraction-limited microscope. We will detail the loading of a BEC in the ground state of the optical lattice and give the band occupancy. Finally, we perform in situ subwavelength imaging with the second lattice of the excited state to image on-site atomic densities and compare the measured atomic density with theory.

FRENCH VERSION

La théorie de la mécanique quantique développée au début du XXe siècle a révolutionné la compréhension des phénomènes microscopiques. Par opposition à la physique classique, où un objet est ponctuel et décrit par une trajectoire, la mécanique quantique attribue des propriétés ondulatoires aux particules. De nos jours les applications d'une telle théorie sont souvent réparties en quatre catégories (O'Brien, Furusawa, and Vučković, 2009) : la communication sécurisée avec la cryptographie quantique (Gisin et al., 2002), l'information quantique pour les ordinateurs quantiques (Ladd et al., 2010; Slussarenko and Pryde, 2019), la métrologie pour des capteurs très sensibles (Degen, Reinhard, and Cappellaro, 2017) et les simulateurs quantiques pour modéliser de nouveaux matériaux (Altman et al., 2021; Georgescu, Ashhab, and Nori, 2014).

Différentes plateformes expérimentales ont émergées et été développées en parallèle pour ces applications. Parmi elles, les circuits supraconducteurs (Stassi, Cirio, and Nori, 2020), les boîtes quantiques (Barthelemy and Vandersypen, 2013), les circuits photoniques

(O'Brien, Furusawa, and Vučković, 2009), les ions piégés (Bruzewicz et al., 2019), les molécules polaires (DeMille, 2002) ou les atomes froids (Schäfer et al., 2020). Chacune ayant leurs propres avantages et inconvénients. Le principal moteur d'amélioration de ces systèmes est de maximiser le temps de cohérence (Wang et al., 2021; Bernon et al., 2013; Rigetti et al., 2012) en limitant le couplage à l'environnement qui est responsable de la décohérence. Cela peut être dû à des couplages résiduels avec des champs électromagnétiques, des phonons, des collisions dans des ensembles denses etc.

Les gaz dilués d'atomes froids ont l'avantage d'être bien isolés des champs électromagnétiques de l'environnement. De plus, de nombreux outils de piégeage et refroidissement par laser ont été développés dans les années 1980s pour les atomes alcalins neutres (Phillips, Prodan, and Metcalf, 1985). À partir d'un gaz atomique à température ambiante (300 K), les techniques de refroidissement laser et par évaporation ont conduit à l'observation de la Condensation de Bose-Einstein (Anderson et al., 1995). C'est une manifestation macroscopique de la caractéristique ondulatoire de particules bosoniques apparaissant à de très faibles températures, en dessous de 200 nK. Comme pour toute onde électromagnétique, il est possible d'associer une longueur d'onde caractéristique à une particule, connue sous le nom de longueur d'onde de De Broglie. Elle définit la longueur typique de cohérence d'un ensemble atomique et varie inversement avec la température. Quand cette longueur de cohérence est plus grande que la distance inter-particules, des interférences constructives des paquets d'ondes atomiques conduisent à une onde macroscopique très bien décrite par une seule fonction d'onde. Ce phénomène a été prédit par Einstein en 1925 (Einstein, 1924) à partir du travail de Bose sur les photons (Bose, 1924) et observé pour la premiére fois avec des atomes de Rubidium en 1995 (Anderson et al., 1995).

Depuis lors, les atomes ultra-froids ont été largement utilisés pour étudier de nombreux phénomènes et développer de nouvelles applications. Par exemple, les atomes froids sont des capteurs très sensibles. Ils sont utilisés dans les horloges atomiques (Campbell and Phillips, 2011) ou les capteurs inertiels utilisant l'interférométrie atomique (Debs et al., 2011). Des expériences pensées avec des condensats ont été proposées pour explorer la théorie quantique de la gravité (Howl, Penrose, and Fuentes, 2019; Howl et al., 2021).

Quand des particles interagissent entre elles via des collisions à deux corps, une théorie de champ moyen décrit très bien la dynamique d'un condensat (Dalfovo et al., 1999). Cette interaction peut être variée d'attractive à répulsive en utilisant des résonances de Feshbach (Inouye et al., 1998). Des corrections théoriques au-delà du champ moyen dues aux fluctuations quantiques (Pitaevskii and Stringari, 1998) sont expérimentalement mesurées. Par exemple, les gaz quantiques dipolaires fournissent une situation expérimentale pour observer des cristaux gouttelettes (Kadau et al., 2016). Dans ces cristaux, une force dipole-dipole magnétique attractive peut être exactement compensée par la somme l'interaction de contact répulsive usuelle et d'une force répulsive de Lee-Huang-Yang venant des corrections au-delà du champ moyen.

Pour le cas d'atomes fermioniques, obéissant au principe d'exclusion de Pauli, des gaz quantiques dégénérés peuvent aussi être réalisés avec les techniques de refroidissement par évaporation (DeMarco and Jin, 1999). Ils sont caractérisés par une fonction d'onde à N corps et tous les états propres en dessous de la température de Fermi sont occupés. Les condensats de Bose-Einstein et les gaz de Fermi dégénérés sont couramment produits en laboratoire car ils sont des objects quantiques macroscopiques bien décrits par une unique fonction d'onde. Elle est utilisée comme point de départ pour aller vers des systèmes corrélés à N corps.

Par exemple, des transitions de phase quantiques ont été observées comme la transition entre état superfluide et isolant de Mott (Greiner et al., 2002) avec des atomes ultra-froids bosoniques dans des réseaux optiques 3D. Des phases antiferromagnétiques ont été réalisées avec des atomes fermioniques ultra-froids dans des réseaux 2D (Mazurenko et al., 2017). Des atomes ultra-froids en dimensions réduites ont conduit à l'observation du passage à un état de Berezinskii-Kosterlitz-Thouless dans un gaz 2D (Hadzibabic et al., 2006) où des propriétés superfluides sont mesurables sans condensation de Bose-Einstein à température finie. Un dernier exemple peut être obtenu en variant l'interaction de contact dans un gaz d'atomes ultra-froids de fermions conduisant à l'observation du passage d'un superfluide type Bardeen-Cooper-Schrieffer avec des paires d'atomes délocalisés vers un condensat de paires liés (Greiner, Regal, and Jin, 2003). Tous ces exemples montrent que les atomes ultra-froids sont utilisés pour simuler des matériaux complexes. Beaucoup d'entre eux utilisent des réseaux optiques qui sont appropriés pour contrôler les énergies cinétiques et d'interaction dans le système.

Les caractéristiques à plusieurs corps peuvent être mesurées avec des effets d'interférence entre les sites du réseau avec des temps de vol (Greiner et al., 2002). Les atomes initialement piégés dans le réseau sont relâchés en chute libre avant d'interférer. Une seconde méthode consiste à mesurer in situ la densité atomique avec des microscopes à gas quantique (Schäfer et al., 2020) pour mesurer des corrélateurs de spin et caractériser l'ordre dans le réseau (Mazurenko et al., 2017). La dynamique de ces matériaux ne peut pas être calculée numériquement avec des ordinateurs en raison du grand nombre de particules impliquées. Les expériences avec des réseaux optiques sont alors utilisées comme simulateurs quantiques (Schäfer et al., 2020). Ce sont de vraies plateformes expérimentales qui reproduisent de façon très contrôlée le comportement des électrons dans les réseaux cristallins en physique du solide.

L'un des challenges en physique de la matière condensée est de réaliser des systèmes quantiques fortement corrélés. Par exemple, l'origine des cuprates supraconducteurs à haute température critique pourrait être trouvée en étudiant le modèle de Fermi-Hubbard à des températures beaucoup plus basses que la température de Fermi $T/T_F \ll 1$ (Moriya and Ueda, 2003; Lee, Nagaosa, and Wen, 2006). Diminuer la température signifie ici diminuer l'entropie par particule S/N pour aller vers de nouvelles transitions de phase quantiques (McKay and DeMarco, 2011). En effet diminuer la température à 500 pK a déjà été réalisé mais à constant S/N (Leanhardt et al., 2003). La température qui est nécéssaire est de l'ordre du picokelvin pour lesquelles les temps de thermalisation à N-corps sont de l'ordre de quelques dizaines de secondes. Ceci n'est pas compatible avec les systèmes d'atomes froids ayant un temps de vie fini venant des pertes par le vide avec la pression résiduelle (Lee, Nagaosa, and Wen, 2006), les sources de chauffage dans des réseaux optiques profonds (Gerbier and Castin, 2010; McKay and DeMarco, 2011) et des pertes par recombinaison à trois corps (Söding et al., 1999; Yoshida et al., 2018).

L'autre voie vers des systèmes fortement corrélés est d'augmenter les échelles d'énergie pour augmenter la température de Fermi. Ceci peut être réalisé dans des réseaux optiques en diminuant leur périodicité. Les réseaux optiques standards en champ lointain sont limités par diffraction à de 'larges' périodicités empêchant l'entrée dans ces régimes. Par conséquent, les réseaux optiques en champ proche offrent une voie vers la réduction des pas de réseau en battant la limite de diffraction. Les réseaux sub-longueur d'onde peuvent être réalisés en amenant des atomes proches de surfaces nanostructurées générant des potentiels de piégeage sub-longueur d'onde. C'est le projet long terme de ce travail de

thèse qui a pour but de réaliser de tels potentiels basés sur un travail théorique (Bellouvet et al., 2018) utilisant des pièges à états doublement habillés. Ceci sera discuté dans le chapitre A. De tels systèmes peuvent être utiles pour étudier différentes géométries de pièges (carré, triangulaire etc.), les propriétés de transport en présence de défauts cristallins et des interactions longues portées via des modes de surface.

Ce travail de thèse a pour objectif d'étudier expérimentalement ces états doublement habillés en espace libre. En particulier, nous les utiliserons pour réaliser des mesures in situ de densités atomiques avec des résolutions sub-longueur d'onde. Des résolutions sub-longueur d'onde sont en effet nécessaires pour les expériences de microscope à gaz quantique afin d'imager des atomes dans des potentiels de piégeage sub-longueur d'onde. Cette thèse est divisée en 6 chapitres:

Le chapitre A est théorique. Il donne une base théorique pour la compréhension de la physique des atomes ultra-froids et des réseaux optiques. Tout d'abord, nous décrivons la théorie du refroidissement par évaporation d'un ensemble atomique thermique qui conduit à la Condensation de Bose-Einstein que nous décrivons avec une théorie de champ moyen. Ensuite, nous discutons de la physique des réseaux optiques standards, en particulier la structure de bande venant d'un potentiel périodique de piégeage 1D. Enfin, nous donnons la motivation long terme de cette thèse basée sur une étude théorique (Bellouvet et al., 2018) pour créer des réseaux sub-longueur d'onde en amenant des atomes ultra-froids proches d'une surface nanostructurée. L'un des ingrédients de la technique de (Bellouvet et al., 2018) est d'interagir avec plusieurs transitions atomiques du Rubidium 87 en utilisant des champs lasers optiques pour réaliser de nouveaux états habillés avec des structures périodiques sub-longueur d'onde. Nous discuterons en détail de ces états habillés.

Le chapitre B développe le montage expérimental qui nous permet de réaliser au quotidien la Condensation de Bose-Einstein en espace libre avec des atomes de Rubidium 87. Nous donnons une description du montage expérimental existant et les modifications qui ont été apportées pour atteindre la CBE. Nous décrivons aussi et caractérisons les trois axes d'imagerie de l'expérience pour les imageries en temps de vol et in situ. La caractérisation du condensat est faite avec une analyse quantitative de l'évolution de la densité dans l'espace des phases. Le condensat peut être manipulé par des champ magnétiques micro-onde que nous décrirons.

Le chapitre C rappelle la théorie de l'interaction entre un système quantique multi-niveaux avec des champs électriques et magnétiques en utilisant le formalisme des équations maîtresses. Les taux de diffusion cohérent, incohérent et total sont calculés en utilisant l'évolution de la densité de matrice. Nous étudierons en détail les modifications de ces taux de diffusion dans des conditions perturbées pour tout régime de saturation: par des variations de polarisation, champs magnétiques de biais et champs incohérents de fond. Ceci conduit à la définition d'un système effectif à deux niveaux (Veyron et al., 2021a) en présence de tous ces effets qui est le point de départ de la description de la réponse d'un système quantique à un champ cohérent dans des conditions perturbées au prochain chapitre.

Le chapitre D étudie l'interaction d'un champ cohérent avec un ensemble de système quantiques en utilisant le taux de diffusion cohérent du système effectif à deux niveaux. En particulier, à travers une série de mesures, nous étudions quantitativement la transmission d'une sonde cohérente saturante à travers un ensemble atomique. Nous montrons

que la réponse de systèmes quantiques indépendants ne permet pas d'expliquer quantitativement les modifications de la section efficace d'absorption même dans des régimes de densité optique modérée (Veyron et al., 2021b). Nous proposons une interprétation des résultats expérimentaux, lorsqu'un ensemble d'atomes optiquement dense est sondé avec une imagerie par absorption saturante, basée sur des diffusions multiples.

Le chapitre E présente la méthode d'imagerie sub-longueur d'onde qui utilise des états excités habillés. Cette méthode utilise une force dipolaire pour habiller l'état excité des atomes de ^{87}Rb avec un réseau optique créant une forte variation spatiale de l'état excité pour avoir des résolutions sub-longueur d'onde de l'état fondamental. Le montage expérimental implémenté pour générer ces potentiels lumineux dans l'état excité est présenté avec sa caractérisation. Enfin, une analyse quantitative de la résolution spatiale est faite en utilisant une imagerie par absorption in situ avec un nuage atomique homogène dans l'état fondamental, pour des transitions optiques ouvertes et fermées.

Le chapitre F est une application de la méthode d'imagerie sub-longueur d'onde à un réseau optique 1D piégeant. Le montage expérimental comprend un double réseau de différentes périodicités avec une commensurabilité globale. Il est utilisé pour résoudre les sites du réseau de l'état fondamental avec un microscope standard, de forte ouverture numérique et limité par diffraction. Nous détaillons le chargement du condensat dans l'état fondamental du réseau et l'occupation des bandes. Enfin, nous réalisons l'imagerie in situ avec le second réseau dans l'état excité pour imager la densité atomique dans les sites et nous comparons la densité atomique obtenue avec la théorie.

Chapter A

Elements of theory for ultra-cold atoms and optical lattices

As mentioned in the general introduction, laser cooling and trapping techniques (Phillips, 1998) lead to a tremendous development of the field of cold atoms. In order to reach the Bose-Einstein condensation (BEC), methods known as evaporative cooling are commonly used to produce Bose-Einstein condensates. In this chapter, we give some relevant elements of context and theory in the field of ultra-cold atoms towards BEC with evaporative cooling.

The whole PhD thesis uses Rubidium 87 atoms. Its atomic structure and properties are given in Appendix I.i. In particular, we are interested in two optical transitions. The first is at 780.24 nm corresponding to the D_2-line which is the transition between $5^2S_{1/2}$ and $5^2P_{3/2}$. The second is at 1529.366 nm which is between $5^2P_{3/2}$ and $4^2D_{5/2}$.

In section A.1, we describe the theory of evaporative cooling of an atomic gas which is a common technique to reach the Bose-Einstein Condensation described in section A.2. The evaporative cooling scalings and the BEC properties will be quantitatively compared to experimental realizations in Chapter B. In section A.3, we discuss the physics of optical lattices which are interesting experimental platforms for implementing new Hamiltonians. Finally, in section A.4 we present the current limits preventing the exploration of new quantum phase transitions. We will discuss a solution using near-field traps for realizing subwavelength lattices widely described in (Bellouvet, 2018). This is among the leading long-term perspective of this PhD thesis.

A.1 Evaporative cooling

In this section, we consider an atomic gas trapped in a conservative potential and described by classical gas thermodynamics. We consider an atomic gas previously cooled down to the Doppler limit with Magneto-Optical Traps (MOT) and sub-Doppler cooling techniques (Phillips, 1998).

Performing evaporative cooling consists in removing high-velocity atoms in a thermal atomic ensemble and waiting for the others to thermalize via elastic collisions. The atomic cloud temperature is then reduced after thermalization. We recall the theory of evaporative cooling of a thermal gas for linear and harmonic traps. As trap geometries dictate the evaporation dynamics, we will give scaling laws for the two traps of interest

in this thesis. The first one is a linear magnetic trap where atomic magnetic moments interact with static magnetic field gradients. In such a trap, the geometry is invariant during spin-flip evaporation under external electromagnetic radiations. The second one is optical traps where atomic electric dipole moments interact with time-oscillating electric laser fields. Such a trap is approximated by a harmonic oscillator where the trap frequency decreases as the optical power decreases to perform optical evaporation.

A.1.1 Classical gas thermodynamics

The thermodynamics of a classical gas in a 3D trapping potential $U(\mathbf{r})$, following a Maxwell-Boltzmann distribution, has the following single-particle partition function (Luiten, Reynolds, and Walraven, 1996):

$$\zeta = (2\pi\hbar)^{-3} \int d^3\mathbf{r} d^3\mathbf{p} e^{-(U(\mathbf{r})+\mathbf{p}^2/2m)/(k_B T)} = \frac{V_0}{\Lambda^3}, \tag{A.1}$$

where $\Lambda = \sqrt{\frac{2\pi\hbar^2}{m k_B T}}$ is the thermal de Broglie wavelength and the effective trapping volume V_0 is given by:

$$V_0 = \int e^{-U(\mathbf{r})/k_B T} d^3\mathbf{r}. \tag{A.2}$$

The dynamics of N atoms at a temperature T in a conservative trap is described by thermodynamics quantities as the free energy A, the phase-space density D, the entropy S and the internal energy E (Lin et al., 2009; Luiten, Reynolds, and Walraven, 1996):

$$\begin{aligned} A =& - N k_B T \ln \zeta, \\ D =& n_0 \Lambda^3 = \frac{N}{\zeta}, \\ S =& - \frac{\partial A}{\partial T}, \\ E =& N k_B T^2 \frac{1}{\zeta} \frac{\partial \zeta}{\partial T}. \end{aligned} \tag{A.3}$$

At thermal equilibrium and for an infinitely deep trap, the 3D atomic density follows a Maxwell-Boltzmann distribution:

$$n(x, y, z) = n_0 e^{-U(\mathbf{r})/k_B T}, \tag{A.4}$$

where in this case, $n_0 = N/V_0$ is the central atomic density.

In practice, the maximum trap depth $U_0 = \eta k_B T$ is finite where η is defined by the ratio of the maximum trap depth over the atomic ensemble temperature. Eqs. (A.3) are used to get evaporative cooling scaling laws. Note that for $\eta < 8$, one has to use a truncated Boltzmann distribution (Lin et al., 2009) to simulate the exact dynamics.

Now, let us compute these thermodynamics properties for general 3D power-law traps (Bagnato, Pritchard, and Kleppner, 1987; Luiten, Reynolds, and Walraven, 1996) such that :

$$U(r) = C r^{3/\delta}, \tag{A.5}$$

where $C = \mu B^{'}$ for a linear trap with $\delta = 3$ and $C = \frac{1}{2}m\omega^2$ for a harmonic trap with $\delta = 3/2$.

The volume for the potential given by Eq. (A.5) reads:

$$V_0 = a\left(\frac{k_B T}{C}\right)^{\delta}, \tag{A.6}$$

where a is an integration constant ($a = 2$ for $\delta = 3$ and $a = \pi^{3/2}$ for $\delta = 3/2$).

The single-atom partition function for such a potential is given by:

$$\zeta = \lambda T^{\frac{3}{2}+\delta} C^{-\delta}, \tag{A.7}$$

where the constant $\lambda = a\left(\frac{mk_B}{2\pi\hbar^2}\right)^{\frac{3}{2}} k_B^{\delta}$ includes all prefactors.

From the partition function of Eq. (A.7), we compute the entropy, the phase-space density and the internal energy:

$$S = S_0(\delta) + Nk_B\left(\left(\frac{3}{2}+\delta\right)\ln(T) - \delta\ln(C)\right), \tag{A.8}$$

$$D = \lambda^{-1} N T^{-\frac{3}{2}-\delta} C^{\delta}, \tag{A.9}$$

$$E = (3/2+\delta) N k_B T, \tag{A.10}$$

where $S_0(\delta) = Nk_B\left(\ln(\lambda) + \frac{3}{2} + \delta\right)$.

An adiabatic compression or decompression where the trap stiffness C is varied at constant N, S is characterized by a constant phase-space density[1]. Setting $S_i = S_f$ with thermodynamics quantities noted as i for initial and f for final, and using the expression of the entropy (A.8) at constant number of particles ($N_i = N_f$), one can compute the scaling of the temperature :

$$\frac{T_f}{T_i} = \left(\frac{C_f}{C_i}\right)^{\frac{\delta}{\frac{3}{2}+\delta}}. \tag{A.11}$$

Eq. (A.11) shows the temperature scaling due to the compression or decompression of the traps for different trap geometries. In Table A.1 we explicit the form of the equations for linear and harmonics traps.

Evaporative cooling consists in removing high-velocity atoms and waiting for the remaining atoms to thermalize thanks to elastic collisions. We describe this collision dynamics in the next section.

[1] It can be easily shown using Eq. (A.8) and Eq. (A.9).

	Linear ($\delta = 3$)	Harmonics ($\delta = 3/2$)
C	$\mu B'$	$\frac{1}{2}m\omega^2$
D	$\frac{N}{T^{9/2}}\frac{1}{2}\left(\frac{2\pi\hbar^2(\mu B')^2}{mk_B^3}\right)^{3/2}$	$\frac{N}{T^3}\left(\frac{\hbar\omega}{k_B}\right)^3$
$\frac{T_f}{T_i}$	$\left(\frac{B'_f}{B'_i}\right)^{2/3}$	$\frac{\omega_f}{\omega_i}$

Table A.1: Phase-space density for linear and harmonic traps and temperature scalings for an adiabatic evolution of the trap for the linear and harmonic traps.

A.1.2 Two-body collision rate

The elastic two-body collision rate γ_c between two atoms is given by (Luiten, Reynolds, and Walraven, 1996; Dalibard, 1999a) :

$$\gamma_c = \sigma\bar{n}\bar{v}, \tag{A.12}$$

where $\sigma = 4\pi a^2$ is the scattering cross-section with a the s-wave scattering length, $\bar{n} = \int n(r)^2 dr^3 / \int n(r) dr^3$ is the mean atomic density with a thermal gas Boltzmann density distribution $n(r) = n_0 e^{-U(r)/k_B T}$ and central density $n_0 = N/V_0$, $\bar{v} = \frac{4}{\sqrt{\pi}}\sqrt{\frac{k_B T}{m}}$ the mean relative velocity. For a harmonic oscillator potential, we have $\bar{n} = n_0/2\sqrt{2}$ and for a linear potential (like a quadrupole magnetic trap) $\bar{n} = n_0/8$, giving respectively $\gamma_c = \sigma n_0 \sqrt{\frac{2}{\pi}}\sqrt{\frac{k_B T}{m}}$ and $\gamma_c = \sigma\frac{n_0}{2\sqrt{\pi}}\sqrt{\frac{k_B T}{m}}$.

Simulations of evaporative cooling show that a time of $3\gamma_c^{-1}$ is enough to consider that the atomic ensemble has thermalized.

A.1.3 Three-body collision rate

Atoms can recombine as pairs of molecules via three-body collisions at large atomic densities leading to atom losses which do not contribute to evaporative cooling. Indeed, both the molecule and the third energetic atom leave the trap. The loss rate scales (Ketterle, Durfee, and Stamper-Kurn, 1999; Brantut, 2009) as the square of the center density n_0 and is given by :

$$\Gamma_{3b} = K_{3b} n_0^2, \tag{A.13}$$

where for the state $|F_g = 2, m_F = 2\rangle$ of ^{87}Rb, $K_{3b} = 1.8 \times 10^{-29}$ s^{-1}cm^6. We will take this value to evaluate the three-body losses in our trap as it gives the order of magnitude of the losses. This value depends on the thermal fraction, condensed fraction and atomic state. For instance for condensed atoms in $|F_g = 1, m_F = -1\rangle$, the proportionality constant is $K_{3b} = 5.8 \times 10^{-30}$ s^{-1}cm^6. (Söding et al., 1999; Burt et al., 1997).

A.1.4 Evaporation scaling laws

In this section, we use the thermodynamics laws of a classical gas given in A.1.1 to compute the scaling laws of evaporation (Cohen-Tannoudji, 1997; Ketterle and Druten, 1996) that depend on the trapping potential $U(r)$. From the expression of the internal energy given by Eq. (A.10), the variation of energy dE is :

$$dE = (3/2 + \delta)Nk_B dT + (3/2 + \delta)Tk_B dN. \tag{A.14}$$

One can find another equation for dE with the evaporated atoms. Indeed, dN atoms of averaged energy $(\eta + \kappa)k_B T$ leave the trap. η has already been defined as $U_0 = \eta k_B T$. κ, depending on η and ranging in $0 \leq \kappa \leq 1$ (O'Hara et al., 2001), is the extra energy above the trap depth threshold. During the evaporation, if trap frequencies evolve then the potential energy changes (O'Hara et al., 2001). A normalized parameter $\nu \equiv \frac{d\omega/\omega}{dU_0/U_0}$ (Brantut, 2009) can be used to quantify that potential energy change. For an optical dipole trap approximated as a harmonic one, $\nu = 1/2$ (O'Hara et al., 2001) as $dU_0/U_0 = 2d\omega/\omega$, and for a linear trap $\nu = 0$ as the trap frequency is independent of the trap depth. The variation of potential energy is then $\nu(dU_0/U_0)E$. Finally, the total energy change reads :

$$dE = (\eta + \kappa)k_B T dN + \nu(dU_0/U_0)E. \tag{A.15}$$

To get Eq. (A.15), three-body collisions and background gas collisions are neglected but they can be included as another loss term (Ketterle and Druten, 1996).

Combining equations (A.14) and (A.15) gives the following scaling law between the ratios of temperature and atom numbers:

$$\begin{aligned} \frac{T_f}{T_i} &= \left(\frac{N_f}{N_i}\right)^{\alpha}, \\ \text{with } \alpha &= \frac{\eta + \kappa - (3/2 + \delta)}{(1 - \nu)(3/2 + \delta)}. \end{aligned} \tag{A.16}$$

A value $\alpha > 1$ means that the temperature decreases for minimum atom number losses and defines the evaporation efficiency. This is the main figure of merit of evaporative cooling.

The phase-space density D changes through variations of N, T and ω. As a result, using Eq. (A.16) and (A.9), the phase-space density becomes:

$$\begin{aligned} \frac{D_f}{D_i} &= \left(\frac{N_f}{N_i}\right)^{\beta}, \\ \text{with } \beta &= 1 - \frac{3}{2}\alpha + \alpha\delta(2\nu - 1). \end{aligned} \tag{A.17}$$

Similarly, using Eq. (A.12), the collision rate variation is :

$$\begin{aligned} \frac{\gamma_{c,f}}{\gamma_{c,i}} &= \left(\frac{N_f}{N_i}\right)^{\kappa}, \\ \text{with } \kappa &= 1 + \frac{1}{2}\alpha + \alpha\delta(2\nu - 1). \end{aligned} \tag{A.18}$$

Runaway evaporation happens when $d\gamma_c > 0$, for $\delta = \frac{3}{2}$ one has $\eta + \kappa > 6$. For optical traps approximated by harmonic traps, the trap frequency decreases when the trap depth decreases making runaway evaporation difficult.

The optical density at the cloud center, as defined later in the thesis in section D.1, is $b(0,0) = \sigma_0 \int n(0,0,z)dz$. Using Eq. (A.4), one can show that $b(0,0) \propto \frac{N}{V_0} T^{\delta/3}$. The collision rate of Eq. (A.12) can be written as $\gamma_c \propto \frac{N}{V_0} T^{1/2}$. This means that for a harmonic trap where $\delta = 3/2$, $b(0,0)$ is directly proportional to the collision rate.

To summarize, we give the scalings laws for evaporative cooling in linear traps and in dipole traps approximated as harmonic traps in Table A.2. It will be compared to experimental characterizations in Chapter B. Note that for an ideal optical trap where the harmonic oscillator trap frequency does not change as the trap depth is reduced, then $\delta = 3/2$ and $\nu = 0$.

	MT ($\delta = 3, \nu = 0$)	DT ($\delta = 3/2, \nu = 1/2$)
α	$2/9\,(\eta + \kappa - 9/2)$	$2/3\,(\eta + \kappa - 3)$
β	$1 - 9\alpha/2$	$1 - 3\alpha/2$
κ	$1 - 5\alpha/2$	$1 + \alpha/2$

Table A.2: Scaling laws for a linear magnetic trap and a harmonic dipole trap.

A.2 Bose Einstein Condensation

In the previous section, we have described evaporative cooling which is commonly used in cold atom experiments to reach the quantum degeneracy. In particular, at low temperatures, in the case of bosons in the dilute regime, atoms form a Bose-Einstein condensate which corresponds to a macroscopic state where all atoms can be described by a single wavefunction. We are going to describe such a state at finite and zero temperatures for a 3D gas.

A.2.1 Bose-Einstein Condensation at finite temperature

The Bose-Einstein condensation (BEC) of N particles happens when the maximum number of accessible excited states becomes equal to the particle number (Dalfovo et al., 1999). Extra particles are then occupying the same ground state.

For a 3D harmonic trap with mean trap frequency $\tilde{\omega}$ and neglecting interactions (Dalfovo et al., 1999), the critical temperature of the phase transition at which the BEC occurs is given by:

$$T_c = 0.94 \frac{\hbar\tilde{\omega}}{k_B} N^{1/3}. \tag{A.19}$$

The density of a Bose gas (Dalfovo et al., 1999) $n(\mathbf{r})$ is characterized by a condensed density $n_0(\mathbf{r})$ and a thermal density $n_T(\mathbf{r})$:

$$n(\mathbf{r}) = n_0(\mathbf{r}) + n_T(\mathbf{r}), \tag{A.20}$$

where $n_0(\mathbf{r})$ is appreciable only below T_c.

The condensed density is given by the ground state wavefunction $\phi_0(\mathbf{r})$:

$$n_0(\mathbf{r}) = N_0 |\phi_0(\mathbf{r})|^2. \tag{A.21}$$

In 3D the thermal density including the full Bose-Einstein statistics in the thermodynamic limit is given by:

$$n_T(\mathbf{r}) = \int d^3\mathbf{p}(2\pi\hbar)^{-3}\left(e^{\beta\epsilon(\mathbf{p},\mathbf{r})}-1\right)^{-1}, \tag{A.22}$$

where the energy includes the kinetic and external potential energies, $\epsilon(\mathbf{p},\mathbf{r}) = p^2/2m + V_{ext}(\mathbf{r})$. Performing the integral[2] of Eq. (A.22) leads to the Bose-enhanced Gaussian density:

$$n_T(\mathbf{r}) = \lambda_T^{-3} g_{3/2}(e^{-\beta V_{ext}(\mathbf{r})}). \tag{A.23}$$

A.2.2 Bose Einstein Condensation at zero temperature

The dynamics of a 3D BEC[3] is usually described at zero temperature in the dilute regime where $a^3 n_0 \ll 1$ (Dalfovo et al., 1999). This is justified as for instance, in ^{87}Rb BECs, the s-wave scattering length is $a = 5$ nm and the density is $n_0 = 10^{20}$ at/m^3 so we get $a^3 n_0 \approx 10^{-5}$.

The mean-field equation (Dalfovo et al., 1999) describing the wavefunction dynamics of N ($N \gg 1$) interacting particles in a potential $V(t,\mathbf{r})$ is the Gross-Pitaevski equation (GPE). It considers that a particle sees a mean-field created by the other $N-1$ particles. The resulting equation is a nonlinear Schrödinger equation that includes the mean-field term. In 3D, the GPE is given by (Dalfovo et al., 1999):

$$i\hbar\frac{\partial\Psi(\mathbf{r},t)}{\partial t} = \left(-\frac{\hbar^2}{2m}\Delta + V(t,\mathbf{r}) + U_0|\Psi(\mathbf{r},t)|^2\right)\Psi(\mathbf{r},t), \tag{A.24}$$

where $U_0 = 4\pi\hbar^2 a_S/m$ comes from the contact interaction of s-wave scattering in 3D. The density is given by $n(\mathbf{r}) = |\Psi(\mathbf{r})|^2$ and is normalized to the atom number $\int n(\mathbf{r})d\mathbf{r}^3 = N$.

The ground state wavefunction of a GPE is given by $\Psi(\mathbf{r},t) = \Psi(\mathbf{r})e^{-i\mu t}$ where μ is the chemical potential. For a time-independent potential, solutions are stationary and given by the resolution of the equation:

$$\left(-\frac{\hbar^2}{2m}\Delta + V(\mathbf{r}) + U_0|\Psi(\mathbf{r})|^2\right)\Psi(\mathbf{r}) = \mu\Psi(\mathbf{r}). \tag{A.25}$$

In the following, we consider the 3D harmonic potential $V(\mathbf{r}) = \sum_{i=1}^{3}\frac{1}{2}m\omega_i^2 r_i^2$ with mean frequency $\tilde{\omega} = (\omega_1\omega_2\omega_3)^{1/3}$ and characteristic length $a_{OH} = \sqrt{\hbar/m\tilde{\omega}}$. We describe the two usual limit cases of the GPE which are the weak and strong interaction regimes (Ketterle, Durfee, and Stamper-Kurn, 1999; Dalfovo et al., 1999):

[2]Using the gamma function $\Gamma(\alpha)$, $g_\alpha(z) = \sum_{n=1}^{\infty} z^n/n^\alpha$ and $\Gamma(\alpha)g_\alpha(z) = \int_0^z \frac{x^{\alpha-1}}{z^{-1}e^x-1}dx$ for $\Gamma(3/2) = \sqrt{\pi}/2$.

[3]Similar equations can be derived in 2D and 1D. These low dimension regimes occur when strong confinements freeze the evolution in certain directions. Comparisons to the 3D equation can be found in (Zamora-Zamora et al., 2019).

Weak interactions : it is the regime where the interaction energy is negligible compared to the kinetic one. Then, the GPE simplifies to the usual Schrödinger equation:

$$\left(-\frac{\hbar^2}{2m}\Delta + V(\mathbf{r})\right)\Psi(\mathbf{r}) = \mu\Psi(\mathbf{r}). \tag{A.26}$$

The solution for the atomic density is a Gaussian function:

$$n(\mathbf{r}) = \frac{N_0}{\pi^{3/2}}\prod_{i=1}^{3}\frac{1}{r_{i,0}}e^{-r_i^2/r_{i,0}^2}, \tag{A.27}$$

where the harmonic oscillator radius in direction i is $r_{i,0} = \sqrt{\hbar/m\omega_i}$.

Strong interactions : this is the Thomas-Fermi regime where the interaction energy is large compared to the kinetic one. In this case, the GPE simplifies to:

$$\left(V(\mathbf{r}) + U_0|\Psi(\mathbf{r})|^2\right)\Psi(\mathbf{r}) = \mu\Psi(\mathbf{r}), \tag{A.28}$$

and the solution for the atomic density is given by :

$$n(\mathbf{r}) = \max\left(\frac{\mu - V(\mathbf{r})}{U_0}, 0\right) = \frac{15}{8\pi}\frac{N}{\prod_{i=1}^{3} r_{i,0}}\max\left(1 - \sum_{i=1}^{3}\frac{r_i^2}{r_{i,0}^2}, 0\right), \tag{A.29}$$

where the chemical potential is $\mu = n(0)U_0 = \frac{\hbar\tilde{\omega}}{2}\left(\frac{15Na_S}{a_{OH}}\right)^{2/5}$ and the Thomas-Fermi radius in direction i is $r_{i,0} = \sqrt{2\mu/m\omega_i^2}$.

A.3 Optical lattices

We have described the formalism to quantify a Bose-Einstein Condensate which is the starting point for loading optical lattices described in this section. We start with a 1D optical lattice and compute the band structure[4]. It enables us to define the Bloch waves that are used to describe the ground-state wavefunction.

A.3.1 1D lattice band structure

We follow (Greiner, 2003) to derive the well-known 1D band structure of a 1D lattice. We start with the Hamiltonian of a single-atom in a periodic trapping potential $V(x)$ given by:

$$H = \frac{p^2}{2m} + V(x). \tag{A.30}$$

[4]It will be used for the experimental calibration of the trap depth of the 1064 nm lattice in IV.ii.

For a 1D sinusoidal potential formed by two counter-propagating plane waves with wavevector $k = 2\pi/\lambda$ and wavelength λ, we have:

$$V(x) = \frac{V_0}{2}\left(1 + \cos\left(\frac{2\pi}{d}x\right)\right), \tag{A.31}$$

where $d = \lambda/2$ is the lattice period.

The corresponding trap frequency ω at the bottom of a lattice site is given by:

$$\omega = \frac{2}{\hbar}\sqrt{V_0 E_r}. \tag{A.32}$$

In Eq. (A.32), the recoil energy is defined as:

$$E_r = \frac{\hbar^2 k^2}{2m}, \tag{A.33}$$

which is the typical energy scale to express lattice depths with an adimensional parameter s such that $V_0 = sE_r$.

The Schrödinger equation with the time-independent Hamiltonian of Eq. (A.30) can be written using Bloch wavefunctions $\Phi_q^n(x)$ for a band n and a quasi-momentum q:

$$H\Phi_q^n(x) = E_q^{(n)}\Phi_q^n(x). \tag{A.34}$$

The solutions of Eq. (A.34) are the Bloch wavefunctions defined by:

$$\Phi_q^n(x) = e^{iqx/\hbar}u_q^n(x). \tag{A.35}$$

The Bloch's theorem states that the function $u_q^n(x)$ has the same periodicity as the potential meaning that $u_q^n(x+d) = u_q^n(x)$ which implies that $\Phi_q^n(x+d) = e^{iqd/\hbar}\Phi_q^n(x)$.

The decomposition of the periodic function $u_q^n(x)$ onto the plane wave basis such that $u_q^n(x) = \sum_l c_l^{(n,q)}(x)e^{i2lkx}$ leads to the expansion of Bloch wavefunctions in the plane wave basis:

$$\Phi_q^n(x) = \sum_l c_l^{(n,q)} e^{i(2l\hbar k+q)x/\hbar}. \tag{A.36}$$

Finally Eq. (A.34) becomes:

$$\sum_l H_{l',l}c_l^{(n,q)} = E_q^{(n)}c_{l'}^{(n,q)}, \text{ where } H_{l',l} = \begin{cases} (2l + \frac{q}{\hbar k})^2 E_r + sE_r/2 & \text{if } l = l', \\ sE_r/4 & \text{if } |l - l'| = 1, \\ 0 & \text{otherwise.} \end{cases} \tag{A.37}$$

In Fig. A.1, we show the band structure as a function of s which are the eigenenergies obtained by the diagonalization of Eq. (A.37). At low trap depths, the energies follow the kinetic energy of a free particle. As the trap depth is increased, a gap between consecutive bands appears at the border of the Brillouin zone $q = \pm\hbar k$. At very large trap depths,

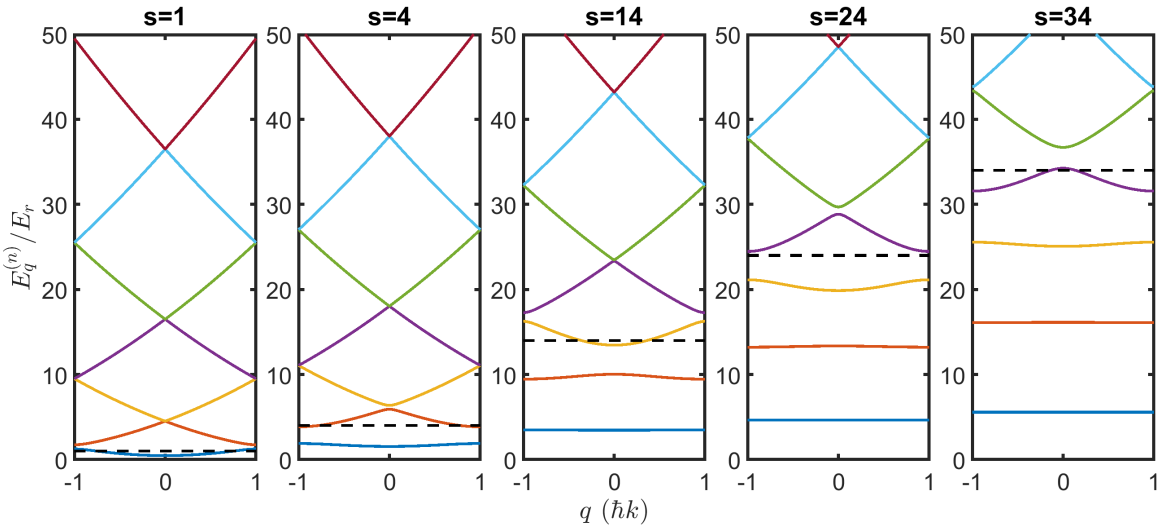

Figure A.1: Band structure from bands $n = 0$ to $n = 6$ for many trap depths s. The dashed black lines are the lattice depth levels.

low index bands are flat and their average energy tends to that of a harmonic oscillator of frequency ω (Eq. (A.32)).

The limit $V_0/E_r \gg 1$ corresponds to the tight-binding limit where Wannier functions $w_n(x)$ can be used to describe localized wavefunctions for the site j and band n. They are linked to Bloch wavefunctions ϕ_q^n by a discrete Fourier transform:

$$w_n(x - x_j) = c^{-1/2} \sum_{q=-\pi\hbar/d}^{\pi\hbar/d} e^{-iqx_j/\hbar} \phi_q^n(x), \tag{A.38}$$

where c is a normalization constant which can be found using the normalization constraint $\int w_n^*(x - x_j) w_m(x - x_{j'}) dx = \delta_{n,m}\delta_{x_j,x_{j'}}$.

A.3.2 Quantum harmonic oscillator

For large trap depths, Wannier functions previously defined can be approximated by a quantum harmonic oscillator (QHO) with trap frequency ω. Its wavefunction $\phi_n^{(HO)}$ for the band n is given by Hermite polynomials $H_n(x)$:

$$\phi_n^{(HO)}(x) = \frac{1}{\sqrt{2^n n!}} \left(\frac{1}{\pi a_0^2}\right)^{1/4} e^{-\frac{x^2}{2}} H_n(x), \tag{A.39}$$

where x is in unit of a_0 which is the harmonic oscillator ground state width:

$$a_0 = \sqrt{\frac{\hbar}{m\omega}}. \tag{A.40}$$

QHO solutions describe well on-site atomic densities in the vicinity of the potential minima. Away from the minima, their exponentially decaying tails lead to underestimated tunneling rates and Wannier functions should be used instead (Greiner, 2003).

A.3.3 Thermal state in a QHO

Following (McDonald et al., 2019), it can be shown that for a thermal state, the probability distribution in a single QHO is exactly given by a Boltzmann weighted sum of the QHO eigenstates:

$$P(x) = \frac{1}{Z}\sum_{n=0}^{\infty} e^{-\frac{E_n}{k_B T}} \left(\frac{1}{2^n n!}\pi^{-1/2} e^{-x^2} H_n^2(x)\right) \propto e^{-\left(1-\frac{2e^{-\hbar\omega/k_B T}}{1+e^{-\hbar\omega/k_B T}}\right)x^2}, \tag{A.41}$$

where $Z = 1/2\sinh(\hbar\omega/2k_B T)$ and x is in unit of a_0.

Eq. (A.41) is a Gaussian function with a width depending on temperature T:

$$\sigma(T) = \sigma_0\sqrt{\coth\left(\frac{\hbar\omega}{2k_B T}\right)}, \tag{A.42}$$

where the width of the density at zero temperature is $\sigma_0 = a_0/\sqrt{2}$.

This solution is exact for a QHO and a very good approximation for strong lattice depths that will be used in Chapter F where such widths are experimentally measured in a 1D lattice. Intermediate trap depths from $s = 0$ to 40 is the interesting regime of cold atoms in standard lattices that takes place where the dynamics is dictated by tunneling times and interaction times. In the following, we describe such a dynamics of a wavefunction in a 3D optical lattice.

A.3.4 Bose-Hubbard Hamiltonian

The dynamics of spinless bosonic particles in a periodic trapping potential is described by a kinetic energy term including the trapping potential and a contact interaction term (Greiner, 2003):

$$H = \int dx^3 \hat{\Psi}^\dagger(\mathbf{x})\left(-\frac{\hbar^2}{2m}\nabla^2 + V(\mathbf{x})\right)\hat{\Psi}(\mathbf{x}) + \frac{1}{2}\frac{4\pi a_s \hbar^2}{m}\int dx^3 \hat{\Psi}^\dagger(\mathbf{x})\hat{\Psi}^\dagger(\mathbf{x})\hat{\Psi}(\mathbf{x})\hat{\Psi}(\mathbf{x}), \tag{A.43}$$

where $\hat{\Psi}(\mathbf{x})$ is a boson field operator and $V(\mathbf{x})$ is the total trapping potential which includes an external confinement and a trapping lattice potential.

The boson field operator is expanded in the Wannier function basis $w(\mathbf{x} - \mathbf{x_i})$ in the single-band approximation, usually the ground state, such that $\hat{\Psi}(\mathbf{x}) = \sum_i \hat{a}_i w(\mathbf{x} - \mathbf{x_i})$, where $\hat{a}_i$ (resp. $\hat{a}_i^\dagger$) are the annihilation (resp. creation) operators of a boson on the i^{th} site. Considering the leading terms in the Hamiltonian (A.43) which are tunneling between only neighboring sites $< i, j >$ and on-site interactions, Eq. (A.43) leads to the Bose-Hubbard Hamiltonian:

$$H = -t\sum_{<i,j>} \hat{a}_i^\dagger \hat{a}_i + \sum_i (\epsilon_i - \mu)\hat{n}_i + \sum_i \frac{U}{2}\hat{n}_i(\hat{n}_i - 1). \tag{A.44}$$

The first term of Eq. (A.44) is a tunneling term between neighboring sites and is given by $t = -\int dx^3 w(\mathbf{x}-\mathbf{x_i})(-\frac{\hbar^2\nabla^2}{2m} + V_{lat}(\mathbf{x}))w(\mathbf{x}-\mathbf{x_j})$.

The second term is due to the external potential confinement which rises the i^{th} site energy by ϵ_i. The excess of energy is $(\epsilon_i - \mu)$ per particle where μ is the chemical potential.

The third term is the on-site repulsion due to interactions with $U = \frac{4\pi\hbar^2 a_s}{m}\int |w(\mathbf{x})|^4 dx^3$.

From Eq. (A.44), the ratio of the kinetic energy given by the tunneling term over the interaction energy is proportional to t/U. Tuning the trap depth enables one to go from the regime of weak interactions ($t \gg U$) known as the superfluid regime where the ground state is delocalized over the lattice, to strong interactions ($t \ll U$) known as the Mott-insulator regime where atoms are localized onto lattice sites.

Such a regime has been observed in a 3D standard optical lattice in (Greiner, 2003) by tuning the lattice trap depth. It allows them to decrease the kinetic energy term by decreasing the tunneling term which can then compete with the interaction term. Scalings of such energies are given in the next section.

A.3.5 Energy scales in far-field optical lattices

For a 3D trapping lattice potential and assuming that the wavefunction is given by the ground state Wannier function well-approximated by the harmonic oscillator ground state ($V_0 \gg E_r$), the tunneling t and interaction U energies are given by (Bellouvet, 2018):

$$t = \frac{4}{3\sqrt{\pi}} E_r \left(\frac{V_0}{E_r}\right)^{3/4} e^{-2\sqrt{V_0/E_r}}, \tag{A.45}$$

$$U = \sqrt{\frac{8}{\pi}}\frac{\pi}{d} a_s E_r \left(\frac{V_0}{E_r}\right)^{3/4}. \tag{A.46}$$

Mott-superfluid transition occurs around $V_0/E_r = 15$ for a 3D lattice (Greiner, 2003; Bellouvet, 2018). For $d = 500$ nm and ^{87}Rb, it corresponds to $t \approx 0.3$ nK and $U \approx 44$ nK (Bellouvet, 2018).

To go into other phase transitions to study for instance quantum magnetism which includes spin-interactions between atoms, in the regime $U \gg t$ the characteristics energy is the super-exchange energy J scaling as t^2/U. For $t \approx 0.3$ nK and $U \approx 44$ nK, we have $J \approx 2$ pK, or equivalently 0.04 Hz, yielding $U \gg t \gg J$. In order to be able to study the dynamics of such systems, atoms have to be kept for a very long time in a deep lattice potential. However, this is not compatible with cold atom systems which have a finite lifetime (three-body losses, heating when increasing the lattice depth, vacuum losses).

One of the solutions[5] to overcome that limit is to increase all energy scales (U, t, J) by decreasing the lattice periodicity d. Standard far-field optical lattices are limited by diffraction to 'large' periodicities and cannot be used anymore. Near-field lattices offer a way to reduce the lattice spacing to beat the diffraction limit by interfacing atoms with a nanostructured surface generating subwavelength periodic trapping potentials. Such potentials generated by a method developed by my predecessor (Bellouvet, 2018; Bellouvet

[5]See (Bellouvet, 2018) for a short review.

et al., 2018) will be described in the following sections using the dipole force and the dressed state picture.

A.4 Towards subwavelength lattices

In order to understand the physics behind doubly dressed states, we first remind the dressed state picture for a two-level system interacting with a laser field which enables us to define the dipole force and the dipole trap potential. Then, we will derive the dipole force in the case of a doubly dressed state and apply it to Rubidium 87 in a simple experimental case. Finally, we will mention how this can be used to generate subwavelength lattice potentials.

A.4.1 Dressed state

In this section, following (Dalibard and Cohen-Tannoudji, 1985) we remind the results of the interaction of a two-level system with internal frequency ω_0 with an external coherent laser field with frequency ω under the second quantization formalism.

We work here in the semi-classical approximation where the position operator is replaced by its expectation value such that $\mathbf{r} =< \mathbf{R} >$. It is justified since the wavepacket width is small compared to the field wavelength ($\Delta r \ll \lambda$). We additionally consider that the Doppler dispersion is small compared to the linewidth of the atomic transition ($k\Delta v \ll \Gamma$). Using these two conditions and the Heisenberg inequality on position and momentum, we find that the change in kinetic energy is small compared to the transition linewidth. In the following treatment, the kinetic energy is therefore neglected.

The total Hamiltonian H_{tot} that describes the system is composed of: an internal two-level Hamiltonian $H_A = \hbar\omega_0 b^\dagger b$, the radiation field Hamiltonian on the laser mode $H_R = \hbar\omega_L a_L^\dagger a_L$ and the interaction given by the electric-dipole Hamiltonian under the rotating wave approximation $V = -\mathbf{d}.\mathbf{E_L}(\mathbf{r})b^\dagger a_L + h.c.$. In the following, we include the detuning as $\delta = \omega_L - \omega_0$.

In the uncoupled basis (bare states), the eigenstates and eigenvalues of $H_A + H_R$ are:

$$\begin{aligned} &\{|g, n-1\rangle\,,\ |e, n-1\rangle\,,\ |g, n\rangle\,,\ |e, n\rangle\,,\ |g, n+1\rangle\}, \\ &\hbar\omega_L(n-1),\ \hbar(\omega_L n - \delta),\ \hbar\omega_L n,\ \hbar(\omega_L(n+1) - \delta),\ \hbar\omega_L(n+1). \end{aligned} \tag{A.47}$$

The energy diagram then consists of pairs of states separated by ω_L. Now if we consider the coupling of the two states $|e, n\rangle$ and $|g, n+1\rangle$, the total Hamiltonian reads:

$$H_{tot} = \hbar \begin{pmatrix} \omega_L(n+1) - \delta & \frac{\omega_1(r)}{2} e^{-i\phi(r)} \\ \frac{\omega_1(r)}{2} e^{+i\phi(r)} & \omega_L(n+1) \end{pmatrix}, \tag{A.48}$$

where $\langle e, n|\, V\, |g, n+1\rangle = -\sqrt{n+1}\mathbf{d}.\mathbf{E_L}(\mathbf{r}) \equiv \frac{\hbar\omega_1(r)}{2} e^{i\phi(r)}$. Therefore, $\omega_1(r)$ depends on the average photon number n. In the following, we will restrict to the case of a coherent state with $n \gg 1$ yielding $n+1 \approx n$. The width of the corresponding Poisson distribution is small compared to n so the states $|n\rangle$ and $|n+1\rangle$ are considered to be described by the same amplitude $\omega_1(r)$.

The eigenstates $\{|1,n;r\rangle, |2,n;r\rangle\}$ and eigenvalues E_{1n}, E_{2n} of Eq. (A.48) are:

$$\begin{aligned} E_{1n} =& \hbar\omega_L(n+1) - \frac{\hbar\delta}{2} + \frac{\hbar\Omega(r)}{2}, \\ E_{2n} =& \hbar\omega_L(n+1) - \frac{\hbar\delta}{2} - \frac{\hbar\Omega(r)}{2}, \\ |1,n;r\rangle =& e^{i\phi/2}\cos(\theta(r))\,|e,n\rangle + e^{-i\phi/2}\sin(\theta(r))\,|g,n+1\rangle\,, \\ |2,n;r\rangle =& -e^{i\phi/2}\sin(\theta(r))\,|e,n\rangle + e^{-i\phi/2}\cos(\theta(r))\,|g,n+1\rangle\,. \end{aligned} \tag{A.49}$$

where $\Omega(r) = \sqrt{\delta^2 + \omega_1^2(r)}$, $\cos(2\theta(r)) = -\delta/\Omega(r)$, $\sin(2\theta(r)) = \omega_1(r)/\Omega(r)$.

Eq. (A.49) defines the dressed atom by the field.

A relaxation term has to be added to properly describe the couplings between the states. This can be done using the optical Bloch equations on the bare states that will be extensively described in Chapter C. The density matrix ρ describes the system whose dynamics is driven by both the total Hamiltonian and the spontaneous emission. The populations and coherences in the uncoupled basis (i,j for g or e) or the dressed basis (k,m for 1 or 2) as follows:

$$\begin{aligned} \rho_{ij} =& \sum_n \langle i,n|\,\rho\,|j,n\rangle\,, \\ \rho_{km} =& \sum_n \langle k,n|\,\rho\,|m,n\rangle\,. \end{aligned} \tag{A.50}$$

For $n \gg 1$, using Eq. (A.50), we get the following relations between the density matrix elements of the two basis:

$$\begin{aligned} \rho_{11} =& \cos^2(\theta)\rho_{ee} + \sin^2(\theta)\rho_{gg} + \sin(\theta)\cos(\theta)\left(e^{i\phi}\rho_{ge} + c.c.\right), \\ \rho_{22} =& \sin^2(\theta)\rho_{ee} + \cos^2(\theta)\rho_{gg} - \sin(\theta)\cos(\theta)\left(e^{i\phi}\rho_{ge} + c.c.\right). \end{aligned} \tag{A.51}$$

Using the results of the optical Bloch equations in the bare basis, one gets the solutions of ρ_{ij}, from which we can compute ρ_{km} in the dressed basis.

The mean value of the force acting on the atom $\mathbf{f}(\mathbf{r}) = <\mathbf{F}(\mathbf{r})>$ is computed using the standard operator for the force $\mathbf{F} = \frac{d\mathbf{P}}{dt}$ and the Heisenberg equation $\frac{d\mathbf{P}}{dt} = \frac{i}{\hbar}[H_{tot}, \mathbf{P}] = -\boldsymbol{\nabla}V$. This mean force is the sum of the dipole force $\mathbf{f}_{dip}(\mathbf{r})$ proportional to the intensity gradient $\boldsymbol{\nabla}\omega_1$ and the radiation-pressure force $\mathbf{f}_{RP}(\mathbf{r})$ proportional to the phase gradient $\boldsymbol{\nabla}\phi$. Using $b^\dagger = |e\rangle\langle g|$ and the bare states variables, the total force reads:

$$\mathbf{f}(\mathbf{r}) = \frac{\hbar\omega_1}{2} i\boldsymbol{\nabla}\phi\left(\rho_{eg}e^{-i\phi} - \rho_{ge}e^{i\phi}\right) - \frac{\hbar\boldsymbol{\nabla}\omega_1}{2}\left(\rho_{eg}e^{-i\phi} + \rho_{ge}e^{i\phi}\right). \tag{A.52}$$

The mean dipole force corresponds to the second term in Eq. (A.52):

$$\mathbf{f}_{dip}(\mathbf{r}) = -\frac{\hbar\boldsymbol{\nabla}\omega_1}{2}\left(\rho_{eg}e^{-i\phi} + \rho_{ge}e^{i\phi}\right). \tag{A.53}$$

Using the dressed state variables and setting $\phi = 0$, the mean dipole force reduces to:

$$\mathbf{f}_{dip}(\mathbf{r}) = -\left(\boldsymbol{\nabla}E_{2n}\rho_{22} + \boldsymbol{\nabla}E_{1n}\rho_{11}\right) - \hbar\Omega\boldsymbol{\nabla}\Theta\left(\rho_{12} + \rho_{21}\right), \tag{A.54}$$

where $\boldsymbol{\nabla}\Theta = -\delta\boldsymbol{\nabla}\omega_1/2\Omega^2$.

In the limit of well-resolved dressed states *i.e.* either $\delta \gg \Gamma$ or $\omega_1 \gg \Gamma$, the steady-state dressed coherences are exactly zero ($\rho_{12}^{(st)} = 0$). So in Eq. (A.54), the second term representing non-adiabaticity vanishes. The dressed state dipole force is then only given by the dressed populations.

We use the mean dipole force in bare state basis of Eq. (A.53) and the steady-state solution of the optical Bloch equations $\rho_{ge}^{(st)} = -\frac{\omega_1/2}{\delta^2+\Gamma^2/4}(i\frac{\Gamma}{2} + \delta)(\rho_{ee} - \rho_{gg})$ (derived later in Chapter C) to get:

$$\mathbf{f}_{dip}(\mathbf{r}) = \frac{\hbar\Gamma}{2}\frac{(\delta/\Gamma)}{1+4(\delta/\Gamma)^2}(\rho_{ee} - \rho_{gg})\boldsymbol{\nabla}s, \tag{A.55}$$

where we have defined the saturation parameter $s(r) = 2\omega_1(r)^2/\Gamma^2 = I/I_{sat}$ for a laser intensity I and a saturation intensity of the two-level transition I_{sat}.

Finally, the dipole potential can be computed for an atom moving by the quantity **dr** by integrating the work of the dipole force:

$$\mathbf{f}_{dip}(\mathbf{r}) = -\boldsymbol{\nabla}U_{dip}(\mathbf{r}). \tag{A.56}$$

A.4.2 Far-detuned dipole trap

Let us consider the limit of a far-detuned laser $\delta \gg \Gamma$, then Eq. (A.55) becomes:

$$\mathbf{f}_{dip}(\mathbf{r}) = \frac{\hbar\Gamma}{2}\boldsymbol{\nabla}s\frac{\Gamma}{4\delta}(\rho_{ee} - \rho_{gg}). \tag{A.57}$$

Therefore, the dipole potential using Eq. (A.56) becomes:

$$U_{dip}(r) = -\frac{\hbar\Gamma}{2}\frac{\Gamma}{4\delta}(\rho_{ee} - \rho_{gg})s(r). \tag{A.58}$$

Using the standard saturation intensity of a perfect two-level atom $I_{sat} = \hbar\omega_0^3\Gamma/12\pi c^2$ and the fact the population is mainly in the ground state ($\rho_{gg} \approx 1$), the dipole potential is then proportional to the laser intensity:

$$U_{dip}(\mathbf{r}) = \frac{3\pi c^2}{2\omega_0^3}\frac{\Gamma}{\delta}I(\mathbf{r}). \tag{A.59}$$

In Eq. (A.59), the proportionality constant is the dipole polarizability α which involves the dipole moment $\mathbf{d} = \alpha.\mathbf{E}/2$ (Grimm, Weidemüller, and Ovchinnikov, 2000). As a result, the dipole potential can be written as $U_{dip}(\mathbf{r}) = -(1/2\epsilon_0 c)\,\mathrm{Re}(\alpha)I(\mathbf{r})$. It is important to mention that these traps are conservative since atoms do not dissipate energy by scattering (or at least on long time scales). Also, as $\delta < 0$ for red-detuned lasers, atoms are attracted to the maximum of the laser intensity.

In order to compare with experimental conditions, in practice, the rotating wave approximation is no more valid if the detuning is not negligible compared to the transition frequency. Keeping the co-rotating and counter-rotating terms leads to the following dipole potential (Grimm, Weidemüller, and Ovchinnikov, 2000):

$$U_{dip}(\mathbf{r}) = \frac{3\pi c^2 \Gamma}{2\omega_0^3}\left(\frac{1}{\omega-\omega_0}+\frac{1}{\omega+\omega_0}\right) I(\mathbf{r}). \tag{A.60}$$

For instance, the influence of the counter-rotating term for experimental parameters $\lambda =$ 1064 nm and $\lambda_0 = 780$ nm are $\left(\frac{1}{\omega-\omega_0}\right) / \left(\frac{1}{\omega-\omega_0}+\frac{1}{\omega+\omega_0}\right) = 1.18$.

For a multi-level atom like ^{87}Rb, in the case of a large detuning compared to the excited state energy splittings and for an hyperfine state F of $5S_{1/2}$ and magnetic state m_F, the dipole potential has contributions from both D1 and D2-lines (Grimm, Weidemüller, and Ovchinnikov, 2000):

$$\begin{aligned} U_{dip}(\mathbf{r}) =& \frac{\pi c^2 \Gamma_2}{2\omega_{2,F}^3}\left(2+Pg_F m_F\right)\left(\frac{1}{\omega-\omega_{2,F}}+\frac{1}{\omega+\omega_{2,F}}\right) I(\mathbf{r}) \\ &+ \frac{\pi c^2 \Gamma_1}{2\omega_{1,F}^3}\left(1-Pg_F m_F\right)\left(\frac{1}{\omega-\omega_{1,F}}+\frac{1}{\omega+\omega_{1,F}}\right) I(\mathbf{r}), \end{aligned} \tag{A.61}$$

where $\omega_{1,F}$ (resp. $\omega_{2,F}$) is the frequency splitting between a particular hyperfine state F of $5S_{1/2}$ and the state $5P_{1/2}$ (resp. $5P_{3/2}$) ($\Delta_{2,F} = \omega - \omega_{2,F}$ and $\Delta_{1,F} = \omega - \omega_{1,F}$). P is the polarization of the beam ($P = 0, \pm 1$ for $\pi, \sigma^{\pm}$ polarizations). Finally Γ_1, Γ_2 are the decay rates of each D-line excited state.
Note that for P=0 and $\lambda = 1064$ nm, the ratio of Eq. (A.60) and Eq. (A.61) is 0.978.

After this short parenthesis for the treatment of a MLS, we consider now the case of a two-level atom interacting with two laser fields that we take as a model system to describe doubly dressed states in ^{87}Rb.

A.4.3 Doubly dressed state: general potential with ^{87}Rb

In the following, we consider two laser fields at 1064 nm and 1529 nm interacting with the transition $5S_{1/2}$ to $5P_{3/2}$ (atomic frequency ω_0) and $5P_{3/2}$ to $4D_{5/2}$ of ^{87}Rb atoms. The corresponding dipole potentials dress the ground state $5S_{1/2}$ with U_{5S} and the excited state $5P_{3/2}$ with U_{5P}. Using Eq. (A.55) and neglecting the population in the second excited state $4D_{5/2}$ ($\rho_{4D} = 0$), the total dipole force acting on the atom is:

$$\mathbf{f}_{dip,tot}(\mathbf{r}) = -\boldsymbol{\nabla} U_{5S\to 5P}(\mathbf{r})\rho_{5S} - \boldsymbol{\nabla} U_{5P\to 4D}(\mathbf{r})\rho_{5P}, \tag{A.62}$$

These dipole potentials are generated by a 1064 nm laser and a 1529 nm laser which are far-off-resonance compared to both transitions $5S_{1/2}$ to $5P_{3/2}$ (780 nm) and $5P_{3/2}$ to $4D_{5/2}$ (1529 nm). The 1529 nm laser can be considered to be at a few GHz from the atomic transition $5P_{3/2}$ to $4D_{5/2}$. Atomic coherences can then be considered at steady-state with respect to the populations. Driving these populations can then be done with a spatially homogeneous third laser at 780 nm driving the dressed atomic transition ($\omega_{5S,5P}(\mathbf{r})$) between $5S_{1/2}$ to $5P_{3/2}$.

The population conservation is verified at any time $\rho_{5S}+\rho_{5P} = 1$ and the internal dynamics is obtained from the optical Bloch equations for a 780 nm laser frequency ω_{780}, Rabi frequency Ω_{780} and detuning $\Delta(\mathbf{r})$:

$$\rho_{5P}(\Delta(\mathbf{r})) = \frac{1}{2}\frac{2\Omega_{780}^2}{\Gamma^2 + 2\Omega_{780}^2 + 4\Delta^2(\mathbf{r})}. \tag{A.63}$$

The detuning can be written as $\Delta(\mathbf{r}) = \omega_{780} - \omega_{5S,5P}(\mathbf{r}) = \Delta_{780} - (U_{5P}(\mathbf{r}) - U_{5S}(\mathbf{r}))/\hbar$ and $\Delta_{780} = \omega_{780} - \omega_0$.

Using the conservation of population, the total dipole potential in Eq. (A.62) can be recast in the following form:

$$\mathbf{f}_{dip,tot}(\mathbf{r}) = -\boldsymbol{\nabla} U_{5S}(\mathbf{r}) + \hbar\Gamma\boldsymbol{\nabla}\left(\frac{\Delta(\mathbf{r})}{\Gamma}\right)\rho_{5P}(\Delta(\mathbf{r})). \tag{A.64}$$

The corresponding dipole force is obtained by integrating the dipole force from infinitely far to the position of interest:

$$\mathbf{U}_{dip,tot}(\mathbf{r}) = \iiint_{-\infty}^{\mathbf{r}} \left[\boldsymbol{\nabla} U_{5S}(\mathbf{r}') - \hbar\boldsymbol{\nabla}\left(\Delta(\mathbf{r}')\right)\rho_{5P}(\Delta(\mathbf{r}'))\right].d^3\mathbf{r}'. \tag{A.65}$$

This total dipole potential is a superposition of dipole potentials in the ground and excited states which is the engineered potential in the realization of subwavelength lattices in near-field traps (Bellouvet et al., 2018). A discussion of the trap properties is done in section A.4.5. In the next section, we explicitely calculate the potential for a 1D geometry.

A.4.4 1D doubly dressed state potential for ^{87}Rb

For a proof of principle of the doubly dressed state (DDS) trapping, we will demonstrate the creation of tunable optical barriers for a 1D case along x. A schematic of the laser frequencies and energy levels are given in Fig. A.4. Using a change of variables, the primitive of a Lorentzian function and the fact that far from the atoms at $x = -\infty$, the potential energy is zero *i.e.* $U_{5S}(-\infty) = U_{5P}(-\infty) = 0$, Eq. (A.64) becomes:

$$\mathbf{U}_{dip,tot}(x) = U_{5S}(x) - \frac{\hbar\Gamma}{4}\frac{s}{\sqrt{1+s}}\left(\operatorname{atan}\left(\frac{2\Delta(x)}{\Gamma\sqrt{1+s}}\right) - \operatorname{atan}\left(\frac{2\Delta_{780}}{\Gamma\sqrt{1+s}}\right)\right). \tag{A.66}$$

where the saturation parameter is $s = 2\Omega_{780}^2/\Gamma^2$ and we remind that as in section A.4.3 the total detuning between the 780 nm laser and the dressed two-level atomic transition is $\Delta(x) = \Delta_{780} - (U_{5P}(x) - U_{5S}(x))/\hbar$.

In the doubly dressed state picture, it is clear from Eq. (A.66) that the 780 nm laser power tunes the trap depth and the 780 frequency detuning tunes the resonant positions.

We consider a 1529 nm laser which is tuned close to resonance (1 GHz) with the 1529 nm transition $5P_{3/2}$ to $4D_{5/2}$ and shifts the excited state energy with a dipole potential:

$$U_{5P}(x) = \hbar\Gamma\Delta_{5P,0}e^{-\frac{2x^2}{w_0^2}}, \tag{A.67}$$

where we have factorized the amplitude factor which leaves $\Delta_{5P,0}$ as a normalized shift.

We consider that the 1064 nm trap has no trapping along x such that $U_{5S}(x) = 0$. We will see that the trapping along x is ensured via the dipole force from the excited state with the 1529 nm laser.

The detuning of the 780 nm radiation is set at $\Delta_{780} = r\Gamma U_{5P,0}$ where $r \in [0, 1]$ describes the position of the resonance within the 5P light shift modulation. In these conditions, the doubly dressed state potential becomes:

$$\mathbf{U}_{dip,tot}(x) = -\frac{\hbar\Gamma}{4}\frac{s}{\sqrt{1+s}}\left(\text{atan}\left(\frac{2\Delta_{5P,0}}{\sqrt{1+s}}\left(r - e^{-\frac{2x^2}{w_0^2}}\right)\right) - \text{atan}\left(\frac{2r\Delta_{5P,0}}{\sqrt{1+s}}\right)\right). \tag{A.68}$$

The maximum trap depth is given by the trap center ($x = 0$):

$$\mathbf{U}_{dip,tot}(0) = -\frac{\hbar\Gamma}{4}\frac{s}{\sqrt{1+s}}\left(\text{atan}\left(\frac{2\Delta_{5P,0}}{\sqrt{1+s}}(r-1)\right) - \text{atan}\left(\frac{2r\Delta_{5P,0}}{\sqrt{1+s}}\right)\right). \tag{A.69}$$

We plot on Fig. A.2 the DDS potential and the initial excited state potential for three particular 780 laser frequencies (black dashed lines): top $r = 0$, middle $r = 1/2$ and bottom $r = 1$ of the excited state potential. These frequencies give the spatially resonant positions.

The atoms at the bottom of the trap will experience a strong off-resonant dipole force when they head towards the edges that brings them back into the trap.

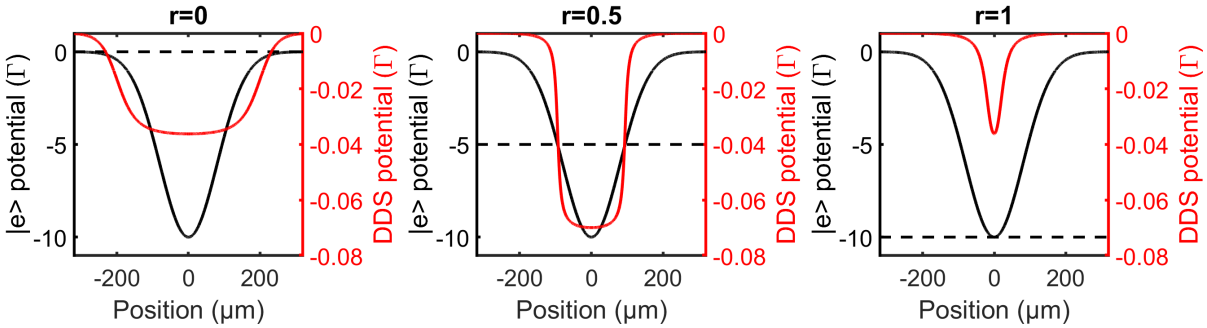

Figure A.2: Potential of the excited state (black) and doubly dressed state potential (red) with $s = 0.1$ and $\Delta_{5P,0} = -10$. The dashed line is the frequency of the 780 laser.

For instance, with this simple 1D case, by varying the 780 detuning, the trap width is changed. Atoms are initially trapped at the crossing of two dipole beams propagating along x and y. The atoms are then released in the beam propagating along x and expand in this direction. During the expansion, optical barriers are created by DDS dressing using 1529 and 780 nm radiations. The beam at 1529 nm propagates along y. It has a Gaussian profile along x.

Our experimental setup will be described in the next Chapters, but we already show here experimental data in Fig. A.3 showing in-situ images of an atomic cloud where the other directions y and z are trapped by dipole trap potentials at 1064 nm and x direction is confined by the DDS composed of a single 1529 nm beam with a waist of 150 µm and a 780 nm cooler beam on the cycling transition of ^{87}Rb with saturation 5.10^{-4} and trap

depth of -14Γ. The x-direction is initially trapped in a crossed dipole trap, then the trap along x is turned off while the DDS trap is ON. The width of the cloud shows that the trap width is well controlled by the 780 nm frequency.

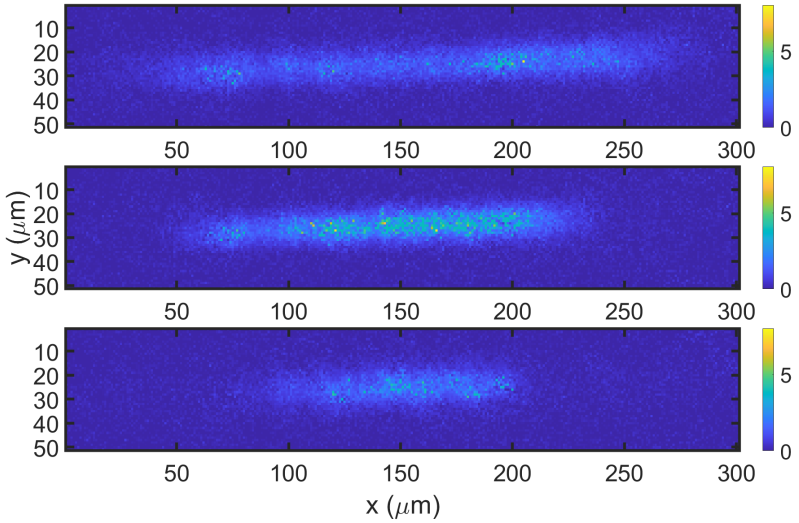

Figure A.3: Optical density from in situ absorption imaging for a DDS trap along the x-direction for top, middle and bottom of the excited state potential, $s = 0.0005$ and a trap depth of -14Γ. The DDS trap corresponds to the red curves of Fig. A.2.

In this PhD, we will focus on a quantitative analysis of subwavelength imaging using the strong slope of the excited state ($r = 1/2$) with the nonlinear atomic response to the excitation in Chapter E.

A.4.5 Near-field subwavelength lattices

DDS potentials can be used to spatially shape the trapping potential as seen in the simple case above and can also be used for generating subwavelength structures as follows.

We remind here some general arguments and limitations of the method that have been thoroughly detailed in a previous PhD thesis (Bellouvet, 2018) and publication (Bellouvet et al., 2018).

In (Chang et al., 2014) it has been theoretically shown that using a metallic surface with a plasma resonance tuned close to the atomic resonance, the excited state could be engineered and expelled from the surface as in our 1529 nm dressing. Unfortunately, engineering a surface with such specific plasma frequency is a very complex material science problem, especially if the surface should be nanostructured. In this perspective, our method involving 1529 nm dressing seems much more versatile for an experimental implementation. In addition, close to a metallic surface, quenching will occur and the scattering rate will be strongly enhanced $\Gamma(z) = \Gamma_0 + d\Gamma(z)$. This issue is much attenuated in the vicinity of dielectric surfaces where the scattering rate can be considered as constant $\Gamma(z) = \Gamma_0$.

The difficulty to trap atoms in the vicinity of a surface is the strong Casimir-Polder force that attracts and tends to collapse atoms on the surface. In the method proposed in (Bellouvet et al., 2018), an evanescent wave at 1529 nm dresses the excited state such that it is expelled from the surface. This repulsive force at short distance is transferred

to the ground state via the 780 nm radiation. As a result, at short distance, DDS forces expel the atom from the surface while at long distances the Casimir-Polder forces attract them. They form together a near-field trap (see Fig. A.4).

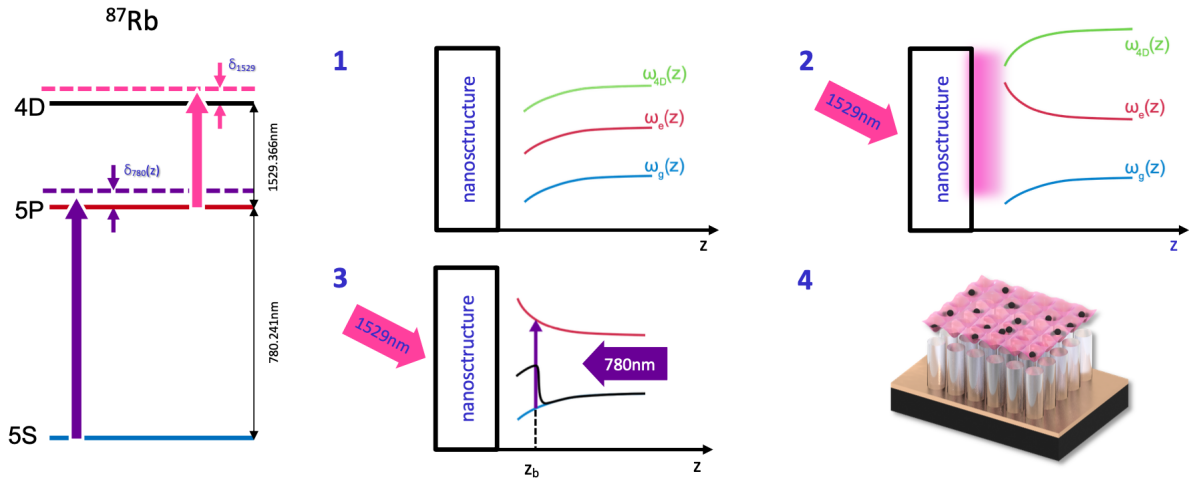

Figure A.4: Method from (Bellouvet et al., 2018) to generate near-field traps. 1) Casimir-Polder forces dress the atom in close vicinity to the surface, 2) A strong laser intensity at 1529 nm generates an evanescent wave dressing the first excited state, 3) A 780 nm laser couples the ground state and the excited state to form a barrier at position z_b, 4) Structuring the surface modulates Casimir-Polder forces and generates a subwavelength lattice with the periodicity of the nanostructure.

The long term project of this AUFRONS project in Bordeaux is to bring atoms close to a nanostructured surface using the above trapping scheme and also a nanostructured surface that would provide a trapping lattice with subwavelength spacings. It has been shown theoretically that such traps can be engineered (Bellouvet et al., 2018) with spacings of 100 nm.

In these DDS traps (Chang et al., 2014; Bellouvet et al., 2018), the lifetime is limited by:

- Photon scattering at the trap edges. It can be computed from the scattering rate.
- Anti-damping which is a non-adiabatic evolution of the trap potential due to a non-zero atomic velocity which occurs because atomic coherences that do not reach equilibrium fast enough compared to the atom velocity.
- Transient heating if the atom is in a pure state (either ground or excited) as it will only feel a single dipole force. This can happen if the atom scatters a photon as it will spend a time of about $1/\Gamma$ in the excited state and will only feel the excited state force, or after a diffusion after which the atom is back to $|g\rangle$ that is not trapped. The atom is accelerated for a time Δ^{-1} before the coherences are recovered and the atom is back in the trapping potential.
- Close to a surface, the tunneling time also limits the lifetime if the atom passes through the trapping potential barrier.

A.5 Conclusion

In this chapter, we gave a theoretical background on evaporative cooling for quantitative analysis of evaporation ramps towards the realization of a Bose-Einstein condensate in Chapter B. To reach BEC, the phase-space density has to increase up to 1 and the trap geometry directly gives the evaporation scaling laws. We gave the necessary theory to characterize a BEC in the mean-field approach at finite and zero temperatures. Such a BEC is the starting point for the physics of optical lattices as it can be adiabatically loaded into a single-band of a 1D lattice whose band structure has been described in both low and high lattice depths. We gave the order of magnitude of relevant energy scales involved in the Bose-Hubbard Hamiltonian in standard optical lattices. Finally, we developed the long-term purpose of this PhD thesis which is the realization of subwavelength lattices using new dressed states. We show experimental data in a simple 1D configuration to demonstrate the dipole force generated by the dressed states providing tunable trap confinement. These dressed states will be studied in more detail for the purpose of developing a new subwavelength imaging technique in Chapters E and F.

Chapter B

BEC apparatus

When I arrived at the laboratory as a pre-doctoral student, the previous members had reached the Bose-Einstein Condensation (Busquet, 2017; Bellouvet, 2018) but the conditions were not stable. The evaporation was realized in a hybrid trap with 2.10^7 atoms at loading. Stray magnetic field had been characterized and compensated using microwave spectroscopy. The condensation threshold could be obtained only for one month and the low resolution imaging system made it difficult to quantitatively analyze the BEC properties. Adding to that recurrent experimental issues like repetitive vacuum leaks and laser system breakdowns, the BEC was quickly lost. A microscope objective had also been designed and installed to make the proof of principle of a new subwavelength imaging method. A proper alignment on the atom had still to be realized.

The first work of my PhD has been to make the experiment more robust and to reach and quantify the BEC properties. In the first part B.1 of this chapter, I shortly recall the experimental apparatus: the vacuum system, the 780 nm and 1064 nm lasers systems, the 2D and 3D Magneto-Optical Traps (MOT). A detailed description of these elements can be found in (Salvador Vasquez Bullon, 2016; Busquet, 2017; Bellouvet, 2018). The second part B.2 describes in detail all the sub-parts that have been implemented and the modifications of the old system that have been made to reach and manipulate a robust BEC. The third part B.3 concerns all imaging systems of the experiment for time-of-flights or in situ absorption imaging. Finally, in part B.4 we describe the evaporation steps, their characterization towards the BEC, and its manipulation with microwave fields.

B.1 Experimental apparatus overview

B.1.1 Experimental Sequence

Fig. B.1 shows an overview of the experimental sequence used to cool down atoms towards the quantum degeneracy. It is divided into 3 steps that are defining acronyms for the rest of the thesis. The red shaded area is composed of a 3-dimensional Magneto-Optical Trap (3DMOT) loaded by a 2-dimensional Magneto-Optical Trap (2DMOT). Then a compressed-Magneto-Optical Trap (CMOT) is performed, followed by an optical red Molasses and an optical pumping (OP) step to polarize the atomic sample. The latter is loaded into a quadrupole magnetic trap (MT) and followed by 4 spin-flip evaporation steps. Finally, a hybrid trap is realized composed of a far-off-resonance dipole trap and the magnetic trap. For all steps in Fig. B.1, we show only a few parameters that are

critical for the understanding. 'R' means that it corresponds to a repumper transition and 'C' corresponds to a cooler transition. For MOT and OP beams, we give the corresponding transitions noted as $(F_g F_e)$ which goes from $|F_g\rangle$ of $5S_{1/2}$ to $|F_e\rangle$ of $5P_{3/2}$. We show the detuning from the corresponding transition $(F_g F_e)$ for each step. Also, we show the amplitudes of the magnetic gradient, the radio-frequency (RF) knife, and the dipole trap depth (corresponding to DT1 in the following sections).

Now, we will shortly describe this experimental sequence before giving all modifications that have been made towards the quantum degeneracy.

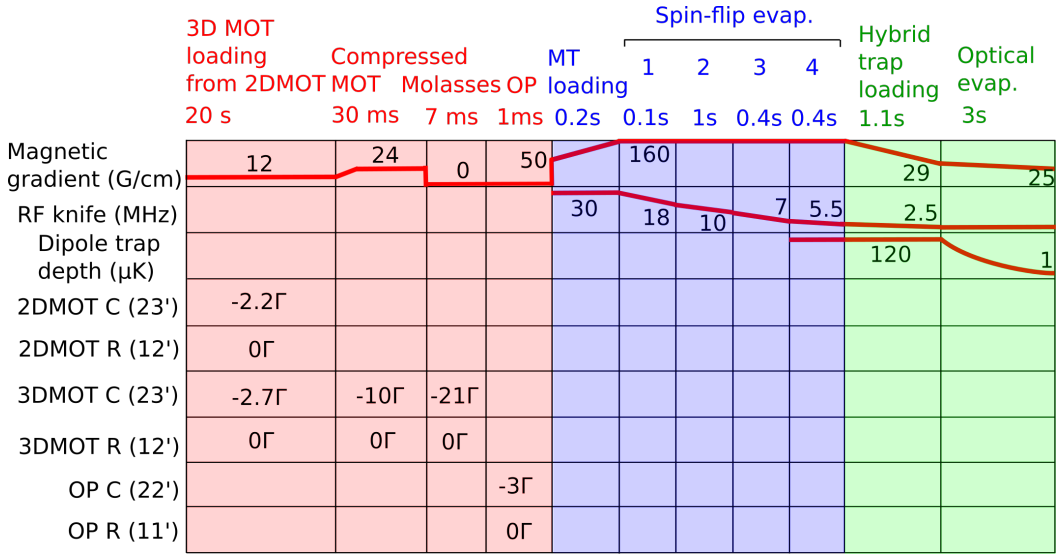

Figure B.1: Overview of the experimental sequence from 2DMOT cooling to optical evaporation in a hybrid trap. It is divided in 3 blocks: laser cooling techniques using MOT traps (red shaded), spin-flips in a magnetic trap (blue shaded) and optical evaporation in a hybrid trap (green shaded).

B.1.2 From laser cooling to magnetic and hybrid evaporation

The physics and optimization of the experimental steps described in this section have been widely covered in the previous thesis (Salvador Vasquez Bullon, 2016; Busquet, 2017; Bellouvet, 2018). Here we summarize the main parameters and results of the experimental sequence up to the magnetic trap.

A 2DMOT purchased from Syrte cools down in two dimensions a Rubidium vapour at room temperature, down to a transverse temperature of 400 μK. It loads the 3DMOT chamber with a flux of 10^{10} atoms/s at a speed of 13 m/s.

The 3DMOT consists of anti-Helmholtz coils providing a vertical magnetic gradient of 12 G/cm and 6 counter-propagating circularly polarized beams of repumper and cooler detuned at -2.7Γ. The horizontal plane is covered by 2x2 counter-propagating fiber collimated beams that avoid shadow effects[1]. To enhance the cooling power, each of these beams is retro-reflected with a crossed polarization. In the vertical direction, only 1 collimator is used because the opposite direction is dedicated to in situ imaging thanks to a movable flip-flop mirror that is used for the MOT when it is closed and for the

[1]For a single beam, the reflection has less intensity at the center due to the attenuation through the cloud. Then, there is an unbalanced power at the cloud center.

imaging when it is open. Those beams cool down the atoms through Doppler cooling whose temperature lower limit is the Doppler temperature $T = \hbar\Gamma/2k_B$ which is 146 µK for ^{87}Rb. The atom number in the MOT saturates for a loading time of 20 s. At best, it can be improved down to 10 s loading time reaching the same atom numbers by optimizing the 2DMOT alignment, maximizing the 2DMOT powers and couplings etc.

A compressed-MOT is then done to increase the atomic density by increasing the magnetic gradient by a factor of 2 and sweeping the cooling light detuning at -10Γ. This CMOT compensates for the decrease of the atomic density during the next steps before magnetic loading.

An optical red molasse is then realized by suppressing the magnetic gradient and detuning the cooler beam to -21Γ. Combined with the increase of density allowed by the CMOT, the Sysiphus cooling mechanism occurring in the molasse rapidly reduces the temperature. If the molasse is operated shortly, the density remains high with a reduced temperature which is ideal for magnetic trap loading. The limit temperature of a molasse scales with $T = \hbar\Omega^2/k_B|\delta|$ where Ω is the Rabi frequency of one of the cooler beam and $\delta < 0$ the detuning (Dalibard, 1999b). In theory, it usually reaches a few tens of the recoil temperature of 349 nK for dilute gasses of ^{87}Rb (low atom numbers). For dense clouds, the cooling is limited by multiple scattering mechanisms (Camara, Kaiser, and Labeyrie, 2014).

At this stage, we have a large atom number of $3.2.10^9$ atoms at a temperature of 30 µK. Since our vacuum is not excellent as we will see in B.2.1.2, evaporation needs to be fast and the initial density (collisional rate) is critical. For instance, with "only" 2.10^9 atoms after the molasses our experiment can hardly evaporate down to BEC. The MOT coils can provide a gradient up to 160 G/cm for quadrupole magnetic trapping and are water-cooled to dissipate heat. The dissipation time is however about 40 s for the coils to come back to their initial temperature setpoint of 18°C when we use them for 4 s at a gradient of 160 G/cm (55 A). This makes our experiment duty cycle[2] about 1 min including the MOT loading time of 20 s.

Magnetic trapping, radio-frequency evaporation and forced optical evaporation are described in more detail in sections B.2, B.4. Compared to the previous thesis (Salvador Vasquez Bullon, 2016; Busquet, 2017; Bellouvet, 2018), important modifications and a quantitative analysis have been made towards the realization of a Bose Einstein Condensate (BEC).

B.1.3 Schematics of the experimental setup

The diagram of Fig. B.2, which will be used in all next sections and chapters, shows the main experiment setup in the plane (x, y) and is composed of the following optical axis:

- OP : Optical Pumping beams of repumper and cooler at 780.2 nm, aligned at 45° in x, y plane.
- Push : push beam of cooler at 780.2 nm to push the atoms from the 2DMOT to the 3DMOT chamber.

[2]It can be reduced with a new coil design with for instance hollow-core coils or a bulk-machined electromagnet.

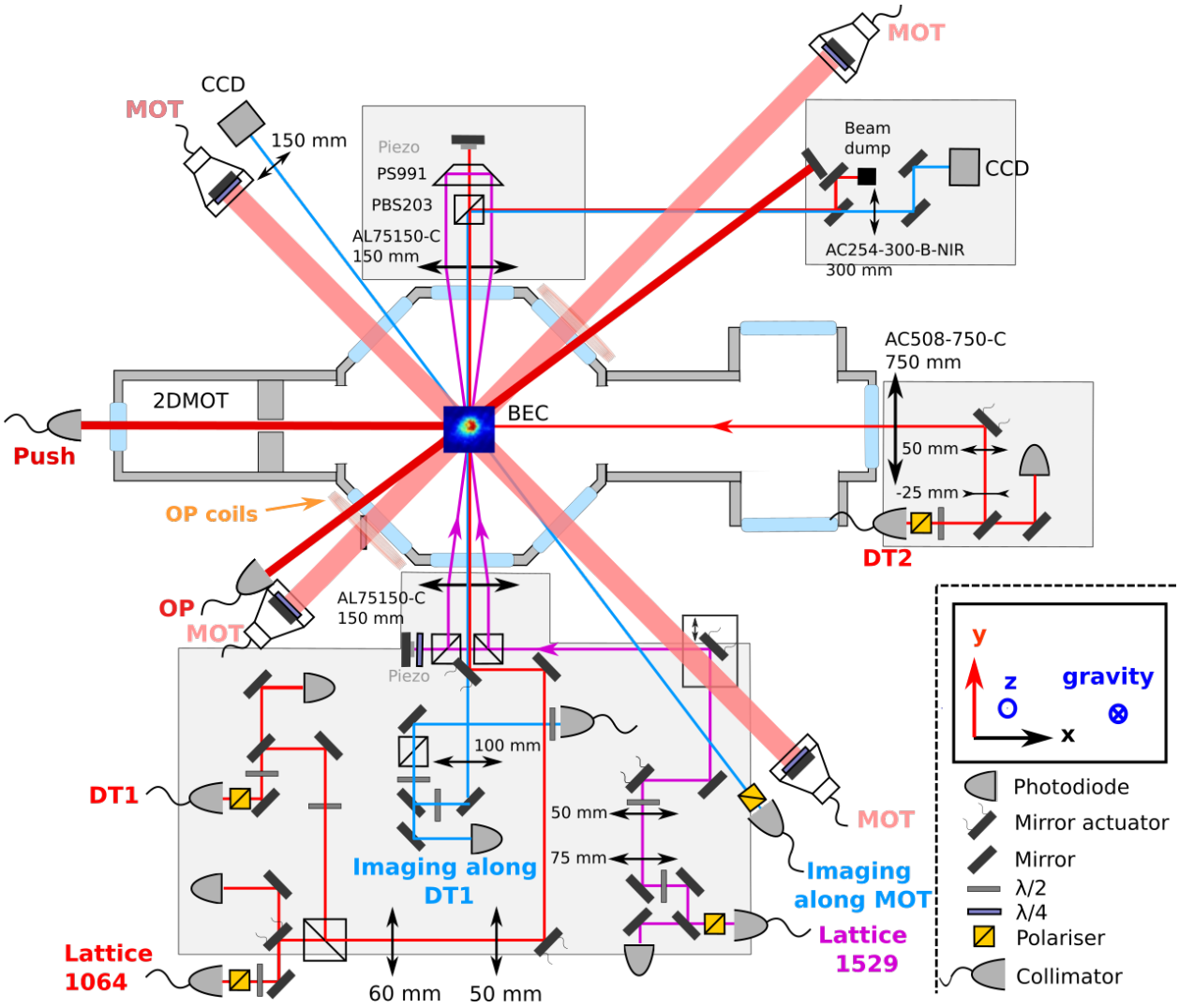

Figure B.2: Schematics of the main experimental setup in the (x, y) plane. MOT collimators schematics are different as they are 2 inches of diameter and have a mounted mirror and quarter waveplate on top of them.

- MOT : Magneto-optical trap collimated beams at 780 nm of repumper and cooler at 780.2 nm.
- Imaging along the MOT: imaging with a magnification of $\times 0.2$.
- Imaging along the DT1: imaging with a magnification of $\times 2$.
- DT1 : dipole trap 1 at 1064 nm, aligned in the y-direction with a waist of 50 µm.
- DT2 : dipole trap 2 at 1064 nm, aligned in the x-direction with a waist of 65 µm.
- Lattice 1064 : counter-propagating beams at 1064 nm along the y-direction.
- Lattice 1529 : accordion lattice at 1529 nm with adjustable angle with a translation stage used to get co-propagating beams (without prism PS991) or counter-propagating beams (with prism PS991 and 1 co-propagating beam only) along the y-direction and interfering onto the atoms.

B.2 Modification and characterization of the apparatus

The experimental apparatus was thoroughly detailed in the previous thesis (Salvador Vasquez Bullon, 2016; Busquet, 2017; Bellouvet, 2018). In the following sections, we summarize the main features of the apparatus and describe the important modifications that were carried within the thesis. This section concerns the improvement of the vacuum conditions, the working conditions of the optical bench for laser manipulation at 780 nm and the microwave spectroscopy for stray magnetic field characterizations and Rabi oscillations on a magnetically sensitive transition.

B.2.1 Vacuum structure and vacuum quality

B.2.1.1 Vacuum chamber structure

The vacuum structure for the main science chamber for the 3D magneto-optical trap (3DMOT) is an octogon with 8 CF40 and 2 DN100CF openings coming from the Kimball Physics company. It is separated from a 2DMOT chamber developed in Syrte by a differential vacuum and connected with a push beam that goes through an aperture of 1.5 mm in diameter. Two ionic pumps NEXTorr D 100-5 (100 L/s) driven by the controller NEXTorr NIOPS-03 are maintaining the 3DMOT chamber pressure to below 10^{-10} mbar limited by the ion pump precision. The residual pressure is responsible for a MOT lifetime of only 20s which was nevertheless sufficient to reach BEC conditions (Scherschligt et al., 2017). The global structure is shown on Fig. B.3 which comes from the thesis (Bellouvet, 2018).

The horizontal viewports have an optical access diameter of 34 mm (5 mm width) and the re-entrant vertical[3] have 75 mm (5 mm width). Vertical viewports are separated by 20 mm inside the chamber while the horizontal ones are separated by 90 mm.

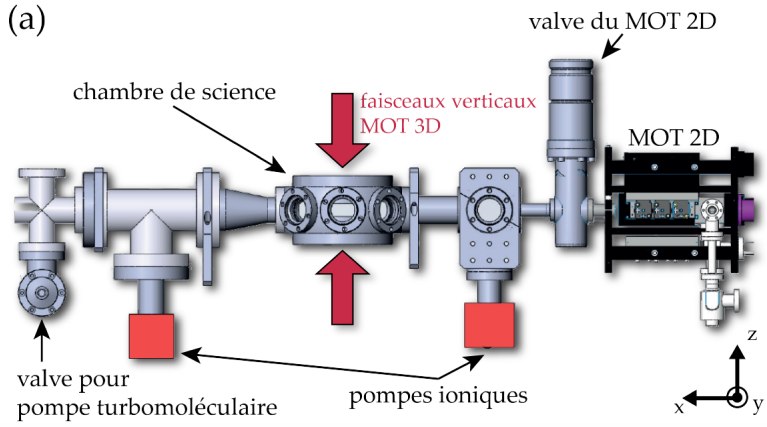

Figure B.3: Schematics of the vacuum system structure from the thesis (Bellouvet, 2018).

B.2.1.2 Rare gas instability

On this experiment, we had the vacuum problem known as 'Argon' or 'rare gas' instability (Vaumoron and De Biasio, 1970). The problem is that rare gases are not very well pumped

[3]From MPF company.

by ionic pumps and periodically, they burst them which degrades the vacuum. It is characterized by a burst period that depends on the vacuum quality, the period is longer when the vacuum is better. Depending on the vacuum quality, the period can range from days to months. Before the burst, the vacuum is slowly degrading in time and after it, the pressure rapidly goes back to the lowest vacuum pressure before slowly rising again.

On Fig. B.4, we show one of the bursts that we measured by monitoring the ionic pump current. In our case, the period of these bursts was 6 months. During a peak, we effectively found that the vacuum is degrading as the MOT lifetime was getting lower during a peak event meaning that the vacuum was really degrading during this event. Fig. B.5 shows the MOT lifetime measured by absorption imaging before and after the peak. When the ionic pump IP2 measures 1000 nA, the lifetime was only 2.8 s. Outside of the peak, the MOT lifetime was about 19 s.

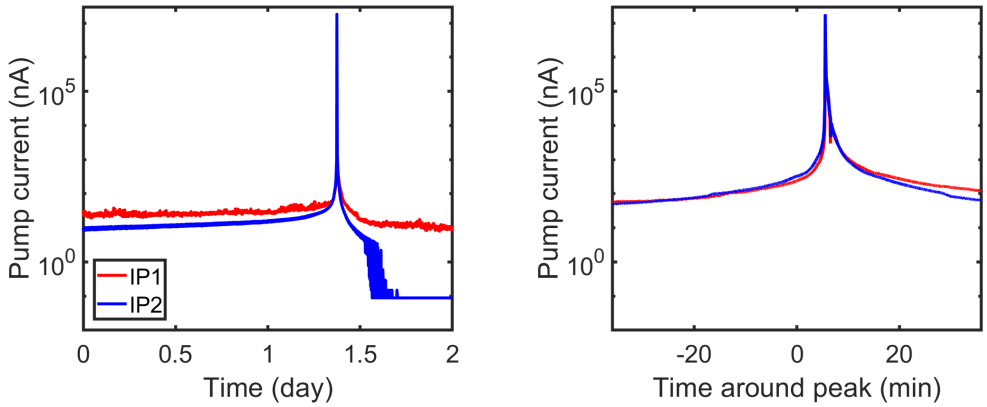

Figure B.4: Ionic pump current around a burst peak and zoom around the main peak. IP1 and IP2 refer to the two ionic pumps: 1 for near 2DMOT and 2 for far from 2DMOT. The conversion factor from the ionic current P_{nA} in nA to the actual pressure in mbar is $P_{mbar} = 1.33\text{x}10^{-10} P_{nA}$.

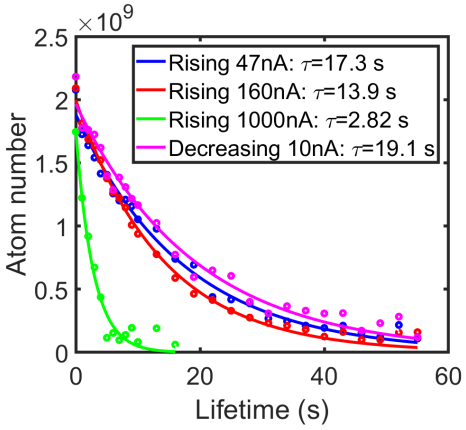

Figure B.5: MOT lifetime during a burst event, during the rise and the fall of the peak. Points are data from 26/09/2019 and solid lines are exponential fits of the type $ae^{-t/\tau} + b$.

We get rid of the problem after heating both ionic pumps up to 100°C while a turbo-molecular pump was connected to the experiment. After that, the getters have also been re-activated according to the datasheet procedure. In our case, this procedure has solved the issue.

B.2.1.3 Vacuum leak from the top viewport

Thanks to a vacuum Helium test of the experiment, we measured a residual leakage from the top viewport that we believe was limiting the MOT lifetime. This leakage was sensitive to the room conditions and was used to recurrently re-open and degrade our vacuum quality. After a few trials, we managed to seal it with the epoxy Torr Seal 'TS10' from Thorlabs. The ionic pump current was constant under Helium leak tests when exposed for tens of seconds. For longer exposure, the current slightly increases indicating that Helium was still able to diffuse through the epoxy. With this epoxy the leak had less impact over the experiment that could be operated for 2.5 years without problems. The epoxy 'VacSeal' used in the previous thesis always degrades rapidly in time (a few months scale) and had to be reapplied.

B.2.2 780 nm optical bench

The 780 nm cooler and repumper are obtained from a Muquans laser system. Details on the schematic of the bench are presented in (Salvador Vasquez Bullon, 2016). It is composed of:

- a Master (M) laser locked by saturating absorption onto the crossover between the excited states $|F_e = 2\rangle$ and $|F_e = 3\rangle$ and used to address the repumper transition of the ^{87}Rb D2-line. The linewidth is below 100 kHz and the frequency is fixed.
- a Slave 1 (S1) and a Slave 2 (S2) which are beatnote phase-locked to the master laser. The linewidths are 100 kHz and the tunability is 3-4 GHz at 780 nm from the Master laser. Their absolute frequency can be tuned during the experimental sequence around the cooling transition by controlling some Direct Digital Synthesizer (DDS) output frequency.

These three laser radiations are manipulated on a free space optical bench that includes polarizing waveplates ($\lambda/2$, polarizer), Polarizing Beam Splitters (PBS), Acousto-Optic Modulators (AOM) and mechanical shutters that are used to distribute and control the optical powers over the experiment. The light from the bench is coupled to the atoms via 8 fibers that are used to drive different transitions of the atom that are reminded in Table B.1

fiber OUT	fiber IN	Transitions F_gF_e	Maximum output powers (mW)
MOT2D H	M, S1	$12'$,$23'$	10, 90
MOT2D V	M, S1	$12'$,$23'$	10, 90
Push C	S1	$23'$	0.6
MOT3D R	M	$12'$	2
MOT3D C	S2	$23'$	16
OP R,C	M,S2	$11'$,$22'$	0.2, 0.6
Imaging C	S2	$23'$	10
Imaging R	M	$12'$	$<$0.5

Table B.1: 780 optical bench taking the Muquans lasers M, S1 and S2 as inputs. The 'Imaging R' is used to frequency lock another independent laser and will be described in section E.2.1. The 'fiber OUT' column is the collimator name where the light is coupled to. The 'fiber IN' is the collimator names where the Muquans lasers come from. The 'Maximum output powers' column is given at the fiber outputs.

The absolute frequency of all the radiations of the bench is given by the repumper saturation spectroscopy lock. This lock has a tunable offset that used to drift depending on the room temperature. We monitor and correct these small deviations ($<\Gamma$) by measuring the imaging detuning. With such corrections, we maintain the absolute frequencies to below 0.2 Γ from the transitions.

In Appendix II, we detail the electronic control of the experiment: the server/client protocol for the sequencer and the laser frequency control by direct digital synthesis, the output buffer circuits for noise reductions of the analog control voltages, the high current generation of the quadrupole coils and the analog circuits for generating stable voltages, for power lock PIDs, etc. The noise reduction part has been crucial for microwave Rabi oscillations described in the next section.

B.2.3 Microwave spectroscopy characterizations of magnetic fields

B.2.3.1 Magnetic dipole transitions

In this section, we give the formulas of the interaction between the magnetic dipole of the $5S_{1/2}$ spin state and a magnetic field oscillating at microwave (MW) frequencies (Treutlein, 2008; Ville, 2019).

Fig. B.6 shows the two hyperfine ground state manifolds $|F_{g1}=1\rangle$ and $|F_{g2}=2\rangle$ of $5S_{1/2}$. Their energy separation corresponds to the clock transition which is equal to $\hbar\omega_0$. The magnetic dipole transitions between Zeeman states from one hyperfine manifold to the other have Clebsch-Gordon coefficients that can be calculated from angular momentum overlaps (Treutlein, 2008).

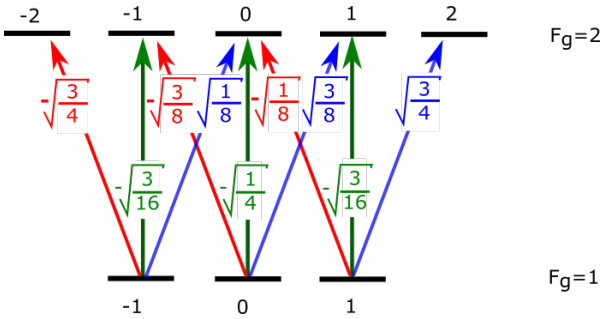

Figure B.6: Clebsch-Gordan coefficients between Zeeman levels for the two hyperfine ground states. π (green), σ^- (red) and σ^+ (blue) transitions.

Under a constant magnetic bias $\mid B_0 \mid = \sqrt{\sum_{x,y,z} B_{i0}^2}$, the Zeeman levels are splitted in energy because of the Zeeman effect as shown on Fig. B.7.

The external microwave (MW) frequency ω_{MW} is resonant with one of the transitions (ij) if:

$$\hbar\omega_{MW} = \hbar\omega(m_i, m_j) = \hbar\left(\omega_0 + \Delta\omega_B(m_i, m_j)\right), \tag{B.1}$$

where the differential Zeeman shift is $\Delta\omega_B(m_i, m_j) = \omega_B(m_j) - \omega_B(m_i) = \frac{\mu_b|B_0|}{\hbar}(g_j m_j - g_i m_i)$ with Landé factors g_i, g_j.

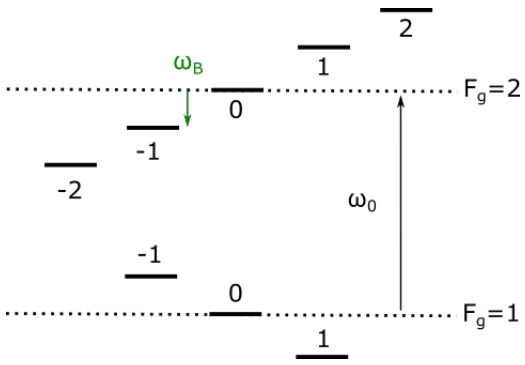

Figure B.7: Zeeman levels for the two hyperfine ground states shifted under a constant magnetic field.

The probability of transferring the atoms for a two-level system between the state i to j for the transition (ij) corresponds to a Rabi oscillation and is given by (Steck, 2019):

$$P(t) = \left(\frac{\Omega_{ij}}{\tilde{\Omega}}\right)^2 \sin^2\left(\frac{\tilde{\Omega}t}{2}\right), \tag{B.2}$$

where $\tilde{\Omega} = \sqrt{\Omega_{ij}^2 + \delta^2}$ is the generalized Rabi frequency with the on-resonance Rabi frequency Ω_{ij} and detuning $\delta = \omega_{ij} - \omega_{MW}$ between the MW frequency and the transition (ij).

B.2.3.2 Microwave frequency rack

A rack presented on Fig. B.8 has been setup to generate and control MW frequencies. The MW signals are generated by a PLDRO oscillating at 7 GHz which is mixed with the output DDS RF frequencies. A Voltage Variable Attenuator (VVA) is used to control the power with a maximum output power of -13.1 dBm for a driving voltage of 10V. The MW signal is then amplified by an amplifier (Stealth Microwave) that has a gain of +55 dB and a 1dB compression point of $P_{1dB} = +43$ dBm. A power loss of about 2dB is given by the optical isolator and the SMA cable at the amplifier output. At the end, the measured maximum power arriving on the MW antenna is +40.7 dBm.

The clock transition being $\omega_0/2\pi$ =6834.682 MHz, a DDS frequency of $f = 82659$ kHz that verifies $\omega_0/2\pi = 7$ GHz $-2f$ will generate a MW frequency exactly tuned on the clock transition.

The bandpass (BP) filter situated before the high power amplifier suppresses spurious harmonics generated by the mixer. Its frequency response ranges at constant power from 6800 GHz to 6880 GHz, and then linearly decreases from 6880 GHz to 6920 GHz by -2 dB. The filter is compatible both with MW transfer at low magnetic fields and MW evaporation in $|F_g = 2\rangle$ in the quadrupole trap. By tuning f from 60 to 82 MHz, the MW frequency can be swept from $\omega_0 + 44$MHz to ω_0. Note that the magnetic evaporation is currently carried in $|F_g = 1\rangle$ by spin-flips with another antenna (see section B.4.1.3).

The MW horn is a Q-par Angus QSH14S20S and has a dipole antenna at about 67 cm from the atoms. The dimensions of the horn, which improves the directionality of the emission by 20 dBi, are 390 mm x 175 mm x 125 mm. The polarization is linear along

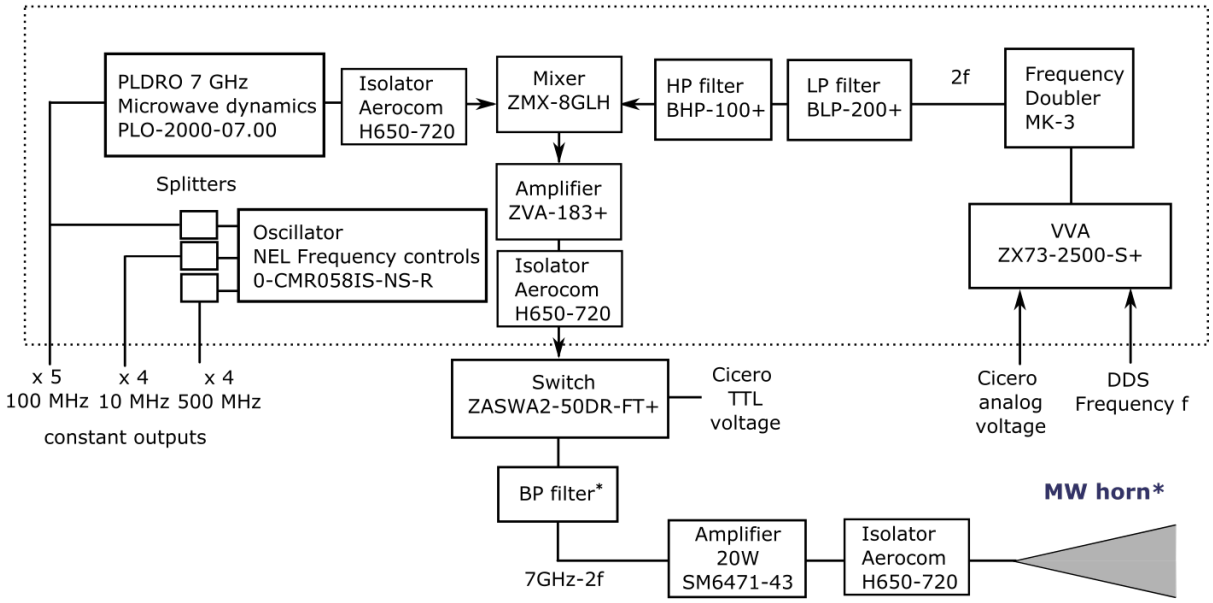

Figure B.8: Electronics rack and channel up to the horn for the micro-wave generation. The dashed line corresponds to components that are not directly accessible as they are in a rack. The components are from Mini-Circuits if not explicitly written. The splitters are power splitters (ZB4PD1-500-S+, ZB4CS-700-10W-N). The BP filter and MW horn are detailed in the main text.

the optical pumping (OP) direction (Fig. B.2). The horn is mounted on a rotation stage which enables us to maximize the transferred atom number by π-transitions with a magnetic field along OP direction. Note that for a magnetic field along z, the radiated field has equal σ^+ and σ^- powers.

B.2.3.3 Current noise impacts on Rabi oscillations

The original current drivers for the magnetic field compensations were using a 3-channel Delta Elektronika EST150 current power supply and homemade current lock circuits to control the current as the EST150 couldn't be externally controlled. However, these current locks were introducing a lot of noise as shown on Fig. B.9 with Rabi oscillations on the (-1-2) transition at two different MW powers: using old current lock circuits or by-passing them and setting manually the current setpoint to the desired one directly on the power supply. We clearly see that the lock circuits add noises as Rabi oscillations are much better without the circuits, especially for long MW durations.

Note that on Fig. B.9, the first oscillation is a bit faster than the other oscillations. It comes from a small power overshoot of our amplifier. In order to have a clean oscillation at the beginning, we turn on the amplifier input power 100 µs before the desired moment at a far-detuned frequency compared to the clock frequency (70 000 kHz on the DDS). The Rabi oscillation starts by setting the desired DDS frequency which is very fast (100 ns).

The sensitivity of coils along z is about 2 mG/mA and along x, y is about 4 mG/mA. For a shift of 700 kHz/G, the sensitivities are 1.4 kHz/mA and 2.8 kHz/mA. For a transition such as (-1-2), the shift is 3 times larger so the sensitivities are 4.2 kHz/mA and 8.4

kHz/mA. This means that the rms current noise has to be low compared to 1 mA to be really negligible. This is particularly important for low Rabi frequencies. We want a low Rabi frequency to have a better sampling of the Rabi oscillation knowing that our limited time resolution is 2 µs.

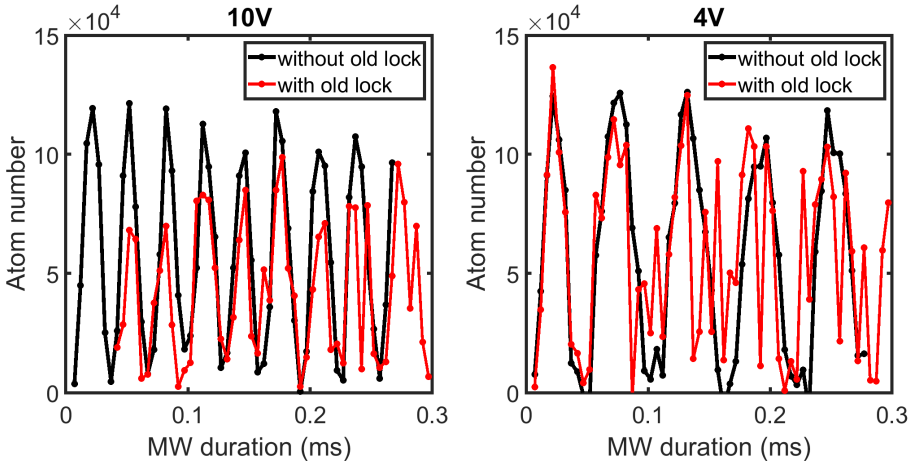

Figure B.9: Rabi oscillations when transferring atoms from $|F_g = 1, m_F = -1\rangle$ to $|F_g = 2, m_F = -2\rangle$. The atom number is measured with the imaging axis along the MOT at TOF=15 ms, and for a BEC in a crossed dipole trap with a bias magnetic field along z of about 280 mG. We made sure that the MW frequency was resonant with the atoms by scanning the MW frequency and finding the peak value.

We decided to change the power supplies by externally controllable low noise drivers. Table B.2 show different power supplies with the rms current noise from different companies.

Company	Model	I (A)	U (V)	i_{rms} (full load)
Delta Elektronika	ES 015-10	10	15	DC-300kHz: 1.5 mA
Delta Elektronika	EST150 (3 channels)	2.5	20	DC-300kHz: 0.5 mA
Wavelength Electronics	MPL2500	2.5	10	DC-9kHz: 10 µA
Koheron	DRV200S-A-400	0.4	15.5	10Hz-6MHz: 530 nA
Koheron	DRV200-A-400	0.4	6	10Hz-1MHz: 520 nA
Koheron	DRV200-A-200	0.2	6	10Hz-1MHz: 255 nA

Table B.2: Current power supply datasheet characteristics for many companies. The columns are: the company name, driver model, maximum current I, compliance voltage U and rms current noise i_{rms}.

We tested the current noise from different power supplies in a circuit composed of the tested power supply and compensation coils along z. The current noise has been measured through a differential measurement across a $R_m = 0.5\ \Omega$ resistor where a current of 0.6 A flows which was our setpoint for MW transitions. Then the voltage is filtered by a homemade high-pass active first order filter composed of a resistor of 47 kΩ and capacitor of 22 µF with an operational amplifier OP27. The measured cutoff frequency was 0.2 Hz and the noise was white up to 1 MHz.

The power spectral density has been measured with a digital Fourier Transform (FFTeur from the electronics workshop, where the input resistor is $R_{AS} = 2$ kΩ) for different

power supplies: MPL2500, ES0510 and EST150. Results are shown in Fig. B.10. For the MPL2500, either we set the setpoint internally which is named as 'direct' or using an external setpoint given by Cicero named as 'Cicero'.

In the range 10 Hz to 10 kHz, we integrate the current noise for all curves using $i_{rms} = \frac{1}{R_m}\sqrt{v_{rms}^2 - v_{rms,ref}^2}$ where $v_{rms}^2 = R_{AS}\int_{10Hz}^{10kHz} 1mW \times 10^{P_{dBm}/10} df$, P_{dBm} is the power spectral density (PSD) and $v_{rms,ref}^2$ is for the noise floor. The current noise floor is $i_{rms}^{(noisefloor)} = 0.010$ mA. After subtracting this noise to all other curves, we have: $i_{rms}^{(MPL2500\ direct)} = 0.027$ mA, $i_{rms}^{(Cicero)} = 0.141$ mA, $i_{rms}^{(ES0510)} = 0.166$ mA and $i_{rms}^{(EST150)} = 0.012$ mA.

Firstly, all these noises are much lower than 1 mA so they should not significantly affect Rabi oscillations.

Secondly, an external voltage setpoint for the MPL2500 is adding more noise, so we decided to filter all Cicero voltage analog setpoints with low-pass filters with a cutoff frequency of 13 kHz using the 'reference voltage' circuits (see Appendix II.iv). We want to be able to tune quickly the fields during the experiment so we cannot filter too much. Also, this noise has been reduced using buffer cards at the output of the NI cards (see Appendix II.ii).

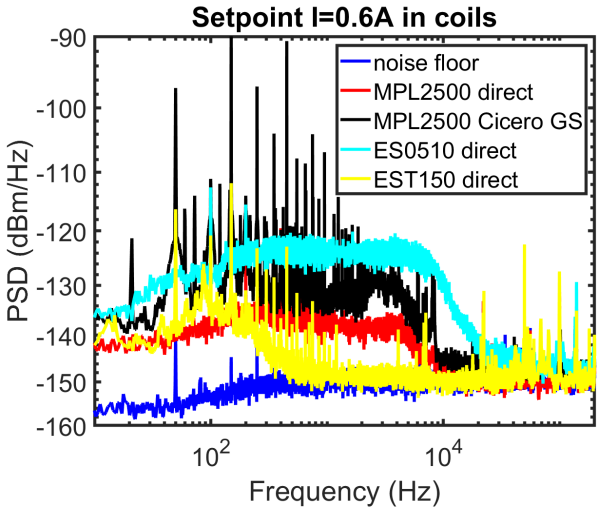

Figure B.10: Power spectral density per unit of frequency for different power supplies at the setpoint of 0.6A. Cicero GS means that the connector block that was at the output of the NI cards had a Ground-Source connection for this particular channel output (see Appendix II.ii).

As we are using low currents for the compensation coils (<0.2A), we decided to use Koheron power supplies which can be externally controlled for x, y and the Wavelength Electronics MPL2500 for z as the current is higher and we want to tune it up to 1A. Fig. B.11 shows the current tunability in the 3 compensation coils with the new current drivers (MPL2500 for z, DRV200 for x, DRV200S for y). For x and y drivers, monitors pins can be used to check that the current are correct: the monitor voltage (in V) is resp. $-819V_{in,y} + 0.658$ and $-1999V_{in,x} + 0.3795$.

Using MW spectroscopy (see next section B.2.3.1) and Fig. B.11, we find that the tunability of the coils are 3.66 G/A for x, 4.67 G/A for y and 2.05 G/A for z.

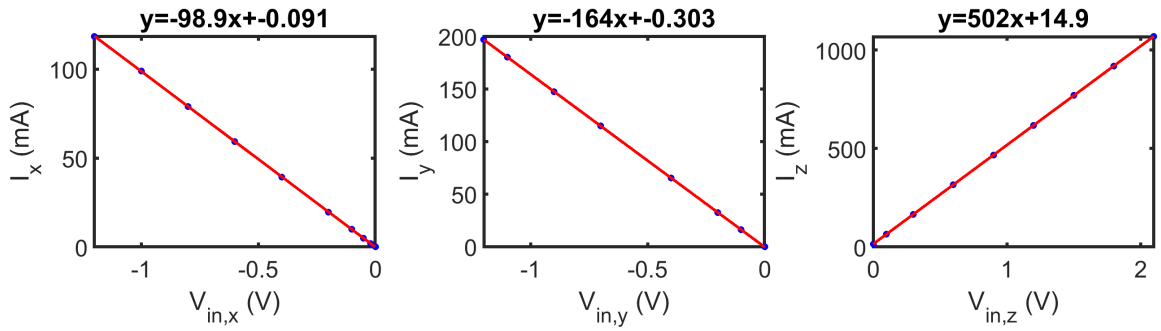

Figure B.11: Characterization of the current drivers: driver input voltage versus current flowing through the coils. The data are fitted with a linear equation shown in the title.

B.2.3.4 Magnetic field zero

In this section, we describe how the magnetic field generated by the compensation coils is precisely calibrated at the atom cloud position using MW transitions.

In previous experimental optimizations (Busquet, 2017; Bellouvet, 2018), the magnetic field bias in a given direction was calibrated with a 2D scan of the number of transferred atoms as a function of the current in the compensation coils pair and the MW frequency ω_{MW}. Our initial calibration method was as follows :

First, we identify a MW transition by putting a magnetic offset. Fig. B.12 shows a scan of the MW frequency with a magnetic bias along the optical pumping axis during the optical molasse step around magnetic field compensation values. The splitting is then only due to the optical pumping coils. We see the different transitions (ij) between a lower state i and upper state j.

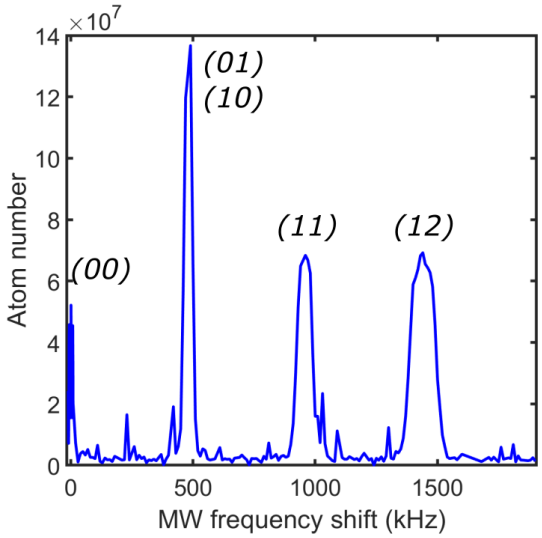

Figure B.12: MW spectroscopy of the molasses without optical pumping but with a BMF of compliance equal to 4V. The MW pulse is 300 µs and the MOT loading time is 500 ms. The MW pulse is done in situ and the atom number is measured along ccd45 axis after TOF=15ms.

Then around a transition, for instance (12), a 2D scan of the magnetic field and microwave frequency is done for a given direction. Fig. B.13 shows such a 2D scan. By fitting the

transferred atoms with Eq. (B.1), we obtain a minimum Zeeman shift which corresponds to the current that best cancels the residual field along the scanned direction. This also calibrates the variation of the field amplitude as a function of the current. Realizing three 2D scans allowed us to calibrate the zero of magnetic field for the optical molasses.

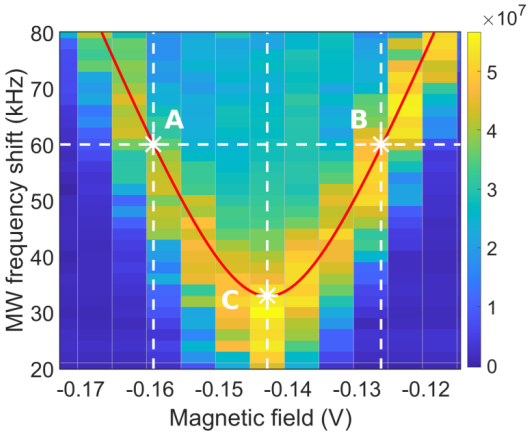

Figure B.13: 2D scan of the transferred atom number as a function of MW frequency and magnetic field for a given direction and for the transition (12).

For a molasse cloud at the best magnetic compensation setpoints, there are still residual magnetic gradients at the position of the atoms, as it can be seen on Fig. B.14, evaluated at about 200 mG/cm.

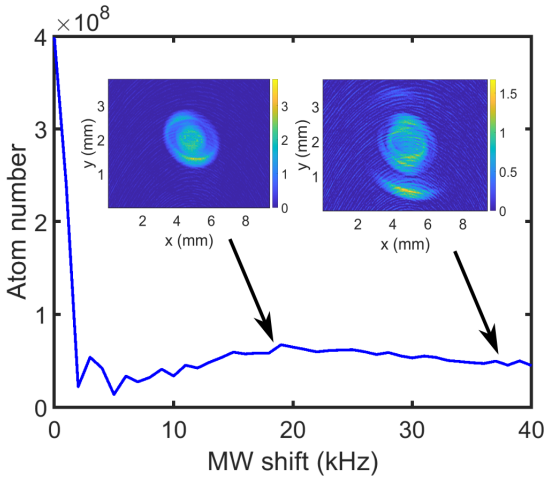

Figure B.14: Residual magnetic gradient inhomogeneties at the best compensation values.

The BEC is usually aligned about 100 µm below the center of the quadrupole zero. Spatial gradient inhomogeneities of 200 mG/cm give variations of 100 μm x (0.2 G/cm) = 2 mG or equivalently 2 mG x (700 kHz/G) = 1.4 kHz. For the transition $(-1 - 2)$ it would be 4.2 kHz so we usually compensate the zero at the BEC position.

Also, as the compensation coil power supplies were changed to reduce the influence of noise, this calibration had to be redone. As our cycling time is long ($\approx$ 1 min), 2D scans such as presented in Fig. B.13 are long to perform when we want to know exactly the field at the BEC position. For the characterization of the residual magnetic field compensation, we rather use only two 1D scans for each direction. The method works as follows: we set a positive (+) bias along z and put x and y at their expected zero.

We know approximately the magnetic bias from old calibrations so we scan ω_{MW} around the expected (-1-2) transition peak as the BEC is initially polarized in $m_F = -1$ state. This gives us the resonant peak frequency ω_{MW} for $B_z^{(+)}$ which is depicted as point A on Fig. B.13. Now at this particular MW frequency, we scan the magnetic field (i.e. the coil current) to get the opposite magnetic field at the atom position. We get the resonant peak for $B_z^{(-)}$. This gives the point B. The residual magnetic field along z is finally obtained as $(B_z^{(+)} + B_z^{(-)})/2$ which is the field at point C. By repeating this procedure for the three directions we obtain the magnetic field calibrations for each direction as summarized in Table B.3. In practice, we also use these values for the molasses.

In Table[4] B.3, we also give useful setpoints to have certain biases along a direction i that have been measured on peak (-1-2). For the z-direction, +0.565 V gives a quantization axis matching with a σ^- imaging beam. The gradients are given in absolute values because it depends on the current direction on the experiment. To determine the right direction for the field in order to compensate for the residual fields, we switch the cables on the power supplies. For the current going from the positive to the negative power supply port (so $I_{i0} > 0$), the magnetic field compensations are along $-x$ (towards 2DMOT), $+y$ (towards EMCCD) and $+z$ (up).

	X	Y	Z
$\Delta\omega_B(-1-2)$	240 kHz (±114 mG)	222 kHz (±106 mG)	586 kHz (±279 mG)
$V_i^{(-)}$	-0.015 V	-0.684 V	+0.565 V
$V_i^{(+)}$	-0.638 V	-0.968 V	+1.110 V
$\mid dB_i/dV_i \mid$	0.366 G/V	0.7465 G/V	1.024 G/V
Coils current I_{i0} for B_{i0}	32.2 mA	135.4 mA	438.5 mA
Coils driver setpoint V_{i0} for B_{i0}	-0.3265 V	-0.826 V	-0.843 V
Monitor pin for B_{i0}	DRV200: 0.655 V	DRV200S: 0.677 V	MPL2500: -

Table B.3: Magnetic field offsets for the symmetric peak (-1-2) along one direction (the two other being at zero), and magnetic field zero setpoints to compensate residual fields at the BEC position. For the MPL 2500, we can measure the current with a Hall probe to check that the current is locked.

B.3 Implementation and characterization of imaging systems

Imaging systems have been key elements for all the experiments performed during this thesis. In this section, we therefore describe the principles of absorption imaging that is an essential characterization method in our experiment. After the general description of the method, we give the characteristics of our two low numerical aperture (NA) imaging systems (magnifications of ×0.2 and ×2) that were used in the low saturation regime to extract the atomic cloud properties and to characterize the BEC's properties (section B.4.2). In the last part, we detail our high NA imaging system that was used for the experiments on cross-section calibration and sub-wavelength imaging.

[4]Again, Cicero does not send directly V_{i0} as there are buffers between the NI cards and the lock circuits (see part II.ii)

B.3.1 Absorption imaging principles and column density

In an imaging process, the information contained in the imaging direction (z for example) is integrated by optical systems. Therefore, experimentally, we have only access to the column density $n_{2D}(x, y)$ of the cloud and not directly the 3D density $n_{3D}(x, y, z)$. This experimentally obtained column density can be compared to the expected one obtained by integrating the theoretical density in the imaging direction:

$$n_{2D}(x, y) = \int_z n_{3D}(x, y, z) dz. \tag{B.3}$$

Below, we give the typical situations encountered in cold atom experiments:

- Thermal atoms in a harmonic trap have a Gaussian atomic density:

$$n_{3D}(x, y, z) = n_0 e^{-\frac{x^2}{2\sigma_x^2} - \frac{y^2}{2\sigma_y^2} - \frac{z^2}{2\sigma_z^2}}, \tag{B.4}$$

  and the column density reads:

$$n_{2D}(x, y) = n_0 \sqrt{2\pi}\sigma_z e^{-\frac{x^2}{2\sigma_x^2} - \frac{y^2}{2\sigma_y^2}}. \tag{B.5}$$

- Condensed atoms in a harmonic potential in the Thomas-Fermi approximation (interactions dominate over kinetic energy) will follow an inverted parabola atomic distribution:

$$n_{3D}(x, y, z) = n_0 \max\left(1 - \left(\frac{x}{r_{x,0}}\right)^2 - \left(\frac{y}{r_{y,0}}\right)^2 - \left(\frac{z}{r_{z,0}}\right)^2, 0\right), \tag{B.6}$$

  and the column density reads:

$$n_{2D}(x, y) = n_0 \frac{4}{3} r_{z,0} \max\left(1 - \left(\frac{x}{r_{x,0}}\right)^2 - \left(\frac{y}{r_{y,0}}\right)^2, 0\right)^{3/2}. \tag{B.7}$$

Absorption imaging is a technique that measures the image of the transmission $T(x, y) = I(x, y)/I_0(x, y)$ of a probe laser beam intensity passing through the cloud ($I(x, y)$) normalized by the same probe beam profile without atoms ($I_0(x, y)$). Assuming an absorption described by the Beer-Lambert law (see Chapter D for a discussion of it) which is valid in the low saturation limit, the optical density profile $b(x, y) = -\ln(T(x, y))$ is related to the column density times the single-atom cross-section:

$$b(x, y) \equiv \sigma_0 n_{2D}(x, y) = -\ln(T(x, y)). \tag{B.8}$$

By measuring the probe intensity profile with a camera, we have therefore directly access to the column density of the cloud. Absorption imaging will be discussed in more detail in Chapter D.

B.3.2 Time-of-flight

In order to extract the atomic cloud kinetic properties, a time-of-flight (TOF) measurement is realized after suddenly turning off all the traps. The atoms are then in free fall under the effect of gravity g, and the kinetic energy is released. The trajectory along z, of the center of mass of the cloud follows a parabola in time that corresponds to a free fall:

$$z(t) = z_0 + \frac{1}{2}gt^2. \tag{B.9}$$

The imaging system magnification is usually calibrated by TOF (Bellouvet, 2018). For t_{pix} the camera pixel size and M the imaging system magnification, t_{pix}/M is the conversion from the image plane to the object plane. Using the standard gravity $g = 9.81$ m/s^2, a fit using Eq. (B.9) calibrates M which ultimately depends on the absolute value of g (changes of a few percents of g due to position on the Earth).

For a thermal cloud far from the condensation temperature threshold (T_c), the expansion during the TOF is linked to its temperature T by:

$$\sigma_i = \sqrt{\sigma_{i0}^2 + \frac{k_B T}{m}t^2}, \tag{B.10}$$

where σ_{i0} is the initial in situ rms width in the direction i.

Well below T_c, it can be shown (Ketterle and Druten, 1996) that for an ideal degenerate gas, the expansion is similar to that of a thermal cloud but the expansion length scale is given by the harmonic oscillator energies and not by the temperature. In the opposite Thomas-Fermi limit, the expansion is dominated by inter-atomic interactions and depends on the trap geometry and chemical potential. For cigar-shaped BECs, the inversion of the cloud ellipticity during TOF is one of the signatures of BECs (or more precisely, of a hydrodynamic expansion). A sudden onset of hydrodynamic behavior as $n\lambda_T^3 > 1$ does not constitute a strict proof of BEC, but it is a very good sign that it is actually taking place.

B.3.3 Low numerical aperture imaging systems

B.3.3.1 Imaging along the MOT ($\times 0.2$)

We resume the important parameters of this imaging axis described in the thesis (Bellouvet, 2018) and depicted on Fig. B.2. This axis that we call 'ccd45' is used to image the atoms from the MOT stage to the dipole trap evaporation stages. It has a low resolution but a large field that allows us to measure large clouds and/or long time-of-flights.

A PM fiber coming from the main 780 optical bench is 25-75% splitted: the 75% power goes to the collimator and the 25 % on a monitoring photodiode. This photodiode is used to monitor the imaging beam power to accurately compute the saturation for saturated absorption imaging. The imaging beam is collimated and has a Gaussian waist measured at the entrance of the science chamber of 6.5 mm. We always use a low saturation parameter for this imaging axis.

The atoms are imaged onto a CCD camera Point Grey Chameleon[5] (pixel size 3.45 μm with two consecutive lenses with focal lengths of 150 mm (Thorlabs Plano-Convex LA1433-B) and 750 mm (Bi-Convex LB1475-B) positioned at 750 mm from the atoms. The magnification ($\approx 150/750$=0.2) is calibrated by time-of-flight : $M = 0.198$.

B.3.3.2 Imaging along DT1 ($\times$2)

Imaging after loading into the hybrid trap is usually done on this imaging system which has a magnification of about 2. This imaging system is very useful to see the BEC double structure and to realize and check all beam alignments (dipole traps, lattices).

In this section we describe this new imaging system that has been implemented. The setup is shown on Fig. B.2. There is a calibrated photodiode for monitoring the power for saturation imaging. The waist at the atom position measured by knife-edge measurements at the input and output of the chambers give a mean waist of 4.8 mm on the atoms. The polarization is linear along z. A telescope made with the second 150 mm aspherical lens and a lens of 300 mm gives the images on the ccd camera[6] Flir Blackfly BFS-PGE-31S4M which main characteristics are given in Table B.4. The magnification is experimentally calibrated by TOF: $M = 1.9$. The numerical aperture is limited by the Thorlabs PBS203 width of 20 mm right after the 150 mm aspherical lens. The distance between the atoms and that PBS is about 170 mm which gives NA=10/170=0.06.

Model	BFS-PGE-31S4M
Serial number	DL - 01385
Quantum efficiency @ 780 nm	33%
Frame rate (Hz)	35
Active pixels (H)x(V)	2048 x 1536
Pixel size (µm)	3.45 x 3.45
Digitalisation ADC (bits)	12
Pixel well depth (e-)	10,067
Sensitivity (e-/ADU)	0.17
Readout method	global shutter
Readout noise (e-)	2.29
Software	SpinView

Table B.4: Camera specifications for the imaging along DT1.

B.3.4 High numerical aperture imaging system

In this section, we detail the high numerical aperture imaging system that has been implemented on the setup. We will focus on the microscope characterization (B.3.4.1) and alignment (B.3.4.3), and on the camera (III.i) for the detection. This imaging axis allows us to get in situ images that were used to precisely calibrate the absorption cross-section in Chapter D as well as to demonstrate sub-wavelength resolutions in Chapters E and F.

[5]The camera is controlled with the software 'FlyCap2'.

[6]Refer to the lab notebook n°6 for the camera setting details. The most important parameters in 'SpinView' software are: the external trigger input is line 0 and the acquisition mode has to be set to continuous.

B.3.4.1 Microscope objective characterization

Microscope characteristics reminder : For a microscope objective (Perez, 2004) with aperture diameter D, effective focal length f in a refractive index n, the f-number N is defined as:

$$N \equiv \frac{f}{D}, \tag{B.11}$$

and the numerical aperture NA:

$$NA \equiv n \sin(\theta), \tag{B.12}$$

where θ is the half-angle between the object and the lens. The half angle is then $\theta = \text{asin}(NA/n)$. It relates to the f-number through $\tan(\theta) = D/2f = 1/2N$.

The impulse response of a circular aperture is the Point Spread Function (PSF). For a diffraction-limited system, the output intensity is given by the Airy pattern:

$$I_{Airy} = I_0 \left(\frac{2J_1(R)}{R} \right)^2, \tag{B.13}$$

where the normalized radius is $R = NA.k.r$ and I_0 is the peak intensity.

The resolution can be defined either with the Abbe limit $d_A = \frac{\lambda}{2NA}$ or the Rayleigh criterion d_R which corresponds to the distance between the maximum of an Airy pattern coinciding with the first minimum of a second Airy pattern. For a circular aperture it is:

$$d_R = 1.22 \frac{\lambda}{2NA}. \tag{B.14}$$

The depth-of-field (DOF) is defined as the longitudinal distance around the object plane over which the image in the image plane is diffraction-limited. It is given by $DOF = 2cN$ where c is the diameter of the circle of confusion in the image plane. From this value the image is considered as blurred. Using the lowest value of c which is $2d_A$ and $\tan(\text{asin}(x)) = x/\sqrt{1-x^2}$, the depth-of-field reads:

$$DOF = \frac{\lambda}{NA^2} \sqrt{n^2 - NA^2}. \tag{B.15}$$

This expression obtained from geometrical optics gives a lower bound of the depth-of-field (Knottnerus et al., 2020) and is valid when $c \ll D$ (Perez, 2004). In our experiment, for the ideal $NA = 0.44$, the depth-of-field is $DOF = 3.6$ µm. It can be increased by low pass filtering with an aperture of diameter D' in the Fourier plane of the imaging plane (Tyson, 2014) which is situated inside the relay telescope. This effectively reduces the numerical aperture by spatial filtering. To compute the new DOF and NA after filtering, we use the angle θ' depicted on Fig. B.18 which is the angle at the intermediate plane and relates to θ through the following equations:

$$\begin{aligned}\tan(\theta) =& \frac{D}{2f_{eff}},\\ \tan(\theta') =& \frac{D}{2f_{500}} = \frac{D'}{2f_{75}}.\end{aligned} \tag{B.16}$$

From Eq. (B.16), the maximum diameter D'_{max} for the maximum numerical aperture $NA = 0.44$ is:

$$D'_{max} = \frac{2f_{eff}f_{75}}{f_{500}}\tan(\theta) = \frac{2f_{eff}f_{75}}{f_{500}}\frac{NA}{\sqrt{n^2-(NA)^2}}. \tag{B.17}$$

We mention a last important microscope parameter: the field-of-view (FOV) which is the area around the optical axis where the objective operates in the diffraction-limited regime (*i.e.* without significant optical aberrations).

Old microscope objective : A homemade 4-lens microscope objective has been previously developed for this experiment in the thesis (Busquet, 2017) based on (Bennie et al., 2013). It was integrating a flip-flop mirror at the back focal plane to reflect the vertical MOT beam. However, its resolution and imaging plane position were not consistent with the optical design of (Bennie et al., 2013) so it couldn't be aligned onto the experiment. We believe the lens spacings were not correct which led to deteriorated specifications.

New microscope objective : A new 5-lens microscope shown on Fig. B.15 has been built following (Li et al., 2018). From (Li et al., 2018), the resolution, the expected field-of-view and the numerical aperture at $\lambda = 780$ nm are: $d_R = 1.08$ µm, $FOV = 210$ µm and $NA = 0.44$.

Our mechanical design, holding the microscope objective with a working distance of 35.9 mm, includes an aperture in the mount tube at the back focal plane position to put the flip-flop mirror to reflect the vertical MOT beam. Modeling the objective using the optical design software OSLO, we find that a collimated beam has a paraxial focus located at 119.95 mm from the atoms which sets the position for the mirror.

(a)

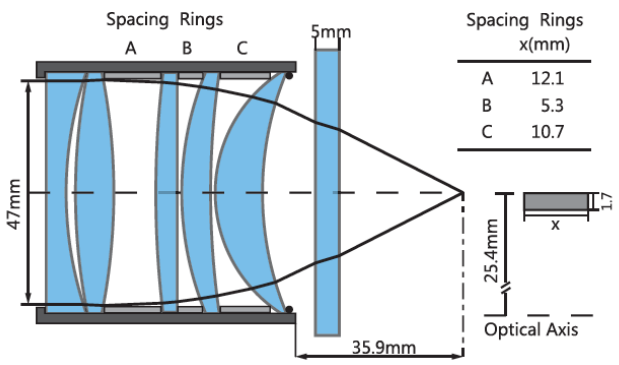

(b)

Surface	Curvature (mm)	Thickness (mm)	Material
1	Infinity	4.0	BK7
2	77.2	1.75	Air
3	127.4	8.1	BK7
4	-127.4	8.7	Air
5	206.0	4.6	BK7
6	Infinity	1.0	Air
7	65.2	6.2	BK7
8	171.6	1.0	Air
9	30.3	9.7	BK7
10	65.8	7.0	Air
11	Infinity	5.0	Silica
12	Infinity	30.9	Vacuum

Figure B.15: Microscope design that has been implemented on the experiment. The 5 singlet lens from Thorlabs are given in the article: from left to right are LC1611, LB1106, LA1725, LE1015, and LE1076 (picture and table from (Li et al., 2018)).

The objective has been tested by imaging both a 1 μm pinhole and silver nanoparticles to directly image the PSF with a magnification of 18.9. Scanning the sample in the transverse plane at the best focus and fitting with an Airy function using Eq. (B.13) or a 2D Gaussian with a standard deviation such that $\sigma \approx 0.45\lambda N$ gives the effective numerical aperture in the field-of-view as shown in Fig. B.17. The pinhole gives a better effective NA around 0.38 while the nanoparticles gives $NA = 0.3$ at $x, y = 0$. Both are lower than the expected 0.44. The flux of photons with the nanoparticles was lower. We attribute the difference between the two measurements to residual vibrations during the acquisition. Possible explanations for the discrepancy with the expected $NA = 0.44$ are :

- the residuals spacing or decentering errors (Li et al., 2018) due to the tube mount. But this error has to be higher than ± 0.1 mm to deviate significantly from diffraction-limited performances.
- A residual translation along z while translating along x and y, which could have happened due to the mechanics supporting the translation stage. Given the low DOF, this can dramatically affect the NA with a strong decrease in the field-of-view. It should be carefully corrected when measuring.
- Residual aberration introduced by the 45-degree mirror. Indeed, during the characterization we observed that the tightening screw of the down mirror was very critical in introducing aberrations (a known source of astigmatism).

In any case, even with $NA = 0.3$ yielding $d_R^{exp} = 1.30$ µm (nb: $d_R^{th} = 1.03$ µm), the objective had satisfying performances and it has been setup on the main experiment.

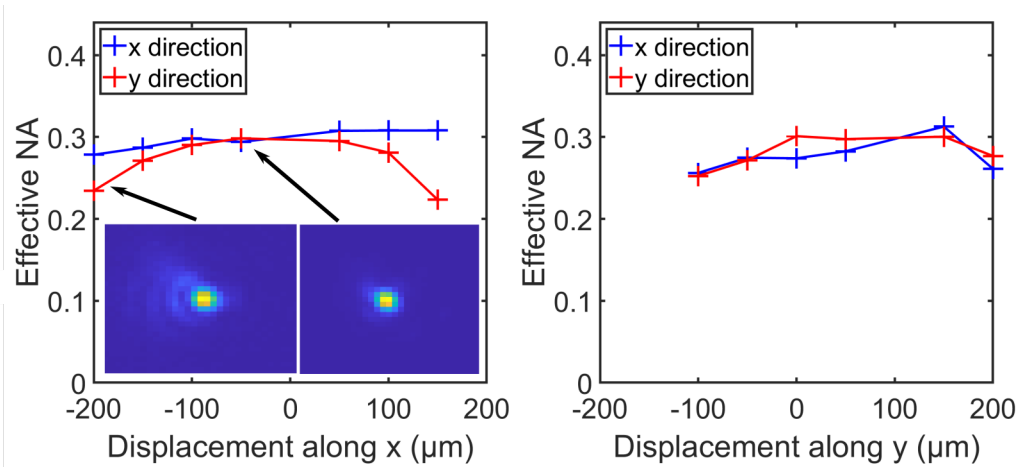

Figure B.16: Characterization using a 1 µm pinhole: NA extracted from a fit with a 2D Gaussian convolved with the 1 µm pinhole as a function of the sample displacement along x and y around the best minimum spot size. The images show raw data of the measured PSF where coma aberrations can be seen.

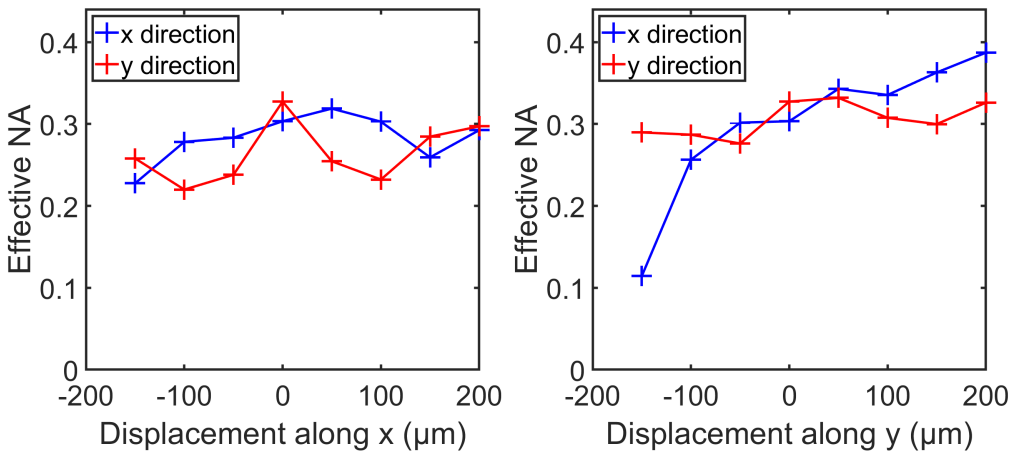

Figure B.17: Characterization using nanoparticles: NA extracted from a fit with a 2D Gaussian function as a function of the sample displacement along x and y around the best minimum spot size.

B.3.4.2 EMCCD cameras and frame transfer

In order to get rid of noise during 2 consecutive images like air turbulences that mainly cause residuals fringes and to take many images of the same cloud in a raw, we used the frame transfer mode (or fast kinetics) of the EMCCD. In the intermediate imaging plane (back focal plane) of the 500 mm lens (achromatic 2 inch doublet Thorlabs AC508-500-B-ML) preserving the diffraction limit, we placed a razor blade that hides a part of the image plane (Fig. B.18). Then, a telecentric telescope with achromatic 2-inch doublets (Thorlabs AC508-150-B, AC508-75-B), which also preserves the diffraction limit according to simulations with the OSLO software, relays the image towards the EMCCD camera with a magnification of 2. They are separated by a slotted lens tube (Thorlabs SM2L30C) that gives access to the Fourier plane for spatial frequency filtering. The whole imaging path from the microscope to the camera is protected with 2-inch black tubes to prevent background light from reaching the camera.

Imaging beam : As depicted on the Fig. B.18, the imaging beam and the MOT vertical beam are combined with a PBS. Both polarizations are crossed at the atom position. The collimated Gaussian beam has a waist of $w = 1.1$ mm on the atoms. It has been measured with a beam profiler before being set up. Such a small waist will be minimally reflected by the 2-inch tubes as the output beam waist is about 10 mm. The durations of the imaging pulses range typically from 4 to 20 µs while the AOM which is before the fiber input has a delay of about 2 µs due to the crystal. It is experimentally difficult to lock the power in a few µs so we decided to monitor the imaging pulse using a beam sampler.

A FPGA[7] is acquiring the pulse in the main Matlab program[8] (section II.i). When the pulse is acquired the saturation parameter is computed and the pulse is saved in a text file together with absorption images. The photodiode power calibration is P(W)= $2.84.10^{-3}\times$V(V) $+15.7.10^{-6}$. In the end of the microscope alignment, the imaging beam width is reduced with an aperture and imaged onto the camera. We used the full field of the camera in the image plane (no frame transfer) to point the centers of the beam and

[7] A 14-bit Red Pitaya.
[8] with the function $SignalAcquisitonOnExternalTrigger\_v3\_function$ with SCPI communication.

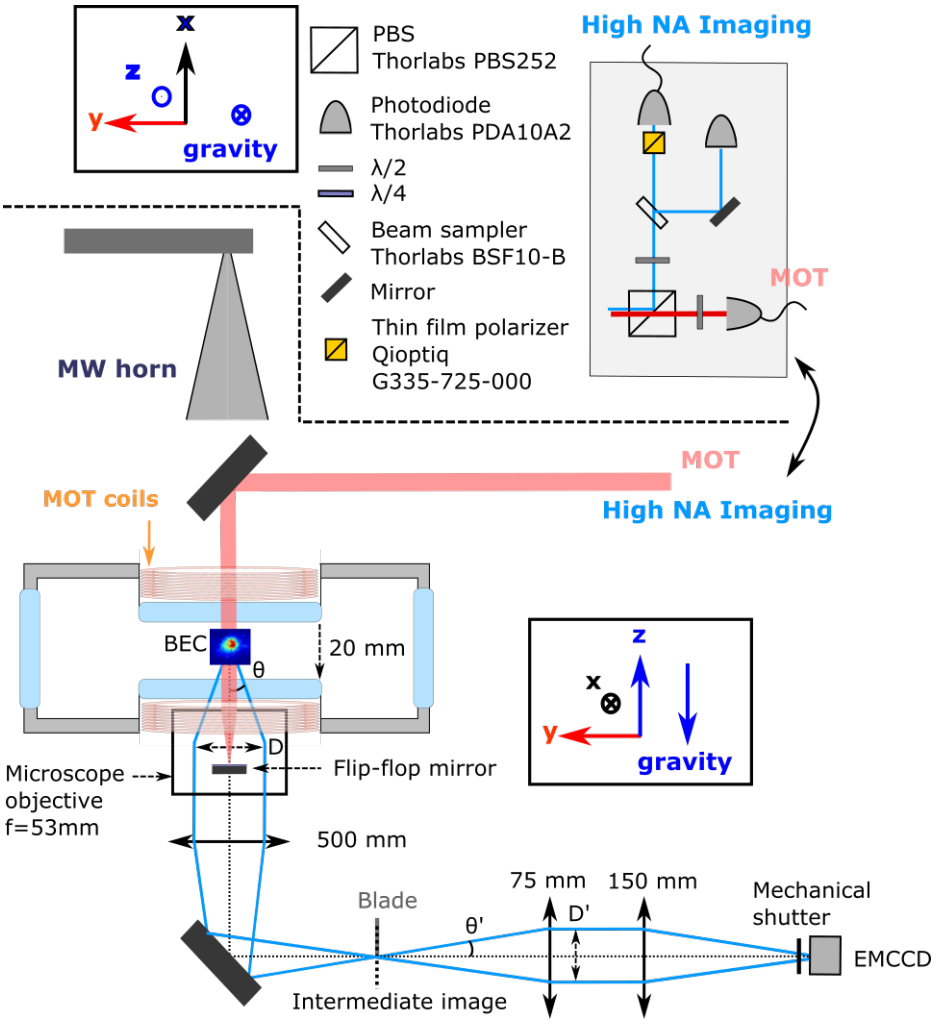

Figure B.18: Schematics of the high NA imaging axis.

cloud. Both centers were aligned by moving the imaging beam angle. For such a small beam, we also did knife-edge measurements at the intermediate plane to exactly know the beam position with respect to the atoms. This calibrates the beam intensity to compute the exact saturation parameter $s = I/I_{sat}$ seen by atoms. The same operation was done for the repumper beam, which gives the saturation for the sub-wavelength imaging.

Mechanical shutter : To avoid residual photons on the sensor during the readout, a mechanical shutter (Shutter assembly group unit for Nikon D40 D40X D60 D3000 D5000 STK0177006500) with a servo motor (micro servo SG90 9G) controlled with an Arduino Uno [9] is used just in front of the camera. It consists of 2 mechanical shutters that can be controlled independently. At rest, shutter down (D) is open and up (U) is closed. 2 voltages are set to high, then the servo motor will arm the shutter which puts D as closed and U as open. Upon the trigger, D is opened with voltage 0 then an adjustable delay later U is closed with voltage 0. At that point the shutter is at rest and closed. It should be rearmed by the servo motor. This mechanical shutter is fast, very reproducible (no oscillations of the shutter at the rise as in (Salvador Vasquez Bullon, 2016) for the 780 nm optical bench) and synchronized with the experiment as it gives a short time window to let the imaging pulse go through. The shutter speed has been characterised with a

[9] 'Servo.h' library for controlling the servo motor in Arduino program 'shutter_camera'

referenced beam. We obtained a speed of 5.2 mm/s and a delay of about 10 ms that is taken into account by pre-trig delay. Typically, the shutter opens 200 µs in advance before the arriving of the imaging pulse. For an image spanning 100 µm × 400 µm in the image plane, the shutter is open in 20 µs over the full range of 100 µm.

EMCCD cameras : In this thesis, we used 2 EMCCDs whose characteristics are reported into Table B.5. The quantum efficiency depends on the temperature sensor and is crucial to compute the exact number of counts for a given incident photon number. A fine calibration of the quantum efficiency has to be done using an incident square pulse of a calibrated waist smaller than the camera sensor which is additionally monitored by an external photodiode. Acquisitions with the pulse and without the pulse has to be done to subtract any residual light. This makes sure that the number of photons is known and that the camera does not saturate. Ultimately, the method calibrates only the product of the quantum efficiency times the conversion factor (e-/ADU) times the camera window transmission at the measured wavelength. Using this method, for the Andor camera assuming the manufacturer conversion factor and a transmission of 1, we measured a quantum efficiency of 36%, close to the datasheet of 40%. For the Princeton camera, the quantum efficiency depends on temperature and we show in Table B.5 the highest from the datasheet. At -20°C, we measured a quantum efficiency (including the input camera window) of 70%.

	Andor Luca R	Princeton ProEM
Model	DL 604M VP	512B eXcelon, coated
Serial number	DL - 01385	2502090010
Quantum efficiency @ 780 nm	36% (measured)	85% at -70°C (datasheet)
Active pixels (H)x(V)	1004 x 1002	visible 512 x 512 + hidden 512 x 512
Pixel size (µm)	8 x 8	16 x 16
Digitalisation (bits)	14	16
Pixel well depth (e-)	26,000	141,000
Vertical clock speed (µs)	0.900	> 0.450
Temperature (Air cooled)	-20°C	Down to -70°C
Sensitivity, no EM (e-/ADU)	1.7	analog gain 3 and @ 100 kHz: 0.75
Readout noise, no EM (e-)	18.2 @ 13.5 MHz	analog gain 3 and @ 100 kHz: 3.15
Dark charge (e-/pixel/s)	0.06 @ -20°C	0.0066 @ -70°C
EMCCD gain	1-1000	1-1000
Software	Andor solis + Andor script	Lightfield + Matlab script

Table B.5: Camera specifications: for the Andor all the parameters are fixed. For the Princeton, analog gains and the readout speed can be tuned, we show only the lowest readout noise and highest sensitivity.

The main camera modes that we used are:

- Single: take 1 image and read it. This is the basic operation to get the 3 images 'atoms, 'no atoms' and 'background'.

- Fast kinetics: take any number of images with a single readout at the end. Fig. B.19 shows the frame transfer principle for the particular case of $N_{tot} = 4$ subimages where 4 triggers have to be sent to the camera to finish the acquisition. In this case the important parameters are: the exposure time upon external trigger which has to be higher than the imaging pulse duration, the sub-area height h, the number of series N_{tot} and the offset from the sensor bottom row (h_b, this last parameter is for Andor only). The camera is constantly cleaning the sensor at the cleaning rate upon the first trigger. This has to be specified in the Princeton software to avoid cleaning the entire sensor and to stop the cleaning. After receiving a trigger, the camera exposes then transfers the pixels below the hidden part and waits for the next trigger. The hidden part is physically a blocking blade at the intermediate image plane (see Fig. B.18). The transfer time is equal to the sub-area height times the vertical clock speed *i.e.* 250×0.9 µs = 225 µs. At the end of the 4^{th} transfer, the readout starts at the specified readout rate (100 kHz for the lowest noise). The readout line for a mechanically normal camera orientation is located at the bottom for both Andor and Princeton cameras.

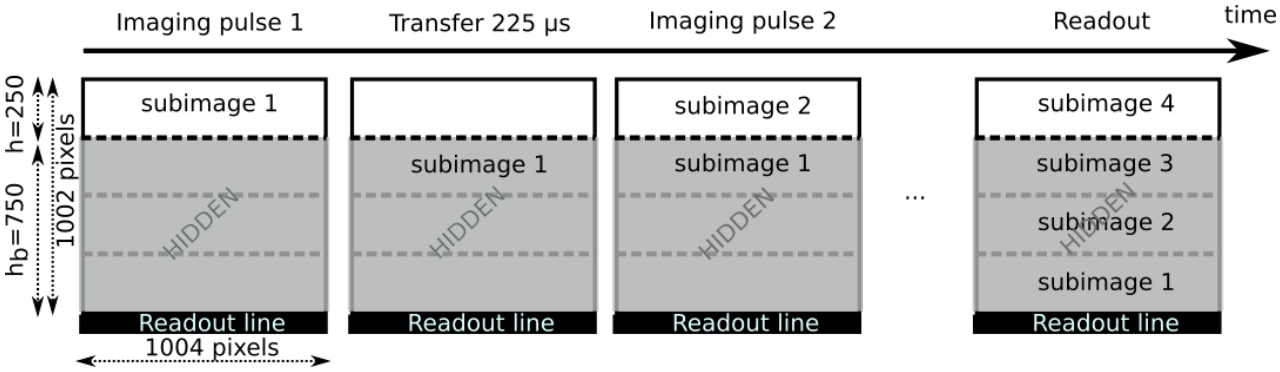

Figure B.19: Example of a fast kinetics sequence: the full sensor is divided into 4 subimages.

B.3.4.3 Alignment procedures

Alignment are critical because of the low field of view (≈ 200 µm) and depth-of-field (< 10 µm). Here we give the best alignment procedures that have been used.

Microscope transverse alignment : Starting with an intermediate magnification of 10 and the camera mechanically centered about the optical axis, the 3 axis translation stage that controls the objective position is moved to center the cloud on the camera. The access being very constrained, it is experimentally difficult to be sure that the microscope operates with the best diffraction limited settings.

Microscope focus alignment : With the camera at the intermediate plane, the focus is mechanically set to match the expected focal length distance from the center of the science chamber to the optical table. It gives an alignment precision about the millimeter. The 3-axis translation stage is then used to move finely the focus by minimizing the cloud width. Note that moving the focus also moves the image on the camera because of the mirror at 45° and changes the relative position of the flip-flop mirror that reflects the vertical MOT beam which is fixed separately from the microscope. Moving the microscope

therefore modifies the reflection of the MOT beams. As a result, the flip-flop mirror has to be manually re-optimized.

For an optical system with 2 converging lenses with focal lengths f_1, f_2 with a distance L in-between them and magnification $m = f_2/f_1$, using the thin lens equations, a defocus from the perfect focus in the object plane dz leads to a defocus in the image plane $dZ = m^2 dz/(1 - mdz/f_1 + mLdz/f_1 f_2)$. For $dz \ll f_1$, we obtain $dZ \approx m^2 dz$. Experimentally, the objective has been initially aligned by moving the translation stage. From time to time the focus has to be realigned (after temperature fluctuations or if dipole traps have been moved). However, due to the hysteresis of the translation stage along the z-direction, we usually correct for the focus by moving either the camera alone or {camera+telescope}. For instance, with our magnification of $500/53 \times 2 = 18.87$, a displacement of the object plane of $dz = 10$ µm corresponds to a displacement of the camera of $dZ \approx 3.6$ mm. This procedure probably does not preserve the best performances of the objective but is experimentally very reproducible and straightforward.

Telescope alignment : A rail (Edmund Optics 36" length doverail optical rail) defines the optical axis direction based on the imaging beam direction. The camera is mechanically fixed at the expected focus of the last focusing lens. The system {camera+telescope} is then moved together to image the intermediate image onto the camera by minimising the cloud width, this enables us to find easily the focus with a good reproducibility.

Knife alignment : Putting the camera in video mode, the focus of the knife is done by minimizing the knife diffraction at the edges by manually moving the knife mount along the imaging direction. The transverse alignment is adjusted with a 2D translation stage (Thorlabs CXY1) to hide the desired part of the EMCCD sensor.

B.4 Realization and characterization of a BEC

B.4.1 Quadrupole magnetic trap

At the end of the molasse phase, the atoms are equi-distributed between Zeeman sublevels. We first perform an optical pumping step to maximize the atom number into the $|F_g = 1, m_F = -1\rangle$ state to load a maximum number of atoms into a quadrupole magnetic trap (MT). Below, we first give the main results of the optical pumping procedure in B.4.1.1 and then characterize the evaporation dynamics in the magnetic trap by RF driven spin flips in B.4.1.2.

B.4.1.1 Optical pumping in a transient field

After the molasse stage, we have 3.10^9 atoms at 30 µK. To load the MT, if we only depump the atoms into $|F_g = 1\rangle$ then the populations are equally distributed among the Zeeman states and at maximum one-third of the atoms can be loaded in the MT. By optically pumping the atoms into $|F_g = 1, m_F = -1\rangle$, we will increase the number of atoms loaded in the MT and consequently increase the collision rate in the magnetic trap which will make the evaporation more efficient. Given our "bad" vacuum (see section B.2.1.2), this is an important step.

The OP mechanism consists of a first step where σ_- cooler and repumper beams as presented on Fig. B.21 transfer the atoms to the $|F_g = 2, m_F = -2\rangle$ and $|F_g = 1, m_F = -1\rangle$

dark state, and a second step where the repumper is removed, effectively depumping the atoms in the $|F_g = 1, m_F = -1\rangle$ state. During these steps, the quantization axis is defined by a magnetic bias B generated by OP coils.

Description of the setup : In order to apply quickly a magnetic bias after the molasses and before loading the magnetic trap, we use the transient regime of the turn on (Fig. B.20) of a current supply Delta Elektronika ES 030-5 that drives the optical pumping coils. These coils are made with 5 turns of a 10 wire rainbow ribbon cable (similar to compensation coils) around 2 viewports of external diameter of 7.5 cm. In series they have a total resistance of 2.2 Ohms. The fast turn on of the current is controlled by a circuit that consists in a MOSFET IXFN200N10P in series with the coils and the current supply. The MOSFET is activated by an amplified TTL which is time-controlled by Cicero. The transient shape of the field as measured by a magnetic field probe is shown on Fig. B.20. After 250 µs, the current in the coil and the B field pass through an extremum and vary by little over 500 µs. We use this 500 µs time slot to perform the OP. Being fast is key to prevent the expansion of the molasse which increases the potential energy transferred in the magnetic trap. The magnitude of the B field during OP can be controlled by the compliance voltage at the turn on. We checked that the shape of the transient regime does not depend on the compliance voltage.

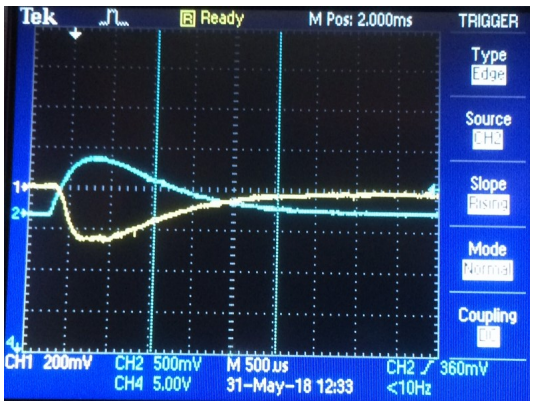

Figure B.20: Transient time evolution of the turn on of the current (blue) giving a constant magnetic field (yellow) window over 500 µs after a rising time of 250 µs.

The repumper and cooling beams are controlled by two AOMs (+80, -200 MHz) placed on the 780 optical bench. Their frequencies match respectively the transitions $|F_g = 1\rangle$ to $|F_e = 1\rangle$ and $|F_g = 2\rangle$ to $|F_e = 2\rangle$. The cooler for OP coming from 3DMOT laser is tuned at $\delta = -3\Gamma$ from $|F_e = 2\rangle$ [10].

The optical axis can be seen on the main experiment diagram of Fig. B.2. Both beams are coupled into a polarization maintaining fiber towards a collimator Schafter-Kirchoff 60FC-4-M40-10 mounted with a quarter waveplate at its output to get a circular polarization. Repumper and cooler are both circular as shown on Fig. B.21 to pump the atoms towards the $|F_g = 1, m_F = -1\rangle$ dark state. The waist of the output beam is 3.6 mm which is larger than the atomic cloud. The beam is retro-reflected in order to average the radiative force to 0 in the direction of the beam.

We note that a π-polarization for the cooler would be better suited but it was experimentally easier and still efficient to just make them circular. The orientation of the

[10] The DDS rf frequency is set at -0.86Γ.

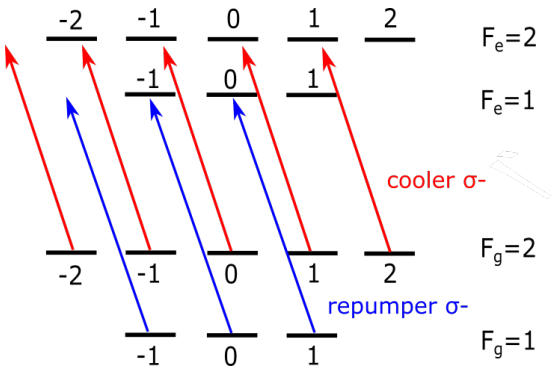

Figure B.21: Optical pumping scheme implemented on the experiment to pump the atoms towards $|F_g = 1, m_F = -1\rangle$.

quantization axis is experimentally determined by reversing the current direction with respect to the beam polarization. At the end of OP, atoms end up in $|F_g = 1\rangle$ and either in $|m_F = +1\rangle$ or $|m_F = -1\rangle$ Zeeman states depending on the direction of the current which are respectively anti-trapped or trapped in the MT. Note that to prepare the atoms into the state $|F_g = 2, m_g = +2\rangle$, the current direction has to be reversed and the repumper pulse duration has to be longer than the one of the cooler.

Optimization of the OP : To optimize the OP, the MT is loaded by increasing abruptly the MT in 6 ms to 50 G/cm (limited by the magnetic field rise time) to catch the atoms and then linearly ramping up to 160 G/cm in 200 ms (Table II.2).

The bias magnetic field (BMF) during OP at the position of the atoms is 370 mG (measured by MW spectroscopy) for a compliance voltage of 2V. Fig. B.22 shows a scan of the loaded atom number in MT vs. the compliance voltage: below 2V the magnetic field is not strong enough so the number of atoms loaded in the MT is decreasing, and above 2V the atom number does not evolve a lot and slightly decreases.

Experimentally, just letting the cooler turned on during 500 µs (800 µW) with a 14 µs (200 µW) repumper pulse at the middle is enough. We tried other schemes with multiple repumper/cooler pulses but it did not improve the OP efficiency. The OP efficiency was not sensitive to repumper saturation and we found an optimum for the power of cooler around 800 µW. Such atoms numbers enabled us to increase the evaporation efficiency in the MT and the loading in DT1. Note that with a single depumping pulse in the MOT, only 8.10^8 atoms can be loaded into MT. At the end, thanks to the OP we get twice more atoms in the MT.

We noticed that the OP was heating the cloud as the cloud temperature is about 100 µK. This is lower than the temperature after loading into MT without OP so we did not try to decrease the heating as the transfer of potential energy in the loading of the MT itself increases the cloud temperature.

A limitation to the loading efficiency could be linked to our BMF that is perpendicular to the main direction of the quadrupole trap z. At certain positions in the cloud, the quantization axis changes by 90° when the quadrupole trap is turned on. The rising time has to be fast to capture the atoms and to minimize the transfer of potential energy to the side atoms, and slow enough to guarantee that the magnetic moment $m_F = -1$ is conserved. Note that the volume matching between the molasses and the magnetically

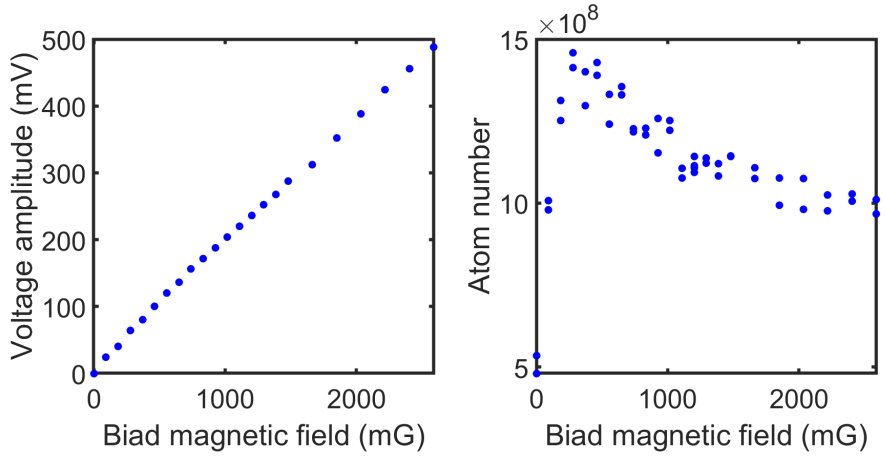

Figure B.22: Left: maximal voltage amplitude measured with a current probe of sensitivity 100 mV/mA versus the magnetic field bias. Right: atom number in $|F_g = 1, m_F = -1\rangle$ in MT as a function of the magnetic field bias.

trapped atoms, and the centering of the molasses with respect to the MT are both crucial for the loading.

Given our experimental conditions, we can wonder if the adiabaticity condition is fulfilled (Condon, 2015). The Larmor frequency $\Omega_L = 2\pi|B|/\hbar$ has to be fast compared to the rotation of the quantization axis $\dot{\Theta}_B$. For a final magnetic bias $\mathbf{B_0} = (B_{0x}, B_{0y}, B_{0z})$ and a time-dependent magnetic field $\mathbf{B_t} = (B_{tx}, B_{ty}, B_{tz})$, we can compute the scalar product between $\mathbf{B_0}$ and $\mathbf{B_t} + \mathbf{B_0}$ to get the angle Θ_B. Here for OP, the ratio $\Omega_L/\dot{\Theta}_B$ is large for the experimental parameters (400 mG, 50 G/cm, rise time 6 ms) so the atoms should always follow the local quantization axis during the magnetic trap loading.

Another limitation for our optical pumping process into a unique state could also come from multiple scattering due to large optical densities that would open the dark state transition via a degraded polarization arising from multiple scattering.

B.4.1.2 Magnetic potential

The anti-Helmholtz configuration coils with total resistance $R_{coils} = 0.45\Omega$ of the experiment can generate a maximum magnetic gradient of $B^{'} = 160$ G/cm at the atom position. This is well suited to realize a hybrid opto-magnetic conservative trap as in (Lin et al., 2009). The trapping potential for a magnetic moment $\mu = g_F m_F \mu_b$ is given by (Lin et al., 2009; Busquet, 2017):

$$U_{mag} = \mu B^{'} \sqrt{\frac{x^2 + y^2}{4} + z^2}. \tag{B.18}$$

And the quadrupole trap volume is:

$$V_0(T) = \frac{32\pi}{(1 - (mg/\mu B')^2)^2} \left(\frac{k_B T}{\mu B'}\right)^3. \tag{B.19}$$

Eq. (B.19) is the in situ MT volume that is used to calculate the phase space density D. This phase space density D could be obtained by interpolating the initial sizes from TOF measurements by cloud width fits but we found this method very inaccurate in practice.

B.4.1.3 RF evaporation in the quadrupole trap

Electronic circuit and control : The frequency chain is composed of an input frequency from a DDS 9959 II.1, a voltage control attenuator (ZX732500-S+) driven by an analog channel from Cicero, a switch ZASWA-2-50-DR+ driven by a TTL channel from Cicero, an amplifier ZHL 3AS+ with a gain of 25 dB and compression at 1dB of +32 dBm, a balun (FTB-1-6*15) and a homemade antenna placed in the top re-entrant viewport (about 15 mm away from the atoms). It has the same spire diameter of 50 mm with 4 copper spires of width 2.2 mm×1 mm.

Sequence : The initial atom number in the magnetic trap is crucial to start the evaporation as it gives the initial collision rate. The evaporation in MT consists in 4 linear rf-knife sweeps as resumed in Table B.6. The first evaporation 'Evap 1' is fast as it just goes down to the frequency 18 MHz which corresponds to about 7 times the initial temperature. It guarantees that hot atoms are removed from the trap. Fig. B.23 gives an example of a typical evaporation optimization. TOF measurements give atom numbers and temperatures, then the phase space density is obtained using the in situ MT volume given by Eq. (B.19). 'h' and 'v' are the horizontal and vertical temperatures obtained from 2D Gaussian width fits. The temperature discrepancy between 'h' and 'v' results is attributed to the fact that the thermalization has not been fully reached. Due to the finite lifetime in our vacuum system, we chose to make the evaporation step fast.

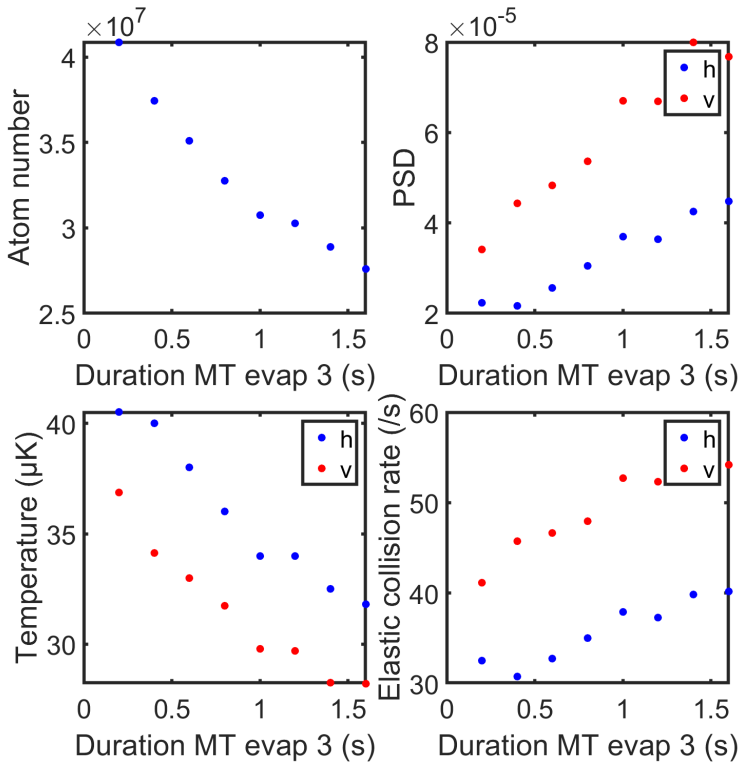

Figure B.23: Example of duration optimizations of the MT Evap 3 ramp (ccd45 imaging axis, $\pi-$polarization).

Evaporation efficiency : An evaporation is characterized by efficiency parameters that are the slopes dT/dN and dD/dN. Our data are interpreted by the evaporation theory given in section A.1 resumed in Table A.2. Using data in Table B.6, we fit the

	Loading	Evap 1	Evap 2	Evap 3	Evap 4
Frequency Set (MHz)	30				
Frequency Sweep (MHz)		30 to 18	18 to 10	10 to 7	7 to 5.5
Duration (s)		0.1	1	0.6	0.6
N	$1.6.10^9$	$1.6.10^9$	$4.5.10^8$	$2.3.10^8$	$1.3.10^8$
T (µK)	112	123	60.6	40	29
$\gamma_c(/s)$	100	79	132	190	240
PSD	9.10^{-6}	$5.8.10^{-6}$	4.10^{-5}	$1.3.10^{-4}$	$3.2.10^{-4}$
max(OD)	2.1	1.9	1.5	1.24	1

Table B.6: Optimized evaporation in MT: durations, frequencies, atom number, temperature, collision rate, phase-space density and maximum optical density (OD), all obtained from a 2D Gaussian fit of the atomic cloud. Experiments are TOF from 8 to 24 ms with step of 4 ms. For MT, data are obtained with $\delta = -2\Gamma$ and a $\pi-$polarized imaging beam on ccd45 imaging axis. T, PSD, γ_c are of the 'h' and 'v' average. Here γ_c is computed using A.12 with $\bar{n} = n_0/2\sqrt{2}$.

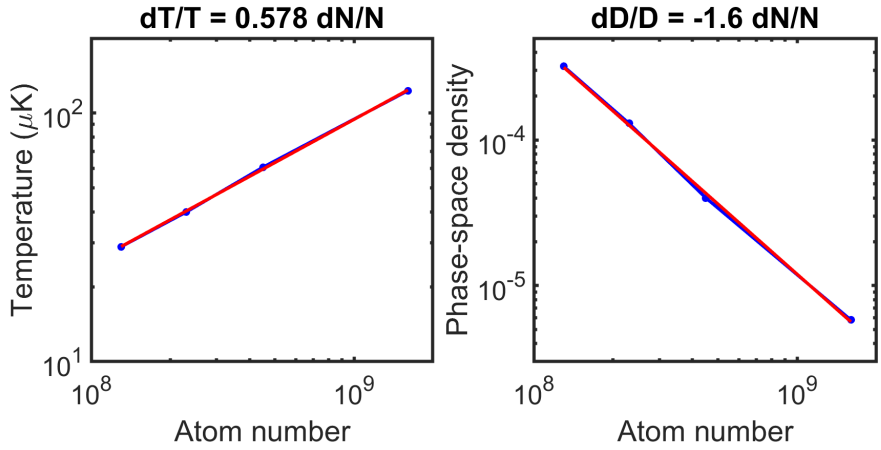

Figure B.24: Data (blue) MT Evap 1, Evap 2, Evap 3 and Evap 4 from B.6 and a linear fit (red) in loglog scale. The fit parameter is displayed in the plot title.

efficiency parameters and plot them in Fig. B.24. We have a good agreement with the theory of evaporative cooling as we measured $\alpha = 0.578$ and the phase-space density should vary for a linear trap as $1 - (9/2)\alpha = -1.6$ which is equal to the $D(T)$ fit in Fig. B.24.

Using the scaling law equations given in section A.16 we find $\eta + \kappa = 7$. This last results combined with the fact that the collision rate increases during the evaporation is compatible with the runaway evaporation condition given in section A.1.4.

Now that we quantified the evaporation dynamics in the MT, we move to the evaporation in the hybrid trap towards the Bose Einstein Condensation in the next section.

B.4.2 Optical evaporation in a hybrid trap and BEC characterisation

First, we describe the optical bench for the dipole traps, the beam alignment procedures onto the atoms and give trap frequency calibrations which enable us to load the hybrid

trap and perform forced evaporation towards BEC. Finally, we quantify the gravity sag for our trap and show that we can coherently manipulate the BEC with MW transitions.

B.4.2.1 1064 optical bench

The optical bench for the 1064 nm laser is explained in the thesis (Salvador Vasquez Bullon, 2016). The laser source is a solid state laser Mephisto MOPA from the company Coherent delivering 55W at 1064 nm. The laser is splitted in free space for the dipole traps: DT1, DT2 and lattice. All of them have an AOM whose diffraction orders are coupled to fibers that cleans the spatial modes before interacting with the atoms. The fiber outputs are the ones shown on the main experimental setup of Fig. B.2. After the fibers, each beam is polarized and then power-locked by PID circuits that feedback the AOMs. The circuits have a typical bandwidth of 100 kHz.

B.4.2.2 Alignment of the dipole traps: example DT1

Actuator mirrors : The last mirror before the last aspheric lens is a Newport AG-M100N piezo actuator mirror mount. It is a controllable mirror mount for fine alignment of the beam. A Matlab program communicates via USB with the Newport AG-UC8 Motor Controller and sends ASCII commands based on the channel, axis and number of steps in the Cicero .txt file[11]. The step amplitude is set by default to 35 in both directions, it can be reduced for fine displacements. By measuring the in situ position of DT1, the step amplitude corresponds to horizontal (H) and vertical (V) displacements resp. of 0.8 step/µm and 0.7 step/µm.

DT1 alignment with respect to the MT : Using the imaging axis CCD along DT1 ($\times 2$), the in situ position of the MT trap is measured. It is our reference position for all alignments. After a rough alignment, using some repumping light, we can load a few atoms in the dipole trap. The Newport mirrors are then used for a fine alignment with a position offset to avoid Majorana losses by measuring the loaded atom number in the dipole trap after a time-of-flight. When scanning the H direction, the atom number is optimum when both DT1 and MT positions match as shown on Fig. B.25. One can notice a slight asymmetry probably due to a coupling between H and V directions after passing the lens. Indeed, the DT1 vertical position is not constant. When scanning the V direction (Fig. B.26), the vertical position of DT1 is optimum about 2 waists below the MT vertical position. This observation relies on the good compensation of strays magnetic fields such that the minimum of the magnetic trap does not move as the magnetic gradient decreases. As the DT1 vertical position is getting closer to the MT, a sharp decrease of the atom number occurs due to Majorana losses. The loading is not sensitive over a large range of vertical positions (constant atom numbers from 100 to 200 µm) at the condition that DT1 is below MT.

Other beam alignments : Once DT1 is aligned on the atoms, DT2 and lattice *'aller'* are aligned by overlapping their in situ position with the one of DT1 using the imaging axis along DT1. The co-propagating 1529 beams are also aligned to overlap DT1's in situ positions using the imaging axis along DT1. Each beam is aligned independently (no

[11] The variable *path* contains the folder name where the Cicero file is saved. The Matlab program is $Data1/DataAnalysis/Agilis\_Piezo\_Control/Piezo\_auto\_run.m$ for automatic runs. For independent control of the mirror without Matlab, we use the software Newport AG-UC2-UC8 Applet on $COM4$.

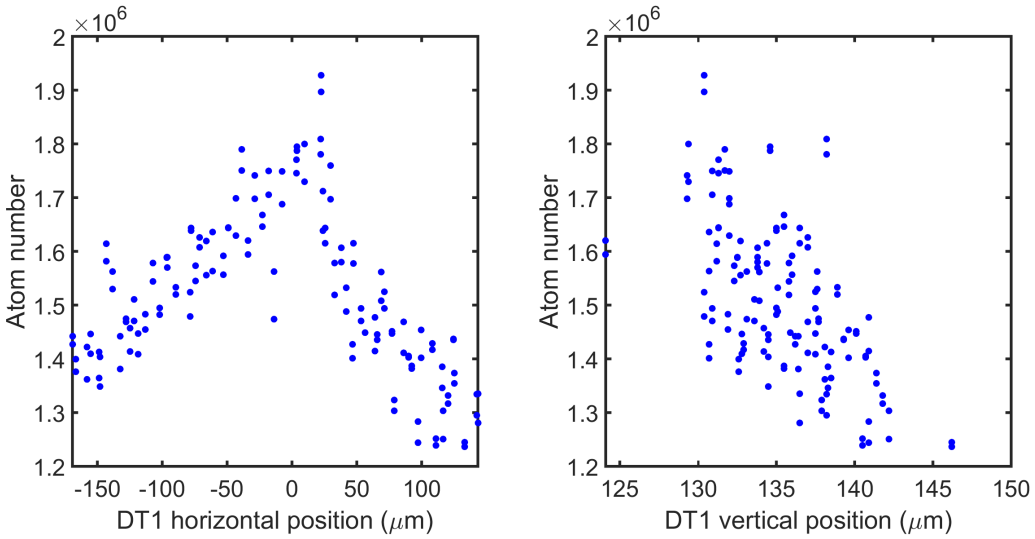

Figure B.25: Scan of the mirror horizontality. The 0 on the x-axis is referenced to the in situ position of the magnetic trap.

interference) by using a small cloud (typically MT evap 4) with low atom numbers (MOT loading reduced to 1s or less). The 1529 nm beam is ON either during the repumper step before imaging or during the imaging step. The idea is to detune either the repumper or the imaging beam to be resonant with the top of the light shift. This gives a small spot of atoms which represents the center of the 1529 nm beam. As the 1529 nm beam propagates along the imaging axis, the atom cloud has to be small to avoid having atoms resonant over a large spatial area.

B.4.2.3 Trap frequency calibrations

The dipole trap waists are calibrated at the BEC position by measuring the trap frequencies. We suddenly increase the dipole trap power with an evaporated thermal cloud in the hybrid trap. This method is called forced oscillations and described in the thesis (Bellouvet, 2018). We do not use a BEC as its breathing mode frequencies are non-trivial (Corgier et al., 2018) for the calibration.

The evolution of the position of the cloud after a TOF gives the center of mass motion at frequency ν and the cloud size evolution give the breathing mode at frequency 2ν. Note that the position is changed vertically due to the gravity sag, horizontally only the breathing mode is excited.

The oscillation frequency ν is obtained with a Fourier transform (which is more robust than a fit with a damped sine function) for a given dipole trap power P. Then, using the 2-level atom dipole potential from A.60, $\nu(P)$ is fitted with one free parameter which is the waist w such that:

$$\nu(P) = \left(\frac{12c^2\Gamma}{m\omega_0^3} \left(\frac{1}{\omega_0 - \omega} + \frac{1}{\omega_0 + \omega} \right) \right)^{1/2} \frac{\sqrt{P}}{w^2}. \tag{B.20}$$

The calibrated optical powers P_{DT1} and P_{DT1} onto the atoms versus the locking voltages $V_{lock,DT1}$ and $V_{lock,DT2}$ with a voltage resolution of 16-bits are:

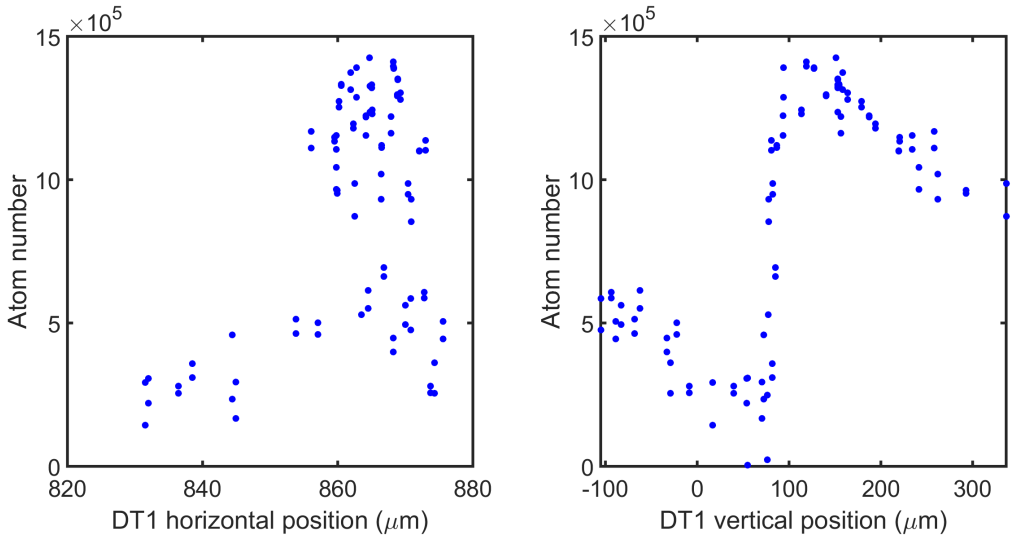

Figure B.26: Scan of the mirror verticality. The 0 on the x-axis is referenced to the in situ position of the magnetic trap. DT1 vertical position of -100μm means that DT1 is above MT by -100μm, and +100μm means that DT1 is 100μm below MT.

$$\begin{aligned} P_{DT1}(W) &= 0.414 V_{lock,DT1} + 0.002, \\ P_{DT2}(W) &= 0.378 V_{lock,DT2} + 0.005. \end{aligned} \tag{B.21}$$

Note that it is possible to use a crossed dipole trap for the evaporation which would give a higher collision rate. However, the trap frequency calibrations would be very sensitive to beam misalignments. For a perfect alignment, the square of the individual trap frequencies would sum up.

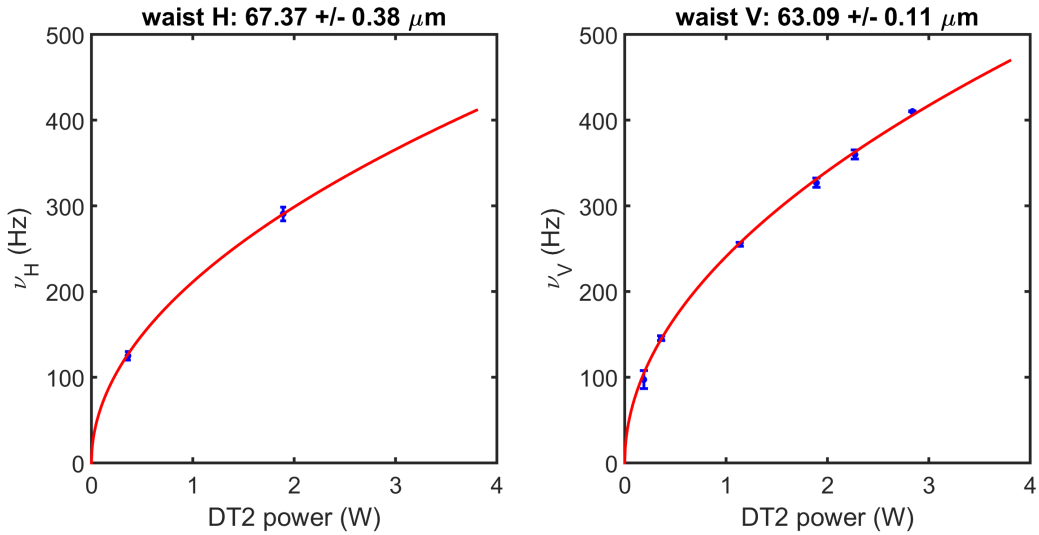

Figure B.27: Trap frequency of DT2 in a hybrid trap for a magnetic gradient of 29 G/cm, TOF=12 ms, trap depth compression pulse of 150 µs at 6V. The vertical frequency is measured with 'imaging along DT1' and the horizontal frequency is measured with 'ccd45' imaging axis. Errorbars are fit errors.

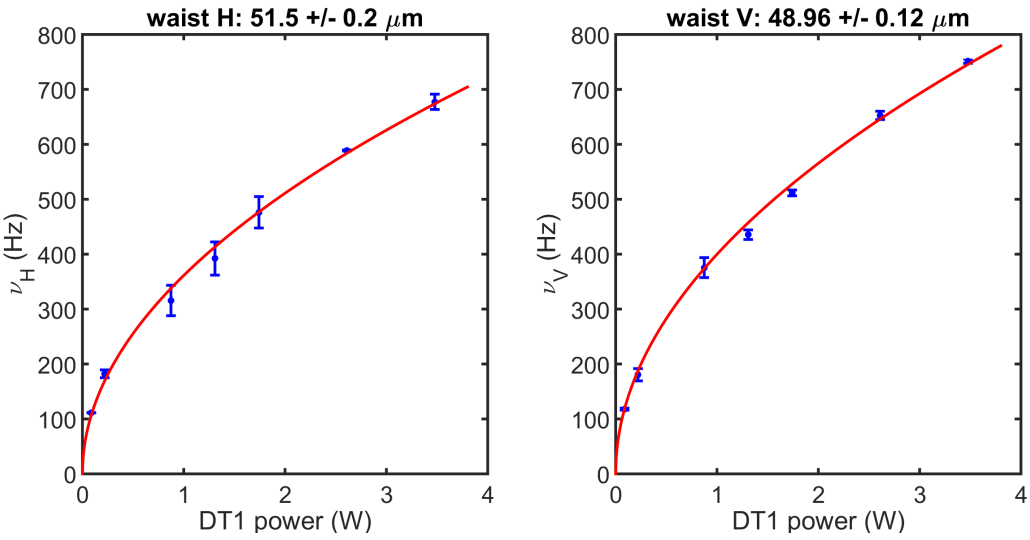

Figure B.28: Trap frequency of DT1 in a hybrid trap for a magnetic gradient of 29 G/cm, TOF=12 ms, trap depth compression pulse of 150 µs at 4V. All frequencies are measured with 'imaging along DT1'. Errorbars are fit errors.

B.4.2.4 Loading in the hybrid trap

The evaporation towards the BEC could be achieved in a quadrupole trap using an optical plug or a time-orbiting magnetic bias to avoid Majorana losses (Morizot et al., 2007). In our case we use a hybrid trap similar to (Lin et al., 2009): it combines a large quadrupole trap volume and a spin insensitive optical dipole trap.

Hybrid trap principle : The hybrid trap consists in an adiabatic expansion of the magnetic trap and transfer of the atoms into the dipole trap. The main point is that the volume changes from linear (MT) to quadratic (DT1) thereby changing the phase-space density D even for an adiabatic transfer. The dipole trap is considered as loaded when the magnetic gradient becomes smaller than the gravity gradient.

The loading is said adiabatic if the magnetic gradient is decreased such that the transfer follows an isentropic line (Lin et al., 2009). This loading strongly depends on the initial conditions for a given trap volume: $(N_0, T_0, \gamma_{c,0}, D_0)$. The higher the collision rate, the more efficient the loading will be as it will ensure that the atoms thermalize, especially atoms in the tails. Once the gradient is below gravity, the hottest atoms *i.e.* in the tails leave the trap at the end of the loading.

Hybrid trap potential : The total trap potential formed by a MT given in Eq. (B.18) and a Gaussian dipole trap at λ =1064 nm with Rayleigh range $y_R = \pi w_0^2/\lambda$, beam radius $w(y) = w_0\sqrt{1+(y/y_R)^2}$ and waist w_0 is given by:

$$U = \mu B' \sqrt{\frac{x^2+y^2}{4} + z^2} - U_0 \frac{w_0}{w(y)} e^{-2\frac{x^2+(z-z_0)^2}{w(y)^2}} + mgz + E_0. \tag{B.22}$$

The trap frequencies in such a hybrid trap are :

$$\begin{aligned}\omega_{x,z} =& \sqrt{\frac{4U_0}{mw_0^2}},\\ \omega_y =& \sqrt{\frac{\mu B'}{4m|z_0|} + \frac{2U_0}{my_R^2}} \approx \sqrt{\frac{\mu B'}{4m|z_0|}},\end{aligned} \tag{B.23}$$

where $|z_0|$ (typ. w_0) is the vertical position of the dipole trap.

The temperature evolution during an adiabatic decompression of the MT is obtained from Eq. (A.3) using the MT volume (B.19) at constant entropy ($S(T) = S(T_0)$):

$$T = T_0 \left(\frac{B'}{B_0'}\right)^{2/3} \left(\frac{1-(mg/\mu B')^2}{1-(mg/\mu B_0')^2}\right)^{4/9}. \tag{B.24}$$

Eq. (B.24) can be used to cross-check the temperature when optimizing the hybrid trap loading. Heating or a too fast opening could lead to a higher temperature than expected.

Lifetime : The initial temperature T_0 in the MT after spin evaporation is high enough to limit Majorana losses at the MT center whose loss rate (Lin et al., 2009), neglecting gravity, scales as $\Gamma_m = 1.85(\hbar/m)(\mu B'/k_B T)^2$. So, in practice, at 160 G/cm our initial temperature of 30 µK is higher than the optimal one to limit Majorana losses. The Majorana loss rate is then $\Gamma_m = 0.4$ s^{-1}.

A typical lifetime that we measure by fitting the atom number versus the holding time when the atoms are loaded into the hybrid trap was 5s. We attribute this lifetime to residual Majorana losses and poor vacuum quality. This short lifetime is not helpful but not critical as evaporating in a dipole trap usually takes only a few seconds due to its large trap frequencies compared to a linear magnetic trap. Note that due to our changing vacuum conditions over month scales, this lifetime evolved. We then opted to make the fastest evaporation possible. For instance, we measured in a raw, lifetimes at different steps in the sequence like 11.4s in a MOT, 5s in a MT and 4s in a CDT. The initial lifetime which is fluctuating over time in the MOT is due to vacuum quality, to Majorana losses in the MT and three-body losses in the CDT.

Sequence : The hybrid trap loading parameters are given in table B.7. The starting conditions are the one from the end of MT Evap 4 in which the dipole trap is turned ON at full power[12] which is equivalent to a trap depth of about 120 µK. During loading, the magnetic gradient is linearly ramped down in 1s to a value a bit lower than $B' = mg/\mu =$ 30.5 G/cm which compensates the gravity for the state $|F_g = 1, m_F = -1\rangle$.

[12]Note that for loading with DT1 at full power, the loading voltage is 7V.

	Loading
Duration	linear 1s + 0.1s thermalization
DT power (V)	constant 8V
$B^{'}$ (G/cm)	linear 160 to 28.8
$V_{c,PS}$ (V)	linear 2.08 to 0.48
VVA power of RF knife (V)	linear 3.6 to 1.7

Table B.7: Hybrid trap loading parameters with DT2.

B.4.2.5 BEC in a hybrid trap: PSD analysis

We can load and evaporate either in hybrid DT1 or hybrid DT2. Here we present the evaporation for a hybrid trap with DT2. The data are obtained using the ccd45 imaging axis ($\times 0.2$).

Fig. B.29 shows (N, T, γ_c, D) as a function of time. Errorbars represents the uncertainty of the magnetic trap frequency 20 ± 5 Hz. Experimentally, we used an exponentially decaying trap depth of duration t_f such that $V(t=0) = V_i$ and $V(t=t_f) = V_f$:

$$V(t) = \frac{V_i - V_f}{1 - e^{-t_f/\tau}} e^{-t/\tau} + \frac{V_f - V_i e^{-t_f/\tau}}{1 - e^{-t_f/\tau}}, \tag{B.25}$$

where t_f and τ have been optimized by maximizing the condensed fraction[13].

	Evaporation
t_f (s)	3
τ (s)	1/3
V_i (V)	8
V_f (V)	0.070
$B^{'}$ (G/cm)	linear 28.8 to 25
$V_{c,PS}$ (V)	linear 0.48 to 0.43
RF (V)	constant 1.697

Table B.8: Hybrid trap evaporation parameters with DT2.

Based on the data of Fig. B.29, we show on Fig. B.30 the evaporation efficiency. We see that the temperature is getting lower than the critical temperature given by Eq. (A.19) around $T = 250$ nK which sets the BEC threshold.

With a linear fit we get $\alpha = 1.58$ from which we deduce $\eta + \kappa = 5.37$. As discussed in section A.1, it shows that the evaporation is efficient, even if the mean trap frequency is decreasing.

The phase-space density for an optical trap is expected to scale as $1 - 3\alpha/2 = -1.37$ with the atom number. Our fit gives a slope of -2.07 meaning that the evaporation is actually more efficient than expected. A possible reason could be that our trap is a hybrid trap which has a trap frequency approximately constant along the dipole trap axis during the evaporation.

[13] An improvement can be done by decreasing the trap depth according to the scaling laws as (O'Hara et al., 2001) $V(t) = V_0(1 + t/\tau)^{-a}$ where τ and a can be empirically tuned.

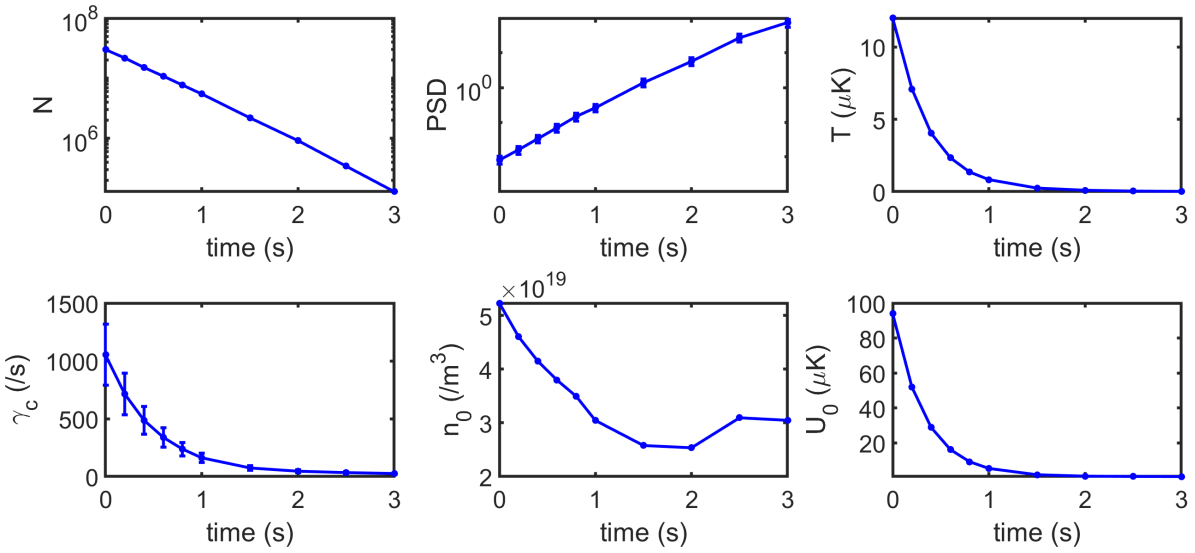

Figure B.29: Atom number, phase-space density, temperature, two-body collision rate, central density and trap depth as a function of the evaporation time using classical gas thermodynamics.

The central density at the end of the evaporation is about 2.10^{19} at/m^3. From Eq. (A.13), we have a three-body loss rate equal to $\Gamma_{3b} = 0.03$ s^{-1} so $\Gamma_{3b}^{-1} = 33.3$ s. Over a time of 3s, it gives 0.09 collisions, which is very low due to the averaged trap frequency which is low at the end of the evaporation. Note that in a crossed dipole trap or for compressed dipole traps, these losses cannot be neglected.

We resume in Table B.9 the BEC properties in this DT2-hybrid trap assuming a Thomas-Fermi distribution (see section A.2.2). This approximation is justified as $Na/a_{HO} = 400 \gg 1$ which means that the interaction term is indeed larger than the kinetic term.

Atom number	$1.5.10^5$
Trap frequencies (Hz)	(42,42,20)
Mean trap frequency (Hz)	33
Central density n_0 (/m^3)	$7.3.10^{19}$
Mean harmonic oscillator length a_{HO} (µm)	1.9
Chemical potential (Hz)	535
Thomas-Fermi radius (µm)	(8.3,8.3,18)

Table B.9: Thomas-Fermi parameters of the BEC in the hybrid trap with DT2 at the end of the evaporation where the dipole trap depth is 0.7 µK. It corresponds to the last point of Fig. B.30.

This BEC characterization is confirmed by the observation of the double structure which is done using ccd along DT1 ($\times 2$).

Our apparatus us allows to get the BEC in any configuration of the hybrid trap : with DT1 or with DT2 alone, or with both dipole traps (crossed dipole trap : CDT[14]).

[14]For a CDT, care has to be taken for the beam relative position with respect to the gravity sag and three-body losses that would be dramatic for the evaporation.

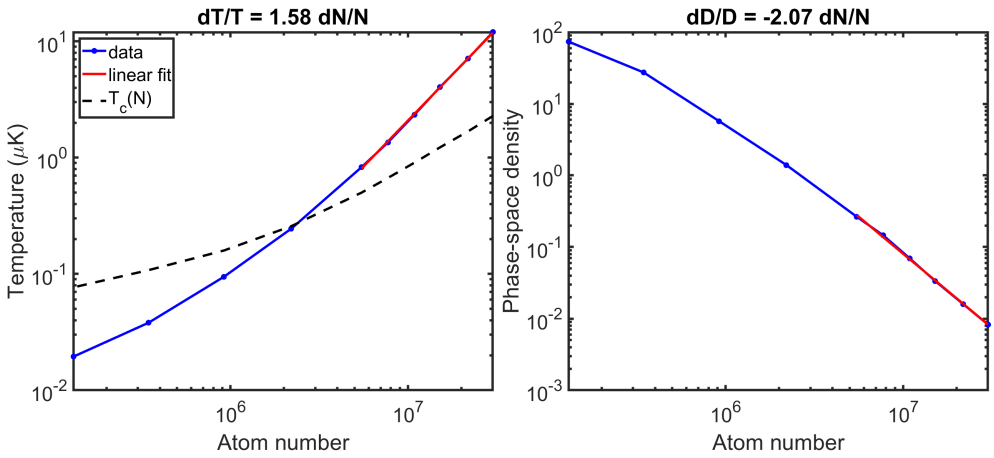

Figure B.30: Forced evaporation in the hybrid trap with a single dipole trap (DT2): data (blue) and linear fit (red). The linear fit parameters are for the temperature $\alpha = 1.58$ and for the phase-space density -2.07.

B.4.2.6 BEC in a crossed dipole trap: double structure

In this section, we show a slightly different evaporation scheme where we finish the evaporation using gravity evaporation (*i.e.* by lowering the magnetic gradient down to 0). This enables us to remove completely the magnetic gradient and to settle an homogeneous magnetic bias (usually along z-direction) that enables us to carry MW transitions.

In the following dataset, the evaporation in the hybrid trap is done by evaporating mainly in DT1 with DT2 turned on at low power. The trap depth of DT1 and DT2 are then further lowered before lowering linearly in 400 ms the magnetic gradient down to 0. The atomic optical density is measured in low saturation after a time-of-flight of 20 ms. We show on Fig. B.31 three different ending dipole trap depths in µK unit: $(U_0^{(DT1)}, U_0^{(DT2)}) = (4.73, 1.73)$, $(3.16, 1.15)$, $(2.10, 0.77)$ where the BEC threshold is clearly visible on the images. Including the effect of gravity, at zero magnetic gradient and assuming perfect beam alignments, Eq. (B.22) gives the respective total trap depths of 8.58, 3.96 and 1.24 µK. Fig. B.31 shows the 3 regimes which are above, at, and below the condensation threshold. The column density is fitted with a bi-modal distribution for all images: a 2D Gaussian as in Eq. (B.5) and a 2D Thomas-Fermi distribution from Eq. (B.7). The projections along y-axis for the data and the fit are shown where we clearly see the double structure [15].

B.4.3 Gravitational sag

The position of the minimum of a trapping potential is sensitive to gravitational sag. It can be exactly compensated with a linear potential. However, experimentally we have either a small gradient at the end of the evaporation in the hybrid trap or there is no quadrupole trap to compensate the gravity in the case of a crossed dipole trap. As a result, the position of the minimum depends on the dipole trap powers.

Experimentally, this position shift can be large, especially at the end of the evaporation in the crossed dipole trap. The consequence of such a shift in our experiment concerns in

[15] At the critical temperature (Ketterle, Durfee, and Stamper-Kurn, 1999), the thermal part follows rather a Bose-enhanced Gaussian distribution given in section A.2.1.

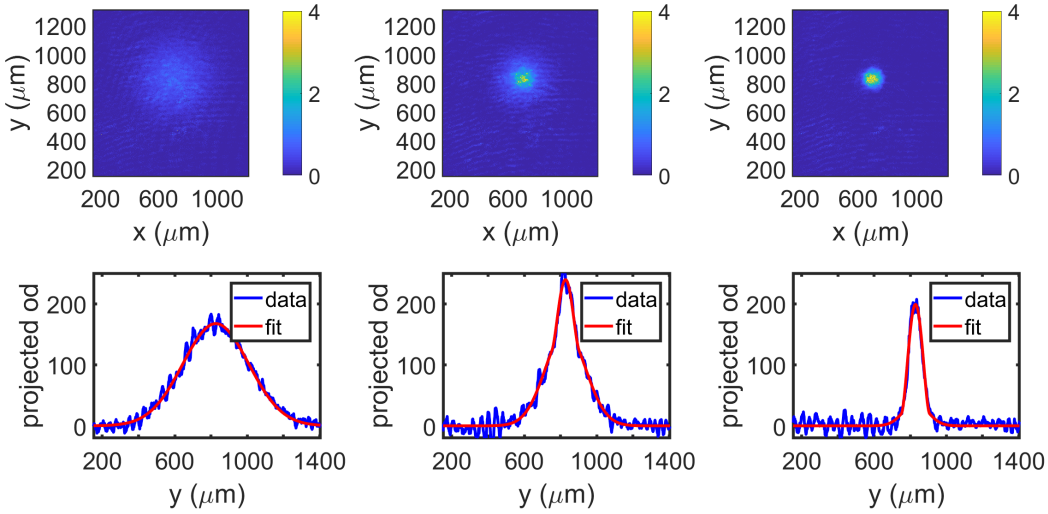

Figure B.31: Optical density after the evaporation by lowering the magnetic gradient while the atoms are loaded in the crossed dipole trap (DT1+DT2). Projections along y-axis are the data and the 2D fit with a bi-modal distribution.

situ imaging where the depth-of-focus of the microscope objective (part B.3.4) is on the order of the gravitational sag.

We find the minimum of the hybrid trap potential given by Eq. (B.22) by differentiating this expression along z (for $x, y = 0$). It gives the position of the minimum z_{min}:

$$(z_{min} - z_0)e^{-2\frac{(z_{min}-z_0)^2}{w_0^2}} = \frac{\mu B' - mg}{4U_0/w_0^2}. \tag{B.26}$$

Fig. B.32 shows $z_{min} - z_0$ versus the dipole trap depth in µK unit for DT1 (waist about $w_0 \sim 50$ µm, DT1 below the magnetic trap zero by $z_0 = -w_0$) and for a few typical magnetic gradients (using $|F_g = 1, m_F = -1\rangle$). Note that the cloud temperature is about a factor of 7 smaller than the total trap depth (see A.1.4).

We emphasize that the shift $|z_{min}|$ cannot be lower than $w_0/2$. Indeed, for lower values, the atoms are not trapped due to the sign of the curvature of a Gaussian beam that changes at $z = z_0 \pm w_0$. [16]. This means that at this position, the linear potential exactly compensates the dipole potential. In addition, there is no shift when we have a vertical magnetic gradient of 30.5 G/cm that exactly compensates the gravity.

We plot a dataset on Fig. B.32 for an evaporated cloud down to a trap depth of about 1 µK in a gradient of about 25 G/cm and the dipole trap depth is then linearly compressed in 100 ms to a tunable final value. The compression is followed by a thermalization time of 100 ms and imaged on ccd along DT1 imaging axis. The agreement is good with the expected shift. By further averaging the data, improving the calibration of the magnetic gradient and taking into account a position offset of the dipole trap along x (which was of 100 µm at the moment of the measurement) could eventually improve the agreement.

To conclude, when the sag is undesired, we usually adiabatically compress the cloud at least by a factor of 10 which reduces the shift to below 1 µm. The compression also ensures

[16] The second derivative of Eq. (B.22) leads to that result.

that the cloud width is within the depth-of-field of our microscope objective.

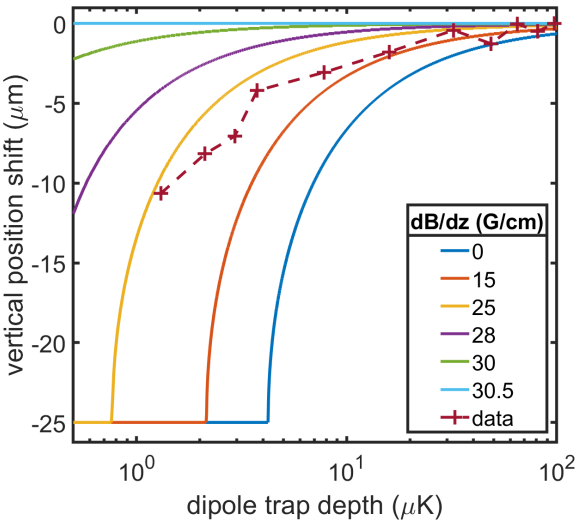

Figure B.32: Expected gravity sag in our hybrid trap potential with DT1 (waist of 50 µm) compared to a single run dataset.

B.4.4 Microwave manipulation of the BEC

In this section, we give the procedure and a quantitative analysis of the MW transfer of the BEC to $|F_g = 2\rangle$. The cross-section results and sub-wavelength imaging results presented in the following Chapters D and E have extensively been using this MW transfer capability of our experiment.

To transfer from $|F_g = 1, m_F = -1\rangle$ to $|F_g = 2, m_F = -2\rangle$, referred below as the (-1-2) transition, we cancel the magnetic bias in x and y and we set a bias $\pm|B_z|$ of about 280 mG along z that defines the quantization axis and lifts the degeneracy of the different Zeeman transitions. The transition between the two states are driven using a MW field generated by the MW chain described in section B.2.3.2. All the possible transitions can be identified on the MW frequency scan. Once the MW frequency of the (-1-2) transition has been found in a specific bias field, the duration of the Rabi pulse is scanned. Such Rabi oscillations are presented in Fig. B.33 for the two field orientations.

Changing the orientation of the field makes the imaging either σ_- or σ_+. The transition are driven 3 dB below the maximum power. This choice of power is first, to have a better time sampling of the Rabi oscillations knowing our limited digital time resolution of 2 µs with Cicero, and secondly to be insensitive to residual inhomogeneities ($\Omega \gg \Delta\omega$).

Here, we compare the transitions (-1-2) and (-10) to check the Rabi frequencies. On the experiment, the linearly polarized MW field is perpendicular to the magnetic bias along z. In Fig. B.33, the circular left polarization part of the MW field drives the transition (-1-2) in a bias $+|B_z|$ and it is the same polarization driving the transition (-10) in a bias $-|B_z|$. The difference in the Rabi oscillation period is determined by the ratio of the coupling strengths[17] of the two transitions (-1-2)/(-10) which is $\sqrt{6} = 2.45$. This compares to the experiment as $144/59.6 = 2.42$.

[17] They are Clebsch-Gordan coefficients detailed in Chapter C.

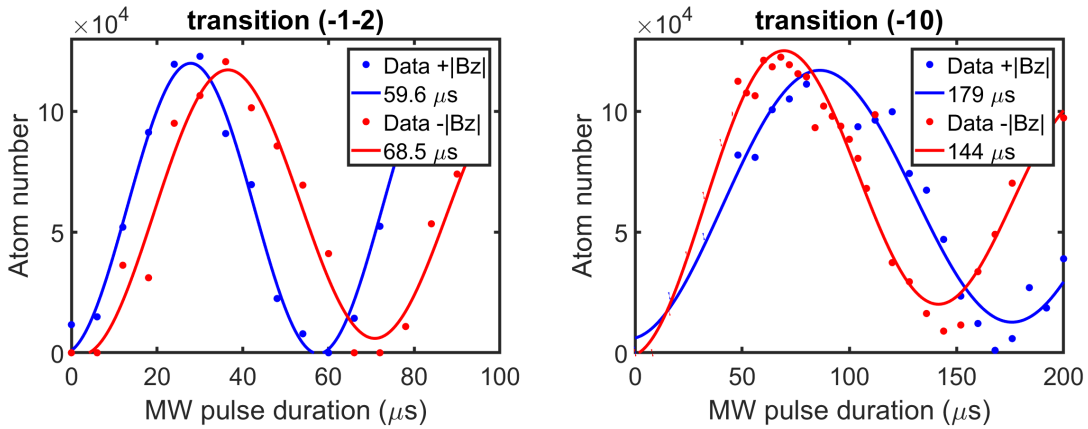

Figure B.33: Rabi oscillation data with their fits with a damped sine function for the two transitions $|F_g = 1, m_F = -1\rangle$ to $|F_g = 2, m_F = -2\rangle$ and $|F_g = 1, m_F = -1\rangle$ to $|F_g = 2, m_F = 0\rangle$. The fit function is a sine function with an exponential damping which takes decoherence into account.

Similarly, the polarization for driving (-1-2) in a bias $-|B_z|$ is the same as for the transition (-10) in $+|B_z|$ and the period ratio is $179/68.5 = 2.61$ which is also close to the expected ratio.

The Rabi periods for $\pm|B_z|$ for a given transition are slightly different because of an unequal projection in both circular polarizations, probably due to the angle between the bias and the linear polarization which is not perfectly 90°.

After a π-pulse, we usually measure in TOF a transfer of about 100% of the atoms in the upper state. It confirms that the Rabi frequency is larger than the inhomogeneities due to the BEC chemical potential or the residual magnetic gradients.

B.5 Conclusion

In this chapter, we describe the modifications of the experimental setup that have been made to reach Bose-Einstein condensation. BECs in $|F_g = 1, m_F = -1\rangle$ can be realized in a lots of configurations on the experiment. The main evaporation is done with a hybrid trap with a single dipole trap and we can also remove the magnetic trapping using a crossed dipole trap.

Evaporative cooling towards BEC has been quantitatively characterized by measuring the phase-space density which requires the knowledge of many experimental parameters: atom numbers, trap frequencies, and temperature. We clearly observed the double structure coming with the realization of Bose-Einstein condensates. Our BECs have typically about a few 10^5 atoms at about 100-200 nK.

Magnetic field biases are well-calibrated through microwave spectroscopy. We shown that we are able to make microwave Rabi oscillations to transfer our BEC between the magnetic field most sensitive ground states from $|F_g = 1, m_F = -1\rangle$ to $|F_g = 2, m_F = -2\rangle$.

We implemented and characterized a high numerical aperture NA=0.3 imaging system to get ex-vacuo in situ absorption images with a measured diffraction-limited radius of 1.3 µm.

The BEC apparatus has been here extensively described and is our starting point for all experiments presented in Chapters D, E and F. The main experimental setup of Fig. B.1.3 shows the global setup with all relevant beams and additional optical setups that will be described in their dedicated Chapters E and F: a 1D optical lattice at 1529 nm for dressing the first excited state $5P_{3/2}$ and a 1D optical lattice at 1064 nm where the BEC will be loaded.

Chapter C

Optical Bloch equations for a multi-level system

This chapter aims at giving the formalism of Optical Bloch equations for a multi-level quantum system. We will define an effective two-level system that best renders the scattering rates of the full multi-level system. It will be used for the analysis of the transmission data in Chapter D in the case of an optically dense homogeneous atomic cloud on a cycling transition. The formalism is also applied on a repumper transition for the analysis of sub-wavelength atom number volumes in Chapters E and F.

In the two first sections, we present the formalism and the derivation of the master equation that allows us to calculate the dynamics of two-level systems (TLS) in C.1 and then multi-level systems (MLS) in C.2 in the presence of coherent and incoherent radiation fields. Our detailed derivation enables us to take into account the role of the polarization of the fields and the presence of a bias magnetic field which are common experimental parameters. We will discuss the role of an incoherent background field on the steady-state atomic properties. This will be useful for including the effect of incoherent multiple scattering on the absolute calibration of atom numbers in Chapter D. In section C.3, we explicit the scattering rates for both TLS and MLS models and define the effective TLS model. In section C.4 this formalism is applied to determine the steady-state scattering cross-section of ^{87}Rb to which the effective TLS is compared. In section C.5, we concentrate on the transient regime of spin-polarized or unpolarized samples. The last section C.6 presents an extension of the formalism to open systems, in the case of a three-level system and a five-level system which will be applied in Chapters E and F.

C.1 Density matrix of a two-level quantum system

C.1.1 Master equation without dissipation

The master equation for a two-level system (TLS) including only an Hamiltonian evolution under a driving field after tracing over the environment is in the Schrödinger picture[1] (Steck, 2019):

$$\frac{d\rho}{dt} = -\frac{i}{\hbar}\left[H_A + H_{AF}, \rho\right], \tag{C.1}$$

[1] We omit hat operator symbols for simplifying the notations.

where:

- $H_A = \hbar\omega_0\sigma_z$ is the free evolution Hamiltonian.
- $H_{AF} = -\hat{\mathbf{d}}.\mathbf{E}$ is the electric-dipole interaction between the atom with dipole moment $\hat{\mathbf{d}} = -e.\hat{\mathbf{r}}$ and a classical oscillating field at the frequency ω such that the electric field is $\mathbf{E} = \mathbf{E_0}e^{i\omega t} + c.c.$. In a more practical form, it can be rewritten as $H_{AF} = \frac{\hbar\Omega_0}{2}\left(\sigma^- e^{i\omega t} + \sigma^- e^{-i\omega t} + h.c.\right)$ where $\Omega_0 = -\hat{\mathbf{d}}.\mathbf{E}/\hbar$ is the Rabi frequency.

It is common to study the master equation in the rotating-frame at ω which artificially removes the fast varying oscillation of the oscillating field at ω from the master equation. In other words, the transformation transfers the time-dependence of the oscillating field on the wavefunction where it almost cancels with the natural oscillation of the dipole. Mathematically, for a unitary operator $U = e^{i\omega t\sigma_z/2}$, the Hamiltonian in the rotating-frame is $\tilde{H} = UHU^\dagger + i\hbar\dot{U}U^\dagger$. The density matrix $\tilde{\rho} = U\rho U^\dagger$ obeys the master equation (Eq. (C.1)):

$$\frac{d\tilde{\rho}}{dt} = -\frac{i}{\hbar}\left[\tilde{H}_A + \tilde{H}_{AF}, \tilde{\rho}\right], \tag{C.2}$$

where:

- $\tilde{H}_A = -\frac{\hbar\Delta}{2}\sigma_z$.
- $\tilde{H}_{AF} = \frac{\hbar\Omega_0}{2}\left(\sigma^- + \sigma^- e^{-2i\omega t} + h.c.\right)$.

where the detuning between the oscillating field and the transition frequency is $\Delta = \omega - \omega_0$.

The link between the density matrix elements in both pictures is:

$$\begin{aligned}\tilde{\rho}_{ee} =& \rho_{ee},\\ \tilde{\rho}_{eg} =& \rho_{eg}e^{i\omega t}.\end{aligned} \tag{C.3}$$

This means that populations ρ_{gg}, ρ_{ee} are equal in different frames while coherences are equal up to a time-varying phase factor. In the rotating-frame, the coherences $\tilde{\rho}_{eg}$ are slowly varying functions (*i.e.* varying a priori on the same timescale as populations). Indeed, they will oscillate in time at the characteristic frequency Δ in time instead of $\omega_0 \gg |\Delta|$ in the laboratory frame.

In the following, we will also make the rotating wave approximation which consists in ignoring fast oscillating terms at $e^{\pm 2i\omega t}$ in H_{AF}. Since these terms vary much more rapidly than the atoms can respond, they average out to very small corrections ($\sim |\Omega/\omega|$) that we take to be zero.

C.1.2 Master equation with dissipation

The master equation for a two-level system (TLS) including an Hamiltonian evolution and damping through irreversible coupling to the vacuum modes can be written, in the rotating-frame as (Steck, 2019):

$$\frac{d\tilde{\rho}}{dt} = -\frac{i}{\hbar}\left[\tilde{H}_A + \tilde{H}_{AF}, \tilde{\rho}\right] + \Gamma D[\sigma]\tilde{\rho}, \tag{C.4}$$

where $D[\sigma]\tilde{\rho} \equiv \sigma\tilde{\rho}\sigma^\dagger - \frac{1}{2}\left(\sigma^\dagger\sigma\tilde{\rho} + \tilde{\rho}\sigma^\dagger\sigma\right)$ is the Lindblad superoperator that describes the spontaneous emission acting on the density operator.

Projecting Eq. (C.4) onto the basis states leads to the well-known optical Bloch equations for the density matrix of a TLS:

$$\begin{aligned}
\dot{\rho}_{gg} =& \frac{i\Omega_0}{2}(\tilde{\rho}_{ge} - \tilde{\rho}_{eg}) + \Gamma\rho_{ee}, \\
\dot{\tilde{\rho}}_{ge} =& -(i\Delta + \frac{\Gamma}{2})\tilde{\rho}_{ge} + \frac{i\Omega_0}{2}(\rho_{gg} - \rho_{ee}), \\
\dot{\rho}_{ee} =& -\dot{\rho}_{gg}, \\
\dot{\tilde{\rho}}_{eg} =& \dot{\tilde{\rho}}^*_{ge}.
\end{aligned} \tag{C.5}$$

C.1.3 Steady-state populations and coherences

Atomic properties like the scattering rates are contained in the populations (diagonal terms) and coherences (off-diagonal terms) of the density matrix. For a 2-level system, they correspond to the expectation values of the raising and lowering operators:

$$\begin{aligned}
\langle\sigma\rangle =& \tilde{\rho}_{eg}, \\
\langle\sigma^\dagger\rangle =& \tilde{\rho}_{ge}, \\
\langle\sigma^\dagger\sigma\rangle =& \rho_{ee}, \\
\langle\sigma\sigma^\dagger\rangle =& \rho_{gg}.
\end{aligned} \tag{C.6}$$

The steady-state density matrix elements are obtained by setting the left-hand side of Eq. (C.5) to zero:

$$\begin{aligned}
\tilde{\rho}_{eg} =& \frac{-i}{\sqrt{2}} \frac{\sqrt{\frac{s_c}{1+4\delta^2}}}{1 + \frac{s_c}{1+4\delta^2}} \frac{1 + 2i\delta}{\sqrt{1+4\delta^2}}, \\
\rho_{ee} =& \frac{1}{2} \frac{\frac{s_c}{1+4\delta^2}}{1 + \frac{s_c}{1+4\delta^2}},
\end{aligned} \tag{C.7}$$

where the normalized detuning and the coherent saturation parameter are defined as:

$$\delta = \frac{\omega - \omega_0}{\Gamma}, \tag{C.8}$$

$$s_c = \frac{2\Omega_0^2}{\Gamma^2}. \tag{C.9}$$

Eq. (C.7) can be used for any monochromatic coherent driving field. We let the saturation expression as $s_c/(1 + 4\delta^2)$ which means that the on-resonance saturation is attenuated by the detuning.

C.1.4 Adding an incoherent background field for the TLS

We would like to take into account an incoherent field background in addition to the main coherent driving field. Such an incoherent term will originate in Chapter D from surrounding atoms saturating incoherently another atom. To do that, we see from Eq. (C.7) for a TLS that coherences between atomic states are driven by the field complex

amplitude as it is proportional to $\sqrt{s_c}$. Therefore, a temporally incoherent field (frequency broadband and/or temporally isotropic polarization) gives an average coherence of zero for averaging times longer than the field spectral width *i.e.* the field coherence time. Thus, only the intensity of the incoherent field affects the OBE by incoherently pumping the populations at a rate of $\Gamma s_i/2$ where s_i is an effective saturation parameter for the incoherent radiation:

$$\frac{\partial \rho_{ee}}{dt} = -\Gamma \rho_{ee} - s_i \frac{\Gamma}{2}(\rho_{ee} - \rho_{gg}), \tag{C.10}$$

Eq. (C.10) is the rate-equation limit of the optical Bloch equations and corresponds to Einstein equations in laser physics (Steck, 2019).

Now we consider a TLS interacting with both a coherent field (s_c) and an incoherent radiation (s_i). As the incoherent radiation does not drive coherences, we can sum up the two contributions in the OBEs (Eq. (C.5) and Eq. (C.10)). For a coherent field with Rabi frequency Ω_c and detuning δ, and an incoherent intensity with saturation parameter s_i, one obtains the following OBEs:

$$\begin{aligned} \frac{\partial \tilde{\rho}_{ge}}{\partial t} &= -(i\delta\Gamma + \frac{\Gamma}{2})\tilde{\rho}_{ge} + \frac{i\Omega_c}{2}(\rho_{gg} - \rho_{ee}), \\ \frac{\partial \rho_{gg}}{\partial t} &= -\frac{s_i}{2}\Gamma\,(\rho_{gg} - \rho_{ee}) + \frac{i\Omega_c}{2}(\tilde{\rho}_{ge} - \tilde{\rho}_{eg}) + \Gamma\rho_{ee}. \end{aligned} \tag{C.11}$$

The steady-state solution of Eq. (C.11) is:

$$\begin{aligned} \tilde{\rho}_{eg} &= \frac{-i}{\sqrt{2}} \frac{\sqrt{\frac{s_c}{1+4\delta^2}}}{\left(1 + \frac{s_c}{1+4\delta^2} + s_i\right)} \frac{1 + 2i\delta}{\sqrt{1+4\delta^2}}, \\ \rho_{ee} &= \frac{1}{2} \frac{\frac{s_c}{1+4\delta^2} + s_i}{1 + \frac{s_c}{1+4\delta^2} + s_i}. \end{aligned} \tag{C.12}$$

Eq. (C.12) shows that populations can be transferred by both the coherent and incoherent light while the coherences are driven only by the coherent field but damped in the saturation regime by both fields *i.e.* the coherences are reduced by the total saturation parameter $s_i + s_c/(1 + 4\delta^2)$.

C.2 Density matrix of a multi-level quantum system

In this section, we intend to expand the definition given above to more general quantum systems that can be either degenerated and/or have more than two levels. In particular, the ground and excited states can be degenerated leading to a sensitivity to polarization and a more complicated dynamics. This complexity arises both from the different coupling strengths associated with the angular algebra of pairs of transitions and from interferences effects between different quantum paths.

C.2.1 Elements of theory for multi-level systems

Here we define the spherical basis and angular momentum formalism useful to construct the multi-level master equation (Steck, 2019). This will enable us to define the Rabi frequency and the lowering operator for Multi-Level Systems (MLS).

C.2.1.1 Electric field in spherical basis

The electric field interacting with the system will be expressed in the spherical basis. The unit vectors of this basis are defined as:

$$\begin{aligned} \hat{\mathbf{e}}_{\pm 1} &= \mp \frac{\hat{\mathbf{x}} \pm i\hat{\mathbf{y}}}{\sqrt{2}} = -\hat{\mathbf{e}}_{\mp 1}^{*}, \\ \hat{\mathbf{e}}_0 &= \hat{\mathbf{z}}. \end{aligned} \tag{C.13}$$

The set $\{\hat{\mathbf{e}}_{\pm 1}, \hat{\mathbf{e}}_0\}$ is an orthonormal basis for ordinary 3D vectors: $\hat{\mathbf{e}}_q.\hat{\mathbf{e}}_q^{*} = 1$ and $\hat{\mathbf{e}}_q.\hat{\mathbf{e}}_{-q}^{*} = 0$ for q in $\{-1, 0, 1\}$.

Any vector $\hat{\mathbf{A}} = \sum_q (-1)^q A_q \hat{\mathbf{e}}_{-q}$, where $A_q = \hat{\mathbf{e}}_q.\hat{\mathbf{A}}$, has the following spherical basis components:

$$\begin{aligned} A_{\pm 1} &= \mp \frac{A_x \pm i A_y}{\sqrt{2}} = -A_{\mp 1}^{*}, \\ A_0 &= A_z. \end{aligned} \tag{C.14}$$

The complex conjugate of $\hat{\mathbf{A}}$ verifies :

$$\hat{A}_q = (-1)^q \hat{A}_{-q}^{*}. \tag{C.15}$$

The scalar product of two vectors can be expressed as:

$$\hat{\mathbf{A}}.\hat{\mathbf{B}} = \sum_q A_q \hat{B}_q^{*}, \tag{C.16}$$

and the norm of $\hat{\mathbf{A}}$ as:

$$|\hat{\mathbf{A}}|^2 = \sum_q |A_q|^2. \tag{C.17}$$

An electric field $\mathbf{E}(t) = \mathbf{E}_0 \cos(\omega t) = \mathbf{E}_0^{(+)} e^{i\omega t} + c.c.$ in Cartesian basis $\{\hat{\mathbf{x}}, \hat{\mathbf{y}}, \hat{\mathbf{z}}\}$ of amplitude $\mathbf{E}_0$ oscillating at ω in the spherical basis reads:

$$\mathbf{E}(t) = \sum_q (-1)^q \hat{\mathbf{e}}_{-q} E_{0q}^{(+)} e^{i\omega t} + (-1)^q \hat{\mathbf{e}}_q E_{0-q}^{(-)} e^{-i\omega t}, \tag{C.18}$$

where the amplitude factor is $|\mathbf{E}_0^{(+)}| = |\mathbf{E}_0|/2$ and the notation $^{(+)}$,$^{(-)}$ refer to co-,counter-rotating terms.

Note that the optical intensity I_0 is directly obtained from the electric field amplitude as:

$$I_0 = \frac{1}{2} c\epsilon_0 |\mathbf{E}_0|^2 = 2c\epsilon_0 |\mathbf{E}_0^{(+)}|^2. \tag{C.19}$$

C.2.1.2 Dipole matrix element and Clebsch-Gordan coefficients

Atomic systems have an angular momentum structure which is due to their fine and hyperfine structure with degenerate sub-levels. The dipole matrix elements are most easily calculated in the spherical basis. We remind here useful identities for the computation of the electric-dipole interaction terms for the case of a single-electron. Indeed, the dipole

operator $\mathbf{d} = q\mathbf{r}$ is proportional to the position operator $\mathbf{r}$ which is hermitian so it verifies properties of the spherical basis such as $r_q = (-1)^q r^*_{-q}$. The Wigner-Eckart theorem for any angular momentum states K (i.e. J, F) and using $q = m_g - m_e$ applied to the dipole operator leads to the following properties (Steck, 2019):

$$\langle K_g, m_g |\, d_q \,| K_e, m_e \rangle = \langle K_g | \,|\mathbf{d}|\, | K_e \rangle \, \langle K_g, m_g | K_e, m_e; 1, q \rangle \,, \tag{C.20}$$

where the radial dependence of the dipole matrix element is given by the reduced matrix element $\langle K_g | \,|\mathbf{d}|\, | K_e \rangle$ and the angular dependence of the dipole matrix element is given by Clebsch-Gordan coefficients that can be expressed with Wigner 3-j symbols:

$$\langle K_g, m_g | K_e, m_e; 1, q \rangle = (-1)^{K_e - 1 + m_g} \sqrt{2K_g + 1} \begin{pmatrix} K_e & 1 & K_g \\ m_e & q & -m_g \end{pmatrix}, \tag{C.21}$$

These Clebsch-Gordan coefficients have the following symmetry property:

$$\langle K_g, m_g | K_e, m_e; 1, q \rangle = (-1)^{K_e - K_g - q} \sqrt{\frac{2K_g + 1}{2K_e + 1}} \, \langle K_e, m_e | K_g, m_g; 1, -q \rangle \,. \tag{C.22}$$

For atomic systems with one outer electron where three angular momenta are summed (nucleus coupling $\mathbf{F} = \mathbf{J} + \mathbf{I}$ and spin-orbit coupling $\mathbf{J} = \mathbf{L} + \mathbf{S}$), the matrix element is reduced twice in order to express the radial part as a function of the reduced dipole element (Steck, 2019) : $\langle J_g | \,|\mathbf{d}|\, | J_e \rangle$.

C.2.1.3 Rabi frequency

Using the reduction of the dipole matrix element, the Rabi frequency between hyperfine states $|F_g, m_g\rangle$ and $|F_e, m_e\rangle$ such as $q = m_g - m_e$ can be expressed as:

$$\Omega(F_g, m_g, F_e, m_e) = (-1)^{F_e - 1 + m_g} \sqrt{2F_g + 1} \begin{pmatrix} F_e & 1 & F_g \\ m_e & q & -m_g \end{pmatrix} \Omega_q^{(F_g, F_e)}, \tag{C.23}$$

where the Rabi frequency amplitude is:

$$\Omega_q^{(F_g, F_e)} = -\frac{2 \, \langle F_g | \mid \mathbf{d} \mid | F_e \rangle \, E_{0q}^{(+)}}{\hbar}. \tag{C.24}$$

Also, the dipole matrix element can be reduced to:

$$\langle F_g | \mid \mathbf{d} \mid | F_e \rangle = \langle J_g | \mid \mathbf{d} \mid | J_e \rangle \, (-1)^{F_e + J_g + 1 + I} \sqrt{S_{F_g F_e}}, \tag{C.25}$$

where the coupling between both hyperfine states is:

$$S_{F_g F_e} = (2F_e + 1)(2J_g + 1) \begin{Bmatrix} J_g & J_e & 1 \\ F_e & F_g & I \end{Bmatrix}^2. \tag{C.26}$$

The full expression of the Rabi frequency is then given by:

$$\begin{aligned} \Omega(F_g, m_g, F_e, m_e) =& (-1)^{F_e + J_g + 1 + I} \sqrt{(2F_e + 1)(2J_g + 1)} \begin{Bmatrix} J_g & J_e & 1 \\ F_e & F_g & I \end{Bmatrix} \\ & \langle F_g, m_g | F_e, m_e; 1, q \rangle \, \Omega_q^{(J_g, J_e)}, \end{aligned} \tag{C.27}$$

where:

$$\Omega_q^{(J_g,J_e)} = -\frac{2\left\langle J_g\right| \mid \mathbf{d} \mid \left|J_e\right\rangle E_{0q}^{(+)}}{\hbar}, \tag{C.28}$$

and:

$$\langle F_g, m_g | F_e, m_e; 1, q\rangle = (-1)^{F_e-1+m_g}\sqrt{2F_g+1}\begin{pmatrix} F_e & 1 & F_g \\ m_e & q & -m_g \end{pmatrix}. \tag{C.29}$$

C.2.1.4 Lowering operator

For a TLS, the lowering operator between $|g\rangle$ and $|e\rangle$ is given by $\hat{\sigma} = |g\rangle\langle e|$. For a MLS, the lowering operator between $|F_g, m_g\rangle$ and $|F_e, m_e\rangle$ ($m_g - m_e = q$) is given by:

$$\hat{\Sigma}_q = \sum_{F_g,m_g,F_e,m_e} (-1)^{F_e+J_g+1+I}\sqrt{S_{F_gF_e}}\,\langle F_g, m_g|F_e, m_e, 1, q\rangle\,|F_g, m_g\rangle\langle F_e, m_e|\,, \tag{C.30}$$

Eq. (C.30) verifies $\sum_q \hat{\Sigma}_q^\dagger\hat{\Sigma}_q = \left(\frac{2J_g+1}{2J_e+1}\right)\sum_{F_e,m_e}|F_e, m_e\rangle\langle F_e, m_e|$. This identity is used to compute the spontaneous term in the MLS master equation.

C.2.2 Total Hamiltonian

The total Hamiltonian that we now consider for the MLS master equation includes the internal atomic structure, the atom electric field interaction, and a magnetic dipole interaction that will lift the Zeeman degeneracy.

C.2.2.1 Internal Hamiltonian

The internal Hamiltonian describes the free evolution of the degenerate hyperfine states:

$$\tilde{H}_A = \hbar\sum_{F_g,m_g}\delta\omega_{F_g}|F_g, m_g\rangle\langle F_g, m_g| + \hbar\sum_{F_e,m_e}(\delta\omega_{F_e} - \Delta)|F_e, m_e\rangle\langle F_e, m_e|\,, \tag{C.31}$$

where $\delta\omega_{F_g}$ and $\delta\omega_{F_e}$ are the hyperfine splittings that will be given in section E.1.2.2 for light shift computations. Here, we will mainly perform simulations on a set of two hyperfine levels with degenerate Zeeman sublevels.

C.2.2.2 DC magnetic-dipole interaction

The Zeeman Hamiltonian $\hat{H}_B$ corresponds to the coupling between a DC magnetic field and the atom magnetic moment $\hat{H}_B = \frac{\mu_b}{\hbar}\mathbf{F}.\mathbf{B}$. In the following, we will consider only small magnetic fields and we therefore only conserve the first-order terms of the interaction. The magnetic field is oriented along z :

$$\tilde{H}_B = \hbar\sum_{F_g,m_g}\left(\frac{\mu_b B_z}{\hbar}g_{F_g}m_g\right)|F_g, m_g\rangle\langle F_g, m_g| + \hbar\sum_{F_e,m_e}\left(\frac{\mu_b B_z}{\hbar}g_{F_e}m_e\right)|F_e, m_e\rangle\langle F_e, m_e|\,, \tag{C.32}$$

where g_α with $\alpha \equiv |F, m_F\rangle$ is the Landé factor for the state α.

C.2.2.3 AC electric field-dipole interaction

The dipole interaction Hamiltonian is similar to the one detailed in section C.1.1, but it includes now all different coupling strengths:

$$\tilde{H}_{AF} = \frac{\hbar}{2} \sum_{F_g, m_g, F_e, m_e} \Omega^*(F_g, m_g, F_e, m_e) \left|F_g, m_g\right\rangle \left\langle F_e, m_e\right| + \Omega(F_g, m_g, F_e, m_e) \left|F_e, m_e\right\rangle \left\langle F_g, m_g\right| . \tag{C.33}$$

C.2.3 Master equation

In the following, we focus on multi-level atomic systems with respectively fine, hyperfine, and Zeeman quantum numbers $\{J_g, J_e\}$, $\{F_g, F_e\}$ and $\{m_{F_g}, m_{F_e}\}$ for the ground and excited states. The time evolution of the density matrix in the rotating-frame is given by the master equation that takes into account both the Hamiltonian and the irreversible spontaneous emission dynamics (Steck, 2019):

$$\frac{d\tilde{\rho}}{dt} = -\frac{i}{\hbar}\left[\tilde{H}, \tilde{\rho}\right] + \Gamma\left(\frac{2J_e+1}{2J_g+1}\right) \sum_q D[\Sigma_q]\tilde{\rho}, \tag{C.34}$$

where the total Hamiltonian is $\tilde{H} = \tilde{H}_A + \tilde{H}_{AF} + \tilde{H}_B$, and the Lindblad superoperator defined as $D[\Sigma_q]\tilde{\rho} = \Sigma_q \tilde{\rho} \Sigma_q^\dagger - 1/2\left(\Sigma_q^\dagger \Sigma_q \tilde{\rho} + \tilde{\rho}\Sigma_q^\dagger \Sigma_q\right)$ acts on the density matrix operator.

Projecting Eq. (C.34) onto states $\langle \alpha, m_\alpha|$ and $|\beta, m_\beta\rangle$ and using Hamiltonians of Eq. (C.31), (C.32) and (C.33), the evolution of the density matrix elements for the MLS is:

$$\begin{aligned}
\dot{\rho}_{\alpha,m_\alpha,\beta,m_\beta} = &-\frac{i}{2}[\sum_{F_e,m_e} \Omega^*(\alpha, m_\alpha, F_e, m_e)\delta_{\alpha g}\rho_{F_e,m_e,\beta,m_\beta} + \sum_{F_g,m_g} \Omega(F_g, m_g, \alpha, m_\alpha)\delta_{\alpha e}\rho_{F_g,m_g,\beta,m_\beta} \\
&- \sum_{F_g,m_g} \Omega^*(F_g, m_g, \beta, m_\beta)\delta_{e\beta}\rho_{\alpha,m_\alpha,F_g,m_g} - \sum_{F_e,m_e} \Omega(\beta, m_\beta, F_e, m_e)\delta_{g\beta}\rho_{\alpha,m_\alpha,F_e,m_e}] \\
&- i\left(\delta_{\alpha g}\delta_{e\beta} - \delta_{g\beta}\delta_{\alpha e}\right)\Delta_{F_gF_e}\rho_{\alpha,m_\alpha,\beta,m_\beta} - i\Delta_{\alpha,m_\alpha,\beta,m_\beta}(B_z)\rho_{\alpha,m_\alpha,\beta,m_\beta} \\
&- \frac{\Gamma}{2}\delta_{\alpha e}\rho_{\alpha,m_\alpha,\beta m_\beta} - \frac{\Gamma}{2}\delta_{\beta e}\rho_{\alpha,m_\alpha,\beta m_\beta} \\
&+ \delta\alpha g\delta g\beta \sum_{q,F_e,F_e'} \Gamma(-1)^{-\alpha-\beta}(2J_e+1) \begin{Bmatrix} J_g & J_e & 1 \\ F_e & \alpha & I \end{Bmatrix} \begin{Bmatrix} J_g & J_e & 1 \\ F_{e'} & \beta & I \end{Bmatrix} \sqrt{2\alpha+1}\sqrt{2\beta+1} \\
&\left\langle F_e, m_\alpha - q|\alpha, m_\alpha, 1, -q\right\rangle \left\langle F_e', m_\beta - q|\beta, m_\beta, 1, -q\right\rangle \rho_{F_e,m_\alpha-q,F_e',m_\beta-q},
\end{aligned} \tag{C.35}$$

where δ_{ij} is the Kronecker symbol.

Eq. (C.35) gives the evolution of the population, atomic optical coherences between a ground state and an excited state, and atomic Zeeman coherences between sub-levels within the same manifold.

In the case of pure polarizations, *i.e.* σ or π polarizations, Zeeman coherences are zero if they are initially equal to zero. The solutions of Eq. (C.35) are well-known and will be

discussed in section C.4. However, for any other polarization with a given phase relation, Zeeman coherences are not vanishing and contribute to the evolution.

Rewriting the density matrix components as a column vector $\boldsymbol{\rho}$, we obtain a set of linear coupled equations :

$$\frac{d\boldsymbol{\rho}}{dt} = \mathbf{M}\boldsymbol{\rho}, \tag{C.36}$$

where the matrix $\mathbf{M}$ contains the matrix elements for all interaction terms M_{i,m_i,j,m_j} according to Eq. (C.35) *i.e.* $d\rho_{\alpha,m_\alpha,\beta,m_\beta}/dt$ depends on ρ_{i,m_i,j,m_j}:

$$\frac{d}{dt}\begin{pmatrix} \vdots \\ \rho_{\alpha,m_\alpha,\beta,m_\beta} \\ \vdots \end{pmatrix} = \begin{pmatrix} \cdots & \vdots & \cdots \\ & M_{i,m_i,j,m_j} & \\ & \vdots & \end{pmatrix} \begin{pmatrix} \vdots \\ \rho_{i,m_i,j,m_j} \\ \vdots \end{pmatrix}. \tag{C.37}$$

For example, for a set of 3 states labelled $1, 2, 3$ (as in a Λ-system), we would have $\boldsymbol{\rho} = \begin{pmatrix}\rho_{11} & \rho_{22} & \rho_{33} & \rho_{12} & \rho_{21} & \rho_{13} & \rho_{31} & \rho_{23} & \rho_{32}\end{pmatrix}'$.

This reformulation of Eq. (C.35) as a linear set of equations C.36 is very powerful to compute either the transient dynamics by looking at the time evolution or the steady-state regime obtained for the stationary solutions (time derivatives equal to zero). In some specific cases, like pure polarizations, analytical solution can be derived (section C.4).

C.2.4 Adding an incoherent background field to the master equation

The last interaction to be added to the master equation is an incoherent field background. The interaction between a broadband incoherent field such as black-body radiation and a MLS has been previously studied (Dodin et al., 2018; Dodin, Tscherbul, and Brumer, 2016; Tscherbul and Brumer, 2015). Master equations enable a detailed description of the system composed of an atom and a bath. The Lindblad form of such equations are obtained via two simplifications.

The first simplification is the same as the one used for deriving Eq. (C.35), leading to a Lindblad type master equation. The Born-Markov approximation assumes a weak coupling ($\Gamma \ll \omega_0$) and a vanishing bath memory time and leads to the Redfield equations. After that, the secular approximation is applied to the tensorial part of the relaxation dynamics (system/environment) which is assumed to be invariant during the Hamiltonian evolution.

The second simplification is the secular approximation for independent evolution of the coherences and populations. It therefore neglects interference effects (Zeeman coherences).

Under these approximations, the master equation of an incoherently driven system with an on-resonance temporally incoherent background field simplifies to rate-equations on the populations only. As a result, the master equation of a coherently driven system Eq. (C.36) is modified by including terms in the matrix $\mathbf{M}$. These terms account for incoherent population transfers.

Under the adiabatic approximation, the optical coherences are always in equilibrium with respect to the population evolution ($\dot{\rho}_{eg} \approx 0$), the coherence for a transition between $|F_e, m_e\rangle$ and $|F_g, m_g\rangle$ driven at resonance is given by[2]:

$$\rho_{e,m_e,g,m_g} \approx -\frac{i}{\Gamma}\sum_{m'_g}\Omega(m'_g, m_e)\rho_{g,m'_g,g,m_g} - \frac{i}{\Gamma}\sum_{m'_e}\Omega(m'_g, m'_e)\rho_{e,m_e,e,m'_e}. \tag{C.38}$$

Finally, to include an incoherent field background in the master equation, Zeeman coherences are neglected in Eq. (C.38). The master equation of an incoherent field pump leads to the following rate-equations:

$$\begin{aligned}\Gamma\dot{\rho}_{\alpha,m_\alpha,\alpha,m_\alpha} =& \delta_{\alpha e}\sum_i \Omega_i^2(m_\alpha, i)\rho_{g,i,g,i} - \delta_{\alpha e}\left(\sum_i \Omega_i^2(m_\alpha, i)\right)\rho_{\alpha,m_\alpha,\alpha,m_\alpha} \\ &+ \delta_{\alpha g}\sum_i \Omega_i^2(i, m_\alpha)\rho_{e,i,e,i} - \delta_{\alpha g}\left(\sum_i \Omega_i^2(i, m_\alpha)\right)\rho_{\alpha,m_\alpha,\alpha,m_\alpha},\end{aligned} \tag{C.39}$$

with saturation $s_i = 2\Omega_i^2/\Gamma^2$.

The complete master equation including all effects is obtained by adding the terms in the right-hand side of Eq. (C.39) to the one of Eq. (C.35).

C.3 Scattering rates

C.3.1 Two-level system (TLS)

The total scattering rate is an essential quantity describing the influence of the light field on the atom. It gives the number of photons emitted per unit of time (Steck, 2019) and is computed as follows:

$$R_{sca}^{(tot)} = \Gamma\rho_{ee}, \tag{C.40}$$

where Γ is the natural linewidth and ρ_{ee} the excited state population. This total scattering rate can be decomposed into two terms. A "coherent" scattering rate $R_{sca}^{(coh)} = \Gamma|\rho_{eg}|^2$ that represents scattering events that are temporally coherent with respect to the driving field, and an "incoherent" scattering rate $R_{sca}^{(inc)} = R_{sca}^{(tot)} - R_{sca}^{(coh)} = \Gamma\left(\rho_{ee} - |\rho_{eg}|^2\right)$ that, by energy conservation, is the difference of the two previous ones. It physically corresponds to the usual Mollow triplet.

Solving the steady-state regime of the OBEs (Eq. (C.7)) driven by a coherent field leads to the following coherent and total scattering rates:

[2]It depends on the population difference and on Zeeman coherences. In the case of a *pure* polarization (aligned with only one element of the spherical basis), if the Zeeman coherences start at zero then they remain zero at steady-state, so the optical coherences are directly given by the population difference. Otherwise, Zeeman coherences can be driven and contribute to the scattering rates.

$$R_{sca}^{(coh)} = \frac{\Gamma}{2} \frac{\frac{s_c}{(1+4\delta^2)}}{\left(1+\frac{s_c}{(1+4\delta^2)}\right)^2}, \tag{C.41}$$

$$R_{sca}^{(tot)} = \frac{\Gamma}{2} \frac{\frac{s_c}{1+4\delta^2}}{1+\frac{s_c}{1+4\delta^2}}. \tag{C.42}$$

In the regime of weak saturation ($s_c \ll 1$), the atom response is linear in s_c and temporally coherent. This is the regime of the linear dipole approximation that is necessary for coupled dipole simulations (Chomaz et al., 2012). In the opposite strong saturation regime ($s_c \gg 1$), the TLS can be saturated and the temporally incoherent scattering dominates. This is the regime where the Mollow triplet (Mollow, 1969; Mollow, 1972a; Mollow, 1972b) appears in the fluorescence spectrum where the incoherent scattering rate scales as $s_c^2/(1+s_c+4\delta^2)^2$.

C.3.2 Effective TLS

To move from an ideal TLS to the effective TLS, we follow the work of (Gao, 1993) where the author computes analytically the scattering rates for the particular case of a π-polarization and shows that the saturation intensity is increased by a factor α (equivalently, the cross-section is reduced by a factor α). We then introduce an effective TLS ansatz under only a saturating driving field of saturation s_c and in perturbed conditions[3]:

$$\begin{aligned} R_{sca}^{(coh)} &= \frac{\Gamma}{2}\frac{\beta}{\alpha} \frac{\frac{s_c}{\alpha(1+4\delta^2)}}{\left(1+\frac{s_c}{\alpha(1+4\delta^2)}\right)^2}, \\ R_{sca}^{(tot)} &= \frac{\Gamma}{2} \frac{\frac{s_c}{\alpha(1+4\delta^2)}}{1+\frac{s_c}{\alpha(1+4\delta^2)}}. \end{aligned} \tag{C.43}$$

Expressions (C.43) correspond to an effective TLS with a corrected saturation parameter $s_c/(\alpha(1+4\delta^2))$. The factor β/α accounts for multilevel corrections as we will see in section C.4.2 where α is a geometric factor due to the coupling strengths of the transitions and β is an amplitude factor of the coherent scattering field due to optical pumping effects. This last coefficient β has been found thanks to numerical simulations of the full multi-level system where we found that β is exactly describing the coherent scattering rate for any input polarization of the coherent driving field (see C.4.2.1).

Now, including an incoherent background of saturation s_i as in section C.2.4 allows us to generalize the effective TLS ansatz of Eq. (C.43) :

$$\begin{aligned} R_{sca}^{(coh)} &= \frac{\Gamma}{2}\frac{\beta_{\text{eff}}}{\alpha_{\text{eff}}} \frac{\frac{s_c}{\alpha_{\text{eff}}}}{\left(1+\frac{s_c}{\alpha_{\text{eff}}}\right)^2}, \\ R_{sca}^{(tot)} &= \frac{\Gamma}{2}\left(\frac{\frac{s_c}{\alpha_{\text{eff}}}}{1+\frac{s_c}{\alpha_{\text{eff}}}} + \frac{\frac{s_i}{\alpha_c}}{1+\frac{s_i}{\alpha_c}}\right), \end{aligned} \tag{C.44}$$

where the corrections to the scattering rates are:

[3] To take into account multi-level effects, magnetic field effects, etc.

$$\begin{aligned}\alpha_{\text{eff}} =&\alpha\left(1+4\delta^2\right)(1+s_i),\\ \alpha_c =&1+\frac{s_c}{1+4\delta^2},\\ \beta_{\text{eff}} =&\beta\left(1+4\delta^2\right).\end{aligned} \tag{C.45}$$

C.3.3 Multi-level system (MLS)

For a multi-level atom, the coherent and total scattering rates in the steady-state are defined as (Steck, 2019):

$$\begin{aligned}R_{sca}^{(coh)} =&\Gamma\sum_q|\langle\Sigma_q\rangle|^2,\\ R_{sca}^{(tot)} =&\Gamma\sum_q\langle\Sigma_q^\dagger\Sigma_q\rangle.\end{aligned} \tag{C.46}$$

We are interested in comparing the rates that we obtain by solving the MLS master equation in the steady-state by setting $d\boldsymbol{\rho}/dt = 0$ in Eq. (C.36) either with symbolic computations for pure polarizations to determine the exact analytical formulas or numerically otherwise. We checked that the results of both methods are totally consistent. Then, from the density matrix solution, we compute the exact coherent and total scattering rates using Eq. (C.46). The parameters α_{eff} and β_{eff} are then obtained by fitting the exact MLS rates with the effective TLS model from Eq. (D.31) where we restrict the study to $\delta = 0$. For simplicity, in the following, these parameters will be noted as α and β.

C.4 Steady-state scattering properties of a closed transition: application to ^{87}Rb

In this section, we study the steady-state scattering properties of the D_2-line closed transition of ^{87}Rb which is depicted on Fig. C.1 with all Clebsch-Gordan coefficients.

We show that an effective TLS can properly approximate the scattering properties of a MLS, with exact correspondence in certain conditions. We numerically solve the optical Bloch equations (OBE) for a single MLS driven by a coherent field that originates either from a probe laser or from neighboring atoms via coherent scattering. We then fit the effective TLS model parameters to the coherent and total scattering response obtained from the density matrix calculations. In the study, we detail the influence of the driving field polarization, stray magnetic fields, and an incoherent resonant electromagnetic field background on the effective TLS parameters.

Part C.4.1 introduces the relevant quantities discussed throughout this manuscript for the cross-section reductions. Part C.4.2 details the calculation for the exact solution of a MLS and its comparison to an effective TLS. As an example, it quantitatively compares the effective TLS that best corresponds to the closed transition of the D_2-line of ^{87}Rb which is formed by the hyperfine states $|F_g = 2\rangle$ and $|F_e = 3\rangle$. The numerics performed in part C.4.2 could be carried for any multi-level quantum system with a closed transition.

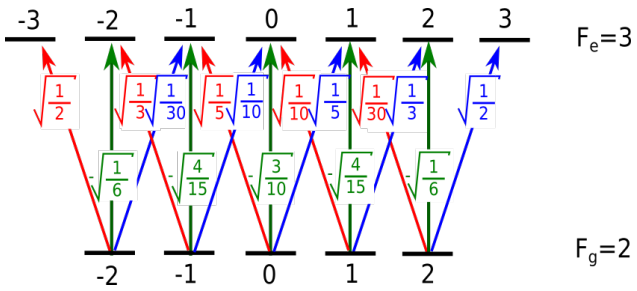

Figure C.1: The closed transition $|F_g = 2\rangle$ to $|F_e = 3\rangle$ for the D_2-line of ^{87}Rb with the Clebsch-Gordan couplings of π and $\sigma_\pm$ transitions.

C.4.1 Reduced scattering cross-section for ^{87}Rb

The scattering cross-section is defined by the radiated power divided by the incident beam intensity. On-resonance and in the low saturation limit it is given by:

$$\sigma_0 = \frac{\hbar\omega\Gamma}{2I_{sat}}, \tag{C.47}$$

where I_{sat} is the saturation intensity.

For an ideal TLS, it can be expressed more generally with the total scattering rate for a saturation of s_0 and detuning $\delta = (\omega - \omega_0)/\Gamma$ as:

$$\sigma = \frac{\sigma_0}{1 + s_0 + 4\delta^2}. \tag{C.48}$$

In general, the steady-state cross-section σ_0 is reduced due to multi-level effects (polarization ellipticity, stray magnetic fields, etc.) by a factor α such that the new cross-section becomes and the saturation intensity increases as:

$$\begin{aligned} \sigma_{eff,0} &= \frac{\sigma_0}{\alpha}, \\ I_{sat,eff} &= \alpha I_{sat,0}, \end{aligned} \tag{C.49}$$

where $I_{sat,0}$ is commonly referred to as the maximum saturation intensity for the transition $|F_g = 2, m_F = \pm 2\rangle$ to $|F_e = 3, m_F = \pm 3\rangle$. This coefficient α is the same as in the previous part C.3.2 for the effective two-level system. The effective saturation intensity is given by the effective dipole matrix element $\mathbf{d_{eff}}$ such that:

$$I_{sat,eff} = \frac{C\epsilon_0\Gamma^2\hbar^2}{4|\hat{\epsilon}.\mathbf{d_{eff}}|^2}, \tag{C.50}$$

where $\hat{\epsilon}$ is the electric field polarization, C the speed of light, and ϵ_0 the vacuum permittivity.

For the particular case of the cycling transitions $|F_g = 2, m_F = \pm 2\rangle$ to $|F_e = 3, m_F = \pm 3\rangle$, $\alpha = 1$ as we neglect depumping to other manifolds *i.e.* we consider a closed transition. The on-resonance cross-section Eq. (C.47) reduces to its maximum value directly given by the atomic transition wavelength λ_0:

$$\sigma_0 = \frac{3\lambda_0^2}{2\pi}. \tag{C.51}$$

Table C.1 resumes the values of $I_{sat,eff}$ and α for circular, linear and isotropic polarizations. Circular and linear cases are typical experimental conditions. We stress that for linear polarization, the populations are not equally distributed among all Zeeman states because of optical pumping effects. Instead, the populations accumulate around $m_F = 0$ and leads to a cross-section reduction of 461/252.

Also, the isotropic case corresponds to equal polarization components that have no phase relation with each other at any time and results in equally distributed populations. In other words, the atom interacts with a coupling amplitude equal to $1/\sqrt{3}$ of the total dipole moment of the closed transition having a coupling strength of $S_{F_gF_e} = 0.7$. This leads to a cross-section reduction of 15/7.

The last comment is that for the case of linear polarization and far-detuned radiation, the field interacts with a coupling amplitude of $1/\sqrt{3}$ of the full transition of $5S_{1/2}$ to $5P_{3/2}$. This gives $\alpha = 1.5$ and a saturation intensity of 2.503 mW/cm^2.

polarization	$\hat{\epsilon}.\mathbf{d_{eff}}$	$I_{sat,eff}$ (mW/cm^2)	α
Circular	$\sqrt{1/2}$	1.669	1
Linear	$\sqrt{126/461}$	3.05	$461/252 = 1.829$
Isotropic	$\sqrt{7/30}$	3.576	$15/7 = 2.143$

Table C.1: Saturation intensities and α parameters for the on-resonance cycling transition $F_g = 2$ to $F_e = 3$ at steady-state. The dipole moment is in units of $\langle J_g = 1/2 \mid \mathbf{d} \mid J_e = 3/2\rangle = 4.227\ ea_0$ where a_0 is the Bohr radius and e the electron charge.

C.4.2 Effective TLS of the closed D_2 transition of ^{87}Rb

To study the role of experimental imperfections such as polarization orientation, DC magnetic fields and incoherent background on the scattering rates, we restrict our model to closed multiple degenerate states. As an example, we choose to perform the numerics of our model on all Zeeman states of the transition $|F_g = 2\rangle \rightarrow |F_e = 3\rangle$ of the ^{87}Rb D_2-line. It represents such type of a closed transition at the condition that the power broadening is much smaller than the hyperfine energy splitting. In the following, we therefore neglect the residual coupling to other hyperfine excited and ground states. In the steady-state regime, these couplings would lead to depumping out of the considered transition. Our study is therefore valid only before depumping occurs and is robust for well-closed transitions.

The role of the driving field polarization (sec. C.4.2.1), DC magnetic field (sec. C.4.2.2) and isotropic incoherent field (sec. C.4.2.3) are studied independently. The quantization axis is taken as $\boldsymbol{\epsilon}_z$.

C.4.2.1 Role of the polarization

In this section, only the coherent drive field polarization is being changed at zero magnetic field and zero incoherent field. We use the spherical basis with respect to the Cartesian as follows:

$$\begin{aligned} \boldsymbol{\epsilon}_\pm &= \mp \frac{(\boldsymbol{\epsilon}_x \pm i\boldsymbol{\epsilon}_y)}{\sqrt{2}}, \\ \boldsymbol{\epsilon}_0 &= \boldsymbol{\epsilon}_z. \end{aligned} \tag{C.52}$$

This polarization $\boldsymbol{\epsilon} = (\epsilon_-, \epsilon_+, \epsilon_0)$ is parametrized in the spherical basis $(\boldsymbol{\epsilon}_-, \boldsymbol{\epsilon}_+, \boldsymbol{\epsilon}_0)$ by an ellipticity $\zeta = E_{0x}/E_{0y}$ and π polarization projection angle Θ (Fig. C.3) as:

$$\begin{aligned} \epsilon_\pm &= \mp \frac{1}{\sqrt{2}\|\boldsymbol{\epsilon}\|}(\zeta \mp \cos(\Theta)), \\ \epsilon_0 &= \frac{i}{\|\boldsymbol{\epsilon}\|}\sin(\Theta). \end{aligned} \tag{C.53}$$

where $\|\boldsymbol{\epsilon}\| = \sqrt{1+\zeta^2}$. Using the TLS ansatz of Eq. (C.43), we evaluate the parameters $\alpha \equiv \alpha_{\boldsymbol{\epsilon}}$ and $\beta \equiv \beta_{\boldsymbol{\epsilon}}$ that best match the exact scattering rates. For a given ζ, both scattering rates $R_{sca}^{(coh)}, R_{sca}^{(tot)}$ are computed numerically as a function of the coherent saturation parameter s_c. $\alpha_{\boldsymbol{\epsilon}}$ and $\beta_{\boldsymbol{\epsilon}}$ are the best fitting parameter for $s_c \in [0.1, 30]$. The ratio of the number of diffusions between $|F_e = 3\rangle$ and $|F_e = 2\rangle$ (44 Γ detuned from $|F_e = 3\rangle$) is about 1000 for $s_0 = 60$ on the closed transition. As a result, the transition from $|F_g = 2\rangle$ to $|F_e = 3\rangle$ is considered as closed in the range $s_c \in [0.1, 30]$. Figure C.2 shows the simulation results for $\zeta = 0.5$ with fits using the effective TLS formulas. The corresponding fit parameters for α and β are plotted in figure C.4.

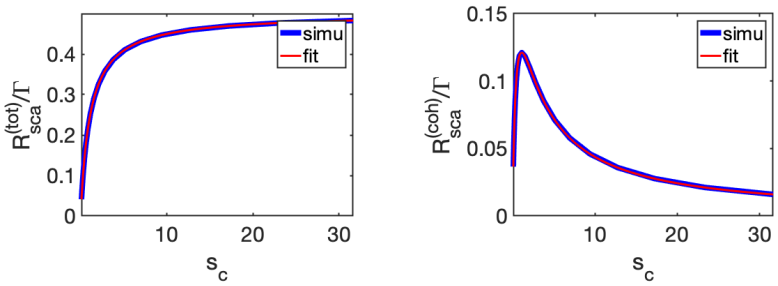

Figure C.2: Example of the total and coherent scattering rates for $\zeta = 0.5$ at zero magnetic field and for $\Theta = 0$: simulation results in blue and fit with the effective TLS in red.

In the limit case of a σ_- circular polarization $\boldsymbol{\epsilon} = (1, 0, 0)$ parametrized by $(\zeta, \Theta) = (1, 0)$, the atom is pumped in a perfect two-level cycling transition and is expected to reach the maximal scattering cross-section $\sigma_0 = 3\lambda^2/2\pi$ with $\alpha_\sigma = \beta_\sigma = 1$. In the opposite limit of a π linear polarization $\boldsymbol{\epsilon} = (0, 0, 1)$, the populations and coherences have been computed analytically (Gao, 1993). The system formed by five π-transitions for $|F_g = 2\rangle$ to $|F_e = 3\rangle$ is equivalent to a TLS with a reduced cross-section for which $\alpha_\pi = 461/252 = 1.829$ and $\beta_\pi = 1$.

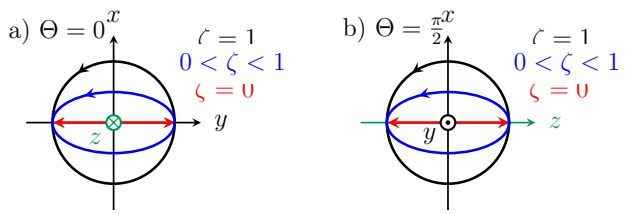

Figure C.3: Two standard polarization cases and their dependence on ellipticity ζ and quantization axis (green) : a) For $\Theta = 0$, the polarization lies in the (x,y) plane and is circular for $\zeta = 1$ with a perpendicular quantization axis, b) For $\Theta = \pi/2$, the polarization lies in the (x,z) plane and is linear for $\zeta = 0$ with a parallel quantization axis.

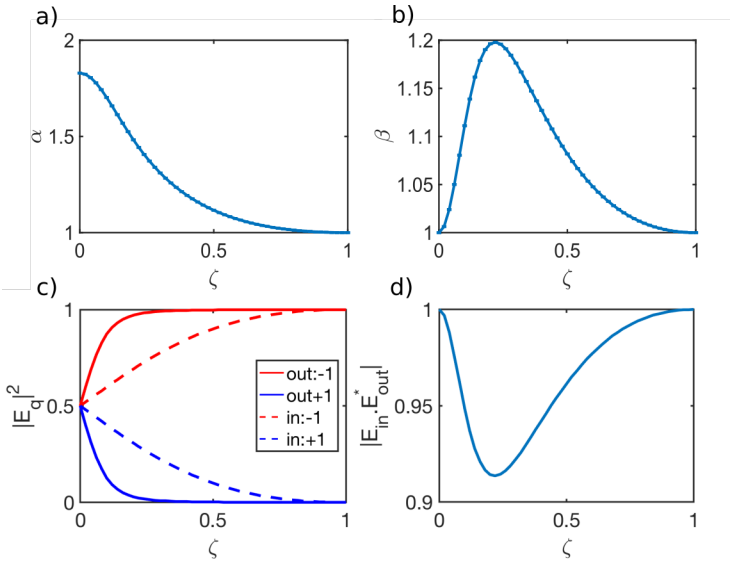

Figure C.4: a) α and b) β as a function of the ellipticity ζ for a polarization in the (x,y) plane ($\Theta = 0$), c) input and output intensities per polarization, d) scalar product of the input and output fields.

In Fig. C.4, intermediate ellipticities are obtained by varying ζ from 1 (circular) to 0 (linear) at $\Theta = 0$. We checked from numerical simulations that the values of $\alpha_{\boldsymbol{\epsilon}}$ and $\beta_{\boldsymbol{\epsilon}}$ are exact, *i.e.* the errorbars go to 0. It means that the scattering rates are exactly described by Eq. (C.43). It does not necessarily mean that this situation is exactly equivalent to a TLS that is a scalar scattering problem while the MLS is vectorial.

The circular and linear polarizations yield the expected values $\alpha_\sigma = 1$ and $\alpha_\pi = 1.829$. Note that the linear polarization is at a 45° angle of the x and y axis. In absence of magnetic field bias, the electric field sets the quantization axis. The same curves would be obtained for $\Theta = \pi/2$. An imperfect polarization, as could occur in experiments, induces little changes for the circular polarization ($\zeta = 0$) -below 10% variation on the parameters- even up to $\zeta = 0.5$, while it has more effect for a linear polarization. This is due to optical pumping in the closed transition that protects the atomic state. For the same reason, the polarization of the radiated field differs from the input polarization at maximum by 8% for an ellipticity about $\zeta = 0.2$.

C.4.2.2 Role of a DC magnetic field

Under a constant magnetic field, magneto-optical effects occur. We refer to the review (Budker et al., 2002) for more detail. The Faraday effect, for example, results in the optical rotation and ellipticity change of the output scattering. The scattering process is therefore a truly vectorial problem that cannot be exactly mapped onto the TLS solution due to the output polarization.

In this section, we focus the analysis on the TLS parameters α and β that best mimic the scattering rate amplitude when the Zeeman degeneracy is lifted by a magnetic field bias such that $\mathbf{B} = B_z \boldsymbol{\epsilon}_z$. The driving field frequency is kept constant and is equal to the unshifted transition. The magnetic Zeeman shift between two states $|F_e, m_e\rangle$ and $|F_g, m_g\rangle$ is $\Delta(B_z) = \mu_b B_z/\hbar \left(g_{F_e} m_g - g_{F_g} m_g\right)$ where $g_{F_{e/g}}$ are the Landé factors and μ_b is the Bohr magneton. The strength of magnetic field considered in this study are up to 2G which

is well below the restriction to first order Zeeman perturbation and smaller than Γ. The state $|F_g = 2\rangle$ (resp. $|F_e = 2\rangle$) has a frequency sensibility to magnetic shift of $0.12\Gamma/\mathrm{G}$ (resp. $0.15\Gamma/\mathrm{G}$).

In a σ_- polarization case, $\alpha = \beta = \alpha_\sigma(1 + 4\,(\delta_\omega + \delta_{B_z})^2)$ where $\delta_{B_z} = \mu_b B_z/\hbar\Gamma$. It simply corresponds to a TLS probed off-resonantly due to the Zeeman shift and the driving field detuning. Due to optical pumping, only the two states $|F_g = 2, m_g = -2\rangle$ and $|F_e = 3, m_e = -3\rangle$ are occupied at steady-state. The atomic response is the one of a TLS and the results of Eq. (C.41) are exactly recovered. In this situation, the Zeeman shift can be experimentally compensated by the driving field detuning. Interestingly, for a linear polarization aligned with a magnetic bias (π polarization), the scattering rates are also exactly given by the effective TLS expressions (D.31) with $\alpha = \alpha_\pi \left(1 + 4\delta_{B_z}^2 \frac{41}{1008\alpha_\pi} + 4\delta_\omega^2\right)$ and $\beta = 1$. These expressions can be derived by solving the linear system (Eq. (C.36)) containing all $\pi-$transitions. In this situation, the sensitivity of the scattering rates to the detuning is reduced by a factor $\frac{41}{1008\alpha_\pi} \approx 0.02$ with respect to the σ polarization case. As a result, for pure σ or π polarizations, α and β have well-known lower and upper limits.

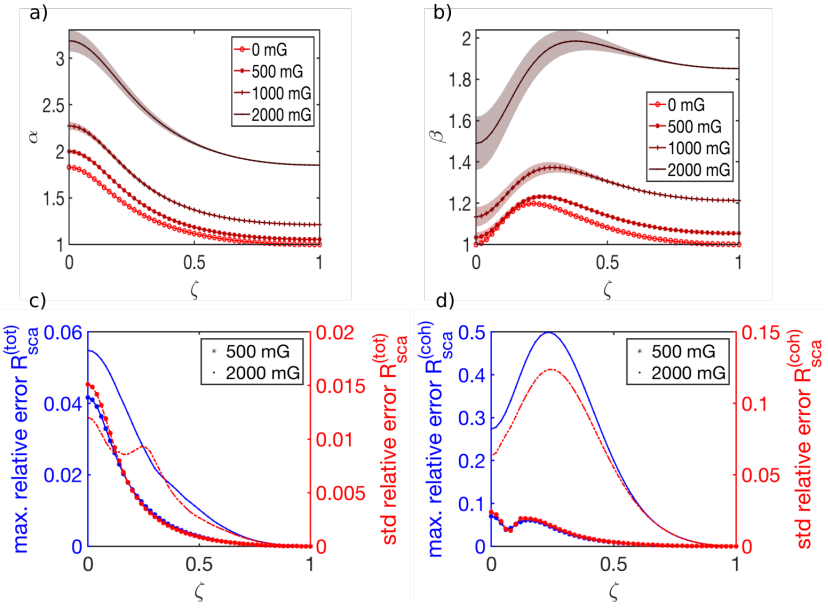

Figure C.5: a) α and b) β as a function of the ellipticity ζ in the case of $\Theta = 0$. $\zeta = 1$ is circular and $\zeta = 0$ is linear along $\boldsymbol{\epsilon}_x$ and does not correspond to a π polarization. For any ellipticity, $\mathbf{B}$ is perpendicular to the electric field. The maximum and the standard deviation of the relative error between the approximated TLS solution and the exact calculation of the c) excited state population and d) density matrix coherence.

We consider now deviations from these ideal cases by studying the influence of the ellipticity ζ in the (x, y) plane corresponding to $\Theta = 0$, and in the (x, z) plane corresponding to $\Theta = \pi/2$. α and β from Eq. (D.31) are together fitted from the scattering rates obtained by numerically solving the MLS master equation and plotted with errorbars within 95% confidence interval of the fits parameters.
As expected, Fig. C.5 ($\Theta = 0$) shows that the scattering rates are sensitive to the polarization. The growing errorbars for an increased ellipticity indicate a growing deviation from the effective TLS behavior. The offset between the curves is merely due to the Zeeman shift. The relative error between the simulated scattering rate and the model of Eq.

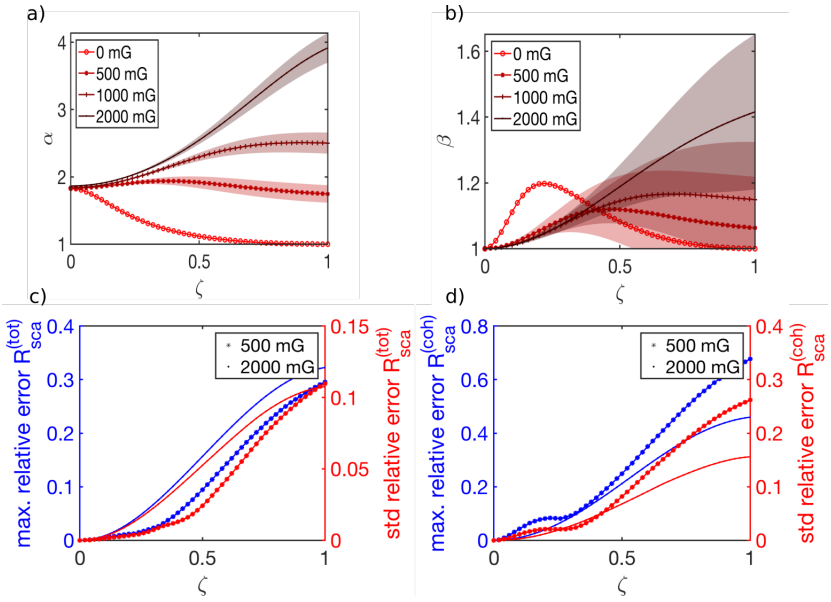

Figure C.6: a) α and b) β as a function of ϵ in the case of $\Theta = \pi/2$. $\zeta = 1$ is circular and $\zeta = 0$ is linear along $\boldsymbol{\epsilon}_z$ and does correspond to a π polarization. The maximum and the standard deviation of the relative error between the approximated TLS solution and the exact calculation of the c) excited state population and d) density matrix coherence.

(C.43) is plotted in terms of the maximum and the standard deviation of the relative error over the range of the saturation parameter s_c used for the fitting. It shows that the model has a maximum relative error which does not exceed 6% for the total scattering rate and it happens only for an ellipticity of 1. The coherent scattering rate is more sensitive to the ellipticity with up to 50% relative error. Nevertheless, for a small ellipticity ($\zeta \approx 1$) as typically used in σ absorption imaging, the MLS stays very equivalent to an exact TLS.

Fig. C.6 presents the influence of the ellipticity in the (x, z) plane. For $\zeta = 0$, corresponding to a π polarization, the TLS is exact with little dependence on magnetic field. As the ellipticity is increased, this TLS behavior becomes less accurate with increasing errorbars on the fitting parameters. As a consequence, π polarization imaging will be less accurate to define the absorption cross-section and the atom numbers.

C.4.2.3 Role of an incoherent drive

The scattering cross-section is also modified in the presence of an incoherent field. It could be for example generated by a thermal lamp, or by the temporally incoherent response of the surrounding atomic gas to the coherent excitation. Here, we consider the influence of a partially polarized incoherent field on the coherent and incoherent scattering response of a MLS probed by a coherent σ_- polarized light under zero magnetic field offset. Electromagnetic fields are here considered as temporally incoherent if their coherence time is smaller than the Rabi period, meaning that the density matrix coherences are zero on average while the excited state populations are non-zero. An incoherent field yields optical pumping without coherence.

We consider a partially σ_- polarized incoherent field that could for example be generated by the incoherent scattering of a σ_- polarized coherent field. This incoherent field is parametrized by a polarization degree $r \in [0, 1]$ in the form $s_i^\sigma = r s_i$ and $s_i^{\text{iso}} = (1 -$

$r)s_i$ where the $s_i^\sigma/s_i^{\text{iso}}/s_i$ are respectively the σ_- polarized / isotropic / total saturation intensities expressed relatively to the saturation intensity of σ_- polarized light. With such definition, $r = 1$ describes a σ_- polarized incoherent field while $r = 0$ describes an isotropic incoherent field.

In the limit $r = 1$, both the coherent and incoherent fields are σ_- polarized. The atomic population is pumped in the closed transition and the situation is exactly described with scattering rates given by Eq. (D.31) where $\delta = 0$ and $\alpha = 1$. In the opposite limit $r = 0$, a purely isotropic incoherent field drive will redistribute the ground state population. In the absence of the coherent field drive ($s_c = 0$), the populations are equally redistributed among the Zeeman states. Interestingly, we notice that for large saturation parameters s_i, the total population in the excited state can be higher than 1/2. It is indeed bounded by the number of excited Zeeman states over the total number of states which is 7/12 for the considered transition of ^{87}Rb. The total excited state population ρ_{ee} in the absence of coherent field $s_c = 0$ and at zero magnetic fields can be analytically[4] derived from the master equation including incoherent terms of Eq. (C.39) and is given by:

$$\rho_{ee} = \frac{7}{12}\frac{s_i/\frac{30}{12}}{1+s_i/\frac{30}{12}}. \tag{C.54}$$

In the low saturation regime *i.e.* $s_i \ll 1$, Eq. (C.54) reduces to $\rho_{ee} = \frac{1}{2}\frac{s_i}{\alpha_{\text{iso}}}$ where $\alpha_{\text{iso}} = \frac{15}{7}$ is the reduction of the cross-section for an isotropic and incoherent field.

We consider now the general case of a MLS driven simultaneously by a partially polarized incoherent field ($r \in [0, 1]$) and by a coherent drive s_c. The master equation given by Eq. (C.35) is expressed in the form of Eq. (C.39) and the steady-state solutions of all elements of the density matrix are obtained by an algebraic solver. The algebraic solution has the form of a ratio of polynomials containing few 100 terms. This exact algebraic solution of the scattering rates is compared to a phenomenological model of a TLS:

$$\begin{aligned}
R_{sca}^{(coh)}/\Gamma &= \frac{\beta}{2\alpha}\frac{s_c/\alpha}{\left(1+s_i^{\text{iso}}/\frac{30}{12}+s_i^\sigma/\alpha+s_c/\alpha\right)^2},\\
R_{sca}^{(tot)}/\Gamma &= \eta(r,s_i,s_c)+\frac{1}{2}\frac{s_c/\alpha}{1+s_i^{\text{iso}}/\frac{30}{12}+s_i^\sigma/\alpha+s_c/\alpha},\\
\eta(r,s_i,s_c) &= \frac{\eta_0-\eta_\infty}{1+\frac{s_c}{\alpha\left(1+s_i^{\text{iso}}/\frac{30}{12}+s_i^\sigma/\alpha\right)}}+\eta_\infty,
\end{aligned} \tag{C.55}$$

where α, β, η_0 and η_∞ are fitting parameters. To minimize the number of fitted parameters, the saturation intensity correction of the isotropic incoherent field was fixed to 30/12. In this model, α quantifies the reduction of the coherent absorption cross-section, $\beta < 1$ quantifies the reduction of coherent field emission with respect to a perfect TLS. $\eta(r, s_i, s_c)$ is the part of the total excited state population induced by the incoherent field drive. This contribution of the excited state population includes states which are coupled to all three fields (e.g. $|F_e = 3, m_F = -3, -2, -1, 0, 1\rangle$) and states coupled only to the isotropic polarization (e.g. $|F_e = 3, m_F = 2, 3\rangle$). This excited state population $\eta(r, s_i, s_c)$ has a complex dynamic that depends on the polarization ratio of the incoherent field r, the value of the incoherent s_i and coherent s_c saturation intensities. For a given couple of parameters r and s_i, we observe that this contribution varies monotonically from

[4]It is straightforward with symbolic computations with Mathematica.

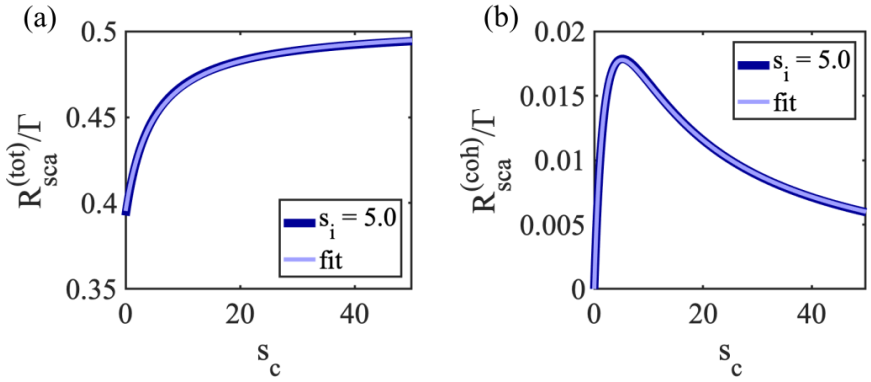

Figure C.7: a) Variations of the total excited state population and b) σ_--polarized coherences with $r = 0.5$ and $s_i = 5$ in blue and the fits in red using Eq. ($C.55$).

η_0 in absence of coherent drive and saturates at η_∞ for large coherent drive $s_c \gg s_i$. The model given in Eq. (C.55) reproduces the saturation behavior with a crossover at $s_c/\alpha = 1 + s_i^{\text{iso}}/\frac{30}{12} + s_i^\sigma/\alpha$.
As an example, the total scattering rate and coherent scattering rate are given as a function of s_c for $r = 0.5$ and $s_i = 5$ in Fig. C.7. We observe that the equivalent TLS given by Eqs. (C.55) describes well the dynamics with a standard deviation of the relative error below 1% on this example. The excited state population offset at $s_c = 0$ is due to the incoherent drive.

We compare the TLS model and the exact solution by fitting the parameters $\alpha(s_i, r)$, $\beta(s_i, r)$ $\eta_0(s_i, r)$ and $\eta_\infty(s_i, r)$. The fits are realized at a fixed incoherent intensity $s_i \in [0, 10]$ and polarization degree $r \in [0, 1]$ and for a coherent intensity s_c varying between 0 and $10s_i$. In this parameter range ($s_c \leq 100$) the closed transition approximation holds at least for 500 scattering events. The results are shown in Fig. C.8. As a comparison, the expected parameters for an exact TLS are $\alpha = 1, \beta = 1$ and $\eta_0 = \eta_\infty$ given by the second term in Eq. (D.31) which are indeed the exact solutions found for a polarized incoherent field ($r = 1$). For $r = 1$, the MLS is optically pumped in an exact TLS. As the incoherent drive polarization is randomized $r \to 0$, the fitted parameters slightly deviate from these initial values with a complex behavior that is mostly driven by optical pumping mechanisms. In absence of coherent drive, the excited state population η_0 increases as a function of the incoherent saturation intensity. For an isotropic incoherent drive, this excited state population can even exceed 1/2 (*cf.* Eq. (C.54)) as all 12 states become equally populated. In our model, the coherent scattering rate only depends on α and β. For large and unpolarized incoherent drive, the coherent scattering rate can be reduced by up to a factor of 1/2 with respect to the pure TLS. This reduction is essentially due to Clebsch-Gordon coefficients entering in the calculation of β. As checked numerically, the polarization of the coherently scattered field is exactly aligned with the input field (σ-polarized). This was expected given that the incoherent field cannot drive coherence between the Zeeman sub-levels and therefore does not alter the scattered polarization (Eq. (C.38)).

C.4.2.4 Discussion and conclusion

The combined coherent and incoherent response of atoms in the saturated regime has a strong impact on the interpretation of fluorescence and absorption imaging of ensembles. Experimental imperfections are the common explanations (Reinaudi et al., 2007) for the

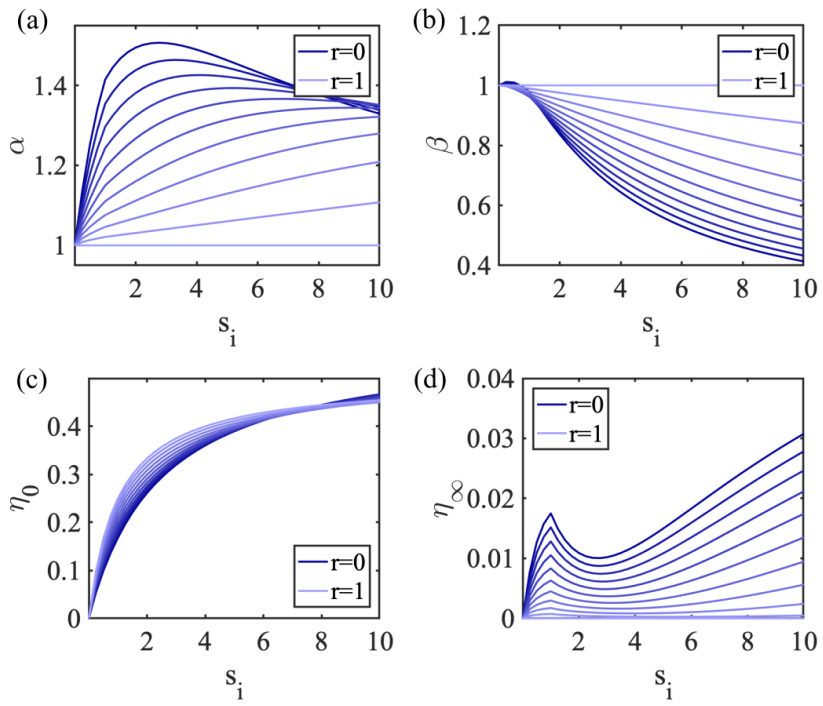

Figure C.8: Model parameters a) α, b) β, c) η_0 and d) η_∞ as a function of the incoherent intensity s_i for polarization degrees $r \in [0, 1]$ by step of 0.1. The shaded area represents the 95% confidence interval of the fits and is very small on the plots. In c), the limit cases $r = 0$ and $r = 1$ exactly coincide with the analytical solutions given in Eq. (C.54) and the second term of Eq. (D.31) respectively.

reduction of the atomic cross-section. With this argument, the absolute determination of atom numbers is subject to a precise calibration of the experimental conditions which is often questioned. In Fig. C.4, we have shown that the effective TLS description of a multi-level atom is very robust to polarization imperfections especially for the case of σ polarized light. We attribute this robustness to optical pumping mechanisms that protects the stretched-state hyperfine transition ($|F_g = 2, m_F = -2\rangle$ to $|F_e = 3, m_F = -3\rangle$ in σ_-). This pumping was additionally observed in the steady-state solutions of the OBE via a strong imbalance of the repartition of the population that favored the $|F_g = 2, m_F = -2\rangle$ state even for $\zeta \in [0.5, 1]$. This optical pumping protection of σ transitions is not specific to the imaging transition of the D_2 line of Rubidium and will be applicable to any Zeeman degenerated closed transition. In the absence of Zeeman degeneracy, it was additionally shown that MLS behaves exactly as an effective TLS for any drive polarization. As expected for ^{87}Rb, the cross-section reduction factor α varies from 1 (σ) to 1.829 (π) depending on the driving field polarization.

On the other hand, stray magnetic fields strongly impact the calibration of the scattering cross-section of a σ polarized probe (Fig. C.5(a)). Nevertheless, this correction which is solely given by detuning of the coherent drive from the extreme TL transition can be exactly compensated for by tuning the drive frequency on-resonance with the extreme TL transition in experiments. It is therefore not a concern for cross-section calibrations. In addition, due to symmetry of the first-order Zeeman splitting, the cross-section correction of a π polarized probe is independent of the stray magnetic field amplitude if it is aligned along the linear polarization axis.

As mentioned earlier, in the presence of a stray magnetic field, light scattering is a vec-

torial process, and the coherent scattered field polarization is not aligned with the drive. Nevertheless, in the specific case of σ and π polarized light with a magnetic bias well-defined with respect to light polarization, both atom-light and magnetic interaction are diagonalized in the same basis leading to an aligned output field. The scattering process is therefore scalar in these two situations with additional robustness to imperfections for the σ polarized drive (Fig. C.4(d)). Polarization and stray magnetic field imperfections have therefore little influence on the reduction of the cross-section.

On the other hand, we have observed that in the presence of an incoherent background that would mimic the temporally and spatially incoherent scattering from other atoms in the ensemble, the cross-section is notably reduced which results in systematics errors on absorption imaging measurements of atom number in the saturation regime and/or at large optical thickness (Corman et al., 2017; Chomaz, 2014) (and see Chapter D). For large optical depths, most of the coherent drive is converted to an incoherent field via multiple scattering mechanisms. A total conversion of field leads to $s_i = s_c$ which gives an upper bound for the modification of $\alpha = 1 + s_i$.

For large saturations, the atom is driven in the Mollow triplet regime, and we expect this large value of α to be mitigated by a reduction of the reabsorption cross-section (Mollow, 1972b). In other words, the converted light will be partly off-resonant with the atomic transition.

C.5 Transient dynamics of a MLS closed transition: application to ^{87}Rb

We have seen in the previous section that steady populations and coherences expressions are analytical for pure polarizations cases. For a circular polarization, the steady-state corresponds to an ideal TLS while for a linear polarization, the steady-state is an effective TLS with a reduced cross-section.

In this section, we study the transient regime that appears after that the beam is turned on and specifically evaluate the impact of the pulse duration on the value of α compared to its steady-state value. This study is carried for σ^- and π polarizations and for different initial state preparations $\rho^{(0)}_{F_g,m_{F_g}}$ at time $t = 0$.

Indeed, due to different Clebsch-Gordan couplings, Rabi frequencies for each transition will be proportional to $\sqrt{s_0/2}\Gamma$ with a Clebsch-Gordan prefactor. This means that a minimum number of scattering events are necessary to reach the steady value α.

Experimentally, the cross-section dynamics is integrated in time by the detector and can lead to wrong quantitative measurements. For short pulses, this dynamics is not negligible and will modify the effective factor α_{eff} that modifies the total scattering rate $R^{(tot)}_{sca} = \Gamma \sum_{m_F} \rho_{3,m_F,3,m_F} = \frac{\Gamma}{2}\frac{s_0/\alpha_{eff}}{1+s_0/\alpha_{eff}}$. The change of α_{eff} is determined for different s_0 in two different ways: either through the instantaneous $\alpha(t)$ at a given time t or by the mean value $\alpha(t_{im}) = \frac{1}{t_{im}}\int_0^{t_{im}} \alpha(t)dt$ where t_{im} is the pulse duration.

For the simulations, the time is linearly spanned from 0.1 µs to 50 µs with 0.1 µs step and the saturation is varied from 0.1 to 32. The detuning and magnetic field are set to zero.

In the following we will show the ground state populations, the values of α for the in-

stantaneous and mean cases for s_0=0.1, and the minimum duration t_{min} necessary for the mean value of α to reach 90% of its steady-state value. This last parameter is experimentally significant as it determines the minimum imaging pulse length necessary to approximate the scattering rate by its steady-state value.

C.5.1 Circular polarized light

Here we consider a σ^--polarization interacting with the MLS for the case where populations are initially either equidistributed or in one of the maximum spin states. The quantization axis is along z and the polarization is in the transverse plane (x, y).

C.5.1.1 Initially equidistributed

We consider here an initially equidistributed population among all Zeeman ground states. The initial density matrix populations are $(\rho^{(0)}_{-2-2}, \rho^{(0)}_{-1-1}, \rho^{(0)}_{00}, \rho^{(0)}_{11}, \rho^{(0)}_{22}) = (0.2, 0.2, 0.2, 0.2, 0.2)$ and a σ^--polarized field. It approximately corresponds to the situation experimentally obtained immediately after a molasses cooling phase. Fig. C.9 shows that the steady-state regime obviously corresponds to all atoms in $m_F = -2$ state. For low optical powers, such as used in the low saturation regime of absorption imaging, the steady-state is reached at 90% after more than $t_{min} > 10$ µs. It is only for large saturation ($s_0 > 1$) that the steady-state is reached within less than 10 µs.

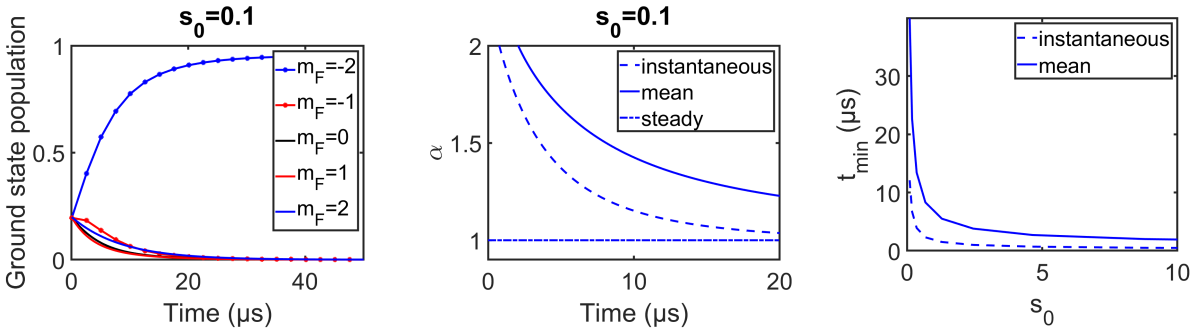

Figure C.9: Case of σ^--polarized light and $(\rho^{(0)}_{-2-2}, \rho^{(0)}_{-1-1}, \rho^{(0)}_{00}, \rho^{(0)}_{11}, \rho^{(0)}_{22}) = (0.2, 0.2, 0.2, 0.2, 0.2)$: ground state population dynamics, instantaneous and mean value of α and minimum pulse duration to reach 90% of the steady-state value.

C.5.1.2 Initially in $|F_g = 2, m_F = 2\rangle$

We consider here an initial ground state population such that $(\rho^{(0)}_{-2-2}, \rho^{(0)}_{-1-1}, \rho^{(0)}_{00}, \rho^{(0)}_{11}, \rho^{(0)}_{22}) = (0, 0, 0, 0, 1)$ and a σ^--polarized field. It can also corresponds to the situation experimentally obtained when all atoms are in $|2, -2\rangle$ after a MW transfer and with a magnetic field along $-z$ which would make an energy shift stronger than the one due to the imaging beam such that the quantization axis is along $-z$. This case is the worse one for σ-polarization as the Clebsch-Gordan for $|2, 2\rangle$ to $|3, 1\rangle$ is the lowest one of all : $\sqrt{1/30}$. The dynamics is dominated by the depumping of that state as shown on Fig. C.10 where the population of $|2, 2\rangle$ is slowly decreasing for $s_0 = 0.1$ and the mean value of α is still 4 even after t=10 µs. We also remark the same behavior as for the equidistributed case in C.5.1.1, *i.e.* high saturations ($s_0 > 2$) are required to reach the steady-state in less than $t_{min} < 10$ µs.

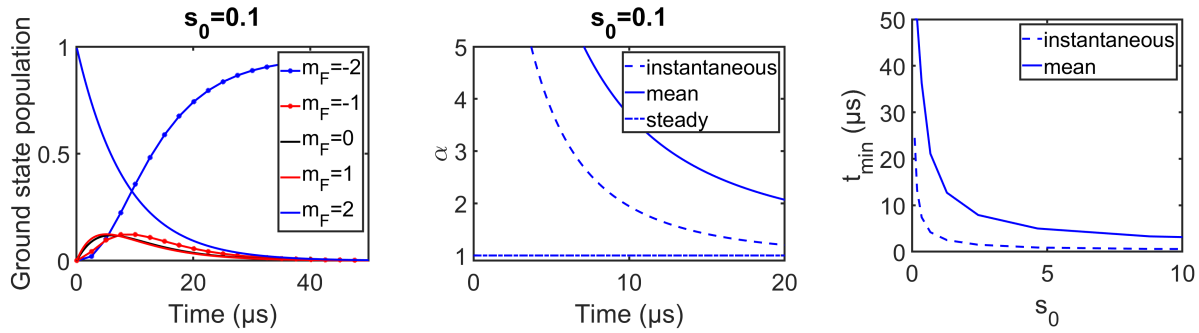

Figure C.10: Case of σ^--polarized light and $(\rho^{(0)}_{-2-2}, \rho^{(0)}_{-1-1}, \rho^{(0)}_{00}, \rho^{(0)}_{11}, \rho^{(0)}_{22}) = (0, 0, 0, 0, 1)$: ground state population dynamics, instantaneous and mean value of α and minimum pulse duration to reach 90% of the steady-state value.

C.5.1.3 Initially in $|F_g = 2, m_F = -2\rangle$

We consider here an initial ground state population such that $(\rho^{(0)}_{-2-2}, \rho^{(0)}_{-1-1}, \rho^{(0)}_{00}, \rho^{(0)}_{11}, \rho^{(0)}_{22}) = (1, 0, 0, 0, 0)$ and a σ^--polarized field. This case is straightforward as it directly corresponds to the cycling transition for the steady-state where all atoms are in $|2, -2\rangle$ with a MW transfer and imaged such that the bias magnetic field is along $+z$. Fig. C.11 shows that strong deviations on the mean value of α occur only for $t \ll 1$ µs. When s_0 is increased, the transient regime tends to 0. The observed fluctuation for large s_0 on Fig. C.11 are due to numerical precision at short durations. The curve tends to 0 if we take a smaller time step for the simulations.

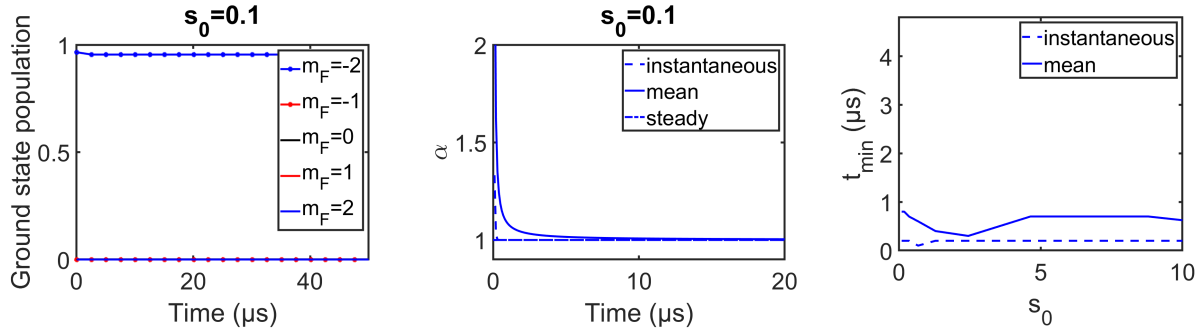

Figure C.11: Case of σ^--polarized light and $(\rho^{(0)}_{-2-2}, \rho^{(0)}_{-1-1}, \rho^{(0)}_{00}, \rho^{(0)}_{11}, \rho^{(0)}_{22}) = (1, 0, 0, 0, 0)$: ground state population dynamics, instantaneous and mean value of α and minimum pulse duration to reach 90% of the steady-state value.

C.5.2 Linearly polarized light

Here we consider a π-polarization interacting with the MLS for the case where populations are initially either equidistributed or in one of the maximum spin states. The polarization axis matches with the quantization axis along z.

C.5.2.1 Initially equidistributed

We consider here an initially equidistributed population among all Zeeman ground states. The initial density matrix population are $(\rho^{(0)}_{-2-2}, \rho^{(0)}_{-1-1}, \rho^{(0)}_{00}, \rho^{(0)}_{11}, \rho^{(0)}_{22}) = (0.2, 0.2, 0.2, 0.2, 0.2)$

and a π-polarized field. This case is encountered in many experiments such as imaging after a molasses cooling phase with a π-polarized probe. Fig. C.12 shows that the steady-state regime is reached for $t_{min} < 1$ µs for $s_0 > 1$. The steady-state population is a larger population in $m_F = 0$ and the population is decreasing as $|m_F|$ increases. About 3-4 µs is necessary in low saturation to reach the steady-state.

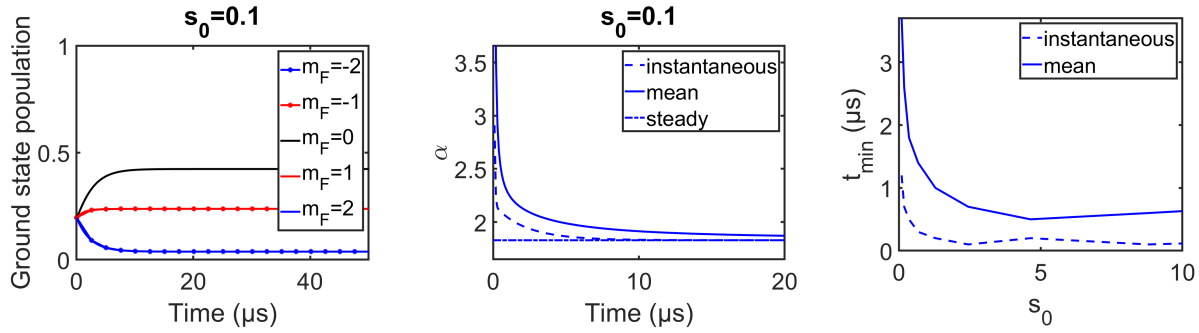

Figure C.12: Case of π-polarized light and $(\rho^{(0)}_{-2-2}, \rho^{(0)}_{-1-1}, \rho^{(0)}_{00}, \rho^{(0)}_{11}, \rho^{(0)}_{22}) = (0.2, 0.2, 0.2, 0.2, 0.2)$: ground state population dynamics, instantaneous and mean value of α and minimum pulse duration to reach 90% of the steady-state value.

C.5.2.2 Initially in $|F_g = 2, m_F = -2\rangle$

Finally we consider here an initial ground state population such that $(\rho^{(0)}_{-2-2}, \rho^{(0)}_{-1-1}, \rho^{(0)}_{00}, \rho^{(0)}_{11}, \rho^{(0)}_{22}) = (1, 0, 0, 0, 0)$ and a π-polarized field. This case is experimentally obtained after spin-flip evaporation where atoms are polarized and we want to image them with a π-polarized light. In Fig. C.13, we see that the steady-state regime is reached for $t_{min} < 2$ µs for $s_0 > 1$. This case is the worst one for π-polarization as population have to be pumped over all states and it will be dependent on the lowest Clebsch-Gordan of the $|2, \pm 2\rangle$ to $|3, \pm 2\rangle$ transitions which is $\sqrt{1/6}$. However the dynamics is much faster than for the same initial density matrix illuminated by a circular polarization. At low saturation, a pulse duration of 10 µs is enough to reach the steady-state.

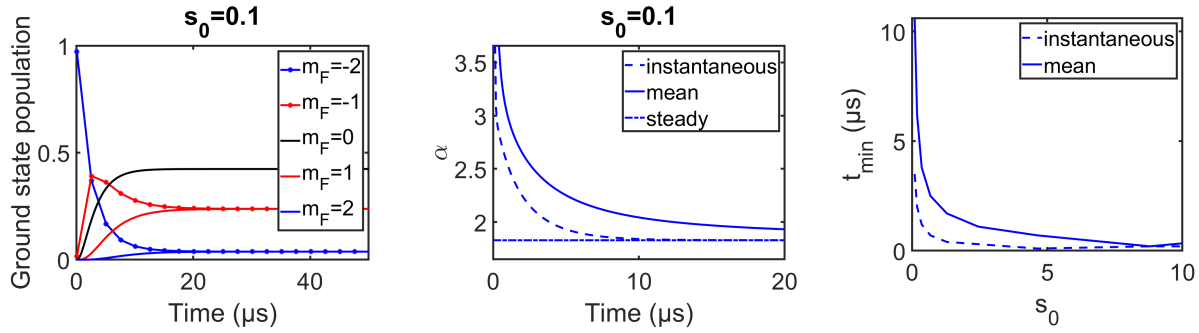

Figure C.13: Case of π-polarized light and $(\rho^{(0)}_{-2-2}, \rho^{(0)}_{-1-1}, \rho^{(0)}_{00}, \rho^{(0)}_{11}, \rho^{(0)}_{22}) = (1, 0, 0, 0, 0)$: ground state population dynamics, instantaneous and mean value of α and minimum pulse duration to reach 90% of the steady-state value.

So far we extensively studied the effects that would reduce the atomic cross-section for a single multi-level atom of ^{87}Rb on a closed transition such that stray magnetic fields, the polarization ellipticity, an incoherent background field or short pulse durations. We will

present in the next Chapter D a series of measurements that will show that the main factor contributing to the reduction of the cross-section is due to cooperative effects between atoms such as multiple scattering and links to the model of the incoherent background field in this Chapter C.

Before that, we are going to give the formulas obtained from the OBEs for an open transition for ^{87}Rb as the repumper transition.

C.6 Dynamics of open transitions : application to ^{87}Rb

In this section, we use the master equation in the case of a 3-level and 5-level systems interaction with a single electric field oscillating at the frequency ω. This will be particularly relevant for evaluating subwavelength resolutions in Chapters E and F where the 3-level system will be used to model pumping/depumping mechanisms and the 5-level system to take into account additional dark states. The model and results are presented here in their general form. Their specific application to model super-resolution dynamics will be done in Chapters E and F.

C.6.1 Three-level system (3LS)

We denote the ground states as $|1\rangle$ and $|2\rangle$ and the excited state as $|2'\rangle$. The linear system of Eq. (C.36) gives the dynamics of the following density matrix ρ:

$$\rho = \begin{pmatrix} \rho_{11} & \rho_{2'2'} & \rho_{22} & \rho_{12'} & \rho_{2'1} & \rho_{12} & \rho_{21} & \rho_{22'} & \rho_{2'2} \end{pmatrix}'. \tag{C.56}$$

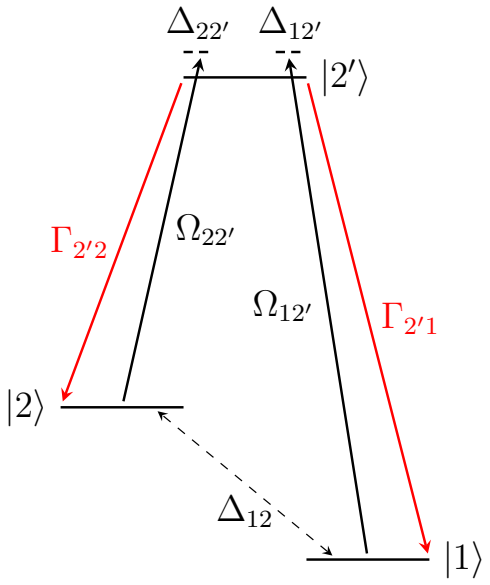

Figure C.14: A 3-level atom with one excited state and two ground states, driven at the laser frequency ω such that $\Delta_{22'} = \omega - \omega_{22'}$, $\Delta_{11'} = \omega - \omega_{11'}$, with Rabi frequencies $\Omega_{22'}$ and $\Omega_{12'}$. The spontaneous decay of the excited state is $\Gamma = \Gamma_{2'2} + \Gamma_{2'1}$ where $\Gamma_{2'2} = c_{2'2}\Gamma$ with $c_{2'2}$ being the coupling strength of the transition ($\Gamma_{12} = 0$: no spin collisions). Similarly, we have $\Gamma_{2'1} = c_{2'1}\Gamma$.

The matrix $\mathbf{M}$ of Eq. (C.36) is given by:

$$\mathbf{M} = \begin{pmatrix} 0 & \Gamma_{2'1} & 0 & \frac{i}{2}\Omega_{2'1} & -\frac{i}{2}\Omega^*_{2'1} & 0 & 0 & 0 & 0 \\ 0 & -\Gamma & 0 & -\frac{i}{2}\Omega_{2'1} & \frac{i}{2}\Omega^*_{2'1} & 0 & 0 & -\frac{i}{2}\Omega_{2'2} & \frac{i}{2}\Omega^*_{2'2} \\ 0 & \Gamma_{2'2} & 0 & 0 & 0 & 0 & 0 & \frac{i}{2}\Omega_{2'2} & -\frac{i}{2}\Omega^*_{2'2} \\ \frac{i}{2}\Omega^*_{2'1} & -\frac{i}{2}\Omega^*_{2'1} & 0 & -\frac{\Gamma}{2} - i\Delta_{12'} & 0 & \frac{i}{2}\Omega^*_{2'2} & 0 & 0 & 0 \\ -\frac{i}{2}\Omega_{2'1} & \frac{i}{2}\Omega_{2'1} & 0 & 0 & -\frac{\Gamma}{2} + i\Delta_{12'} & 0 & -\frac{i}{2}\Omega^*_{2'2} & 0 & 0 \\ 0 & 0 & 0 & \frac{i}{2}\Omega_{2'2} & 0 & -i\Delta_{12} & 0 & 0 & -\frac{i}{2}\Omega^*_{2'1} \\ 0 & 0 & 0 & 0 & -\frac{i}{2}\Omega_{2'2} & 0 & i\Delta_{12} & \frac{i}{2}\Omega_{2'1} & 0 \\ 0 & -\frac{i}{2}\Omega_{2'2} & \frac{i}{2}\Omega_{2'2} & 0 & 0 & 0 & \frac{i}{2}\Omega^*_{2'1} & -\frac{\Gamma}{2} - i\Delta_{22'} & 0 \\ 0 & \frac{i}{2}\Omega^*_{2'2} & -\frac{i}{2}\Omega^*_{2'2} & 0 & 0 & -\frac{i}{2}\Omega_{2'1} & 0 & 0 & -\frac{\Gamma}{2} + i\Delta_{22'} \end{pmatrix}. \tag{C.57}$$

We consider a driving field at frequency ω close to the transition $1 \to 2'$ with Rabi frequency $\Omega_{2'1}$. As the detuning is large ($\Delta_{12'} \gg \Gamma$), we neglect off-resonant coupling between $2'$ and 2 ($\Omega_{2'2} = 0$). We consider that $c_{2'2} + c_{2'1} = 1$ in the following.

We will focus on slow dynamics ($t \gg \Gamma$) so we can apply the adiabatic approximation which assumes that the coherences are always in equilibrium with respect to the populations such that $\dot{\rho}_{12'} \approx 0$. In this case, the matrix (C.57) simplifies to:

$$\frac{d}{dt}\begin{pmatrix} \rho_{11} \\ \rho_{2'2'} \\ \rho_{22} \\ 0 \\ 0 \end{pmatrix} = \begin{pmatrix} 0 & \Gamma_{2'1} & 0 & \frac{i}{2}\Omega_{2'1} & -\frac{i}{2}\Omega^*_{2'1} \\ 0 & -\Gamma & 0 & -\frac{i}{2}\Omega_{2'1} & \frac{i}{2}\Omega^*_{2'1} \\ 0 & \Gamma_{2'2} & 0 & 0 & 0 \\ \frac{i}{2}\Omega^*_{2'1} & -\frac{i}{2}\Omega^*_{2'1} & 0 & -\frac{\Gamma}{2} - i\Delta_{12'} & 0 \\ -\frac{i}{2}\Omega_{2'1} & \frac{i}{2}\Omega_{2'1} & 0 & 0 & -\frac{\Gamma}{2} + i\Delta_{12'} \end{pmatrix} \begin{pmatrix} \rho_{11} \\ \rho_{2'2'} \\ \rho_{22} \\ \rho_{12'} \\ \rho_{2'1} \end{pmatrix}. \tag{C.58}$$

From Eq. (C.58) the coherences reduce to $\rho_{12'} = \frac{\Omega^*_{2'1}(\rho_{11} - \rho_{2'2'})}{\Gamma(1+4\Delta^2_{12'})}(i + \frac{\Delta_{12'}}{\Gamma/2})$ leading to the rate-equations of a 3-level system:

$$\frac{d}{dt}\begin{pmatrix} \rho_{11} \\ \rho_{2'2'} \\ \rho_{22} \end{pmatrix} = \begin{pmatrix} -\frac{s\Gamma}{2} & \frac{s\Gamma}{2} + \Gamma_{2'1} & 0 \\ \frac{s\Gamma}{2} & -\frac{s\Gamma}{2} - \Gamma & 0 \\ 0 & \Gamma_{2'2} & 0 \end{pmatrix} \begin{pmatrix} \rho_{11} \\ \rho_{2'2'} \\ \rho_{22} \end{pmatrix}, \tag{C.59}$$

where the saturation parameter is here defined as:

$$s = \frac{2|\Omega_{2'1}|^2/\Gamma^2}{1 + 4\Delta^2_{12'}} \equiv \frac{s_0}{1 + 4\Delta^2}. \tag{C.60}$$

Eq. (C.59) corresponds to rate-equations with a spontaneous decay rate, an absorption rate and a stimulated emission rate. The analytical solution is easily found using symbolic computations[5] for the diagonalization of $\mathbf{M}$ giving eigenvalues $(\Lambda_0, \Lambda_+, \Lambda_-)$ and the population evolution starting with $\rho_{11}(t = 0) = 1$:

[5]The solution of $\dot{\rho} = M\rho$ where M is independent of time and such that $M = PDP^{-1}$ is $\rho = e^{M\tau}\rho_0 = Pe^{D\tau}P^{-1}\rho_0$.

$$
\begin{aligned}
\Lambda_0 &= 0, \\
\Lambda_\pm &= -\frac{\Gamma}{2}\left(1+s\pm\sqrt{1+2sc_{2'1}+s^2}\right), \\
\rho_{11} &= \frac{\Lambda_-}{\Lambda_- - \Lambda_+}\left(1+\frac{\Lambda_+}{\Gamma c_{2'2}}\right)e^{\Lambda_+ t} + \frac{\Lambda_+}{\Lambda_+ - \Lambda_-}\left(1+\frac{\Lambda_-}{\Gamma c_{2'2}}\right)e^{\Lambda_- t}, \\
\rho_{2'2'} &= \frac{\Lambda_-}{\Lambda_- - \Lambda_+}\frac{\Lambda_+}{\Gamma c_{2'2}}e^{\Lambda_+ t} + \frac{\Lambda_+}{\Lambda_+ - \Lambda_-}\frac{\Lambda_-}{\Gamma c_{2'2}}e^{\Lambda_- t}, \\
\rho_{22} &= 1 - \frac{\Lambda_-}{\Lambda_- - \Lambda_+}e^{\Lambda_+ t} - \frac{\Lambda_+}{\Lambda_+ - \Lambda_-}e^{\Lambda_- t},
\end{aligned}
\tag{C.61}
$$

where all coupling coefficients c_{ij} are defined in Fig. C.14.

One can show that in Eq. (C.61) the plus sign solution will quickly decay to 0 such that only the minus sign solution remains. Then, in the low saturation limit $s \ll 1$ where $\frac{\Lambda_+}{\Lambda_+ - \Lambda_-} = 1$, the populations become:

$$
\begin{aligned}
\rho_{11} &= \left(1 - \frac{1}{2}\frac{s}{1+s}\right)e^{\Lambda_- t}, \\
\rho_{2'2'} &= \frac{1}{2}\frac{s}{1+s}e^{-\frac{c_{2'2}\Gamma t}{2}\frac{s}{1+s}}, \\
\rho_{22} &= 1 - e^{-\frac{c_{2'2}\Gamma t}{2}\frac{s}{1+s}}.
\end{aligned}
\tag{C.62}
$$

In Eq. (C.62), the long time limit is $\rho_{22} = 1$ as $|2\rangle$ is indeed a dark state. However, for spatially modulated saturation parameters (either by power or detuning) the population in $|2\rangle$ will be spatially modulated with different time constants in the exponential. The transferred population in $|2\rangle$ will then be given by:

$$
\rho_{22} = 1 - e^{-\frac{c_{2'2}\Gamma t}{2}\frac{s(x)}{1+s(x)}}, \tag{C.63}
$$

where $s(x) = \frac{s_0}{1+4\Delta^2(x)}$.

The spatial dependence of the population is the idea behind the subwavelength imaging method presented in Chapters E and F where we modulate the detuning thanks to a dressed excited state.

C.6.2 Five-level system (5LS)

We could of course use the full MLS system to describe the evolution of the populations but we are interested in analytical results. The above 3-level model can be refined to include MLS effects by including another excited state $|1'\rangle$ to which the light can couple to ($|F_e = 2\rangle$ state for ^{87}Rb) and another 'trash' ground state $|3\rangle$ from which the population cannot be pumped back into other states. This is a 5-level system as shown on Fig. C.15.

Analytical solutions are obtained for the 5-level system from rate-equations including the absorption and the spontaneous emission but neglecting stimulated emission terms which are second order terms in the limit of low saturation $s_i \ll 1$. The saturation parameters for the two possible transitions are noted $s_i = \frac{2|\Omega_{i'1}|^2/\Gamma^2}{1+4\Delta^2_{1i'}}$ for $i = 1, 2$. From the master

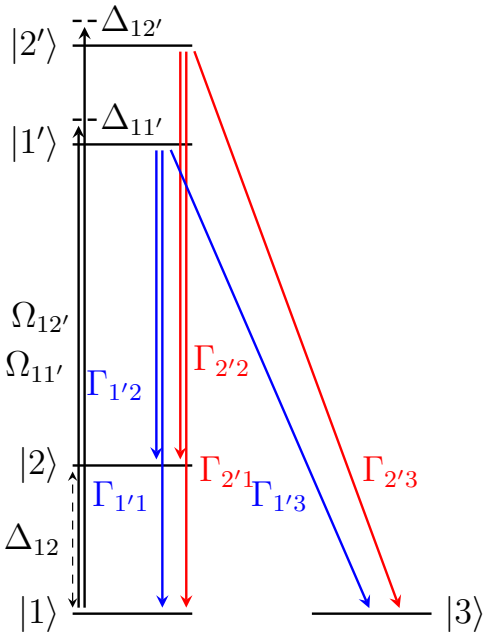

Figure C.15: A 5-level atom with one more excited state and one more ground state compared to the 3-level system.

equation (C.36) and performing the adiabatic approximation, the density matrix evolution for the 5-level system is:

$$\begin{pmatrix} \frac{d\rho_{11}}{dt} \\ \frac{d\rho_{22}}{dt} \\ \frac{d\rho_{33}}{dt} \\ \frac{d\rho_{1'1'}}{dt} \\ \frac{d\rho_{2'2'}}{dt} \end{pmatrix} = \begin{pmatrix} -\frac{s_1\Gamma}{2} - \frac{s_2\Gamma}{2} & 0 & 0 & \frac{s_2\Gamma}{2} + c_{1'1}\Gamma & \frac{s_1\Gamma}{2} + c_{2'1}\Gamma \\ 0 & 0 & 0 & c_{1'2}\Gamma & c_{2'2}\Gamma \\ 0 & 0 & 0 & \Gamma\left(1 - c_{1'2} - c_{1'1}\right) & \Gamma\left(1 - c_{2'2} - c_{2'1}\right) \\ \frac{s_2\Gamma}{2} & 0 & 0 & -\frac{s_2\Gamma}{2} - \Gamma & 0 \\ \frac{s_1\Gamma}{2} & 0 & 0 & 0 & -\frac{s_1\Gamma}{2} - \Gamma \end{pmatrix} \begin{pmatrix} \rho_{11} \\ \rho_{22} \\ \rho_{33} \\ \rho_{1'1'} \\ \rho_{2'2'} \end{pmatrix}. \tag{C.64}$$

Similarly to section C.6.1, we find the solution of Eq. (C.64) with a diagonalization matrix method for the transferred population into $|F_g = 2\rangle$:

$$\rho_{22} = 1 - \frac{s_1\left(1 - c_{2'1} - c_{2'2}\right) + s_2\left(1 - c_{1'1} - c_{1'2}\right)}{s_1\left(1 - c_{2'1}\right) + s_2\left(1 - c_{1'1}\right)} - \frac{\Gamma^2\left(c_{2'2}s_1 + c_{1'2}s_2\right)}{2\left(\Lambda_- - \Lambda_+\right)}\left(\frac{e^{\Lambda_+ t}}{\Lambda_+} - \frac{e^{\Lambda_- t}}{\Lambda_-}\right), \tag{C.65}$$

where $\Lambda_\pm = -\frac{\Gamma}{4}\left(2 + s_1 + s_2 \pm \sqrt{4 - 4s_1 + 8c_{2'1}s_1 + s_1^2 - 4s_2 + 8c_{1'1}s_2 + s_2^2 + 2s_1s_2}\right)$.

Eq. (C.65)[6], obtained for $s_1, s_2 \ll 1$, shows that in the long time limit, the transferred population has an upper limit that is connected to Clebsch-Gordan couplings.

To conclude, in this section we derived the population dynamics for an open transition for two different models: a 3-level system (3LS) that has the minimum number of states to describe the dynamics and a 5-level system (5LS) which takes into account a dark ground state and another excited state due to the atomic structure. Both models are valid only in the adiabatic approximation and will be applied in Chapters E and F.

[6]The 5LS equation of the population given by Eq. (C.65) (stimulated emission neglected) differs from the 3LS population given by Eq. (C.61) (stimulated emission included).

C.7 Conclusion

This chapter aimed at modeling a multi-level quantum system to extract scattering rates from the evolution of the density matrix in the presence of a coherent driving field, a constant magnetic bias, and an incoherent pumping. The main purpose is to point out the mechanisms that would be responsible for a reduction of the scattering atomic cross-section.

For that purpose, we remind the theory of master equations giving the density matrix evolution for a two-level quantum system (TLS) in the form of optical Bloch equations with the usual solutions for the coherences and populations. We introduced an incoherent field taken as temporally incoherent if its coherence time is smaller than a Rabi period. Also, we gave the master equation in the case of a multi-level quantum system (MLS) that can be solved numerically.

In section C.3, we proposed to map the scattering properties of a MLS to the one of an effective TLS model. For ^{87}Rb, in section C.4 we have shown that, at zero magnetic fields, our effective TLS model describes exactly the scattering rates of a MLS for any saturation parameter. In the presence of stray magnetic fields that lift the Zeeman degeneracy, the amplitude of the scattered fields is well described by the TLS model, with an exact mapping for the specific case of σ and π polarizations. For other polarizations, vectorial scattering (magneto-optical effects) can occur. Our scalar model cannot exactly render such rotations but proved to be robust for σ polarized scattering. In the limit of strong saturation, incoherent scattering dominates. In dense ensembles, the dynamic of a single-atom will be affected by this incoherent electromagnetic background. We have shown that, while the MLS dynamics becomes complex, an equivalent TLS model can be adapted to enlighten the general behavior and main scattering response.

In section C.5, we studied transient regimes where pulse durations contribute to the reduction of the cross-section α at short time scales on the order of a few scattering events. This depends both on the initial atomic populations (Zeeman state) and probe polarization. The longer dynamics is when many scattering events have to occur to reach the steady-state regime. It happens when scatterings in the transient regime pass through optical transitions with weak Clebsch-Gordan coefficients.

Finally, using the density matrix formalism, we gave the dynamics for open transitions such as a repumper transition with one interacting beam under a three-model system (3LS) and (5LS) that will be useful for the data analysis in Chapters E and F.

Chapter D

Atom number calibration in saturating absorption imaging

The response of dense atomic ensembles to coherent optical illumination is a paradigmatic situation to study multiple scattering dynamics in which collective effects can be prominent. They lead, for instance, to modifications of the scattering properties such as line shifts and broadening (Jennewein et al., 2018) in 1D (Glicenstein et al., 2020) and 2D systems (Corman et al., 2017), sub- (Guerin, Araújo, and Kaiser, 2016) and super-radiance (Cottier, Kaiser, and Bachelard, 2018), the optical phase profile engineering (Jenkins and Ruostekoski, 2012) to control the reflection properties (Rui et al., 2020) of a single-atomic layer or the localization of light in different regimes (Cottier et al., 2019; Wiersma et al., 1997). Simulations of the coupled dipole equations in the linear-optics regime include interference effects such as coherent backscattering (Chabé et al., 2014; Sokolov and Guerin, 2019)which was also predicted using random walk simulations including the atomic internal structure (Labeyrie et al., 2003; Labeyrie et al., 2000).

In practice, these light scattering effects due to dipole-dipole couplings depend usually either on the optical depth or on the atomic density (Guerin, Rouabah, and Kaiser, 2017).

For the case of an infinite 3D bulk medium, only the atomic density n_{3D} is relevant. At low atomic densities, far-field interactions between atoms, scaling as $1/r$, are enough to describe all transport properties. At high atomic densities where the inter-particle distance is on the order of the light wavelength $\lambda = 2\pi/k$ *i.e.* $n_{3D}k^{-3} \geq 1$, near-field interactions scaling as $1/r^3$ between atoms play an important role.

As soon as the propagation length in the ensemble is important, the relevant parameter is the optical depth which refers to the logarithm of the transmission. Usually, two regimes take place depending on the value of the mean-free path $l_{sc} = 1/(n_{3D}\sigma)$ of a photon in the atomic ensemble compared to the cloud size, where σ is the single-atom cross-section. The first regime is when the optical depth is lower than 1. It is well explained by Beer-Lambert law where single scattering events occur. The second regime is when the optical depth is much larger than 1, corresponding to optically dense mediums where multiple scattering effects occur.

Collective effects are usually measured by fluorescence imaging as absorption imaging is inappropriate in low saturation for dense mediums, or for off-resonant measurements due to refraction and diffraction. The analysis of the physical effects is difficult. For instance,

in (Pellegrino et al., 2014), fluorescence measurements show broadening and scattering saturation explained by dipole-dipole simulations to include collective effects, but it turns out that the measurements can also be explained by a simple 'shadow' effect of the probe beam (Guerin, Rouabah, and Kaiser, 2017). Absorption imaging in low saturation for dense mediums can be used only with dedicated experiments with dense 2D thin slabs of atoms (Chomaz et al., 2012; Corman et al., 2017).

In the literature, when it comes to cross-section calibrations, collective effects are usually neglected and single-atom physics models are used. In particular, we focus on the calibration method presented in (Reinaudi et al., 2007) which is widely used in cold atom experiments to calibrate atom numbers. It consists in measuring the optical density for a large range of saturation parameters and finding the appropriate value of the cross-section reduction factor (α) such that the optical density does not depend on the probe beam as it is a property of the cloud only. In this Chapter, we present series of experiments showing that collective effects correspond to the dominant effect contributing to the reduction of the cross-section.

Especially, we studied the absorption of a saturating probe by an optically dense continuous atomic cloud. We derive in section D.1 the light propagation equation for a saturating medium (Beer-Lambert law). In section D.2 we discuss conditions on the probe parameters that have to be considered to perform in-situ absorption imaging in order to avoid systematic errors in the calibration of the cross-section. In section D.3 we give the characterization and useful calibrations of the experimental setup that are used to take absorption images of section D.4. They show a reduction of the cross-section depending on the optical density. Finally, we propose a model modifying the Beer-lambert law to include the effect of an incoherent saturating radiative background that mimics incoherent multiple scattering mechanisms.

D.1 Light propagation in a continuous medium: Beer-Lambert law

D.1.1 Linear-optics regime

In the experiment that we present in this Chapter, the interacting wavelength for ^{87}Rb is 780.24 nm and the peak density of our Gaussian shape cloud is of $n_{3D} = 2.1.10^{19}$ at/m^3 so we have $n_{3D}k^{-3} = 0.04 \ll 1$. In addition, we will experimentally deal with even lower densities by transferring only a controlled fraction of the initial cloud to a bright state for imaging using a microwave transition. Therefore, we consider that the atoms can be described as classical dipoles radiating in the far-field regime.

Let us compute the electric field at point $\mathbf{r}$. It is the sum of the incident field $\mathbf{E}(\mathbf{r}) = \frac{E_A}{2} e^{ikz}\epsilon$ propagating along z and of the field scattered by the atoms (Tey et al., 2009):

$$\mathbf{E}(\mathbf{r}') = \mathbf{E}(\mathbf{r}) + \iiint_V n_{3D}(\mathbf{r}) \frac{3E_A}{2k} e^{ikz} i \frac{e^{ik|\mathbf{r}'-\mathbf{r}|}}{|\mathbf{r}'-\mathbf{r}|} \left(\epsilon - (\epsilon.\mathbf{u}_{\mathbf{rr}'})\,\mathbf{u}_{\mathbf{rr}'}\right) d\mathbf{r}^3, \tag{D.1}$$

where $\mathbf{u}_{\mathbf{rr}'} = (\mathbf{r}' - \mathbf{r})/|\mathbf{r}' - \mathbf{r}|$ is a vector unit, $n_{3D}(\mathbf{r})$ is the atomic density and V is the integration volume which assumes a continuous medium ($n_{3D}\Delta z \sigma_0 \gg 1$ where the parameters will be defined later in the text) and therefore neglects granularity.

For now, we consider a homogeneous slab of atoms of width Δz and infinite in the transverse directions. The atomic density is constant as $n_{3D}(\mathbf{r}) = n_0$ and the polarization of the incident field is circular. The integral of Eq. (D.1) is computed in cylindrical coordinates over a circle $R_0 \gg 1/k$ such that we ignore edge effects (fast oscillation terms average to zero by configuration averaging). The first term of the integral (on-axis scattering) reads $-n_0 \frac{3E_2}{2k^2} e^{ik(z+\Delta z)} 2\pi\epsilon_+ \Delta z$. The second term (off-axis scattering) reads $n_0 \frac{3E_2}{2k^2} e^{ik(z+\Delta z)} \pi\epsilon_+ \Delta z$. Finally Eq. (D.1) becomes:

$$\mathbf{E}(z+\Delta z) = \mathbf{E}(z)\left(1 - \frac{n_0}{2}\frac{6\pi}{k^2} e^{ik\Delta z}\Delta z\right). \tag{D.2}$$

We identify the on-resonance absorption cross-section as $\sigma_0 = 6\pi/k^2$ and obtain from Eq. (D.2) the Beer-Lambert law for the field amplitude:

$$\frac{\Delta \mathbf{E}}{\Delta z} = -\mathbf{E}\frac{n_0\sigma_0}{2} e^{ik\Delta z}. \tag{D.3}$$

Rewriting Eq. (D.3) in intensity and in the limit $\Delta z \to dz$ ($k\Delta z \ll 1$), we obtain Beer-Lambert law in intensity:

$$\frac{d|\mathbf{E}|^2}{dz} = -|\mathbf{E}|^2 n_0 \sigma_0, \tag{D.4}$$

which is the commonly used form.

D.1.2 Including the saturation

The coherent field emitted on-resonance by a single-atom can be saturated with the saturation parameter $s_0 = \frac{2\Omega_c^2}{\Gamma^2}$ where Ω_c is the Rabi frequency proportional to the electric field amplitude E_A. The amplitude of the coherent scattering rate for a two-level system is given by $|\rho_{eg}|^2 = \frac{\Gamma}{2}\frac{s_0}{(1+s_0)^2}$ (Eq. (C.41)). The scattered field is then proportional to $\frac{\sqrt{s_0}}{(1+s_0)}$. Equivalently, the electric amplitude $\propto s_0$ is attenuated by a factor of $1/(1+s_0)$. This enables us to modify Eq. (D.2) as:

$$\mathbf{E}(z+dz) = \mathbf{E}(z)\left(1 - \frac{1}{(1+s_0)}\frac{n_0}{2}\frac{6\pi}{k^2} e^{ikdz} dz\right). \tag{D.5}$$

In intensity, Eq. (D.5) leads to the Beer-Lambert law including the saturation of a two-level system:

$$\frac{dI}{dz}\left(1 + \frac{I}{I_{sat}}\right) = -n_0\sigma_0 I, \tag{D.6}$$

where I_{sat} is the saturation intensity which is related to the cross-section by $\sigma_0 = \hbar\omega\Gamma/(2I_{sat})$.

Note that identical results are obtained for a linearly polarized electric field.

D.1.3 Including multi-level effects

Now we can include multi-level system effects in a heuristic way by reducing the cross-section σ by a factor α where $\sigma = \sigma_0/\alpha$ (and $I_{sat} = \alpha I_{sat,0}$) as seen in section C.4.1. Including this correction, Eq. (D.6) becomes:

$$\frac{dI}{dz}\left(\alpha + \frac{I}{I_{sat}}\right) = -\, n_0\sigma_0 I. \tag{D.7}$$

Integrating Eq. (D.7) over the propagation direction in the saturating regime leads to the optical density (OD) noted mathematically as $b(x,y) \equiv n_{2D}(x,y)\sigma_0$:

$$b(x,y) = -\alpha \ln(T(x,y)) + s_0(1 - T(x,y)), \tag{D.8}$$

where $s_0 = I_0/I_{sat}$ is the saturation parameter and I_0 is the incident imaging beam.

Eq. (D.8) can also be written using the Lambert W function as[1]:

$$T(x,y) = \frac{\alpha}{s_0} W\left(\frac{s_0}{\alpha} e^{\frac{s_0 - b(x,y)}{\alpha}}\right). \tag{D.9}$$

Note that we can also include the detuning of the probe beam $\delta = \Delta/\Gamma$ and we end up with the following relation between the optical density and the transmission:

$$b(x,y) = -\alpha\left(1 + 4\delta^2(x,y)\right)\ln T(x,y) + s_0\left(1 - T(x,y)\right), \tag{D.10}$$

$$T(x,y) = \frac{\alpha(1 + 4\delta^2(x,y))}{s_0} W\left(\frac{s_0}{\alpha(1 + 4\delta^2(x,y))} e^{\frac{s_0 - b(x,y)}{\alpha(1+4\delta^2(x,y))}}\right). \tag{D.11}$$

However, in this case, off-resonant effects (refraction) due to a spatially varying phase will change the absorption signal. We will then restrict to the on-resonance case in the experiment.

Experimentally, the transmission is measured with a camera which integrates over the pixel size L_x, L_y to get the atom number N_i in the pixel i such that:

$$N_i\sigma_0 = -\int_{L_x}\int_{L_y} (\alpha(1 + 4\delta^2(x,y))\ln T(x,y) + s_0(T(x,y) - 1))dxdy, \tag{D.12}$$

where $N_i = \int_{L_x}\int_{L_y} n(x,y)\sigma_0 dxdy$.

If L_x, L_y are small compared to the atomic cloud width and to the variation of the detuning, then $T(x,y) = T_i$ and $\delta(x,y) = \delta_i$ meaning that it is homogeneous over the pixel size. Eq. (D.12) then becomes:

$$N_i\sigma_0 = -\left(\alpha(1 + 4\delta_i^2)\ln T_i + s_0(T_i - 1)\right) L_x L_y, \tag{D.13}$$

[1] It is defined for real numbers x such that $W_0(x)e^{W_0(x)} = x$. For complex numbers, it corresponds to the principal branch of the Lambert W function.

where the transmission for the pixel i is computed as usual as $T_i = (I_{at} - I_{back})/(I_{no,at} - I_{back})$.

D.1.4 Atom number calibration in saturation: the method

For absorption imaging, one must calibrate the cross-section by making the optical depth independent of the imaging beam intensity as the optical density should be independent of the probe beam (Reinaudi et al., 2007). Following (Reinaudi et al., 2007) one should measure the transmission for many saturations s_0 and find α numerically that makes the optical density given by Eq. (D.8) independent of the saturation.

The technique of (Reinaudi et al., 2007) has been widely used to calibrate atom numbers in the literature. We show in Table D.1 results of calibrations using this method for ^{87}Rb performed by different groups. We see that the value of α can cover values above 2 and the most common explanations given in the literature are experimental imperfections: imperfect polarization, residual stray magnetic fields, and optical pumping mechanisms. For ^{87}Rb, a resonant circularly polarized probe has $\alpha = 1$ and a linear has $\alpha = 1.829$ which are in any case smaller than 2. Moreover, we have seen in Chapter C that α is robust against polarization ellipticities around the typical σ, π polarizations thanks to optical pumping. Also, any residual detuning can be experimentally compensated by active feedbacks and transient regime effects on the cross-section can be minimized using long probe durations. As a result, experimental imperfections should not be playing a huge role for an optimized experimental setup.

α	b_0	Cloud type	Probe polarization	Ref.
1.13(2)	0.5	BEC	Circular	(Seroka et al., 2019)
1.11	1.2	BEC	Circular	(Riedel et al., 2010)
2.0(2)	2.5	1D Li condensate	Circular	(Horikoshi et al., 2017)
3.15(12)	5	1D BEC	Circular	(Mordini et al., 2020)
2.12(1)	4.8	2D MOT	Linear	(Reinaudi et al., 2007)
2.6(3)	-	Quasi 2D BEC	-	(Yefsah et al., 2011)
2.9	8.4	MOT	Linear	(Reinaudi, 2008)

Table D.1: Review of the cross-section calibrations performed by different groups.

Other calibration methods of atom numbers exist, like pushing atoms in the imaging direction and measuring the center of mass displacement (Hueck et al., 2017). However, this works only when all atoms see the same beam intensity *i.e.* the beam is not attenuated through its propagation.

In the following, we will show particular probe conditions that should be verified to avoid systematic errors when measuring the transmission of a probe beam through an atomic cloud.

D.2 Probe conditions

In this section, inspired by (Horikoshi et al., 2017), we give the order of magnitude of some mechanisms, as shown on Fig. D.1, that lead to systematic errors in absorption imaging. We will do the numerical applications for ^{87}Rb. The first effect is atom random walks where an atom can diffuse in the transverse direction of the probe beam over a

width larger than a camera pixel size. The second effect is the displacement along the probe direction and microscope depth-of-field. The third effect is the acquired Doppler shift which is due to recoil velocities from scattering events. The last effect comes from the signal-to-noise ratio on the optical density which links to the transmission noise, given by either photon shot noise or camera noises.

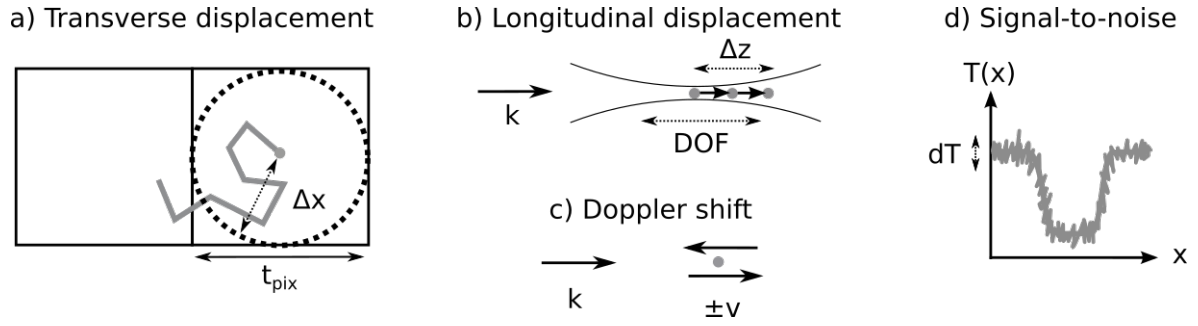

Figure D.1: a) Transverse displacement due to atom random walks compared to a camera pixel size, b) longitudinal displacement along the depth-of-field of the microscope after scattering events, c) Doppler shifts due to scattering and d) signal-to-noise amplitude of the transmission.

D.2.1 Random walk and longitudinal displacements

In this section, we evaluate the impact of probe parameters, *i.e.* duration, and saturation, on the atomic displacements, either due to scattering events along the probe propagation or heating due to a random walk of an atom in the probe transverse plane under many scattering events by spontaneous emission.

A random walk of N steps of a variable x, in a space with an average of $< x >= 0$, has its mean square displacement equal to N times the square of the step length (Foot, 2005).

The random walk of an atom by photon scattering is due to the transfer of the photon momentum $\hbar k$ to the atom. In our case the variable of interest is the velocity v, the step length is the recoil velocity $v_{rec} = \hbar k/m$ and the number of steps is the number of diffusion during the time Δt. For ^{87}Rb, the recoil velocity is 5.8845 mm/s.

The average number of diffusion events N is the total scattering rate times Δt. For a two-level atom, it is given by:

$$N = \Delta t \frac{\Gamma}{2} \frac{s_0}{1 + s_0 + 4\Delta^2}. \tag{D.14}$$

The average number of diffusion events at resonance is $N(\Delta = 0)$:

$$N(\Delta = 0) = \Delta t \frac{\Gamma}{2} \frac{s_0}{1 + s_0}. \tag{D.15}$$

Let us consider a beam propagating along z. Close to resonance, an absorption of a photon transfers a momentum $\hbar k$ in the direction of the probe beam so the mean value of the velocity along z is not zero:

$$< v_z >_{abs} = N(\Delta t) v_{rec}. \tag{D.16}$$

An emitted spontaneous photon also transfers to the atom a momentum in the z-direction of $\hbar k \cos(\theta)$. Since θ is random, the mean value is $< v >_{spont} = 0$. However, the mean square velocity is $< v^2 >_{spont} = N v_{rec}^2$. If we look at the contribution along the z-axis, we have to perform the angular average $\eta =< \cos^2(\theta) >$ giving:

$$< v_z^2 >_{spont} = \eta N v_{rec}^2. \tag{D.17}$$

For the simple case of an isotropic emission, $\eta = 1/3$ and the heating is the same in all directions, $< v_x^2 >_{spont} = < v_y^2 >_{spont} = < v_z^2 >_{spont}$. This value gives a good estimation of the random walk and it can be corrected to include the radiation pattern of the emitting dipole. The angular distribution function which normalizes over the solid angle $d\Omega = \sin(\theta) d\theta d\phi$ as $\int f_{\boldsymbol{\epsilon}}(\theta, \phi) d\Omega = 1$ is given by (Steck, 2019):

$$f_{\boldsymbol{\epsilon}}(\theta, \phi) = \frac{3}{8\pi} \left(1 - |\mathbf{r}.\boldsymbol{\epsilon}|^2\right). \tag{D.18}$$

For instance, for a linear polarization $\boldsymbol{\epsilon} = \mathbf{z}$ along z and a circular polarization $\boldsymbol{\epsilon} = \epsilon_{\pm}$:

$$\begin{aligned} f_{\mathbf{z}}(\theta, \phi) =& \frac{3}{8\pi} \sin^2(\theta), \\ f_{\boldsymbol{\epsilon}_{\pm}}(\theta, \phi) =& \frac{3}{16\pi} \left(1 + \cos^2(\theta)\right). \end{aligned} \tag{D.19}$$

In practice, the transverse random walk Δx has to be compared to the pixel size t_{pix}, taken in the object plane, which is the limiting factor in the imaging system:

$$\Delta x = \sqrt{\frac{N(\Delta = 0)}{3}} v_{rec} \Delta t < t_{pix}. \tag{D.20}$$

The longitudinal displacement dz along z has to be much smaller than the depth-of-field DOF of the imaging system:

$$dz = N(\Delta = 0) v_{rec} \Delta t \ll DOF. \tag{D.21}$$

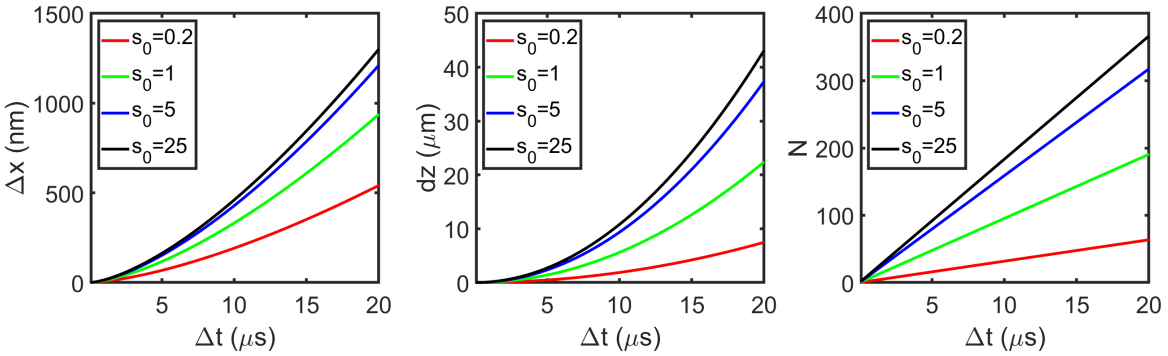

Figure D.2: Random walk displacement in the transverse plane Δx, longitudinal displacement along the beam propagation dz and scattering number N vs. the probe durations for many saturation parameters. We have $DOF = 22$ µm ($NA = 0.185$) and $t_{pix} = 848$ nm.

The transverse displacement Δx is not an issue for moderate saturations and durations ($t < 10$ µs and $s_0 < 50$) as they are smaller than a pixel size. The displacement along the beam propagation is lower than 5 µm for pulses below 10 µs and saturation above 1 which is the limit of our depth-of-field. At the end of section D.2.3, we will evaluate Eq. (D.20) and (D.21) for our experimental parameters.

D.2.2 Doppler shift condition

As the number of diffusion increases, an atom acquires a longitudinal velocity that corresponds to a Doppler shift that reduces the scattering rate. Here we evaluate the residual detuning dependent term $r = 4\delta^2$ by considering that the detuning is given by $\delta = \frac{1}{2}\frac{s_0}{1+s_0} v_{rec} k \Delta t$ where it is assumed that all photons are resonant. This leads to the following criterion for the pulse duration:

$$\Delta t_{max} = \frac{1+s}{s v_{rec} k} \sqrt{r}. \tag{D.22}$$

And the total number of scattered photons is:

$$N_{max} = \frac{\Gamma}{2} \frac{\sqrt{r}}{v_{rec} k}. \tag{D.23}$$

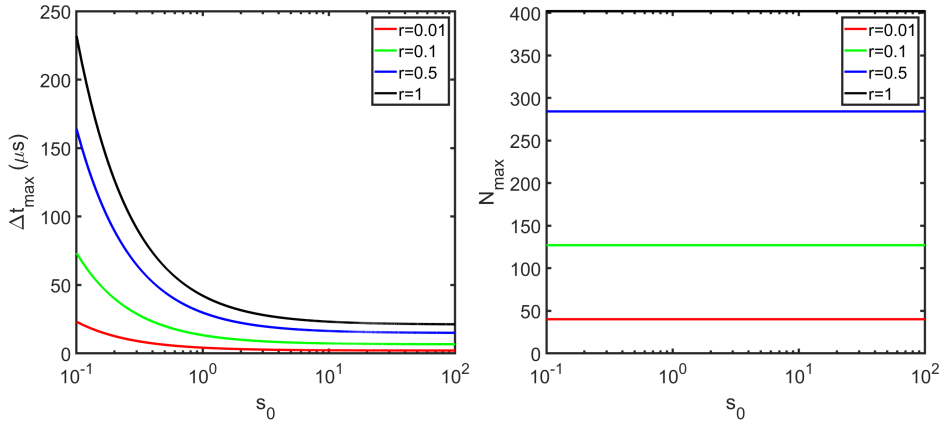

Figure D.3: Doppler condition on the maximum pulse duration and maximum scattering number vs. the saturation for different parameter r.

On Fig. D.3, we plot the Doppler condition of Eq. (D.22) and the corresponding total scattering number of Eq. (D.23). For $r = 1$ which is a strong effect, the number of diffusion is about 40 and correspond in general to pulse durations longer than 20 µs for any saturation. For a moderate error of $r = 0.1$, the number of diffusion is 130 and for saturation larger than 1, it corresponds to durations about 10 µs. For $s < 1$, longer durations up to 75 µs for $s = 0.1$ are possible. We will plot the Doppler condition in section D.2.3 for our experimental conditions.

D.2.3 Signal-to-noise on the optical density

In this section, we evaluate the signal-to-noise (SNR) on the optical density that we can measure experimentally. Indeed, the photon shot noise and camera noise are affecting the

signal-to-noise. The condition is considered as not limiting for measuring optical densities if SNR$\geq$ 1.

We remind the optical density on-resonance in the saturation regime given by Eq. (D.8):

$$b(x,y) = -\alpha \ln \frac{I_{out}}{I_{in}} + \left(\frac{I_{in} - I_{out}}{I_{sat}}\right), \tag{D.24}$$

where we replaced the saturation parameter by $s_0 = I_{in}/I_{sat}$ and the transmission by $T = I_{out}/I_{in}$ where I_{in} and I_{out} are experimentally measured quantities.

The signal-to-noise (SNR) on the optical density is computed as $SNR = b/\sqrt{\sigma_b^2}$ where the optical density variance σ_b is given by:

$$\sigma_b^2 = \left(\frac{\partial b}{\partial I_{in}}\right)^2 \sigma_{I_{in}}^2 + \left(\frac{\partial b}{\partial I_{out}}\right)^2 \sigma_{I_{out}}^2. \tag{D.25}$$

The derivatives are obtained from Eq. (D.24):

$$\begin{aligned} \frac{\partial b}{\partial I_{in}} =& \frac{\alpha + s}{I_{in}}, \\ \frac{\partial b}{\partial I_{out}} =& -\frac{\alpha + sT}{I_{out}}. \end{aligned} \tag{D.26}$$

The camera counts are given by $I_{in} = AGsN_{sat}$ and $I_{out} = AGTsN_{sat}$ where A is the conversion factor from photon to camera counts (quantum efficiency and camera conversion factor), G is the EMCCD gain and $N_{sat} = I_{sat} t_{pix}^2 t T_l \lambda / hc$ for pixel widths of t_{pix}, imaging time t and transmission losses T_l. Using these definitions and Eq. (D.26) leads to:

$$SNR(s,t,b) = \frac{b\sqrt{sN_{sat}(t)T(s,b)}}{\sqrt{(\alpha+s)^2 T(s,b) \frac{\sigma_{I_{in}}^2}{A^2G^2sN_{sat}} + (\alpha + sT(s,b))^2 \frac{\sigma_{I_{out}}^2}{A^2G^2TsN_{sat}}}}. \tag{D.27}$$

Usually, the background offset $I_{back} = AGN_b$ is subtracted from the images where N_b is the residual count number due to background light. This gives $I_{in} = I_{probe} - I_{back}$ and $I_{out} = I_{abs} - I_{back}$ so variances are $\sigma_{I_{in}}^2 = \sigma_{I_{probe}}^2 + \sigma_{I_{back}}^2$ and $\sigma_{I_{out}}^2 = \sigma_{I_{abs}}^2 + \sigma_{I_{back}}^2$.
Including the photon shot noise $\sqrt{N}$, camera readout noise σ_R, dark current noise σ_{DC}, an excess noise factor F^2 (Robbins and Hadwen, 2003) proportional to the variance of the signal due to EM amplification and neglecting atomic shot noise, we get:

$$\begin{aligned} \sigma_{I_{in}}^2 =& A^2G^2F^2\left(sN_{sat} + 2N_b + \sigma_{DC}^2\right) + 2\sigma_R^2, \\ \sigma_{I_{out}}^2 =& A^2G^2F^2\left(TsN_{sat} + 2N_b + \sigma_{DC}^2\right) + 2\sigma_R^2. \end{aligned} \tag{D.28}$$

From Eq. (D.28), we can do the following remarks:

- The dark current offset depends on the readout time. It is the largest for the last read pixels. For instance, our Princeton camera has a dark current noise per pixel at -70°C is 0.0066 e^-/s (Table B.5). Reading at the lowest rate of 100 kHz the full sensors 2*512*512 pixels gives 0.03 e^- for the last read pixel which is negligible compared to the camera sensitivity of 0.85 e^-/photon.

- The background offset can be reduced close to zero using a fast mechanical shutter and blocking room light.

- The excess noise factor is $F^2 = 1$ without EMCCD gain ($G = 1$) and saturates to $F^2 = 2$ for large gains (Robbins and Hadwen, 2003). For photon counting, the EMCCD gain G is very useful as it enables one to eliminate the camera readout noise. However, for a few photons where the shot noise is dominating, the EMCCD gain will add more noise. As a conclusion, for calibration and atom number measurements with the Princeton camera, it is better to work in a low noise mode without EMCCD gain as the readout noise is low (3.15 e^- at 100 kHz).

In general, with our experimental parameters, the best SNR is obtained for a saturation of about 1 and durations from 10 to 20 µs. To give an order of magnitude, the number of photons per pixel (size of 848 nm) for a beam intensity of $I = I_{sat} = 16.7$ W/m^2 corresponds to a photon number of $I_{sat} t_{pix}^2 \times 1\mu s \times \lambda/hC = 47$ ph/pix/µs. For our Princeton camera, it gives $47 * 0.7/0.75 = 44$ ADU/pix/µs.

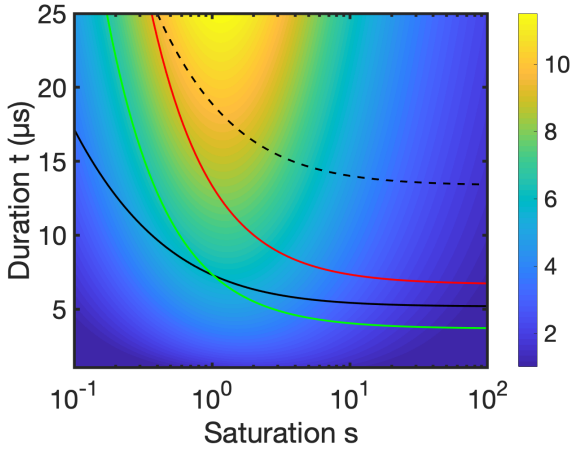

Figure D.4: Signal-to-noise of Eq. (D.27) vs. the pulse duration and saturation for $OD = 1$, $N_b = 0$, $\sigma_{DC} = 0$, $F = 1$, $G = 1$, $A = QE/0.75$ where $QE = 0.7$ and 0.75 is the conversion in e^-/ADU, $L_x = L_y = 848$ nm, $T_l = 0.76$, $I_{sat} = 16.7$ W/m^2 and $\sigma_R = 3.15/0.75$. The black solid line and dashed line are resp. the displacement along the propagation direction for DOF=3 µm and DOF=20 µm. The red solid line is the Doppler condition for $r = 0.1$. The green solid line is for a constant scattering number of 70.

To conclude, we plot Eq. (D.28) for our experimental parameters on Fig. D.4 where the colorbar starts at SNR> 1. For low saturation and durations, the SNR is limited by camera noises (mostly readout noise) and for strong saturation, photon shot noise becomes limiting. The displacement along the propagation direction sets an upper limit on the pulse duration given by Eq. (D.21) which we plot for DOF=3 µm (black solid line) and DOF=20 µm (black dashed line). Also, the Doppler condition of Eq. (D.22) gives another upper limit on the pulse duration that we plot for $r = 0.1$ (red solid line). For a DOF of 20 µm, the area below the red line and where SNR> 1 corresponds to good probe conditions. We plotted a green curve at fixed total scattered photons of 70 which will be our experimental conditions in section D.3. This curve lies well below the red curve limit so our probe parameters are satisfying.

D.3 Experimental setup

In this section, we explicit all experimental parameters that have been used for the experiments presented in this chapter: the cloud characteristics, the MW transfer between $|F_g = 1, m_F = -1\rangle$ and $|F_g = 2, m_F = -2\rangle$ and the saturation parameter s_0 of the imaging beam.

D.3.1 Cloud preparation

We start with thermal atoms prepared in a crossed dipole trap with DT1 and DT2 with dipole trap depths U_i of 33(3) µK and 11(1) µK.

Using the camera along DT1, we performed TOF measurements in low saturation and with a π-polarized beam with a TOF large enough such that the peak OD is always lower than 0.5, we extract a temperature of $T = 2.2(2)$ µK and a total atom number of $N_{tot} = 1.92(15).10^5$.

The expected width for a thermal cloud in an harmonic trap is given by $\sigma_i = \sqrt{k_b T/m\omega_i^2}$ where ω_i is the trap frequency $\omega_i = \sqrt{4U_0/mw_i^2}$. In our case we have $\sigma_x = 6.5(5)$ µm and $\sigma_y = 14.6(9)$ µm.

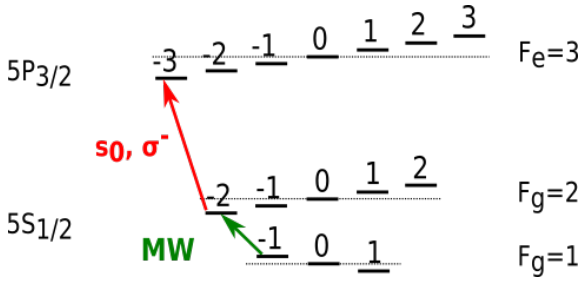

Figure D.5: D_2-line of ^{87}Rb atomic structure where atoms are transferred with a MW transition to $|F_g = 2, m_F = -2\rangle$ and imaged on the cycling transition using a σ-polarized light.

For a given polarization, the transition between the hyperfine states $F_g = 2$ and $F_e = 3$ can be considered as closed if the diffusion to other hyperfine excited states is negligible. An atom in $F_g = 2$ couples to $F_e = 3$ with a coupling of $S_{23} = 0.7$, to $F_e = 2$ with $S_{22} = 0.25$ and to $F_e = 1$ with $S_{21} = 0.05$. The excited state $F_e = 2$ is off-resonant by 266.65 MHz so $\Delta \approx 44\Gamma$. The ratio of the number of diffusions between $F_e = 3$ and $F_e = 2$ is about 1000 for a saturation[2] $s_0 = 60$ on the closed transition taking the full coupling of $S_{22} = 0.25$. As a result, the transition from $F_g = 2$ to $F_e = 3$ is considered as closed for most experimental parameters.

The magnetic field at the position of the atoms is compensated by adjusting the compensation coils in all directions using MW spectroscopy as detailed in section B.2.3.1. This cancels the magnetic field below 10 mG precision. Then a constant offset of $B_0 = 512$ mG is set along the main imaging beam propagation axis (along the gravity) and its direction matches with the σ_- polarization of the imaging beam. The atoms are then transferred from $|F_g = 1, m_F = -1\rangle$ to $|F_g = 2, m_F = -2\rangle$ state by MW coupling as shown on Fig. D.5.

[2] s_0 being referred to 1.67 mW/cm^2.

After transferring the atoms with a MW pulse of duration t_{MW}, they are in-situ imaged with the high NA imaging axis using a σ^- imaging beam. The imaging beam is tuned on-resonance with the cycling transition by maximizing the absorption as a function of the imaging detuning. At $t_{MW} = 6$ µs, we measured a shift of 0.2Γ which is due to both the magnetic field bias and light shift of the trapping potential at 1064 nm.

We use the Princeton camera in fast kinetics mode to acquire the images. The camera has an offset around 600 counts when there is no incoming light. We acquire all images without imaging beam and we measure on average a residual count number of 1 ADU due to room light.

In addition, a circular aperture with a 3 mm diameter is put in the Fourier plane between the two lenses of the telescope to decrease the numerical aperture to NA=0.185. It increases the depth-of-field to 22 µm which is larger than the cloud width.

The data consists in measuring the transmission by varying the saturation parameter s_0 of a resonant σ^--polarized imaging beam for many MW durations t_{MW}. In the following, we then give the calibrations of the MW oscillations and the saturation.

D.3.2 Calibration of the MW Rabi oscillation

In this section, we give the calibration of the microwave Rabi oscillation which has been used to finely control the atom number in order to measure different optical densities.

Fig. D.6 shows the Rabi oscillation where each data point has been averaged over 5 realizations. The amplitude has been normalized to the total atom number obtained via optical repumping. The data are fitted with the following transfer probability function :

$$P(t_{MW}) = P_{tot} \sin^2 \left(\frac{\pi t_{MW}}{T_{MW}} \right), \tag{D.29}$$

where the measured Rabi period is $T_{MW}/2 = 28$ µs and the maximum amplitude is $P_{tot} = 0.96$. To achieve such high contrast on a magnetically sensitive probe, it has been crucial to reduce magnetic noises by improving current source noises as discussed in section B.2.3.3. In Table D.2 we give the corresponding MW repumped fraction.

t_{MW} (µs)	2	4	6	8	10	12	28
$P(t_{MW})/P_{tot}$	0.0125	0.0495	0.1091	0.1883	0.2831	0.3887	1

Table D.2: MW repumped fraction for the experimental MW durations.

The peak atomic density is then $2.1.10^{19}$ at/m^3 and the central optical density for a circular polarized beam using the cross-section $\sigma_0 = 2.907.10^{-13}$ m^2 is then about 1.1(1) for the shortest MW pulse that we can do of 2 µs.

D.3.3 Calibration of the imaging beam saturation

It is crucial to be as precise as possible on the value of s_0. According to the optical density Eq. (D.8), for fixed b and T, α is linear with s_0 so an error on s_0 directly gives an error on α. A relative error on s_0 of $\frac{\Delta s_0}{s_0}$ will directly impact the relative error $\frac{\Delta \alpha}{\alpha}$ on α.

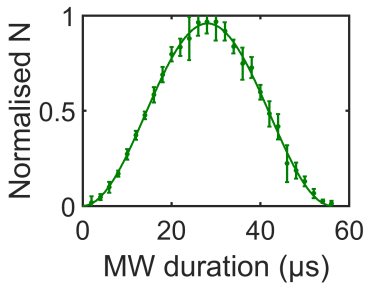

Figure D.6: Rabi oscillation of the normalized atom number (points) between $|F_g = 1, m_F = -1\rangle$ and $|F_g = 2, m_F = -2\rangle$ as a function of the MW duration and a sinusoidal fit (solid line). The data are normalized with an optically repumped total atom number.

In order to use the correct saturation parameter for the analysis, we acquired all imaging pulses with a monitoring photodiode connected to a FPGA (Red Pitaya). Regardless of shot-to-shot fluctuations, we can compute the exact power sent onto the atoms. Fig. D.7 shows pulses corresponding to the minimum and maximum value of s_0. We show these curves to demonstrate that the pulses have sharp rising/falling edges and low voltage noises. They can reliably be used for calibrating the saturation parameters.

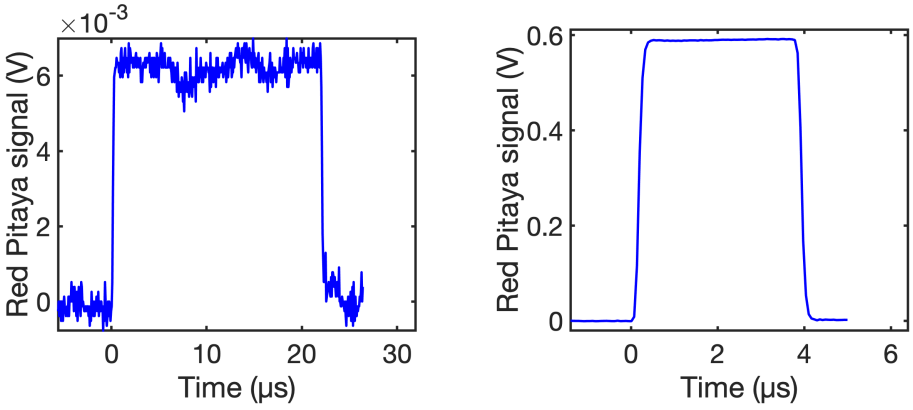

Figure D.7: Examples of the acquired imaging pulses with a Red Pitaya for the lowest (left) and highest (right) value of the imaging beam intensity. There are monitored for each run and used to compute the saturation parameter.

The saturation also depends on the exact position of the cloud in the Gaussian imaging beam. The imaging beam center position with respect to the atoms is determined by doing a knife-edge measurement in the intermediate image plane. The knife-edge measurement consists in moving a knife mounted on a translation stage, across the beam transverse direction and measuring the power which is not blocked by the knife. The power P as a function of the knife displacement y follows an error function for a Gaussian beam (Bernon, 2011): $P(y) = P_0/2(1 + \mathrm{erf}(\sqrt{2}(y - y_0)/w_0))$ where P_0 is the total power, y_0 the beam central position and w_0 the waist. These 3 parameters are free parameters that are fitted to the data with this function. The results are shown on Fig. D.8 from which we deduce the central position of the beam with respect to the translation stage.

To determine the position of the atoms with respect to the translation stage (millimeter precision), we image both the knives and the atoms onto the Princeton camera. Aligning the knife edges onto the position of the atoms on the camera gives the reference position

(dashed line on Fig. D.8). From these measurements, we know that the atoms and the beam center are separated by -2 mm vertically and 3.9 mm horizontally in the intermediate plane. In the atomic plane, they correspond to offsets of -212 µm and 413 µm using the magnification of 500/53. Waists have an uncertainty of ±50 µm from the beam profiler measurement. The saturation parameter is then computed with the following intensity: $I = 0.71 \times 2P_0/(\pi w_0^2)$. We assume that it is homogenous over the cloud widths (6×15 µm^2).

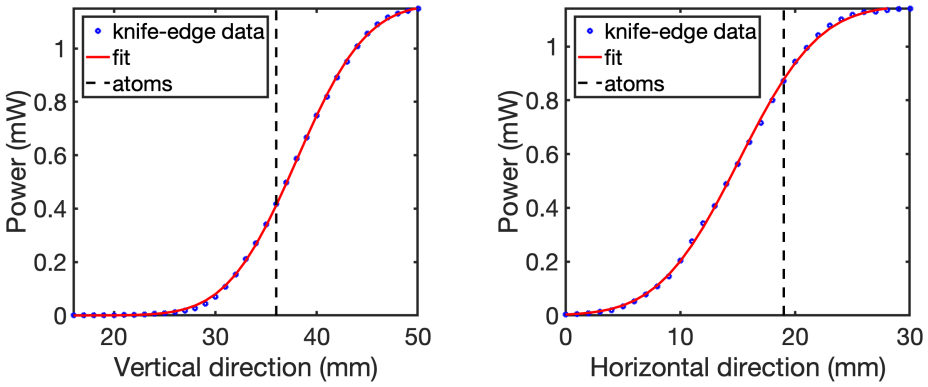

Figure D.8: Knife-edge measurements (blue circles) along vertical (left) and horizontal (right) directions at the intermediate plane of the imaging beam; fit with an error function (red solid line) giving the central position of the beam; and position (black dashed line) of the atomic cloud. The total power, central position and waist fit values are 1.167(7) mW, 38.03(7) mm, 10.8(2) mm for the horizontal direction and 1.153(7) mW, 15.10(8) mm, 10.9(2) mm for the vertical direction.

Finally the beam waist at the position of the atoms is measured by deviating the beam towards a beam profiler positioned at an equivalent distance. It directly gives the waist at the atom position of $w = 1.13$ mm. This is compatible with the knife-edge measurements (Fig. D.8) as a waist of 10.8 mm in the intermediate plane gives in the atomic plane with a magnification of 500/53 a waist of 1.14(2) mm.

The knowledge of the power, waists, and position offsets enables us to compute precisely the beam intensity seen by the atoms.

We compare the saturation parameter computed with the signal of the photodiode to the one that we can measure with the EMCCD camera. For this, we measure the intensity I_{ADU} in count number (or ADU unit) on the camera and convert it in intensity I_0 in unit of W/m^2 with the following conversion factor:

$$I_0 = \frac{hC/\lambda}{G^2 T Q E \eta t_{pix}^2 t} I_{ADU}, \tag{D.30}$$

where $G = 18.87$ is the magnification of the high NA imaging axis, $T = 0.76$ is the transmission loss through the microscope and telescope to the camera, $QE = 0.7$ is the quantum efficiency, $t_{pix} = 16$ µm is the pixel size, $\eta = 1/0.75$ ADU/e$^-$, t is the pulse duration and $\lambda = 780.24$ nm. Using these parameters, we get on average a ratio between the value of s_0 measured by the photodiode over the value of s_0 measured by the camera of 1.2 as shown on Fig. D.9. The agreement is quite good knowing that the computation of the intensity on the camera depends on many constants, in particular

the quantum efficiency which is not easy to calibrate experimentally as it depends on the sensor temperature and requires the knowledge of any loss and conversion factors.

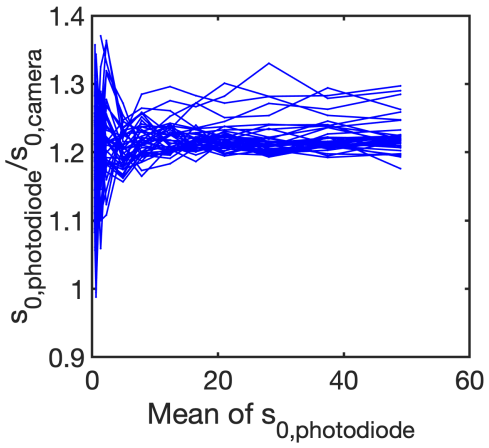

Figure D.9: Ratio of the saturation parameter measured by the photodiode and the camera vs. the mean value of the saturation parameter measured by the Princeton camera. All datasets are plotted altogether.

For the data analysis we will use the saturation given by the photodiode which is more reliable than the one given by the camera.

Experimentally we vary the beam power such that the saturation parameter s_0 ranges from 0.4 to 49. The number of scattered photons per atom is kept fixed to about 70 scattered photons per atom for all runs by adjusting the imaging pulse duration from 22 µs to 3.7 µs.

D.4 Results

D.4.1 Transmission raw data

Three images are taken for each run: the first one with atoms, the second one without atoms, and the last one for the background. A dead time between the images of 400 µs is let for the fast kinetics image transfer. The transmission can then be computed as $T = (I_{at} - I_{back})/(I_{no,at} - I_{back})$. For each value of s_0 and t_{MW} we repeat 5 times each run for averaging.

Fig. D.10 shows a typical 2D transmission curves of the atomic cloud. All curves have been recentered around $(X, Y) = (0, 0)$ with a 2D fit.

D.4.2 Local reduction of the cross-section

For each pixel of a given image, we compute the optical density by varying in the analysis the value of α. We show on Fig. D.11 the results for a few MW durations and two different pixels where we plotted 10 curves of b vs. s_0 corresponding to α from 1 (black) to 11 (light gray).

We found the best value of α that minimizes the standard deviation of b vs. s_0 in the range where T is in $[0.05, +\infty[$. We use this specific range of transmission as it rejects

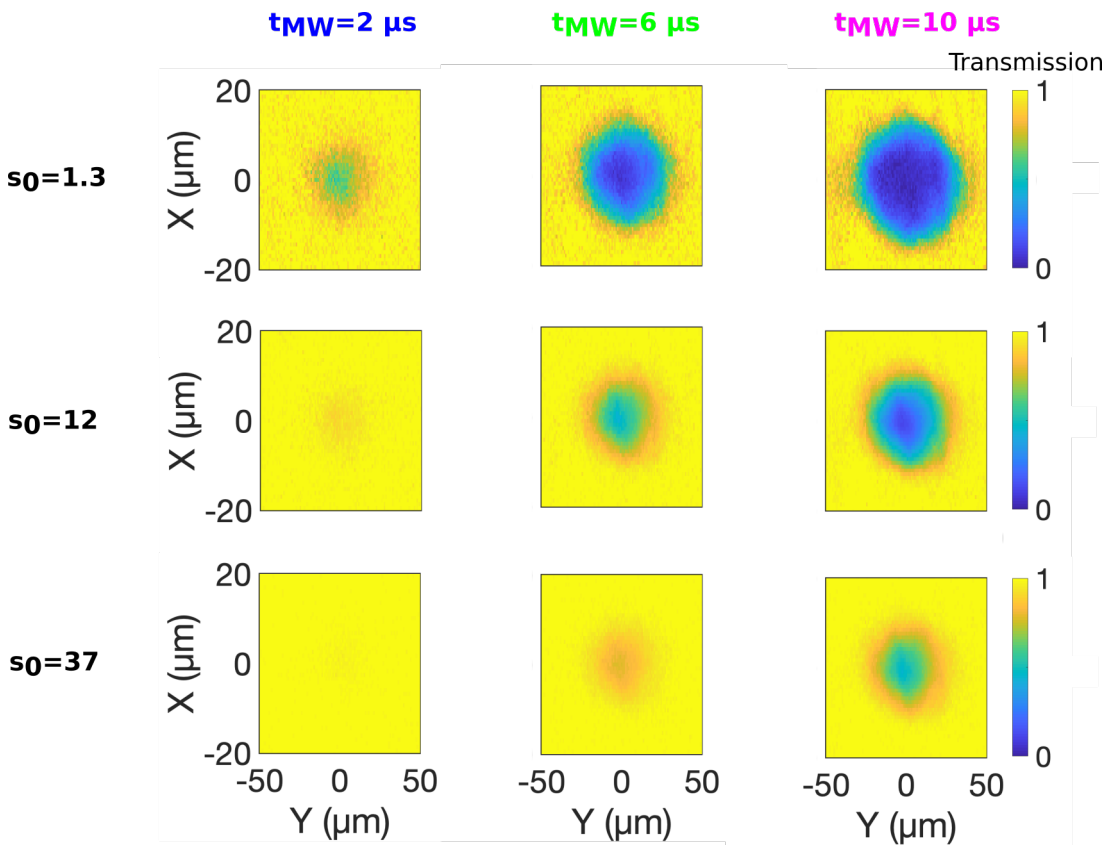

Figure D.10: 2D transmissions for many saturation s_0 and MW durations t_{MW}.

noises for very low transmissions which are due to readout noise and residual fluorescence, and keep noises for transmissions around 1 such that noisy transmissions average to 1. After finding the best value of α, we get the corresponding optical density by averaging b over all values of s_0.

At the cloud center, for a MW pulse of 6 µs, we clearly see that taking $\alpha = 1$ would not make the optical density independent of the saturation parameter. So the correct value is rather $\alpha = 2.9$ and b = 8.5 which gives the green curve. Interestingly, a shifted pixel on the side of the cloud for a longer MW pulse of 10 µs gives $\alpha = 3$ and b = 8.3 as shown by the flat magenta curve on the right bottom panel. This means that equivalent optical densities lead to the same reduction of the cross-section.

Finally we plot all couples of (α, b) on Fig. D.12. All MW curves converge towards $\alpha = \alpha_0$ at low optical densities. The exact value of α_0 (here close to 1) depends on the experimental calibration of the saturation parameter. Using the calibration detailed in section D.3.3, we fitted the curve $\alpha(b)$ with a linear function and extract a slope of 0.26 and $\alpha_0 = 1.1$.

As a conclusion, we measured that α strongly depends on the optical density b. More importantly, a unique value of α cannot be inferred for a single cloud as the optical density, is spatially varying so as α. For a σ^- polarized imaging beam, the dependency that we found is $\alpha = 0.255(2)b + 1.17(9)$. This dependence on b seems almost universal for a large range of optical density parameters as all MW curves collapse on each other.

The uncertainty on $\alpha_0 = 1.17(9)$ is dominated by the uncertainty of the saturation parameter. This offset close to 1 shows that in the limit of low densities the atomic response

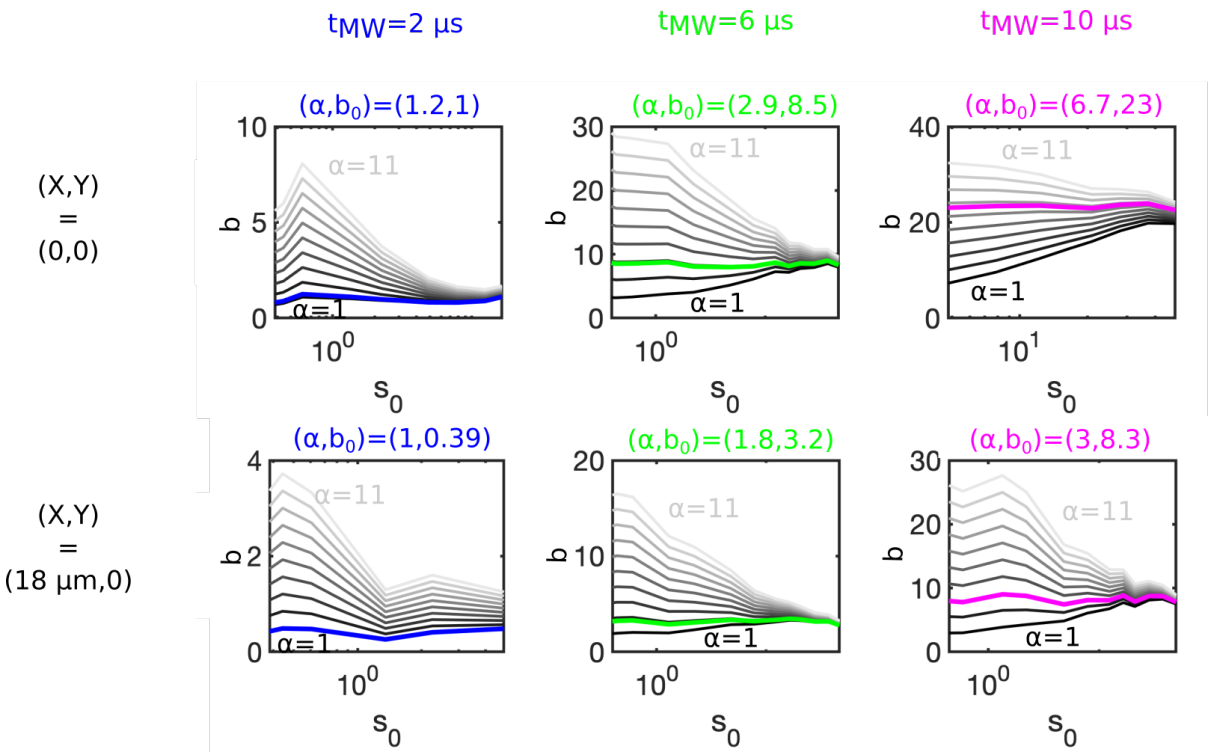

Figure D.11: Cross-section calibrations curves for $t_{MW} = 2$ µs, $t_{MW} = 6$ µs and $t_{MW} = 10$ µs at two positions in the cloud. Black curves correspond to different values of α. The colored curve is the one which has the value of α which minimizes $std(b)$ with the corresponding values of α and b in the plot title.

is well modeled by an ensemble of independent TLS. The value of α at low atomic density depends both on the probe polarization and magnetic field direction but also linearly depends on the calibration of the saturation intensity as observed by the atomic cloud. The calibration of the offset between probe center and atoms was important in this respect. The dependence of α on b shows that α is not solely determined by the probe properties but also depends on the optical density which is a signature of the influence of multiple scattering.

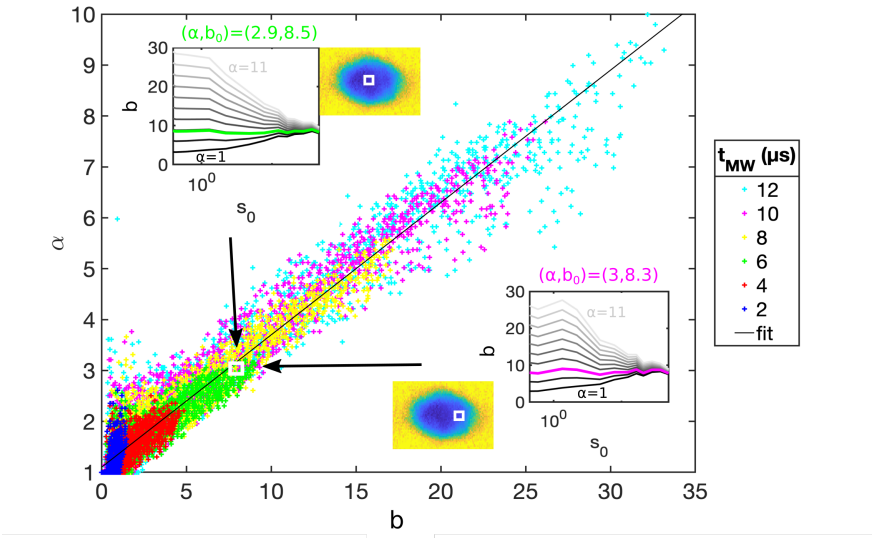

Figure D.12: Correction factor α vs. the optical density for all MW datasets $(2, 4, 6, 8, 10, 12$ µs). Each point corresponds to 1 pixel and the solid line is a linear fit.

D.4.3 1D propagation model including an incoherent scattering

Here, we show that an incoherent background (s_i) could arise from an incoherent scattering $(R_{sca}^{(inc)})$ that mimics multiple scattering. We propose a model of propagation that can be quantitatively compared to the data. In the model, we consider the propagation of the coherent probe in a cloud that is homogeneous in the transverse directions and has a Gaussian density profile in the propagation direction. The system is translation invariant in the transverse plane (x, y). The electromagnetic field and intensity therefore only depend on z.

D.4.3.1 Propagation equations from the single-atom scattering rates

For a resonant σ polarized probe, the scattering properties of an atom embedded in an incoherent electromagnetic background are well described by an effective TLS given in section C.3.2:

$$\begin{aligned} R_{sca}^{(coh)} &= \frac{\Gamma}{2\alpha} \frac{\frac{s_c}{\alpha}}{\left(1+\frac{s_c}{\alpha}\right)^2}, \\ R_{sca}^{(tot)} &= \frac{\Gamma}{2} \left(\frac{\frac{s_c}{\alpha}}{1+\frac{s_c}{\alpha}} + \frac{\frac{s_i}{\alpha_c}}{1+\frac{s_i}{\alpha_c}} \right), \end{aligned} \tag{D.31}$$

where the corrected scattering rates are $\alpha = \alpha_{\mathrm{SA}}\,(1 + s_i)$ and $\alpha_c = 1 + s_c$, where α_{SA} is the single-atom reduction of the cross-section that depends on polarization, detuning and offset field. Here, we have $\alpha_{SA} = 1$ corresponding to on-resonance σ polarization.

To numerically solve our model, we divide the propagation direction in infinitely small slabs of width dz. For each slab, we derive from the scattering rate expressions a set of differential equations that relates the intensity profile of the coherent intensity $I_c(z)$, forward incoherent intensity $I_i^+(z)$ and backward incoherent intensity $I_i^-(z)$. The set of

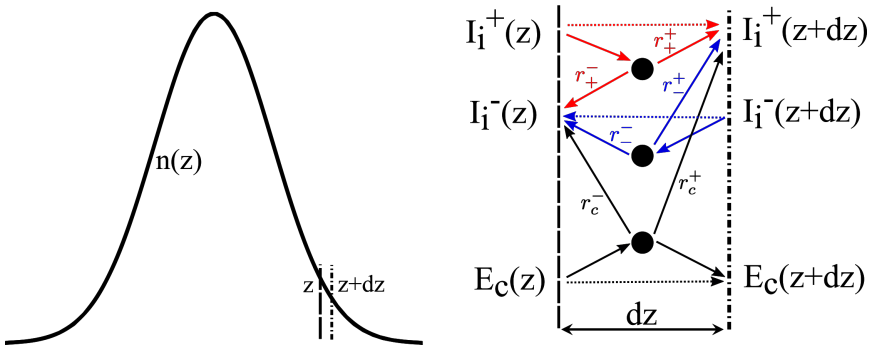

Figure D.13: 1D model for the coherent and incoherent propagation and conversion of light between adjacent layers. The coherent and incoherent scattering rates are given by Eq. (D.31). The spatial repartition are taken as $r_+^+ = 1-r_+^- = r_-^- = 1-r_-^+ = r_c^+ = 1-r_c^- = 1/2$ (see text).

equations is expressed in terms of the nondimensionalized saturation intensity parameters $s_c(z) = I_c(z)/I_{\rm sat}$, $s_i^+(z) = I_i^+(z)/I_{\rm sat}^{\rm iso}$, $s_i^-(z) = I_i^-(z)/I_{\rm sat}^{\rm iso}$ where $I_{\rm sat}^{\rm iso} = \alpha^{\rm iso} I_{\rm sat} = 2.12 I_{\rm sat}$.

$$\begin{aligned}
\frac{ds_c}{dz} &= -\, n(z)\sigma_0 \frac{s_c}{1+s_c+s_i}, \\
\frac{ds_i^{(+)}}{dz} &= -\,\frac{n(z)\sigma_0^{\rm iso}}{2}\left(\frac{s_i^{(+)}-s_i^{(-)}}{1+s_c+s_i} - \frac{s_c(s_c+s_i)}{(1+s_c+s_i)^2} - \frac{s_c}{(1+s_c+s_i)^2}\right), \\
\frac{ds_i^{(-)}}{dz} &= -\,\frac{n(z)\sigma_0^{\rm iso}}{2}\left(\frac{s_i^{(-)}-s_i^{(+)}}{1+s_c+s_i} - \frac{s_c(s_c+s_i)}{(1+s_c+s_i)^2} - \frac{s_c}{(1+s_c+s_i)^2}\right),
\end{aligned} \tag{D.32}$$

where the isotropic cross-section is $\sigma_0^{\rm iso} = \hbar\omega\Gamma/(2I_{\rm sat}^{\rm iso})$ and the total incoherent intensity is $s_i = s_i^{(+)} + s_i^{(-)}$. The prefactor $1/2$, corresponding to $r_{c/+/-}^{+/-}$ in Fig. D.13, accounts for equally distributed of backward and forward scattered intensities. In the derivatives of $s_i^{\pm}$ in Eq. (D.32), the first term accounts for re-scattering of incoherent field which is isotropic ($r_+^+ = r_+^-$ and $r_-^- = r_-^+$), the second one accounts for the temporally incoherent (ti) scattering of the coherent field (*i.e. resonant fluorescence*) which is also isotropic ($r_c^{-,ti} = r_c^{+,ti}$). The last term that conserves energy corresponds to the coherent field scattering in a temporally coherent but spatially incoherent (si) field arising from the discrete random position of atoms in an ensemble that we assume to be isotropic ($r_c^{-,si} = r_c^{+,si}$). This spatially incoherent field is out-of-phase with the coherent probe and its effect on the coherence term of the density matrix ρ_{eg} will spatially average to 0. As checked numerically, for large saturation, the scattering being mostly temporally incoherent, this assumption has very little consequence on the results. This means that the spatial redistribution of the third term (forwards, backwards or both) has little influence on the simulation results. In the model, both temporally and spatially incoherent contributions are summed in the incoherent intensity : $r_c^{+/-} = r_c^{+/-,ti} + r_c^{+/-,si}$.

We find the solution of Eq. (D.32) by an iterative process between steps (i). We first determine the spatial profile of the coherent intensity ($s_c^{(0)}(z)$) with no incoherent background ($s_i^{+/-,(0)} = 0$). We then solve the equation for $s_i^{+,(0)}(z)$ including $s_c^{(0)}(z)$ and $s_i^{-,(0)} = 0$ and then for $s_i^{-,(0)}$ including $s_c^{(0)}(z)$ and $s_i^{+,(0)}$. We iteratively reinject the solution of the step (i) into the equation for step (i+1) and converge towards an autoconsistent solution

where the intensity profiles do not evolve anymore. At this stage, our set of equations is considered as solved for the particular input coherent intensity and atomic density. The results are presented in the next section.

D.4.3.2 Saturation intensity profiles

Fig. D.14 shows the profiles along the propagation direction of Eq. (D.32) for many saturation s_c and optical density b. At a low saturation ($s_c(0) = 0.5$), as b increases, the coherent field gets converted into incoherent light at the entrance of the cloud. Most of the incoherent intensity is converted into s_i^- as the probability for a photon to pass through the cloud gets reduced. As $s_c(0)$ increases, more coherent intensity passes through the cloud. The cross-section is then mostly determined by the coherent saturation parameter. At large saturation ($s_c(0) = 50$), the incoherent intensity is homogeneous along the propagation direction as most of the coherent light is mostly transmitted.

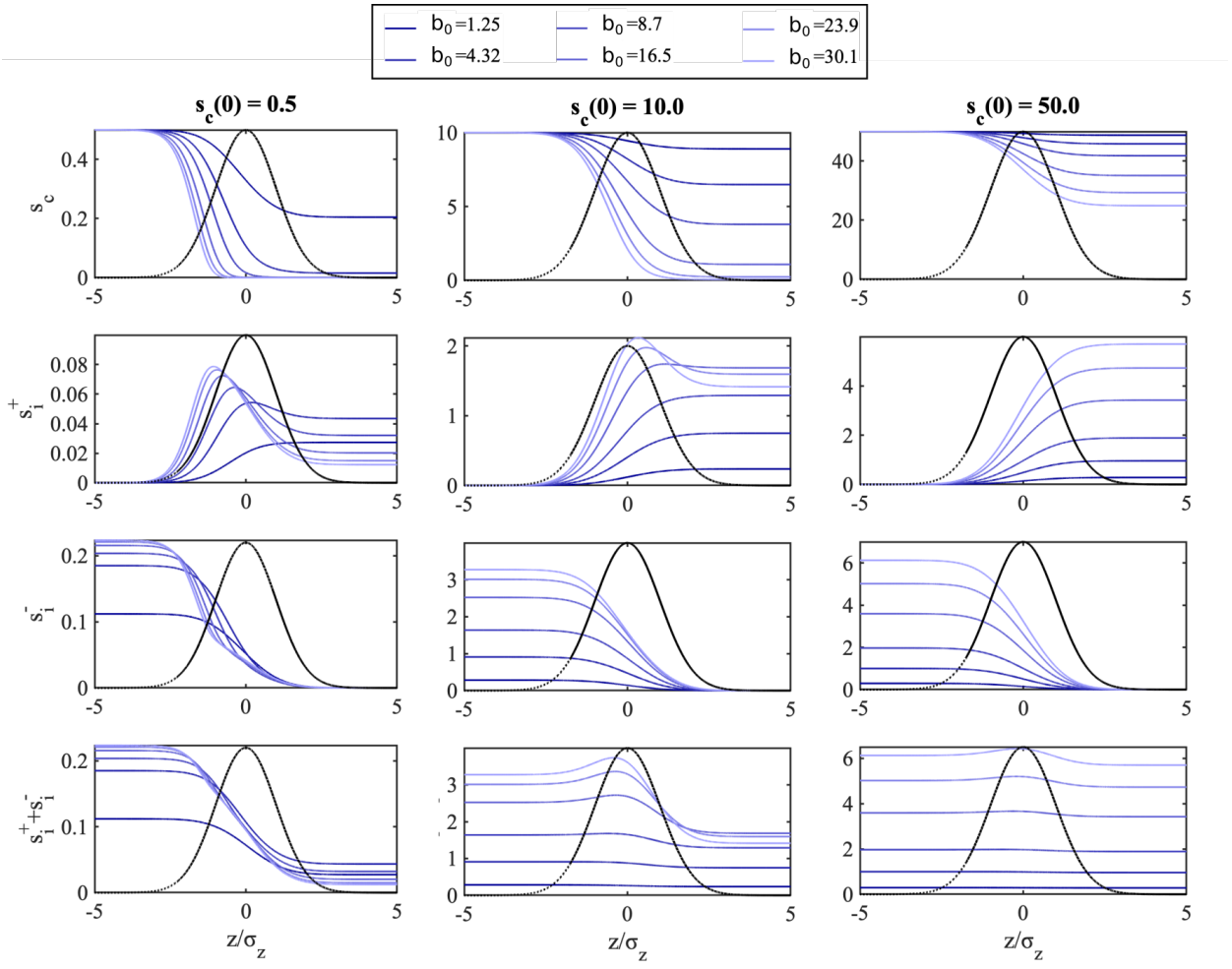

Figure D.14: Saturation profiles for the coherent $s_c(z)$ and incoherent parts $s_i^+(z)$, $s_i^-(z)$ and $s_i^+(z)+s_i^-(z)$, for coherent input saturations of $s_c(0) = 0.5, 10, 50$ and optical densities b_0 from 1.25 (dark blue solid line) to 30.1 (light blue solid line). The black dotted line is the Gaussian atomic density profile with an arbitrary amplitude to match the plot size. The x-axis is normalized by the Gaussian width $\sigma_z = 5$ µm.

From these profiles, the expected α can be computed using the transmitted intensities.

D.4.3.3 Value of α

The reduction of the cross-section α is computed numerically from the coherent transmission ($s_c(\infty)$) and the incoherent intensity ($s_i^+(\infty)$) collected in a solid angle Ω and obtained by inverting the usual equation of the optical density (Eq. (D.8)):

$$\alpha = \frac{-b - (s_c(\infty) + s_i^+(\infty)\Omega\alpha_{iso} - s_c(0))}{\ln\big((s_c(\infty) + s_i^+(\infty)\Omega\alpha_{iso})/s_c(0)\big)}. \tag{D.33}$$

The value of α for different probe intensities are presented in Fig. D.15 as a function of the integrated optical density. For small probe saturation, the conversion of the coherent probe field into incoherent intensity (s_i) cannot generate high incoherent intensity ($s_i \ll 1$) and should therefore not affect the value of α in the coherent propagation (Eq. (D.32)). Nevertheless, for high optical density, we are in the diffusive regime. Along the propagation, while the coherent field is exponentially reduced in the mean free path length $l_{sc} = 1/(n\sigma_0)$ and quickly disappears, the incoherent field, that will also be detected on the camera, is only algebraically reduced $T_{diff} \propto 1/b = C/b$ (Garcia, Genack, and Lisyansky, 1992; Guerin, Rouabah, and Kaiser, 2017). In this regime, it is the dominating contribution that scales as $\alpha \approx b/\ln(b/C\Omega)$ where Ω is the solid angle of the imaging system (dashed red asymptote in Fig. D.15 with $C = 1$). Here ($b \gg s_c$), the increase of α does not correspond to a reduction of the absorption cross-section but rather to an excess of detected light. In the opposite high saturation regime ($s_c \gg b$), the probe intensity is little depleted, and the incoherent saturation intensity becomes almost homogeneous along the propagation. By energy conservation we have $s_i = s_c(1-T)/(2\alpha^{\text{iso}})$. For high saturation, the last term in Eq. (D.8) dominates in the expression of the optical density $b \approx s_0(1-T)$. It leads to an expected reduction of the coherent absorption cross-section that scales as $\alpha = 1 + s_i \approx 1 + b/(2\alpha^{\text{iso}})$ (red curve in Fig. D.15). Fig. D.15 shows the expected value of α for a scalar TLS model where both coherent and incoherent scattering are considered σ polarized ($\alpha^{\text{iso}} = 1$). We observe that it over-evaluates α while an effective TLS with isotropic incoherent scattering $\alpha^{\text{iso}} = 2.12$ has a slope $1/(2*2.12)$=0.24 in good correspondence with the experimentally measured one (0.26). Given that the experimental value of α is averaged over all s_c for a given b and that this model does not take into account the transverse inhomogeneity of the cloud or the Mollow spectrum of the incoherently scattered light, the so close correspondence of the slopes is certainly fortuitous. We nevertheless believe that this model captures most of the physical origin of the increase of α with b, namely the saturation coming from the incoherent scattering.

D.4.3.4 Diffuse transmission

Let's focus on the transmitted incoherent intensity $\frac{s_i^+(+\infty)}{s_c(0)}$. Fig. D.16 gives this incoherent transmission as a function of the optical density for three initial values of $s_c(0)$. At fixed $s_c(0)$, as the optical density increases, the increase in incoherent transmission means that more coherent intensity is converted into incoherent scattering. For large optical densities, the transmission tends towards a diffuse transmission and decreases with the optical density. It comes from the collection of the incoherent light into a solid angle at the output of the cloud. Interestingly, the residual diffuse transmission in the low saturation limit tends towards the limit $T_{diff} = \frac{1+0.7104}{b+2\times0.7104}$ (Guerin, Rouabah, and Kaiser, 2017) which is obtained from a model of light propagation that does not include coherence and interference effects (diffuse equation or random walk).

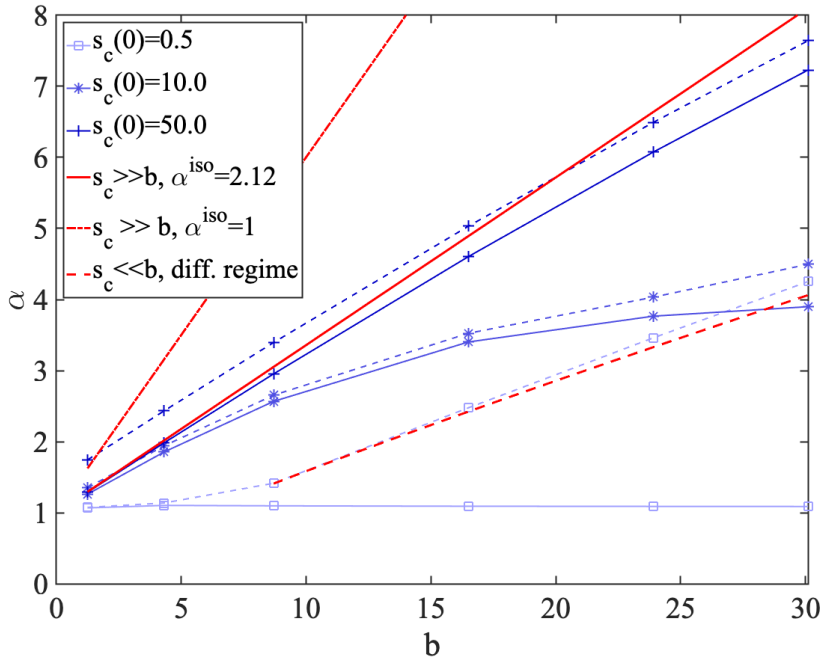

Figure D.15: α parameters calculated from the saturated scattering model (Eq. D.32). The simulated probe saturation intensities are comparable to the experiment : $s_c = 0.5$ in light blue (bottom) to $s_c = 50$ in dark blue (top). The line (resp. dashed line) corresponds to the value of α as calculated from the coherent transmission $T_c = s_c(L)/s_c(0)$ (resp. the total transmission $T = (s_c(L) + \alpha^{\text{iso}} s_i^+(L)\Omega/(2\pi))/s_c(0)$, where $\alpha^{\text{iso}} s_i^+(L)\Omega$ is the fluorescence background emitted in the solid angle Ω of the imaging system). In red, the analytical large saturation limit for (plain line) an effective TLS approximation of a MLS with $\sigma_0^{\text{iso}} = \sigma_0/\alpha^{\text{iso}}$, (dot-dashed line) an ideal scalar TLS corresponding to $\sigma_0^{\text{iso}} = \sigma_0$ and (dashed) the diffusive regime (see text).

D.4.3.5 Impact of the solid angle

The impact of the solid angle $\Omega \in [0, 0.018]$ on α for a diffusive regime for a large optical density $b_0 = 30.1$ is given in Fig. D.17. The value 0.018 corresponds to the experimental case ($NA = 0.185$). We see that for $s_c(0) \gg 1$, the value of α is not very sensitive to the solid angle and remains almost constant. The effect is more important for low saturations where the sensitivity for low transmissions is sharp, due to the logarithm term in the optical density.

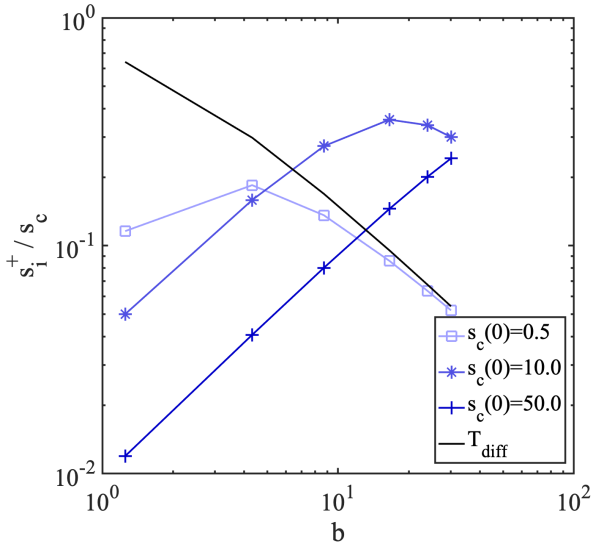

Figure D.16: Forwards incoherent transmission vs. the optical density for three initial coherent saturations (blue lines). The black line is the diffuse transmission given by $T_{diff} = \frac{1+0.7104}{b+2\times0.7104}$ (Guerin, Rouabah, and Kaiser, 2017).

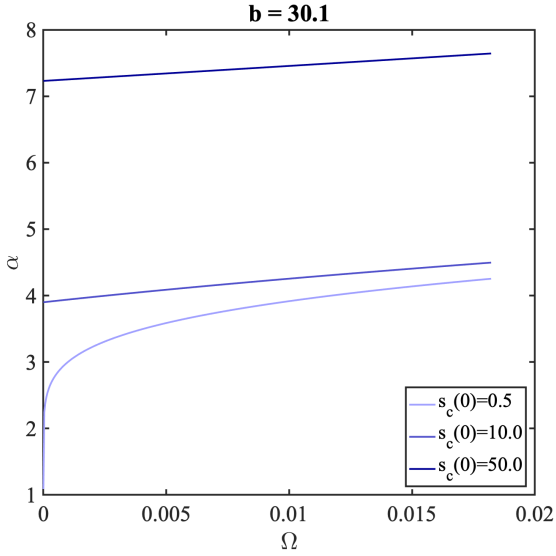

Figure D.17: Influence of the solid angle on the value of α at fixed optical density and for three initial coherent saturations (blue lines).

D.4.4 Data analysis per saturation and per microwave duration

We have observed in the previous section that the 1D model indicates some dependencies of α on the coherent saturation parameter s_c[3]. We want to check if there is a dependence on the coherent saturation parameter s_c from experimental data. For that purpose, we fit only the whole dataset of $t_{MW} = 2$ µs for all saturation parameters, setting $\alpha = 1.1$, with three free parameters: b_0, σ_x and σ_y which are parametrizing the Gaussian optical density:

$$b(x, y, t_{MW}) = \frac{P(t_{MW})}{P(t_{MW} = 2\mu s)} b_0 e^{-\frac{x^2}{2\sigma_x^2}} e^{-\frac{y^2}{2\sigma_y^2}}, \tag{D.34}$$

where $P(t_{MW})$ is given by Eq. (D.29).

We found that b_0=1.04, σ_x=13.1 µm and σ_y=5.6 µm. These three parameters are very close to the predictions obtained by TOF measurements given in section D.3.

Then, for all other MW durations (4 to 12 µs), we keep $b_0 = 1.04$, $\sigma_x = 13.1$ µm and $\sigma_y = 5.6$ µm constant. For each dataset composed of a fixed t_{MW} and s_c, we fit the value of the slope a such that $\alpha = \alpha_0 + ab(x, y)$ where $\alpha_0 = 1.1$. Each dataset is then fitted by the following transmission including a transmission offset as a free parameter:

$$T(x, y) = T_0 + \frac{\alpha_0 + ab(x, y)}{s_c} W\left(\frac{s_c}{\alpha_0 + ab(x, y)} e^{\frac{s_c - b(x,y)}{\alpha_0 + ab(x,y)}}\right). \tag{D.35}$$

Results of 2D fits on the experimental transmission images are shown on Fig. D.18. It shows only transmission cuts along Y (points), the corresponding fitted transmission with a slope (solid lines), and transmission in the case where $a = 0$ (dashed lines).

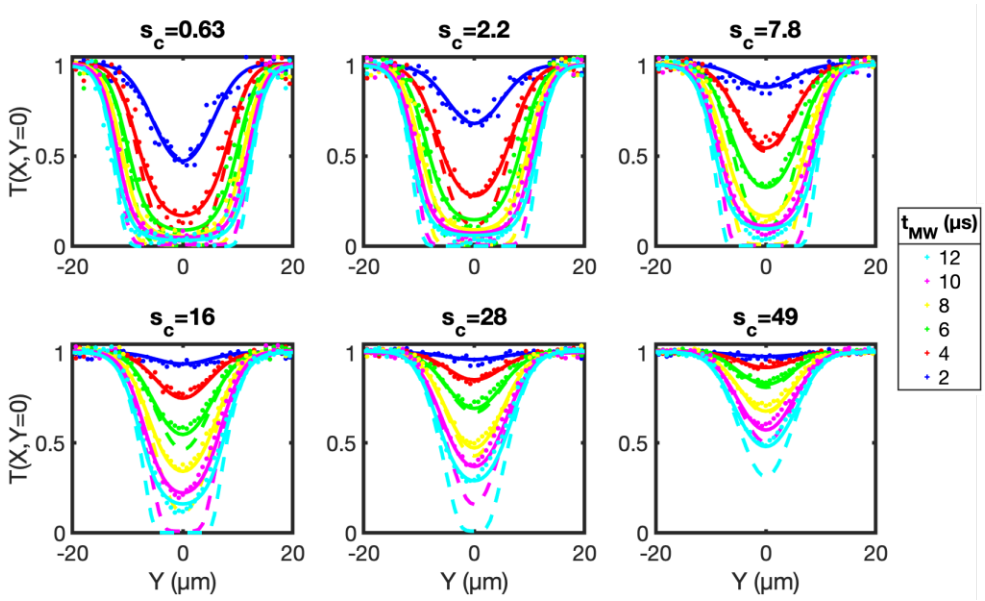

Figure D.18: Raw 1D transmission curves (points) for the cut along $Y = 0$, transmission using $a = 0$ (dashed lines) and results from 2D fits (solid lines) with a slope a.

[3]We note the coherent saturation parameter s_c in this section to distinguish between s_c and s_i. s_c is equivalent to s_0 in previous sections.

We clearly see that $a = 0$ does not match with the experimental transmission when $T < 0.5$. By contrast, the fit describes well the transmission shape at the cloud center corresponding to optically denser regions.

For s_c large compared to the optical density, we repeat the fit procedure to get a slope a by increasing (resp. decreasing) b_0 by +10% (-10%). Fig. D.19 gives the results of slopes a vs. the center of the optical density profile for a given MW pulse. We did not show the second fit parameter which is a transmission offset as it is below 1% for all datasets. Fig. D.18 also contains the transmission within ±10% uncertainty for the peak optical density. The corresponding errors are smaller than the plot solid line widths.

For a low coherent saturation, the slope has a moderate uncertainty as a small error on b_0 leads to a small error on α. By contrast, for larger s_c, the slope has a much larger uncertainty. It means that a large value of α is needed to change the optical density for $s_c > b$.

We conclude that to study the variation of the slope a for $s_c > b$, the optical density has to be known with an uncertainty much smaller than 10%. For $s_c > b$, the value of the slope is found to be constant around 0.25 and seems to not depend on the saturation parameter s_c.

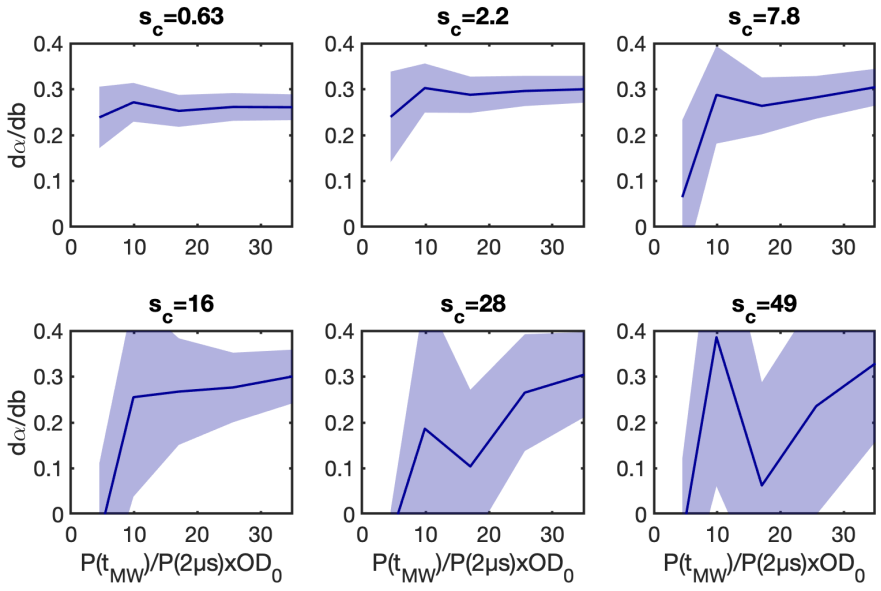

Figure D.19: Fit results of a for each coherent saturation s_c and micro-wave durations. It corresponds to the fit parameters which give solid lines in Fig. D.18. The shaded areas correspond to an uncertainty of ±10% on the peak optical density b_0.

D.5 Conclusion

In this chapter, we derived in section D.1 the usual Beer-Lambert law from coherent scattered fields of a continuous medium of two-level scatterers and showed that it leads to the usual optical density found in the literature. The multi-level structure was included heuristically with a correction factor α based on (Reinaudi et al., 2007).

In section D.2 we focused on relevant probe conditions that have to be studied to avoid systematic errors in atom number measurements. In particular, we determine the expected

signal-to-noise for the measurement of the optical density as a function of the saturation parameter and duration of the imaging pulse. Our optimization protocol ensures that atom random walks, longitudinal displacements, and Doppler shifts can be neglected and gives the optimal parameters that maximize the signal-to-noise ratio.

In section D.3, we presented the experimental setup for measuring the transmission of a coherent σ^- probe through a thermal atomic ensemble of ^{87}Rb atoms in a well-calibrated environment. We showed that time-of-flight measurements give good estimations of in situ optical densities and atomic cloud widths. We finely calibrated the saturation parameter using a monitoring photodiode and checked the beam position and waist. We gave the calibration of the MW Rabi oscillation in a homogeneous magnetic field aligned with the probe direction which enables to coherently transfer atoms into $|F_g = 2, m_F = -2\rangle$ which is directly a state of the cycling transition for our σ^- probe. Based on all these calibrations, we expect to find $\alpha = 1$ from single-atom physics. In other words, there should be no effects of the multi-level atomic structure.

In section D.4, we have shown that the reduction of the apparent absorption cross-section is connected, in the diffusive regime ($b \gg s_c$), to the residual diffuse transmission and, in the saturating regime, to the electromagnetic background originating from multiple incoherent scattering in the cloud (s_i). In both cases, this correction is shown to scale mainly linearly with the optical density and reproduces well the experimentally observed dependence of α. In contrast to previously proposed calibration methods (Reinaudi et al., 2007) that are commonly used in the community, this study shows that the reduction of the cross-section is local as different positions in the cloud lead to different reductions. For a circular probe polarization under well-controlled magnetic field orientation and laser detuning, the measured correction factor: $\alpha = 1.17(9) + 0.255(2)b$ seems "universal" in the sense that it is independent of the position in the cloud. The offset $\alpha_0 = 1.17(9)$ ultimately depends on a fine calibration of the saturation parameter and should be equal to 1 for a perfectly calibrated σ light.

A strength of the proposed model is to take into account both the saturated response of a single-atom embedded in an electromagnetic environment and the collective participation of the surrounding atoms in this environment in a self-consistent solution. At the cost of numerical computation power, the proposed 1D model could certainly be extended to 3D. Also, modifications on the reabsorption cross-section could be considered, which consists in treating the off-resonant effect of the Mollow spectrum.

We found that the value of the slopes $d\alpha/db$ does not seem to depend on the saturation parameter in the regime $s_c > b$. In the opposite regime, the optical density and cloud widths have to be known with high accuracy in order to quantitatively compare the experimental data to the 1D model ($< 10\%$ precision on the optical density).

A similar calibration could certainly be performed for other typical configurations such as π-polarized probes. From what we know, similar observations where the correction factor varies linearly with the optical density have been seen in (Chomaz, 2014) for the case of π polarization. In (Chomaz, 2014), in the limit of low optical densities $\alpha_0 \approx 3.73$, which is higher than the expected 1.829 for linear polarizations. A systematic calibration in π polarization would have to be performed with a fine calibration of stray magnetic fields and saturation parameters as we did in the chapter for a σ^- polarization.

Chapter E

In situ absorption imaging with a subwavelength resolution using a dressed excited state

In this chapter, we discuss in detail a new imaging method for reaching subwavelength resolutions using a dressed excited state. In section E.1, we give the ingredients of the method and detail the theoretical computations of the light shifts that are a prerequisite of the method. We derive the spatial resolutions for a closed or an open atomic transition corresponding respectively to a cooler and repumper transition. In section E.2, we present the experimental setup used for dressing the excited state in different beam geometries. In the last two sections, we give experimental results that we compare to theoretical models where subwavelength resolutions can be indirectly quantified by measuring atom numbers. On a repumper transition in section E.3, and on a cycling transition in section III.ii, we will see that the atom number is at first order proportional to the subwavelength widths. In particular, we will see that the results of Chapter D make the atom number volume measurements much closer to what we expect from time-of-flight measurements.

E.1 Principle, exact light shifts and spatial resolutions

In this section, we describe the subwavelength imaging method applied to the ^{87}Rb atomic structure, then we compute the AC Stark shifts for the imaging method and finally we give the expected theoretical spatial resolutions for a closed or an open transition.

E.1.1 Method principle with an optical lattice at 1529 nm

The subwavelength imaging method shown on Fig. E.1 consists in dressing only the excited state $5P_{3/2}$ with a spatially varying intensity profile close to the 1529.366 nm transition between the two excited states $5P_{3/2}$ and $4D_{5/2}$. The energy shift due to the 1529 nm laser on the ground state $5S_{1/2}$ is weak as the interaction is far-off-resonance and the 1529 intensity is small. Then, a 780 nm laser radiation is shined on the cloud, driving the transition between $5S_{1/2}$ and $5P_{3/2}$ which is resonant only at a few positions.

On Fig. E.1 we show a dressed state with an optical lattice at 1529.360 nm which creates a positive shift of the state $5P_{3/2}$. A 780 laser detuning $\Delta_{780} = \omega_{780} - \omega_0$, where ω_0 is the atomic transition between $5S_{1/2}$ and $5P_{3/2}$, is then tuned such that the frequency is

resonant with the middle of the lattice modulation. In this configuration, the variation of energy over space is the strongest. As a result, a very narrow spatial area is resonant and the width of this area can be smaller than the diffraction limit. This will be quantified in section E.1.3.

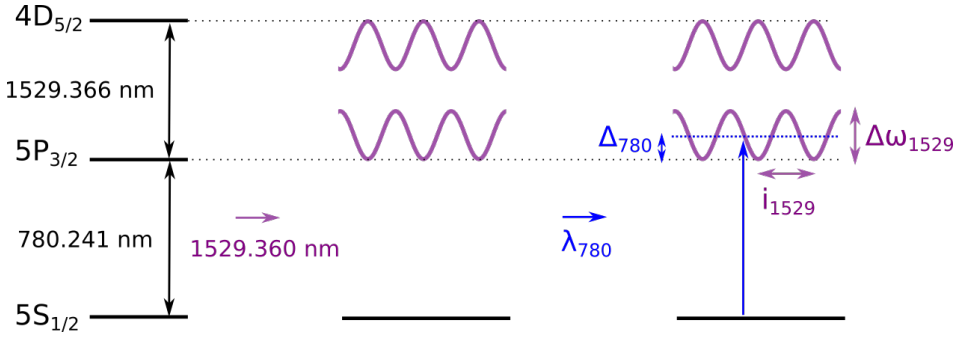

Figure E.1: Subwavelength imaging principle: a 1529 optical lattice intensity dresses the $5P_{3/2}$ state and a 780 probe is resonant only with certain positions.

Two different cases for the 780 nm laser will be considered: a repumper transition or a cooler transition.

The first case is a repumper transition as shown on Fig. E.2 where the 780 nm laser is tuned from $|F_g = 1\rangle$ to $|F_e = 2\rangle$. Atoms are then transferred due to absorption and spontaneous decay into $|F_g = 2\rangle$ with only a few repumper photons. At this stage subwavelength excitation has been achieved. The subwavelength volume that has been repumped will then be probed by a standard resonant absorption imaging carried on the cycling transition.

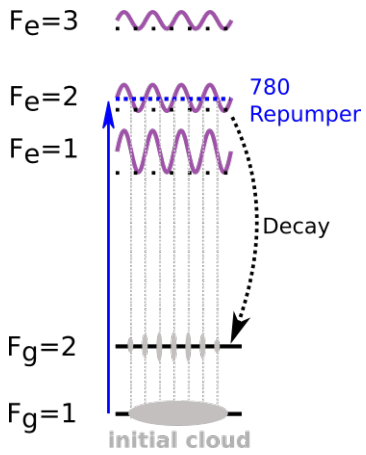

Figure E.2: Subwavelength imaging principle where a 780 repumper laser is used. The blue dashed line represents the resonant position of the 780 laser. The ground state $|g\rangle$ refers to $5S_{1/2}$ and the excited state $|e\rangle$ to $5P_{3/2}$.

The second case is an imaging transition as shown on Fig. E.3 where the full cloud is first transferred with a microwave transition into $F_g = 2$ and imaged on the cycling transition from $|F_g = 2, m_F = -2\rangle$ to $|F_e = 3, m_F = -3\rangle$ at 780 nm with 1529 laser radiations that are turned on during the imaging process. This means that the subwavelength resolution occurs on the cycling transition during the imaging. This can be useful to probe only a fraction of the cloud thanks to a microwave transition without destroying the entire sample.

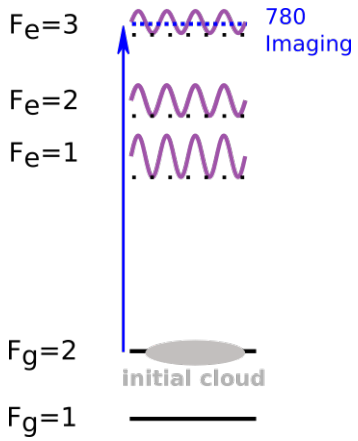

Figure E.3: Subwavelength imaging principle where a 780 imaging laser is used. The blue dashed line represents the resonant frequency of the 780 laser. The ground state $|g\rangle$ refers to $5S_{1/2}$ and the excited state $|e\rangle$ to $5P_{3/2}$.

As the 1529 nm laser is tuned close to resonance, the energy shift of each hyperfine state in the $5P_{3/2}$ manifold is modified. In E.1.2 we will compute the light shifts for any hyperfine level and any 1529 nm intensity which are crucial to compute the spatial resolutions in E.1.3.

E.1.2 AC Stark shift computations

E.1.2.1 Perturbation theory

In the limit of small energy shifts compared to hyperfine splittings, we can use second-order perturbation theory from quantum mechanics to compute the energy shifts due to the electric-field dipole interaction. The unperturbed basis is $|n\rangle \equiv |F, m_F\rangle$ with hyperfine eigenenergies $E_n^{(0)}$.

In the case of an oscillating electric field at frequency ω, the total Hamiltonian is directly given by the AC Stark Hamiltonian $H_{Stark} = -\mathbf{d}.\mathbf{E}$ which leads to the following energy shift for the state $|n\rangle$:

$$\Delta E_{F,m_F} = \left\langle n^{(0)} \right| H_{Stark} \left| n^{(0)} \right\rangle + \sum_{|k\neq n\rangle} \frac{|\left\langle k^{(0)} \right| H_{Stark} \left| n^{(0)} \right\rangle|^2}{E_n^{(0)} - E_k^{(0)}}. \tag{E.1}$$

The first term in Eq. (E.1) is zero due to the parity of the dipole operator. In the perturbation approximation but without making the rotating wave approximation it can be shown (Steck, 2019) that the energy shift is given by:

$$\begin{aligned} \Delta E_{F,m_F} = &- \alpha^{(0)} |E_0^{(+)}|^2, \\ &- \alpha^{(1)} (|E_{0-1}^{(+)}|^2 - |E_{0+1}^{(+)}|^2) \frac{m_F}{F}, \\ &- \alpha^{(2)} (3|E_{00}^{(+)}|^2 - |E_0^{(+)}|^2) \frac{3m_F^2 - F(F+1)}{2F(2F-1)}, \end{aligned} \tag{E.2}$$

where E_{0q} are the electric components in the spherical basis $q \in \{-1, 0, 1\}$ and $|E_0^{(+)}|^2 =$

$2\mu_0 CI$ with intensity I (see section C.2.1.1 for the spherical basis). In this notation, $|E_0| = 2|E_0^{(+)}|$ is the real amplitude of the electric field. The light shift is then proportional to the intensity with proportionality factors which are the scalar, vectorial and tensor polarizabilities given by:

$$\begin{aligned}
\alpha^{(0)} &= \sum_{J_e,F_e} \frac{2\omega_{F_eF}}{3\hbar(\omega_{F_eF}^2-\omega^2)}(F_e+1)(J_g+1)\begin{Bmatrix} J & J_e & 1 \\ F_e & F & I \end{Bmatrix}^2 |\langle J|\,|\,\mathbf{d}\,|\,|J_e\rangle|^2, \\
\alpha^{(1)} &= \sum_{J_e,F_e} (-1)^{F+F_e+1}\sqrt{\frac{6F(2F+1)}{(F+1)}}\begin{Bmatrix} 1 & 1 & 1 \\ F & F & F_e \end{Bmatrix} \\
&\quad \frac{\omega_{F_eF}}{\hbar(\omega_{F_eF}^2-\omega^2)}(F_e+1)(J+1)\begin{Bmatrix} J & J_e & 1 \\ F_e & F & I \end{Bmatrix}^2 |\langle J|\,|\,\mathbf{d}\,|\,|J_e\rangle|^2, \\
\alpha^{(2)} &= \sum_{J_e,F_e} (-1)^{F+F_p}\sqrt{\frac{40F(2F+1)(2F-1)}{3(F+1)(2F+3)}}\begin{Bmatrix} 1 & 1 & 2 \\ F & F & F_e \end{Bmatrix} \\
&\quad \frac{\omega_{F_eF}}{\hbar(\omega_{F_eF}^2-\omega^2)}(F_e+1)(J+1)\begin{Bmatrix} J & J_e & 1 \\ F_e & F & I \end{Bmatrix}^2 |\langle J|\,|\,\mathbf{d}\,|\,|J_e\rangle|^2 .
\end{aligned} \tag{E.3}$$

Experimentally, in the thesis, we will always deal with a linear polarization for the 1529 nm beams ($E_{0\pm1} = 0, E_{00} = E_0$). Expressing the light shift of Eq. (E.2) for a linear polarization and in terms of the intensity I leads to:

$$\Delta E_{F,m_F} = -\,2\mu_0 C\alpha_{F,m_F} I, \tag{E.4}$$

where the total polarizability α_n for the state $|F, m_F\rangle$ and for a linear polarization is given by:

$$\alpha_{F,m_F} = \alpha^{(0)} + \alpha^{(2)}\frac{3m_F^2 - F(F+1)}{F(2F-1)}, \tag{E.5}$$

We will see in section E.3.1.2 that the light shifts computed from Eq. (E.2) match with experimental data for small displacements. This perturbation theory is very practical as the energy shift is directly proportional to the intensity. However, for stronger fields we need to diagonalize the full Hamiltonian, as given in the next section.

E.1.2.2 General case: diagonalization

At large light shifts compared to hyperfine splittings, hyperfine states mix. Eigenstates will be a superposition of hyperfine states $|F, m_F\rangle$ that tend to the fine structure eigenstates $|J, m_J\rangle$ in the strong-field limit. Note that in the strong-field regime (or Paschen-Back regime), analytical formulas similar to Eq. (E.2) can be found (Steck, 2019). In this thesis, we work in the intermediate regime and neither formula can be used.

For intermediate cases, the diagonalization of the full Hamiltonian $H = H_{Stark} + H_{hfs}$ is necessary. It is composed of the AC Stark Hamiltonian H_{Stark} and the hyperfine Hamiltonian H_{hfs}. In the following, we give the matrix elements of the full Hamiltonian that has to be diagonalized.

The hyperfine Hamiltonian is the interaction between the nuclear **I** and total electron **J** angular momenta which obey the usual angular momentum properties[1]. The sum of them gives the total angular momentum $\mathbf{F} = \mathbf{I} + \mathbf{J}$. The hyperfine Hamiltonian including magnetic-dipole and electric-quadrupole terms is given by :

$$H_{hfs} = A_{hfs}\frac{\mathbf{I}.\mathbf{J}}{\hbar^2} + B_{hfs}\frac{\frac{3}{\hbar^2}(\mathbf{I}.\mathbf{J})^2 + \frac{3}{2\hbar}(\mathbf{I}\mathbf{J}) - I(I+1)J(J+1)}{2I(2I-1)J(2J-1)}, \tag{E.6}$$

where A_{hfs} and B_{hfs} are respectively the magnetic-dipole and electric-quadrupole hyperfine constants that depend on fine structure states. The values for ^{87}Rb can be found in (Steck, 2001).

In the basis $|F, m_F\rangle$, the hyperfine Hamiltonian is always diagonal and the eigenvalues $E_{n,hfs}$ are given by:

$$\langle F, m_F| H_{hfs} |F, m_F\rangle = \frac{1}{2}A_{hfs}K + B_{hfs}\frac{\frac{3}{2}K(K+1) - 2I(I+1)J(J+1)}{4I(2I-1)J(2J-1)}, \tag{E.7}$$

where $K = F(F+1) - I(I+1) - J(J+1)$.

Then, in the same basis $|F, m_F\rangle$, the Stark Hamiltonian $H_{Stark} = -\mathbf{d}.\mathbf{E}$ can be expressed using the general atom-field Hamiltonian in the rotating-frame and under the rotating-wave approximation given by Eq. (C.33) leading to the matrix element:

$$\langle F, m_F| H_{Stark} |F', m'_F\rangle = \frac{\hbar}{2}\left(\Omega^*(F, m_F, F', m'_F)\delta_{F,g}\delta_{F',e} + \Omega(F, m_F, F', m'_F)\delta_{F,e}\delta_{F',g}\right), \tag{E.8}$$

where $\delta_{i,j}$ is the Kronecker symbol.

From Eq. (E.8), we can compute matrix elements using the formalism of Chapter C with the generalized Rabi coupling Ω given by Eq. (C.27) and Eq. (C.28).

Diagonalizing the total Hamiltonian composed of diagonal elements given by $\langle F, m_F| H_{hfs} |F, m_F\rangle$ and off-diagonal elements given by $\langle F, m_F| H_{Stark} |F', m'_F\rangle$ leads to light shifts and new states for any field amplitude. To compute the light shift for far-off-resonance laser radiations, the counter-rotating term of the atom-field interaction has to be included. As both terms oscillate rapidly compared to each other, both light shifts computed independently from each other can be added after their respective diagonalization in their own rotating-frame.

E.1.2.3 Light shifts at 1529 nm for ^{87}Rb

In this section we compute the light shifts for the state $5P_{3/2}$ of ^{87}Rb. The dipole moments for all transitions of ^{87}Rb can be found in (Arora and Sahoo, 2019), (Arora, Safronova, and Clark, 2007) where they take the convention (Steck, 2001) $(J_g \mid \mathbf{d} \mid J_e)$ for the dipole matrix elements. This means that to be consistent with our equations we have $\langle J_g| \mid \mathbf{d} \mid |J_e\rangle = (J_g \mid \mathbf{d} \mid J_e)/\sqrt{2J_g+1}$.

To numerically compute the lights shifts of the state $5P_{3/2}$ with a laser at exactly 1529.36098 nm, the following states are included for the diagonalization: $5S_{1/2}$, $5P_{1/2}$, $5P_{3/2}$, $6P_{1/2}$,

[1]For instance $\mathbf{I}^2 |n\rangle = \hbar^2 I(I+1) |n\rangle$ and so on (Steck, 2019).

$4D_{3/2}$ and $4D_{5/2}$. The main transitions that contribute to the light shifts are $5P_{3/2}$ to $4D_{5/2}$ at 1529.366 nm with dipole moment of 10.899 ea_0 and $5P_{3/2}$ to $4D_{3/2}$ at 1529.262 nm with dipole moment of 3.628 ea_0 where e the electron charge and a_0 the Bohr radius. A laser wavelength of $\lambda = 1529.36098$ nm means that the laser is at about $\Delta\lambda = \lambda - \lambda_0 = -5$ pm from the transition $5P_{3/2}$ to $4D_{5/2}$ at $\lambda_0 = 1529.366$ nm between the fine structure states. In frequency unit it corresponds to $\nu - \nu_0 = -c\Delta\lambda/\lambda\lambda_0 = 0.6$ GHz.

To compare the diagonalization method and the weak field approximation given by Eq. (E.4), we vary the 1529 beam intensity for a linear polarization with a wavelength of 1529.36098 nm and we plot the light shifts of the states $F_e = 1, 2, 3$ of $5P_{3/2}$ on Fig. E.4 where we fixed the vertical axis to emphasize the hyperfine state dependency on the light shift. We plotted only negative m_F states as for a linear polarization, the lights shifts are symmetric. The hyperfine splittings at zero intensity have been subtracted from all curves to compare them. We see that both methods agree as expected in the low field limit for shifts smaller than hyperfine splittings (100 MHz scale) but deviate at high intensities

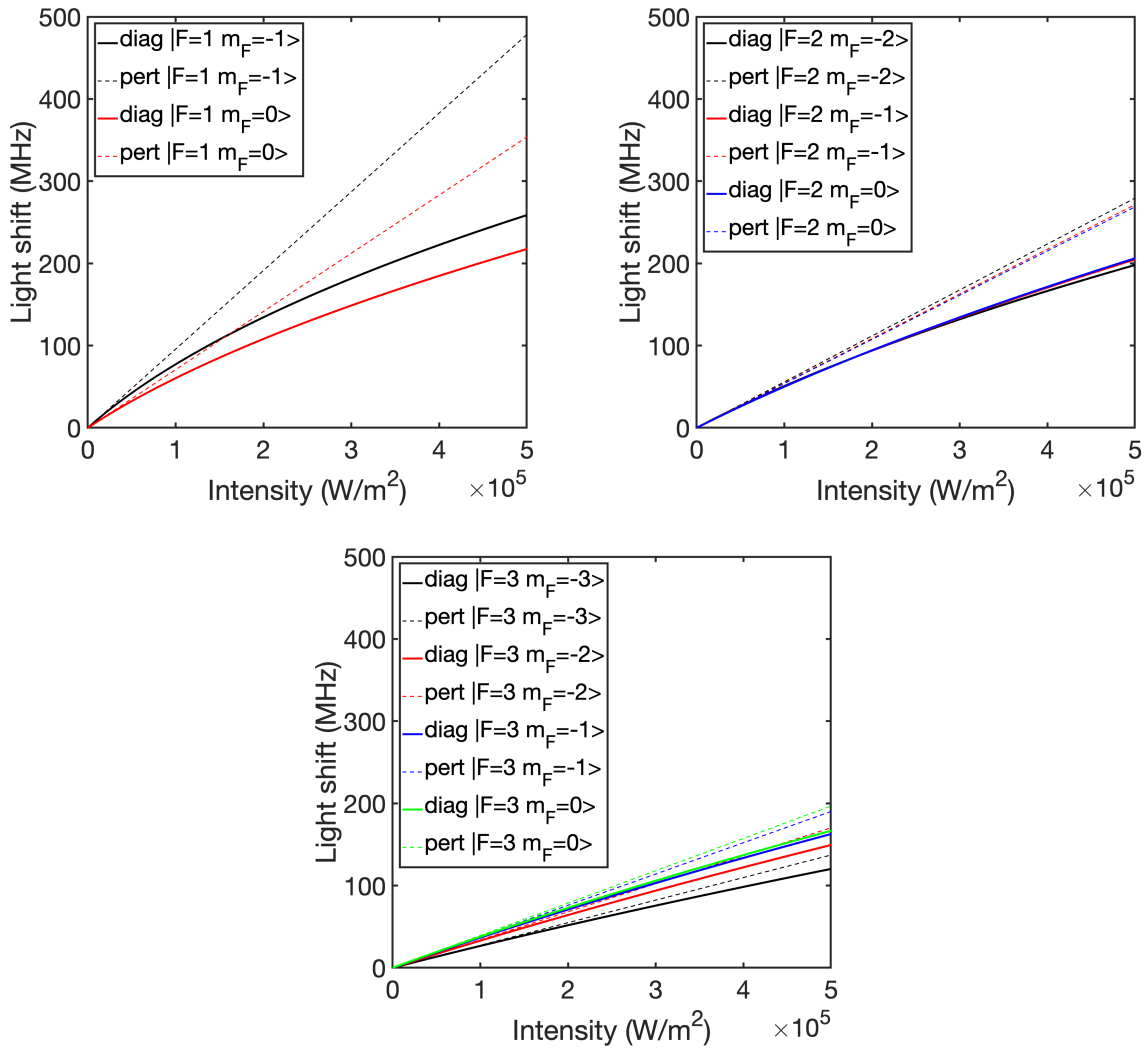

Figure E.4: Light shifts for a linearly polarized 1529.36098 nm laser for the states $F = 1$, $F = 2$ and $F = 3$ of $5P_{3/2}$ vs. the 1529 intensity. Solid lines are the diagonalization ('diag') of the full Hamiltonian and dashed lines the perturbation theory ('pert'). All energies are referred to the hyperfine shift of the particular state considered.

It is easier to describe the spatially repumped fraction in the low field approximation as the hyperfine states will not mix. Experimentally, we will work with detunings in $\pm[5, 10]$ pm from the main transition. Light shifts will be up to 100 to 150 MHz for $F = 2$ (section E.3.1.2).

Finally, as we are close to resonance, a small 1529 intensity is required to get large light shifts for the excited state while the shift on the ground state $5S_{1/2}$ is negligible. For instance, typical experiments presented in this thesis have the following parameters: a 1529 maximum power of 10 mW per beam, a typical waist of 150 µm, and a linear polarization. This gives a maximum intensity for a single beam of $2.83.10^5$ W/m^2. For a 1529 lattice, it would be 4 times the intensity of a single beam so $11.32.10^5$ W/m^2. This gives a total light shift of about 300 MHz on the state $|F_e = 2\rangle$ of $5P_{3/2}$. Using a far-detuned dipole trap (Eq. (A.4.2)), we get a light shift for a single 1529 beam on the state $5S_{1/2}$ of 0.5 kHz and 4 kHz for a 1529 lattice. It is negligible compared to 1064 dipole trap depths which are about 100 kHz for all measurements. This high value of the dipole trap depth is required to keep the atoms within the depth-of-field of our microscope objective.

For completeness, in Fig. E.5 we show the energy levels of $F = 0, 1, 2, 3$ of $5P_{3/2}$ vs. the 1529 intensity. At large intensities, the eigenstates tend towards two groups of states that correspond to the fine structure basis.

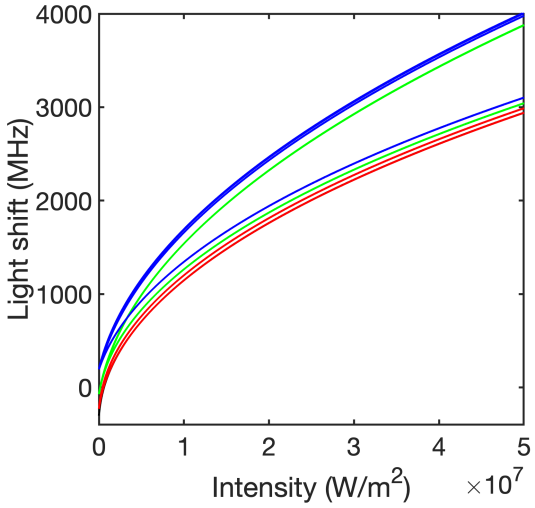

Figure E.5: Light shifts at the laser frequency of 1529.36098 nm for all states of $F = 0$ (black), $F = 1$ (red), $F = 2$ (green) and $F = 3$ (blue) of $5P_{3/2}$ vs. the 1529 intensity. All curves start at their hyperfine shift at zero intensity and referred to the fine structure energy. The black curve is at the bottom, very close to the first red curve.

Knowing the energy shifts, we will now evaluate the spatial resolutions that can be achieved.

E.1.3 Expected theoretical spatial resolutions

We consider a sinusoidal 1529 nm intensity profile of the 1529 nm light shift of one the hyperfine levels of the $5P_{3/2}$ manifold:

$$U_{5P}(x) = -\frac{\Delta\omega_{1529}}{2}\left(1+\cos\left(2\pi\frac{x}{i_{1529}}\right)\right), \tag{E.9}$$

where $\Delta\omega_{1529}$ is the total light shift amplitude and i_{1529} the period of the 1529 nm lattice and both correspond to notations of Fig. E.1. This light shift detunes the 780 nm laser from resonance such that the total detuning is:

$$\Delta(x) = \Delta_{780} - U_{5P}(x), \tag{E.10}$$

where $\Delta_{780} = \omega_{780} - \omega_0$.

The detuning of Eq. (F.4) will give us analytical expressions for the spatial resolutions of 4 cases for a two-level system (TLS) and a three-level system (3LS) as shown on Fig. E.6: 2LS with a 780 nm laser tuned at the A) bottom B) middle and 3LS with a 780 nm laser tuned at the C) bottom D) middle.

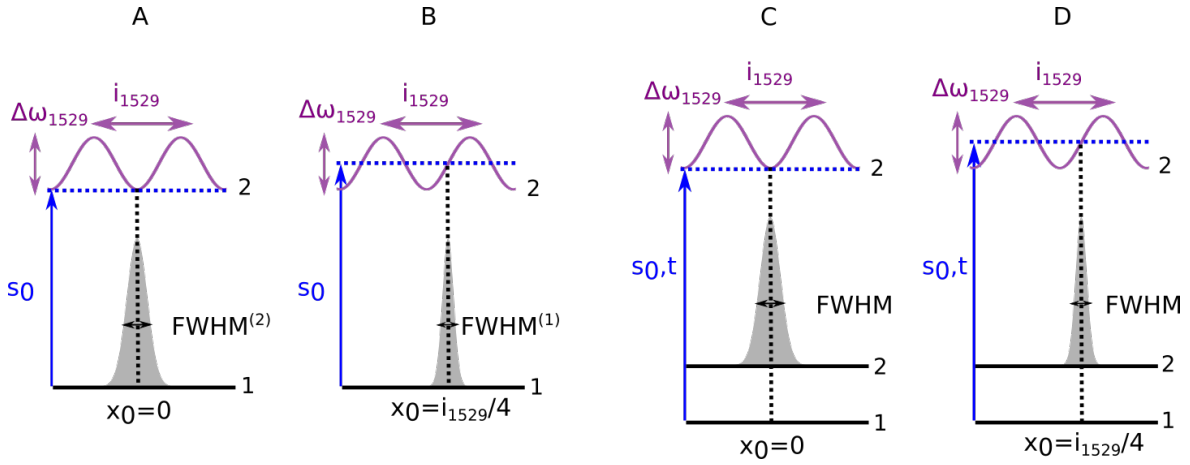

Figure E.6: Representation of FWHMs for a 2LS with a 780 nm laser tuned at the A) bottom B) middle and a 3LS with a 780 nm laser tuned at the C) bottom D) middle.

E.1.3.1 Full width at half maximum of a TLS

The spatial resolution for an ideal TLS with atomic frequency ω_0 is determined by the spatially dependent scattering rate which is itself given by the excited state population at steady-state (Eq. (C.7)):

$$\rho_{ee}(x) = \frac{s_0}{2}\frac{1}{1+s_0+4\left(\frac{\Delta(x)}{\Gamma}\right)^2}, \tag{E.11}$$

where s_0 is the saturation parameter for the 780 laser.

We expand in series up to the second order in x and for a resonant position at x_0 the detuning of Eq. (F.4):

$$\Delta(x) = \Delta(x_0) + \frac{d\Delta}{dx}(x_0)(x-x_0) + \frac{1}{2}\frac{d^2\Delta}{dx^2}(x_0)(x-x_0)^2. \tag{E.12}$$

The first and second spatial derivatives of Eq. (E.9) are:

$$\begin{aligned}\frac{d\Delta(x)}{dx} &= -\frac{\Delta\omega_{1529}}{2}\frac{2\pi}{i_{1529}}\sin\left(2\pi\frac{x}{i_{1529}}\right),\\ \frac{d^2\Delta(x)}{dx^2} &= -\frac{\Delta\omega_{1529}}{2}\left(\frac{2\pi}{i_{1529}}\right)^2\cos\left(2\pi\frac{x}{i_{1529}}\right).\end{aligned} \tag{E.13}$$

In the following, we consider the two limit cases: the 780 laser is tuned either at the bottom or at the middle of the lattice modulation (see Fig. E.6).

At the bottom of the modulation : It corresponds to the case $x_0 = 0$ where the first derivative is zero (Fig. E.6 A). The shift of Eq. (E.12) is quadratic such that $\Delta(x) = \Delta(x_0) - \Gamma\left(x/\Gamma_x^{(2)}\right)^2$ with the characteristic spatial width:

$$\Gamma_x^{(2)} = \sqrt{\frac{\Gamma}{\Delta\omega_{1529}}}\frac{i_{1529}}{\pi}. \tag{E.14}$$

For the resonant case where $\Delta(x_0) = 0$, the excited state population is:

$$\rho_{ee}(x) = \frac{s_0}{2}\frac{1}{1 + s_0 + 4\left(\frac{x}{\Gamma_x^{(2)}}\right)^4}. \tag{E.15}$$

The full width at half maximum (FWHM) of Eq. (E.15) is given by:

$$FWHM^{(2)} = \sqrt{2}\Gamma_x^{(2)}\left(1 + s_0\right)^{1/4}, \tag{E.16}$$

and in the limit $s_0 \ll 1$ it tends to $FWHM^{(2)} = \sqrt{2}\Gamma_x^{(2)}$.

Also, the total excited state population f_{ee} in the fringe at x_0 is defined as the integral of Eq. (E.15) from $-\infty$ to $+\infty$ and reads:

$$f_{ee} = \frac{s_0}{2\sqrt{s_0 + 1}^{3/2}}\frac{\pi\Gamma_x^{(2)}}{2}, \tag{E.17}$$

where we have neglected the population from neighboring fringes.

Eq. (E.17) shows that the total excited state population f_{ee} is proportional to a fringe width $\Gamma_x^{(2)}$.

At the middle of the modulation : It corresponds to the case $x_0 = i_{1529}/4$ where the second derivative is zero (Fig. E.6 B). The shift of Eq. (E.12) is linear such that $\Delta(x) = \Delta(x_0) - \Gamma(x - i_{1529}/4)/\Gamma_x^{(1)}$ with the characteristic spatial width given by:

$$\Gamma_x^{(1)} = \frac{\Gamma}{\Delta\omega_{1529}}\frac{i_{1529}}{\pi}. \tag{E.18}$$

For the resonant case where $\Delta(x_0) = 0$, the excited state population for a fringe at x_0 is:

$$\rho_{ee}(x) = \frac{s_0}{2} \frac{1}{1 + s_0 + 4\left(\frac{(x - i_{1529}/4)}{\Gamma_x^{(1)}}\right)^2}. \tag{E.19}$$

The FWHM of Eq. (E.19) is given by:

$$FWHM^{(1)} = \Gamma_x^{(1)} (1 + s_0)^{1/2}. \tag{E.20}$$

Similarly to the bottom case, the total excited state population f_{ee} in the fringe at x_0 is defined as the integral of Eq. (E.19) from $-\infty$ to $+\infty$:

$$f_{ee} = \frac{s_0}{2\sqrt{s_0 + 1}} \frac{\pi \Gamma_x^{(1)}}{2}, \tag{E.21}$$

where we have neglected the population from neighboring fringes.

In this case, Eq. (E.21) also shows that the total excited state population f_{ee} is proportional to a fringe width $\Gamma_x^{(1)}$.

To conclude, we have found expressions for the full width at half maximum that characterizes a perfect TLS such as a cycling transition for the cases where the 780 nm laser is tuned at the bottom of the light shift or at the middle of it (maximal resolution).

E.1.3.2 Full width at half maximum of a 3LS

Now we consider the case of a repumper transition that we first model as a three-level system (3LS). Based on the density matrix solution of the master equation, we found in section C.6 the evolution of the populations as a function of time. Applied to the ground $5S_{1/2}$ and excited $5P_{3/2}$ states of ^{87}Rb, the states in Fig. C.14 correspond to $|1\rangle \leftrightarrow |F_g = 1, m_F = -1\rangle$, $|2\rangle \leftrightarrow |F_g = 2, m_F = -1\rangle$ and $|2'\rangle \leftrightarrow |F_e = 2, m_F = -1\rangle$.

We consider the situation where all atoms are initially prepared into $|1\rangle$. In the low saturation limit for the repumper laser such that $s_0 \ll 1$, we found that the repumped fraction in the state $|2\rangle$ was given by Eq. (C.63) for a three-level system (3LS):

$$\rho_{22}(x) = 1 - e^{-c_{2'2}\Gamma t \frac{s_0}{2} \frac{1}{1 + s_0 + 4\Delta^2(x)}}, \tag{E.22}$$

where we remind that $c_{2'2}$ is the coupling ratio for spontaneous emission from $|2'\rangle$ to $|2\rangle$.

For long pulse durations verifying $s_0 \Gamma t \gg 1$ and for well-resolved fringes such that $\Gamma / \Delta\omega_{1529} \ll 1$, we can compute the full width at half maximum using the 3LS model of Eq. (E.22) and a sinusoidal detuning given by Eq. (F.4).

At the bottom of the modulation : It corresponds to Fig. E.6 C where the full-width at half maximum is:

$$FWHM = \sqrt{2} \Gamma_x^{(2)} \left(\frac{c_{2'2} \Gamma s_0 t}{2 \ln(2)}\right)^{1/4}. \tag{E.23}$$

At the middle of the modulation : It corresponds to Fig. E.6 D where the full width at half maximum is:

$$FWHM = \Gamma_x^{(1)} \left(\frac{c_{2'2}\Gamma s_0 t}{2\ln(2)} \right)^{1/2}. \tag{E.24}$$

The formulas above describe with a very good precision the expected full width at half maximum. They directly show scaling laws in terms of the light shift amplitude, the saturation parameter, and pulse duration for a repumper laser.

Similarly to the TLS model of section E.1.3.1, the total repumped fraction f_{22} per unit of interfringe is defined as :

$$f_{22} = \frac{1}{i_{1529}} \int_0^{i_{1529}} \rho_{22}(x)dx. \tag{E.25}$$

This quantity is physically proportional to the total number of atoms transferred into the state $|2\rangle$. In section E.3 it will be compared with experimental atom numbers measured by absorption imaging. If both atom numbers are equal, it means that $\rho_{22}(x)$ has been properly evaluated. At first order[2] $f_{22} \propto FWHM$, then measuring an atom number lead to measuring subwavelength spatial resolutions.

E.1.3.3 Numerical applications for TLS, 3LS and 5LS

We compare the FWHM for the different models at the top and bottom of the modulation. For the TLS, we plot $\text{FWHM}^{(1)}$ and $\text{FWHM}^{(2)}$ which are the best resolutions that can be achieved. For the 3LS, we plot the expressions (E.23) and (E.24). We also compute the FWHM for the 3LS and 5LS that are numerically computed from the full expressions of Eq. (C.61) (3LS) and Eq. (C.65) (5LS) without approximation. FWHMs are computed from the minimum and maximum values of the repumped fraction.

In addition to the levels of the 3LS model, the five-level system (5LS) takes into account the possibility to decay into other ground states that are not coupled to the repumper. All these possible decay channels are summarised by a decay towards a 'trash' state $|3\rangle \equiv |F_g = 1, m_F \neq -1\rangle$. This 'trash' state reduces the maximum value of the repumped fraction into $|2\rangle$. Also, the model takes into account the excited state $|1'\rangle \equiv |F_e = 1, m_F \neq -1\rangle$ for which the light can couple to when the light shift of the state $|1'\rangle$ is on the order of the hyperfine splitting between $|1'\rangle$ and $|2'\rangle$ (about 26Γ).

We use the Clebsch-Gordan coefficients[3] to compute the repumped fractions for all transitions except for the decay of the 3LS model where we use $c_{22'} = 1/2$ which is equal to the sum of squares of all Clebsch-Gordan coefficients from $|2'\rangle$ to $|2\rangle$ or $|2'\rangle$ to $|1\rangle$. Indeed, we consider that any m_F state of $|2\rangle$ can be reached: it represents a total coupling strength of $1/2$.

We plot the repumped fractions and FWHM for all models for the bottom and middle cases. We used a lattice interfringe of 8.3 µm and a light shift ranging from 5 to 40 Γ for $|2\rangle$.

[2] We consider $c_{2'2}\Gamma t \frac{s_0}{2} \frac{1}{1+s_0+4\Delta^2(x)} \ll 1$ for simplicity.

[3] See Chapter C or Ref. (Steck, 2001).

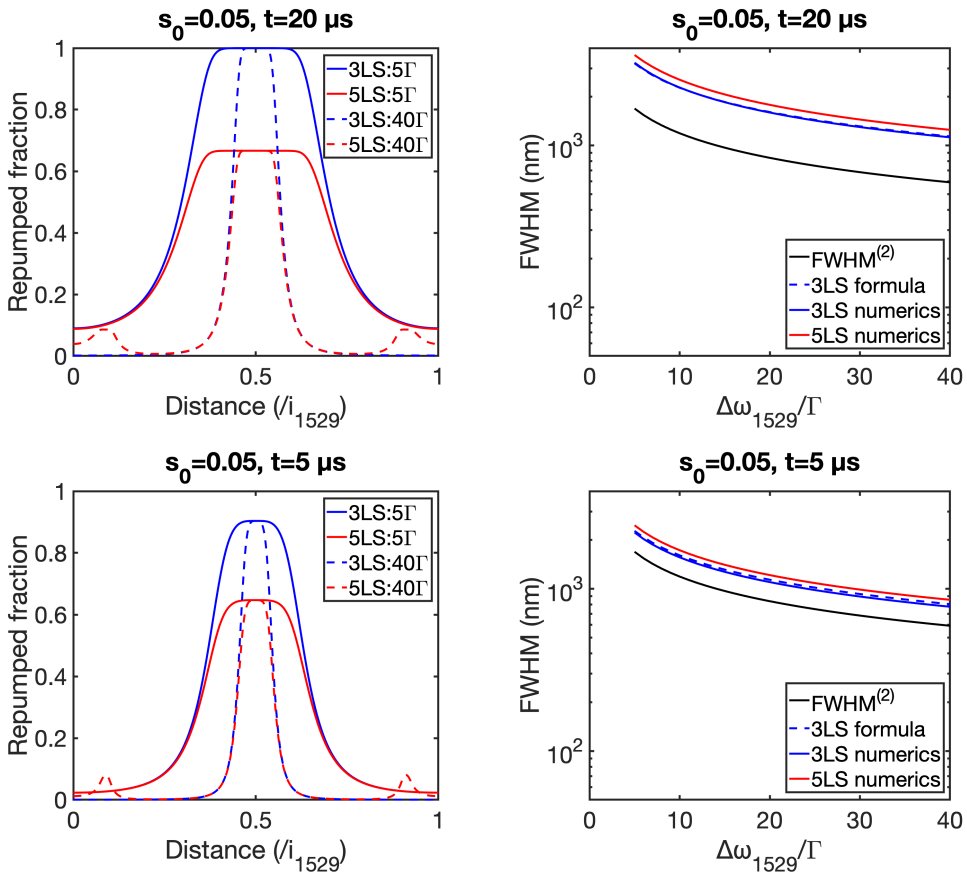

Figure E.7: Repumped fraction and FWHM for the repumper detuning tuned at the bottom of the modulation of $F_e = 2$ as a function of the light shift of $F_e = 2$. The modulation interfringe is 8.3 µm. We show them for a pulse duration of 5 µs and 20 µs.

For the bottom case, Fig. E.7 shows that the 5LS model has side peaks around the main one which correspond to the coupling to the top of the modulation of the excited state $|1'\rangle$. The light shift ratio[4] between $|2'\rangle$ and $|1'\rangle$ is equal to 0.7 which is obtained with the perturbation theory of section E.1.2.1 for a wavelength of 1529.35782 nm.

For the middle case as shown on Fig. E.8, spatial resolutions are really lower and can go down to 100 nm. This resolution is limited by the interfringe which sets a lower bound on the best achievable spatial resolution. We emphasize that the method is scale-invariant. If we achieve 100 nm resolution with a 8.3 µm lattice period, we could reach better than 10 nm for counter-propagating periods of $\lambda/2 \approx 765$ nm.

Both Fig. E.7 and E.8 show that as the pulse duration decreases from $t = 10$ µs to $t = 5$ µs, FWHMs tend towards the limit given by the TLS model given by Eq. (E.20) and (E.16).

As it could be expected from Clebsch-Gordan coefficients, we observe that the repumped fraction from the 5LS model saturates as it considers the worst case where some atoms go to a 'trash' state that does not contribute to the repumped fraction anymore. This picture is relevant if there is a differential light shift between m_F states much larger than Γ. However, this barely affects the achievable FWHM. Both the 3LS and the 5LS models

[4]This ratio depends on the value of the wavelength. Indeed in E.1.2.1 the ratio was 0.58 because it was computed with 1529.36098 nm.

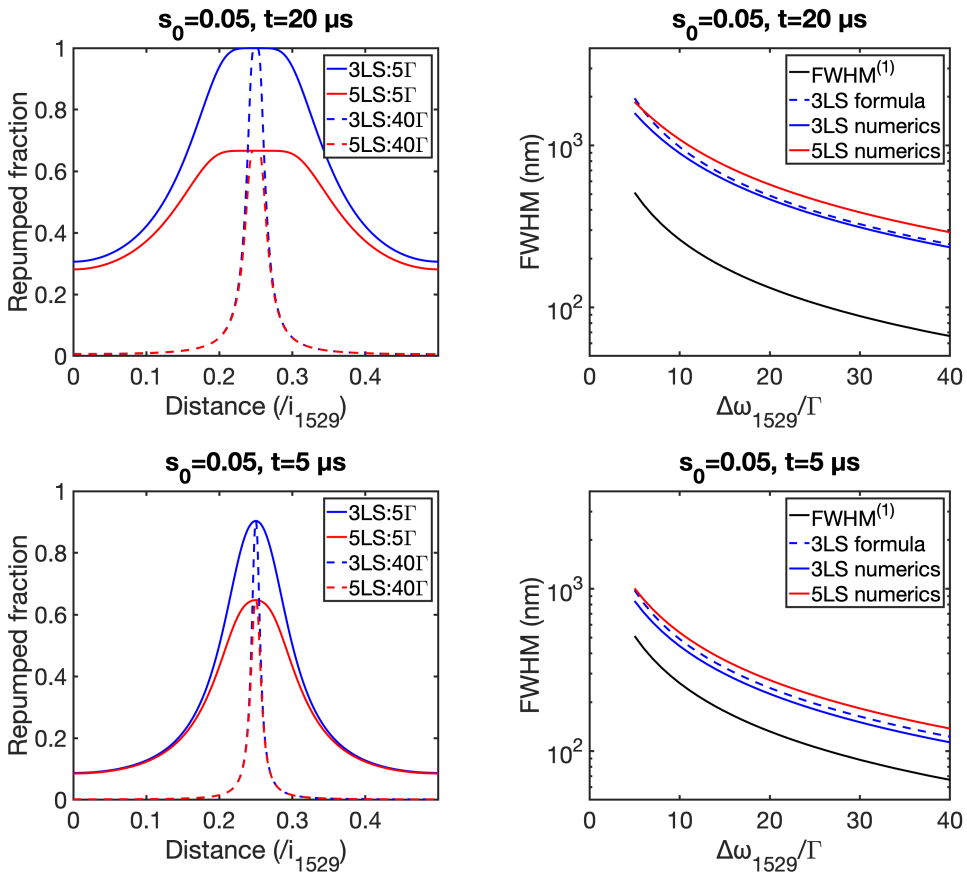

Figure E.8: Repumped fraction and FWHM for the repumper detuning tuned at the middle of the modulation of $F_e = 2$ as a function of the light shift of $F_e = 2$. The modulation interfringe is 8.3 µm. We show them for a pulse duration of 5 µs and 20 µs.

stay very close to each other. This means that the simple analytical formulas given by Eq. (E.23) and Eq. (E.24) describe quantitatively the FWHMs in all cases.

E.2 Experimental setup

Due to the diffraction limit of the imaging objective, subwavelength resolution widths cannot be directly spatially measured. In order to measure the values of the resolution predicted in the previous section, we will rather measure the integrated repumped fraction in a single fringe which is directly linked to the resolutions. As we have seen in E.1.3.2, the repumped fraction is proportional to the subwavelength resolutions.

In section E.2.1 we describe the 780 frequency tunable laser systems that were developed to address different parts of the light shift. We then detail in sections E.2.2, E.2.3 the experimental setup and its characterization to generate an optical lattice at 1529 nm and finally in section III.i comment on different issues that can occurs when imaging lattices with in situ absorption imaging.

E.2.1 780 repumper laser and 780 imaging laser

The 780 nm repumper optical bench that is dedicated to subwavelength imaging on the repumper transition can be tuned in frequency with a frequency beat note lock.

The free space optical setup is shown on Fig. E.9. The main laser is a free space laser diode VBG-780-0818-00124 in a butterfly package from Sacher Lasertechnik GmbH which can deliver 100 mW at maximum at 780.24 nm. It is locked in temperature and driven in current by a Koheron CTL200-1 driver[5]. The laser is single-mode with a current tunability of 0.3 GHz/mA. The free running laser has a measured linewidth of 1 MHz which is larger than the datasheet value of 100 kHz[6]. The impact of this large linewidth is a broadening of the repumped fraction for our subwavelength imaging method. However, it is small compared to Rb excited state linewidth as it is $<0.2\Gamma$.

The laser frequency is locked through a beat note with the Master laser of our Muquans system described in section B.2.2. The 'frequency/voltage converter' electronic circuit as described in Appendix II.iv is used to feedback the laser diode current to lock the repumper frequency. The tunability of the frequency lock is -108.12 MHz/V from -16Γ to +45Γ. As a result, this repumper laser is locked at the same frequency as the Master Muquans laser which is locked by saturated absorption onto the crossover of $F_e = 1$ and $F_e = 2$ of $5P_{3/2}$ of ^{87}Rb, i.e. at -78.5 MHz from $F_e = 2$.

An AOM shifts the frequency by -200 MHz. The diffracted order is coupled to a PM fiber outcoupled on the experiment. When the beat note is equal to 278.5 MHz, the laser is resonant with $F_e = 2$.

Depending on the performed experiment, the tunable repumper fibre is either outcoupled on the 'Imaging along DT1' collimator or on the 'Imaging along MOT' as shown on Fig. B.2. Both axis gives a linearly polarized beam along z at the atom position.

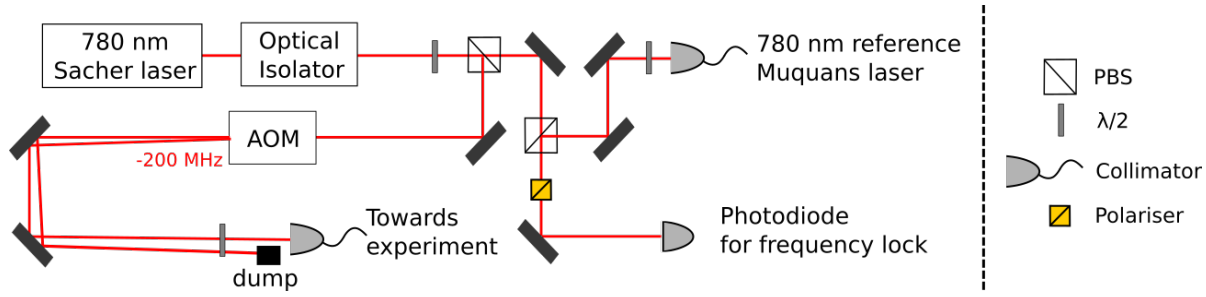

Figure E.9: 780 optical setup schematics for the frequency controlled repumper laser.

Finally, to interact with the cycling transition of ^{87}Rb, the 780 laser is Slave 2 from our Muquans laser as described in section B.2.2.

E.2.2 1529 nm laser

The 1529 nm laser is a distributed feedback laser[7] in a butterfly package from Emcore with a maximum output power of 100 mW at 1529 nm. It is controlled with a CTL200-2 current driver from Koheron which locks the temperature setpoint of the diode.

The laser has a PM fiber output which goes into a polarization-maintaining isolator (Advanced Fibre Resources), then a 10/90 polarization-maintaining fused coupler (Advanced Fibre Resources) where the 90% output goes onto a fiber-coupled 80 MHz AOM (Gooch

[5]It is controlled via the computer software Graphical User Interface from Koheron.

[6]We suspect that the laser itself has an issue as it has already been returned for repair due some optics that moved in the laser cavity which shifted the wavelength to 788 nm.

[7]Model: 1782 DWDM High Power CW Source Laser.

& Housego) which goes directly onto the collimator of the main experimental setup in Fig. B.2.

As shown on Fig. B.2, a monitoring photodiode has been set up to lock the 1529 power that we send onto the atoms using a homemade integrator circuit (Appendix II.iv) to feedback the AOM.

E.2.2.1 1529 resonance

The wavelength of the laser is tuned by varying the temperature setpoint (thermistor value). The absolute frequency is characterized by measuring the remaining atom number when a single 1529 beam is turned ON while the cloud is imaged on the cycling transition. The characterization is performed on a cloud smaller than the 1529 nm beam waists. Atoms are dressed by the 1529 nm radiation so the atomic transition is shifted by a light shift. Tuning a 780 nm imaging beam on resonance with the bare atomic transition, the atom number should decrease at the 1529 nm resonance. Fig E.10 gives a calibration curve for the position of the resonance for the cycling transition[8].

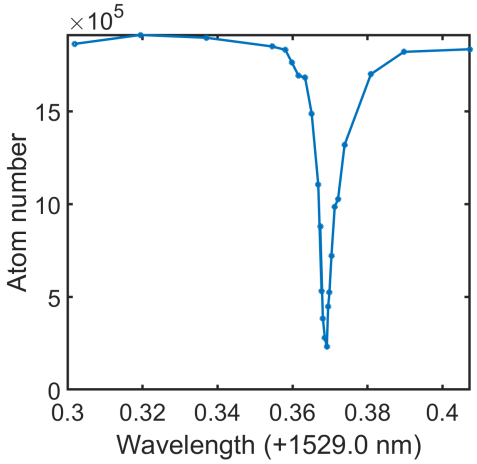

Figure E.10: Atom number vs. thermistor setpoint for a single 1529 nm beam during the imaging.

The resonance shown on Fig. E.10 corresponds the transition between $5P_{3/2}$ and $4D_{5/2}$. To refine the determination of the resonance position, the measurement can be carried either on the imaging cycling transition ($|F_g = 2\rangle$ to $|F_e = 3\rangle$) or on the repumper transition ($|F_g = 1\rangle$ to $|F_e = 2\rangle$). In each case, the exact position of the resonance depends on the hyperfine splittings of the states $5P_{3/2}$ and $4D_{5/2}$ that are given in Table E.1. Taken into account these shifts, the laser frequency can be characterized at the picometer level. The transition wavelength and the expected dip wavelengths are given in Table E.2.

E.2.2.2 1529 beam tomography

The 1529 beam waists are measured directly at the atom position using a tomographic method (Bertoldi et al., 2010). For that purpose, the 1529 nm beams are turned on during

[8]This value has to be re-calibrated about every 6 months because there are long term drifts as the wavelength is not locked. It has been checked by measuring the position of the resonance (13620 Ω) that it is stable during all measurements. The calibrated wavelength with a wavelength meter is $\lambda = 1529 + \left(-1.756 \times 10^{-4}(nm/\Omega)R + 2.760\ nm\right)$.

$5P_{3/2}$	$5D_{5/2}$
$F = 0 : -302.07$ MHz	$F = 1 : 90.83$ MHz
$F = 1 : -229.85$ MHz	$F = 2 : 54.01$ MHz
$F = 2 : -72.91$ MHz	$F = 3 : 1.9028$ MHz
$F = 3 : 193.74$ MHz	$F = 4 : -61.764$ MHz

Table E.1: Hyperfine splittings for the state of the transition at 1529.366 nm. The zero energies corresponds to fine structure states.

$5P_{3/2}$	$4D_{5/2}$	Transition wavelength (nm)	Expected dip wavelength (nm)
F=2	F=1	1529.3647 (uncoupled for π polarization)	
F=2	F=2	1529.3650	1529.3652(2)
F=2	F=3	1529.3654	
F=3	F=2	1529.3671 (uncoupled for π polarization)	
F=3	F=3	1529.3675	1529.3677(3)
F=3	F=4	1529.3680	

Table E.2: Transition wavelengths between hyperfine states from $F = 2, 3$ of $5P_{3/2}$ to all possible hyperfine states of $4D_{5/2}$.

the imaging step on the cycling transition. For a given 780 nm imaging beam detuning, atoms are imaged only at positions where the 780 nm is resonant with the excited state. Scanning the 780 nm detuning and measuring the resonant position is a direct image of the 1529 nm beam. We give an example on Fig. E.11 showing the results of a single 1529 nm beam tomography. A small initial cloud is prepared up to the last evaporation step in the magnetic trap. A TOF of 5 ms is used such that the cloud is spatially homogenous over the 1529 nm beam waist size. We fit the position of the resonant positions and plot it as a function of the 780 nm imaging detuning. The maximum light shift was chosen to stay in the validity domain of the perturbation theory. It is then linear with the 1529 nm intensity. Finally, the detuning vs. resonant positions is fitted with a Gaussian function where the amplitude, the central position, and waist are free parameters[9]. From Fig. E.11, we got a waist of 155 µm.

The 1529 nm optical setup had 2 versions over this PhD thesis that will be given in section E.2.3.1. For quantitative interpretations in the next sections, we will always state the calibrated waists. In the following, we will see that we can also calibrate experimentally the light shifts seen by the atoms for a 1529 lattice using a tomographic method that we will name as 'BAT' curves due to their 'BAT' shape.

E.2.3 Accordion lattice at 1529 nm

Now we describe the 1529 nm optical setup used to generate the 1529 nm lattices in two geometries: co-propagating or counter-propagating beam configurations.

E.2.3.1 Intensity profile and beam configurations

The optical setup for generating the 1529 nm lattice is shown in Fig. B.2. We show on Fig. E.12 the most recent setup which offers the possibility to dynamically change

[9]In theory the amplitude also depends on the waist and that could reduce fit parameters to only waist and position.

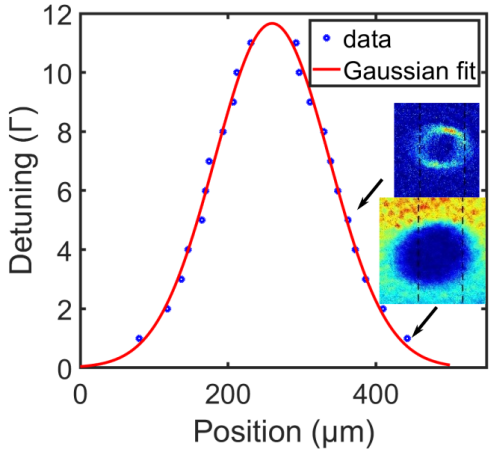

Figure E.11: Tomography of a 1529 nm beam by scanning a 780 nm probe detuning and measuring the positions where atoms are resonant (yellow regions). Blue data points are positions along the vertical direction on the raw images which show optical densities at two detunings. Images are taken using the imaging axis along DT1. The red solid line is a Gaussian fit to extract the waist.

the beam angle between the 1529 nm beams during the experiment. This is done using aspheric lenses that prevent the focus to move due to spherical aberrations when the angle is varied. In this PhD, we use this setup mainly at fixed angles.

The old version of the setup has been used to get the data presented in this Chapter. The setup was the same except that 2 mirrors mounted on a translation stage were replacing the 2 PBS and the translation stage in Fig. B.2. A PBS was separating the 1529 nm beam into two paths which were going towards each of the two mirrors. The lenses were achromatic doublets of 150 mm focal length. The position of the focus was not fixed when the angle was varied. This is the reason for updating the setup based on the work of (Ville et al., 2017).

Let us now compute the total intensity profile to describe the 1529 lattices for each beam configuration as depicted on Fig. E.12. The total intensity $I(\mathbf{r})$ of two plane waves with electric fields $E_1(\mathbf{r},t) = E_1(\mathbf{r})e^{i(\phi_1(\mathbf{r})-\omega t)}$ and $E_2(\mathbf{r},t) = E_2(\mathbf{r})e^{i(\phi_2(\mathbf{r})-\omega t)}$ is proportional to $|E_1+E_2|^2$ and reads:

$$I(\mathbf{r}) = I_1(\mathbf{r}) + I_2(\mathbf{r}) + 2\sqrt{I_1(\mathbf{r})I_2(\mathbf{r})}\cos(\phi(\mathbf{r})), \tag{E.26}$$

where $I_1(\mathbf{r})$ and $I_2(\mathbf{r})$ are single beam Gaussian intensity profile. In the following, we consider the beam configuration depicted on Fig. E.12 where the main axis in red are dipole trap directions.

For beams separated by the full angle 2α, the phase term in Eq. (E.26) is :

$$\phi(\mathbf{r}) = 2\pi\frac{r}{i_{1529}}, \tag{E.27}$$

where $i_{1529} = \frac{\lambda}{2\sin(\alpha)}$ is the lattice interfringe and r the fringe direction.

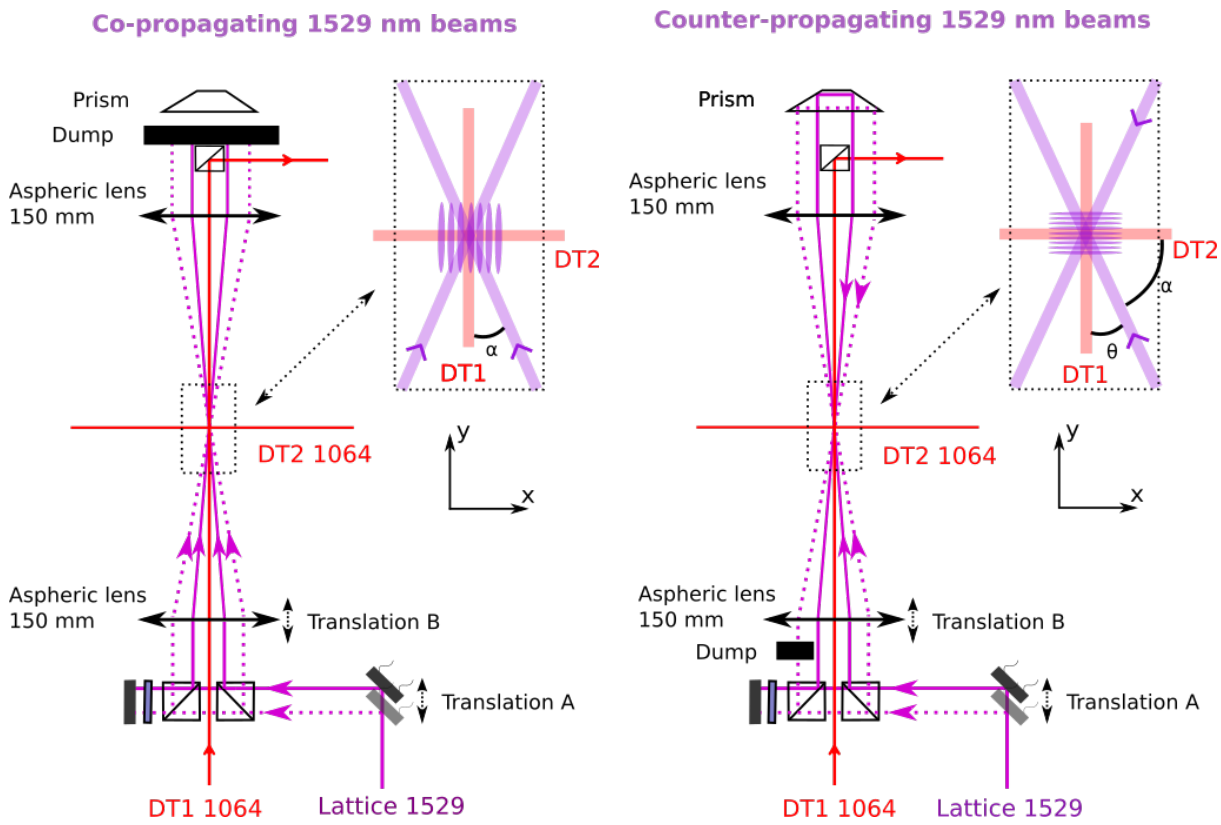

Figure E.12: Co- and counter-propagating 1529 beam configurations that can be realized on the experiment. DT1 and DT2 are dipole traps. All beams can be seen on the main experimental setup of Fig. B.2.

E.2.3.2 Co-propagating beam configuration

For two quasi co-propagating beams separated by the full angle 2α as shown on Fig. E.12, the interfringe is:

$$i_{1529} = \frac{\lambda}{2\sin(\alpha)}. \tag{E.28}$$

Beam parallelism : For the co-propagating case, one 1529 nm beam is aligned on the same path as DT1 by translating both PBS with a translation stage, whose motion is perpendicular to DT1, until DT1 passes through one of the cubes. The 1529 nm beam is then aligned onto DT1 with two mirrors. After that, the cubes are displaced again such that DT1 passes in-between both PBSs. Finally, the second 1529 nm beam is aligned directly in the focal plane by overlapping it with the first 1529 nm beam. This makes sure that both beams are parallel before the first 150 mm lens.

Beam focus : The focus is aligned by a translation stage along DT1 axis that moves both PBS at the same time. We use the fact that parallel beams before the 150 mm aspheric lens will focus at the same position after the lens. So we measure the position of a single beam for two different angles by moving the mirror before the PBS with the translation stage A depicted on Fig. E.12. The intersection point of the two clouds of the two images (*i.e.* two angles) gives the position of the focus. We show on Fig. E.13 the focus position for three values of the translation stage B that moves the 150 mm lens.

From this we find the focus position matching with DT1 for a translation stage around 1 mm.

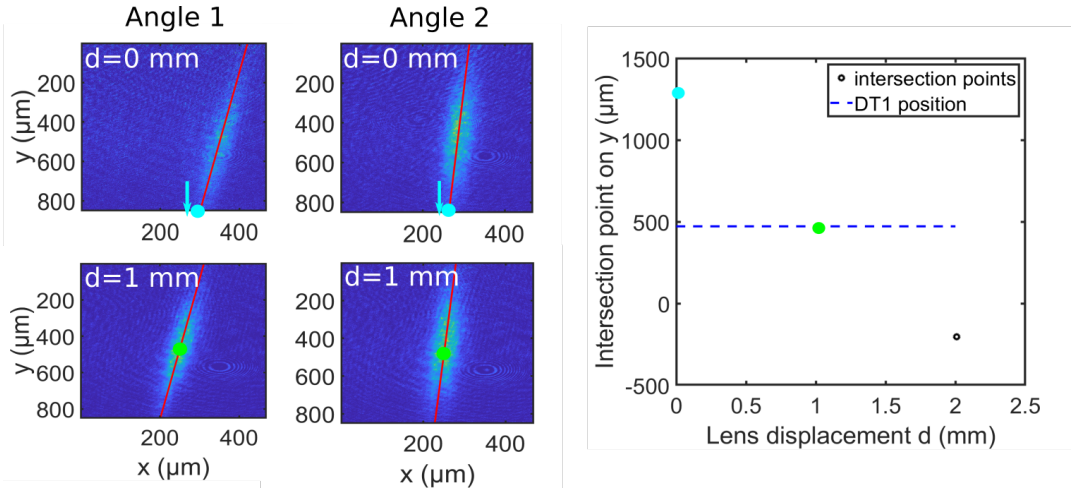

Figure E.13: Position of the 1529 focus as a function of the translation stage displacement which moves a 150 mm aspherical lens : The 4 images are in situ optical densities of the repumped cloud for a 780 nm repumper tuned at the top of the light shift, for two different angles and two lens displacements. Red solid lines are direction fits and filled circles are the positions of the expected focus position at the intersection of two red solid lines at the same lens displacement. Blue arrows indicate that intersection points are further on the images. The plot on the right is the intersection points vs. the lens displacement compared to the position of DT1.

Angle calibration : To calibrate our translation stage, we scan the angle and measure the interfringe by repumping atoms using the 1529 co-propagating lattice. For the calibration, we put 1529 beams with a light shift about 100 MHz with a repumper tuned on the top modulation of the lattice. Atoms are then imaged on resonance on the cycling transition. Fig. E.14 shows in situ 2D raw images of 1529 nm repumped layers that are then integrated along the y-direction. This integrated optical density is plotted as a function of the run number. The x-axis 'run number' is a linear scaling of the full travel range of the translation stage A. The translation stage is controlled with a piezo actuator[10]. For each run number, a Fourier transform gives the interfringe value and the half-angle is deduced from Eq. (E.28). The target angle indicates the translation stage position for imaging in a ground state lattice as discussed in Chapter F.

Lattice tomography : Experimentally, we measured tomographic images after a pulse of repumper at 780 nm. The images are taken in situ, on resonance, with the high NA imaging system on the cycling transition. The Talbot effect, described in Appendix III.i, can then lead to the observation of a lattice while the microscope focus is actually not well-adjusted. This can lead to wrong estimations of the integrated atom number. It needs to be corrected by moving the microscope objective or the camera to image the correct plane.

[10]New focus picomotor actuator 8302 with a step size of 30 nm controlled with the single-axis picomotor driver of model 8703. An external voltage generated by Cicero is applied to control the motion: in $\pm 1V$ the motor is at rest, +10V for clockwise motion and -10V for counter-clockwise motion.

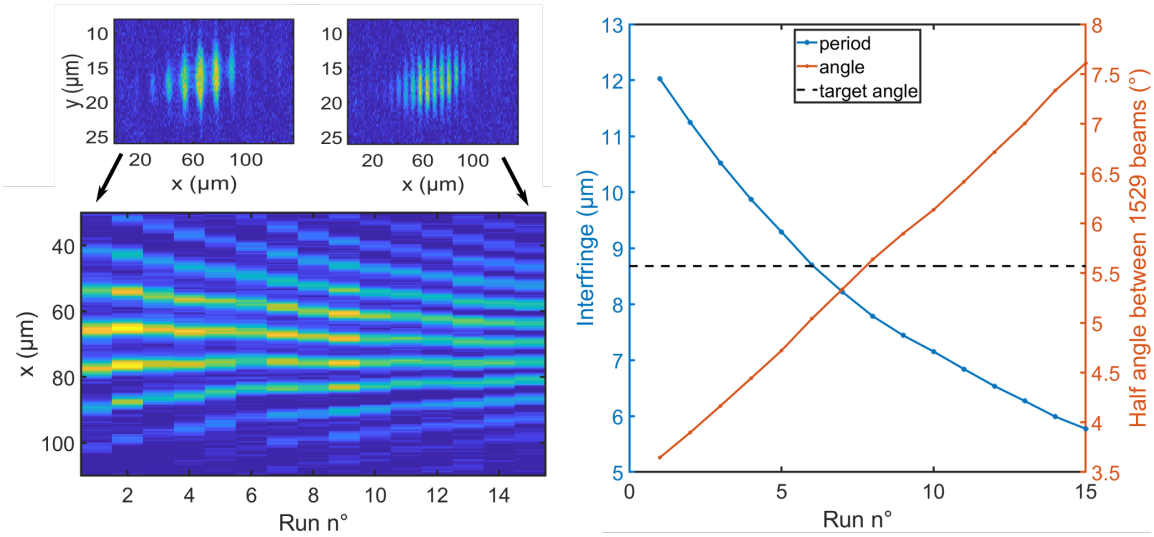

Figure E.14: Calibration of the co-propagating 1529 beam configuration: 2D raw optical density images (left) showing the 1529 repumped layers and integrated optical density along the y-direction as a function of the run number (equiv. translation stage values). Interfringe and half-angle (right) as a function of the run number.

The on-focus tomographic image of Fig. E.15 shows that the image intensity at the lattice top and bottom is higher than at the middle. This means that the 'volume' of repumped atoms at the middle is lower than at the extremities. Plotting this volume of atoms vs. the repumper detuning will lead to what we will call 'BAT' curves. In the following, we focus on counting the atom number for each repumper detuning and comparing it with what we expect from time-of-flight measurements.

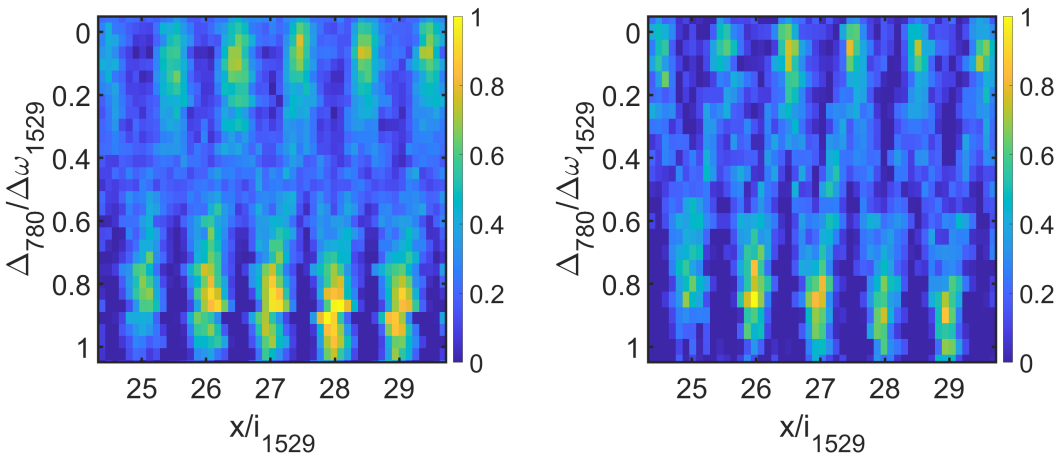

Figure E.15: Out-of-focus (left) and on-focus (right) in situ images of the integrated optical density profile as a function of the repumper detuning for a co-propagating 1529 lattice during a repumper pulse. For both images the conditions are similar, the light shift is 130 MHz. The colormap is normalized to the maximum value of the projected optical density and an area without atoms averages at 0.

E.2.3.3 Counter-propagating beam configuration

The experimental setup can also generate two quasi counter-propagating beams separated by the full angle $2\alpha = \pi - 2\theta$ as shown on Fig. E.12 where the interfringe is:

$$i_{1529} = \frac{\lambda}{2\cos(\theta)}. \tag{E.29}$$

Prism alignment : After aligning the co-propagating configuration, 1529 nm beams of the co-propagating configuration are retroreflected with the prism by retro-injecting them into the 1529 fiber input. A fiber circulator is used to maximize the re-injected power into the fiber. As in the co-propagating case, the light shift experienced by the atoms is used to finely calibrate the intensity. This is particularly important in this counter-propagating case as the returning beams are difficult to align onto the atoms because of the presence of the incoming beams (co-propagating beams) and their waists are difficult to evaluate.

In this configuration, the lattice sites are not individually resolved by the imaging system. The interfringe is on the order of $1529.366/2 \approx 765$ nm and our microscope PSF radius is about 1.3 µm.

E.3 Results on the repumper transition

E.3.1 Data in the co-propagating configuration

E.3.1.1 Experimental sequence

The experimental sequence is depicted on Fig. E.16 which starts after evaporating in a hybrid trap and just before gravity evaporation as discussed in section B.4.2.6. The first step in Fig. E.16 corresponds to gravity evaporation where the magnetic gradient is

reduced to zero in 400 ms.

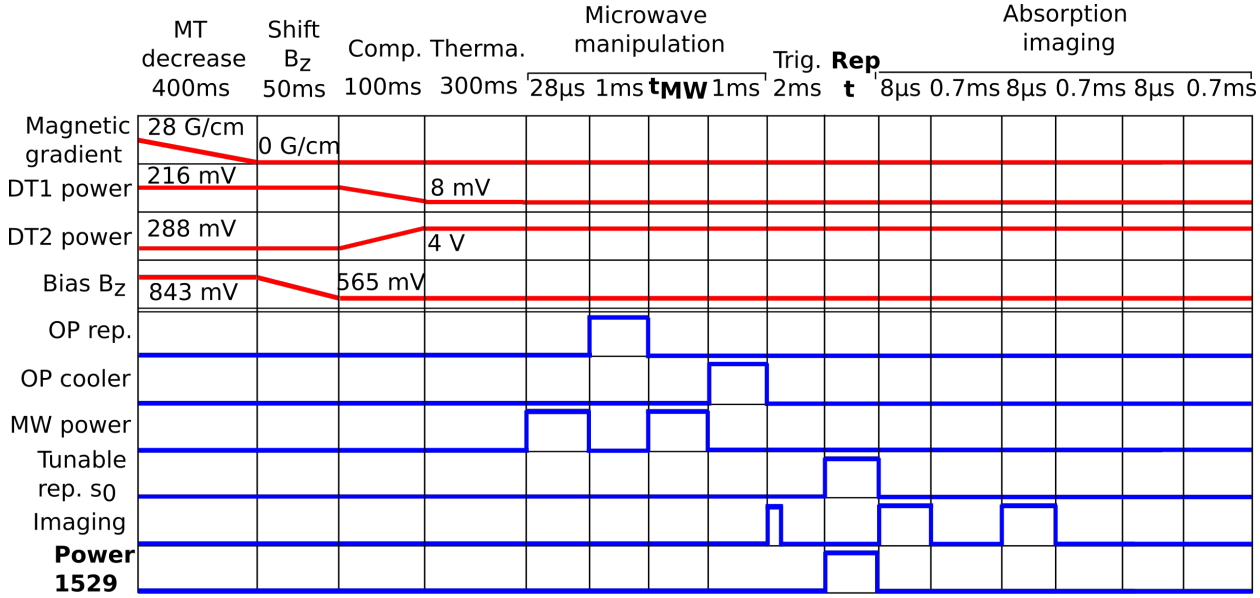

Figure E.16: Experimental sequence for evaluating subwavelength resolutions on the repumper transition. In red are analog channels and in blue TTL channels.

After ramping down the MT gradient, a magnetic bias of 280 mG is set along z. After that, DT2 is compressed and DT1 decreased to make a cigar shape atomic cloud. A thermalization time ensures that magnetic fields are stable. The atomic density is then homogeneous over a few 1529 fringes.

Then a first MW pulse ($t_{MW} = 28$ µs) is applied to transfer all atoms into $|F_g = 2, m_F = -2\rangle$ followed by a short optical repumper on the OP axis. The repumper pulse is here to make sure that the ground state $|F_g = 1, m_F = -1\rangle$ is empty.

After that, a second MW pulse of duration t_{MW} is used to transfer a controlled population back into $|F_g = 1, m_F = -1\rangle$. The transferred population in $|F_g = 1, m_F = -1\rangle$ is then given by $P(t_{MW}) = \sin^2(\pi t_{MW}/T_{MW})$ where the Rabi period is $T_{MW} = 28$ µs. The remaining atoms in $|F_g = 2, m_F = -2\rangle$ are pushed away with a cooler pulse on the OP axis (the retroreflection mirror being hidden with a mechanical shutter).

Then a first imaging pulse of 20 µs is sent to heat up the AOM of the imaging beam. On Fig. E.16, this step lasts 2 ms as there is a wait time used to transfer the first subimage of the Princeton camera used in kinetics mode on the high NA imaging axis. During this step, the imaging beam is frequency trigged to be shifted on resonance with the cycling transition.

The 1529 nm lattice beams are turned ON and a repumper pulse is sent along DT1 with a π polarization. We made sure that none of the pulses overlap.

The 1529 nm beams are in the co-propagating configuration with a measured interfringe of 8.3 µm. The waists were 131 and 138 µm, the power tunabilities with the power lock were 0.5848 mW/V and 0.5775 mW/V and the wavelength was 1529.35898 nm. With these powers and waists, a power lock value of 5V corresponds to a lattice peak intensity of $4.1.10^5$ W/m^2.

The repumper and imaging beam powers are acquired by a Red Pitaya. It is used to compute the exact saturations sent on the atoms. For the repumper transition, the saturation parameter s_0 includes the Clebsch-Gordan coefficient $-\sqrt{1/8}$ of the π-transition $|F_g = 1, m_F = -1\rangle$ to $|F_e = 2, m_F = -1\rangle$ which leads to a saturation intensity 6.67 mW/cm^2 computed using Eq. (C.50). The coefficient for the transition from $|F_g = 1, m_F = -1\rangle$ to $|F_e = 1, m_F = -1\rangle$ is $-\sqrt{5/24}$.

An image with atoms, a reference image of the imaging beam, and an image for the background are taken (with the frame transfer mode for the camera). These 3 images enables us to compute the transmission T and the optical density $b = -\alpha \ln(T) + s_{im}(1-T)$ where we assume that $\alpha = 1$ and the saturation parameter for the imaging beam is constant at $s_{im} = 1$. The atom number is then computed using the cross-section for a σ polarized light of $2.907.10^{-9}$ cm^2.

The cloud is a thermal gas which has been characterized by time-of-flights after the compression step by repumping all atoms and imaging them along DT1. After the MT decrease step, the cloud is thermal and it is compressed in 100 ms. The trap frequency along DT1 axis is about 20 Hz at the end which is slow compared to the ramp time so the atoms do not have time to thermalize. In low saturation and at low optical densities, after the compression step we measured a total atom number of $N_0 = 1.03(16).10^5$ and a temperature along the gravity direction of 169(10) nK. It is on the order of the critical temperature $T \approx T_c$.

We measured in situ the cloud widths by imaging the cloud without the 1529 nm beams at a short MW pulse of 2 µs. Due to the thermalization time, the measured Gaussian width along the long direction is $\sigma_x = 64$ µm. The transverse direction has been deconvolved with a Gaussian PSF of radius 1 µm giving a cloud width along y of $\sigma_y = 2.4$ µm. The maximum density at the cloud center using these Gaussian widths is $1.8.10^{19}$ at/m^3. This gives a central optical density of 31.4 at maximum when transferring the total atom number with a MW Rabi pulse of 28 µs.

To fully quantify the subwavelength volume that is transferred by this imaging method, in the next section, we will characterize the sensitivity of the method to the repumper duration t, the repumper saturation s_0, the repumper detuning Δ_{780} and the 1529 nm power. The saturation and duration of repumper have been chosen such that the photon scattering on the repumper transition varies from 1 to 10.

E.3.1.2 Results: BAT curves and resolution

The form of the 1529 nm lattice tomography in atom numbers looks like a 'BAT', so we name the curves $N(\Delta_{780})$ as 'BAT' curves.

BAT curves : To compare the data with theory, we use the 3LS model of section E.1.3.2 for the repumped fraction ρ_{22} and we assume a 3D Gaussian atomic density. The repumped atom number N in a width i_{1529} is given by:

$$N = \frac{P(t_{MW})N_0}{\sqrt{2\pi}\sigma_x} \int_0^{i_{1529}} \rho_{22}(x, s_0, t, \Delta_{780}, \Delta\omega_{1529})dx. \tag{E.30}$$

Scanning the repumper detuning for different light shifts gives a tomographic scan of the 1529 nm lattice as shown on Fig. E.17. Each scan has been averaged over only two

runs. Atom numbers have been integrated in a box having a width of 3 interfringes. The atom number N estimated using an on-resonance cross-section and normalized to one interfringe (the previous total atom number in 3 interfringes divided by 3) vs. the repumper detuning Δ_{780} are presented in Fig. E.17. For each scan, we know the initial atom number $P(t_{MW})N_0$, the cloud width σ_x along the long direction, the repumper pulse duration t and the value of the saturation parameter s_0 of repumper. As the 1529 nm trap depth increases, the number of atoms decreases. The center of a BAT has fewer atoms as the spatial extent where the atoms are resonant is narrower due to the strong variation of the light shift at the middle of the modulation. The influence of the saturation and duration is a broadening of the BAT curves.

The BAT curves are fitted with only two free parameters c_1, c_2 such that:

$$N = c_1 \frac{P(t_{MW})N_0}{\sqrt{2\pi}\sigma_x} \int_0^{i_{1529}} \rho_{22}(x, s_0, t, \Delta_{780}, c_2)dx, \tag{E.31}$$

where c_1 is an amplitude factor on the atom number[11] and c_2 the total light shift amplitude at 1529 nm of $|F_e = 2, m_F = -1\rangle$.

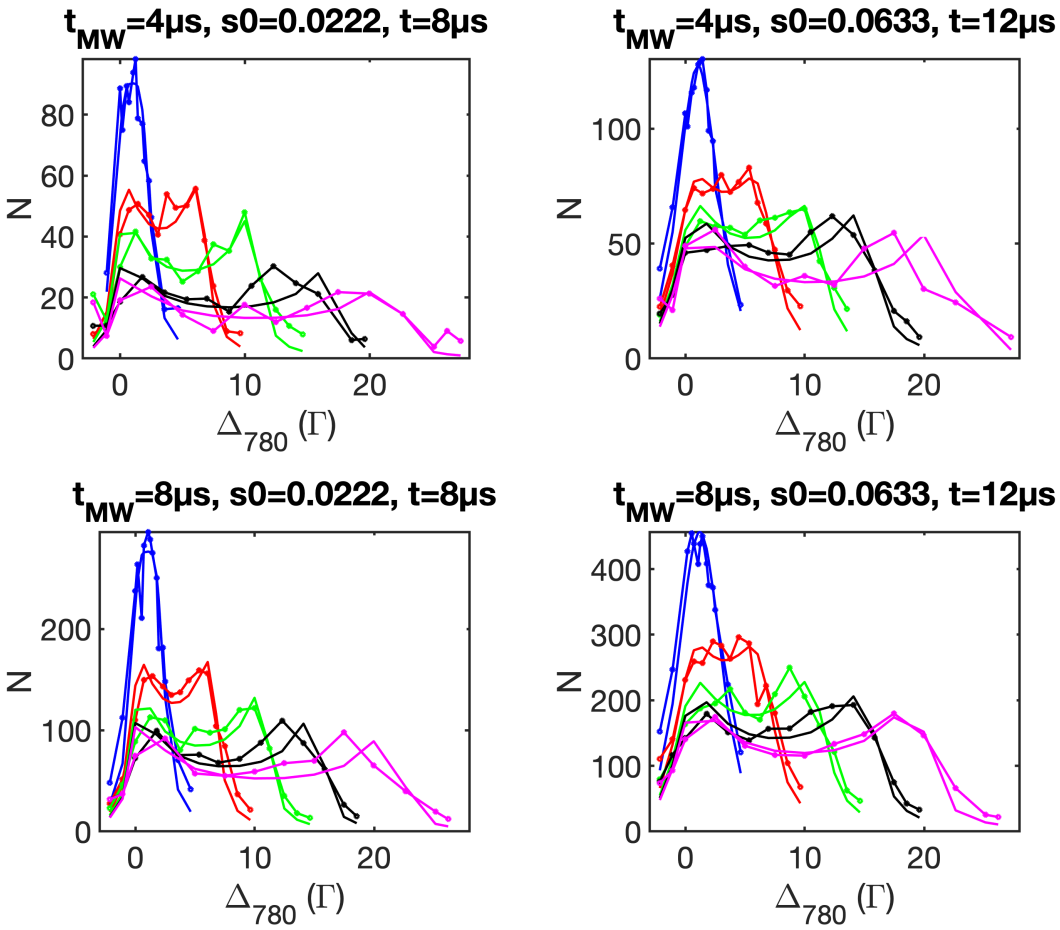

Figure E.17: BAT curves for the co-propagating case: number of atoms integrated in 1 interfringe vs. the repumper detuning. Within a plot, the curves from top to bottom correspond to powers per beam of: 0.29, 0.87, 1.45, 2.03 and 2.9 mW.

[11] We will see that it can be explained by a reduction of the single-atom scattering cross-section.

Solid lines without points of Fig. E.17 are fits with Eq. (E.31). The agreement is very good in general for only 2 free parameters. These two parameters are plotted on Fig. E.18.

For the light shift free parameter c_2, we also plotted the expected light shift based on the diagonalization of the full Hamiltonian of section E.1.2.2 using waists/detuning/powers of the 1529 nm beams previously given. The agreement is very good with no adjustable parameter which means that the spatial overlap between the 1529 nm beams is correct and the 1529 nm interference has a contrast close to 1. As a result, these BAT curves provide a way to quantitatively calibrate the excited state lattice depth. In section E.3.2, it will be used to calibrate the light shifts for the counter-propagating case where it is difficult to know exactly the waist and position of the returning beam.

For the amplitude factor, we see that as the 1529 power increases, all factors seem to tend linearly towards 1. At the shortest MW duration of 4 µs and the shortest repumper duration of 8 µs, the amplitude factor is constant and close to 1. Inversely, as the initial atom number increases with increasing t_{MW}, the correction factor decreases.

An explanation of the reduced amplitude is linked to Chapter D where the imaging reduction of the cross-section can occur as the optical density increases. Indeed, all factors are smaller than 1. This means that we measure, in situ, fewer atoms than what we expected. Either there are effectively less atoms, which is not consistent with all data, or the cross-section has been reduced. Also, we can expect that the rediffusion of photons from the imaging beam would decrease as the fringes get well-separated from each other. Also, the number of atoms is decreasing for larger light shifts so the optical density is decreasing. This can be for instance the observed behavior on Fig. E.18 where the amplitude factors tend towards 1 as the light shift is getting larger. We are going to focus on the middle of the modulation in the following for quantitative atom number measurements including the cross-section reduction.

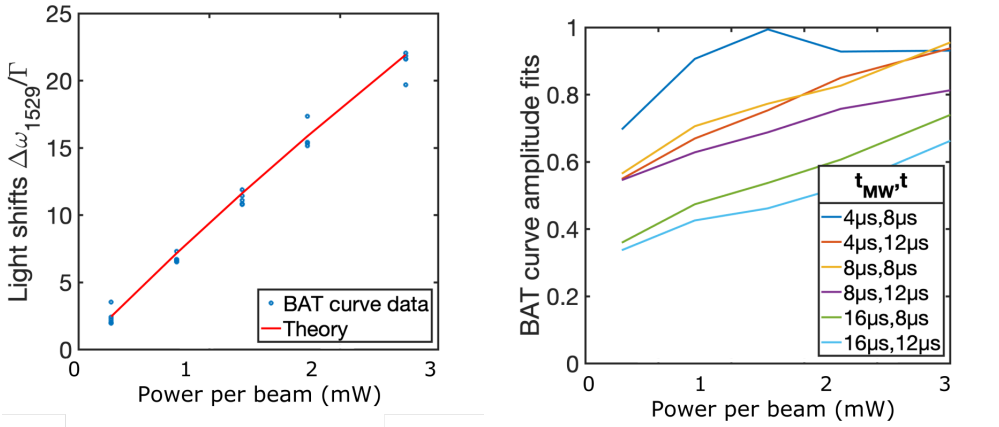

Figure E.18: The two fit parameters from the BAT curves in the co-propagating case with $i_{1529} = 8.3$ µm. Left: total light shift amplitude c_2 extracted from the fit (blue circles) and the expected theoretical light shift (red). Right: atom number scaling factor c_1.

Resolution at middle of the modulation : Finally the atom number is measured for a repumper tuned at the middle of the modulation *i.e.* $\Delta_{780} = \Delta\omega_{1529}/2$. It corresponds to the highest sensitivity situation. This sweep point will be characterized as a function of the 1529 nm light shift $\Delta\omega_{1529}$, repumper saturation intensity s_0 and MW pulse duration.

We repeat each measurement 10 times to average the atom number. We plot the atom number vs. the theoretical light shift on Fig. E.19 and the expected atom number from the 3LS and 5LS models without any free parameters using Eq. (E.30). Also we plot on the same graph the expected FWHM using Eq. (E.24).

In general, the analysis is similar to the BAT curve analysis: for the shortest MW pulse, the agreement is good but we cannot increase the light shift to values higher than 12Γ as we are in the detection limit of our absorption imaging system. We have to start with a larger atom number to be able to measure an atom number with a good signal to noise for larger light shifts. The drawback is that at small light shifts, we measure in situ a smaller atom number than expected which can be linked to a reduction of the cross-section.

We do the analysis of the experimental data but using the calibration of optical density effects of Chapter D for the cross-section reduction factor. We use $\alpha(b) = \alpha_0 + ab$ where $\alpha_0 = 1.1$, $a = 0.255$, and b is the usual optical density given by $b = -\alpha \ln(T) + s_0(1-T)$. Using these two expressions, we get the optical density reformulated as follows:

$$b = \frac{-\alpha_0 \ln(T) + s_0(1-T)}{1 + a\ln(T)}. \tag{E.32}$$

On Fig. E.19, the experimental atom number from the in situ imaging axis is computed either from Eq. (E.32) (black solid line) or with the usual optical density formula using $\alpha = 1$ (green solid line). The variation of the experimental atom number for low light shifts is much better after correcting with the expression $\alpha(b)$. This confirms the role of the cross-section reduction in optically dense regions.

Finally, for larger light shifts (40Γ), hyperfine states probably start to mix which would put in default the 5LS model as it assumes that eigenstates are hyperfine states. For such an intermediate range of light shifts, an improvement could be to include the effect of level mixing. However, this is probably just changing the repumped atom numbers by exciting more transitions. The resolution should however not change significantly.

The in situ measured atom number is consistent with the prediction from the repumped fraction (from the knowledge of $\rho_{22}(x)$). As a result, the repumped fraction can be trusted and its corresponding width (FWHM using Eq. (E.24)) demonstrates subwavelength spatial resolutions. Indeed, Fig. E.19 shows that a resolution of about 100 ($\lambda_{780}/8$) to 200 nm ($\lambda_{780}/4$) is achievable for light shifts between 20 and 40Γ with a lattice period of 8.3 µm which compares with theoretical models given in section E.1.3.2. Now we will see that in the counter-propagating 1529 nm configuration, the resolution is directly divided by 10 due to the lattice geometry having a period around 0.8 µm.

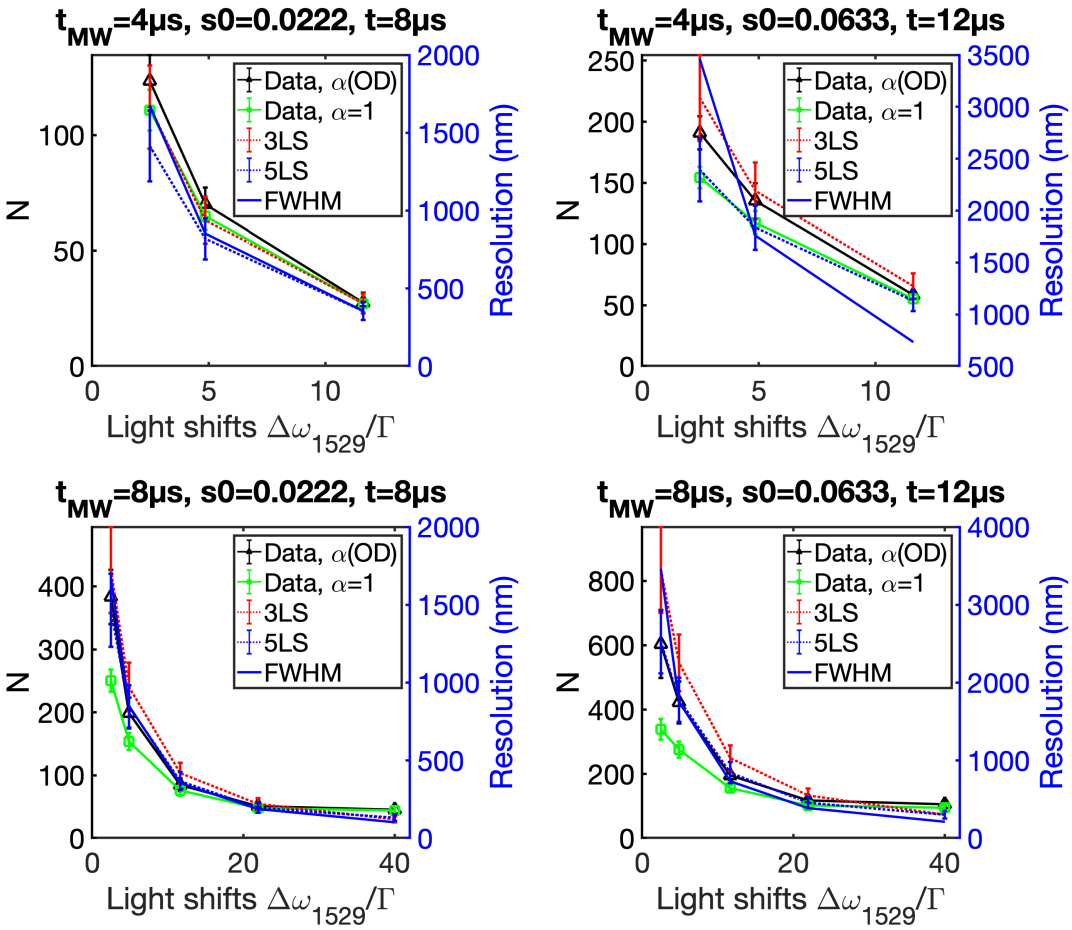

Figure E.19: Number of atoms at the middle of the modulation integrated in 1 interfringe in the co-propagating 1529 configuration: experimental data measured with the high NA imaging axis and 3LS and 5LS expectations for the total number of atoms in the cloud based on the total atom number measured by TOF. Error bars for each data point correspond to the average atom number over 10 realizations and error bars for TOF are from 14 realizations.

E.3.2 Data in the counter-propagating configuration

E.3.2.1 Experimental sequence

To evaluate the resolution using the counter-propagating 1529 nm lattice configuration with an interfringe of $i_{1529} = 0.77$ µm, we use a sequence similar to the one of the co-propagating case of Fig. E.16 except that now atoms are in DT1. The differences with respect to Fig. E.16 for this dataset are the following. The dipole trap DT1 is compressed such that the transverse width along y is $\sigma_y = 3.5$ µm and DT2 is decompressed and controls the width along x: $\sigma_x = 29$ µm. With time-of-flight measurements, we measured a temperature of 420 nK and an atom number of $N_0 = 1.5.10^5$. The camera used for absorption imaging on our high NA imaging axis is the Andor one used in normal mode. The rest of the sequence is the same as for the co-propagating case.

The datasets that we present in the following consist in measuring the atom number by varying the MW duration t_{MW}, the repumper saturation s_0 of duration t.

E.3.2.2 Results: BAT curves and resolution

We perform the same analysis as in section E.3.1.2 for the co-propagating case. The main difference being that the lattice interfringe is smaller than the resolution of our microscope. A measured interfringe of 0.768 µm has been deduced from the angle of the co-propagating case at the time of the measurement of 5.57° (it is not the one of section E.3.1.2).

We integrate the atom number in a box with a width of 11 fringes which corresponds exactly to 10 pixels where we assume that the atomic distribution is homogeneous. Then the total atom number is normalized to 1 interfringe.

On Fig. E.20 we show BAT curves for the counter-propagating case for a given MW pulse of 8 µs. Even if we don't resolve the lattice, we are still able to recover the BAT curve shapes in the atom number. The points are data points and the solid line are fits with Eq. (E.31). In this 1529 beam configuration, it is difficult to measure the waist and position of the returning beam onto the atoms[12]. That is why we use the measured light shifts from the BAT curves as a calibration for further analysis of the resolutions. The fit parameters, which are the light shift and amplitude factor, are plotted on Fig. E.21 and show the same behaviour as for the co-propagating case in section E.3.1.2.

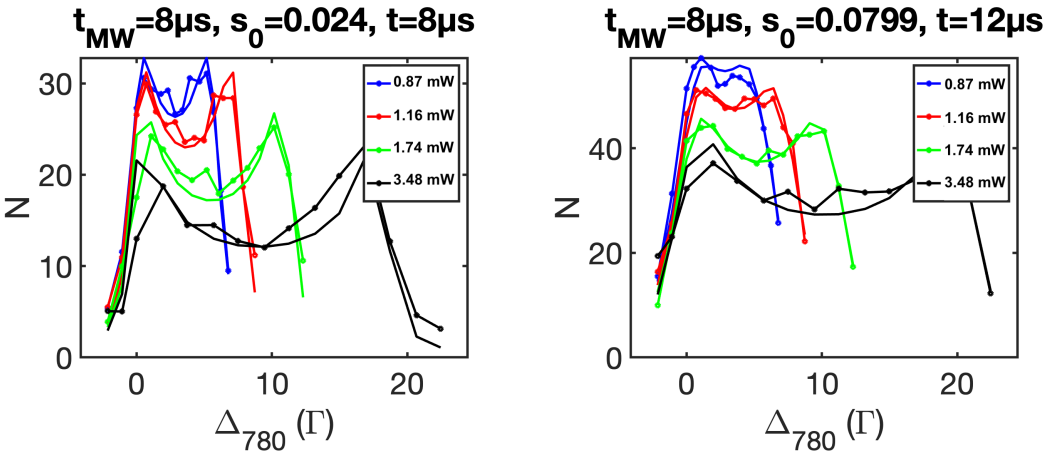

Figure E.20: BAT curves for the counter-propagating case: number of atoms integrated in 1 interfringe vs. the repumper detuning. The legend corresponds to the 1529 power setpoint with a conversion factor for the power per beam of 0.58 mW/V. Solid lines with points are experimental data and pure solid lines are fits using a 3LS model for the repumped fraction with two free parameters: a light shift and an atom number amplitude factor.

Finally, we measure the atom number where the repumper detuning is tuned always at the middle of the modulation i.e. $\Delta_{780} = \Delta\omega_{1529}/2$. We repeat each measurement 10 times to average the atom number over a large light shift range. We plot the atom number vs. the measured light shift on Fig. E.22 and the expected atom number from the 3LS and 5LS models without any free parameters using Eq. (E.30). We plot on the same graph the expected FWHM at the middle of the modulation using Eq. (E.24). We see that the full-width at half maximum goes down to 20 nm for a light shift of 20 Γ. The main

[12]The 1529 propagates towards the prism and goes back to the atoms. The traveled distance is not negligible compared to the Rayleigh range so the returning beam waist cannot be assumed equal to the incoming 1529 nm beams.

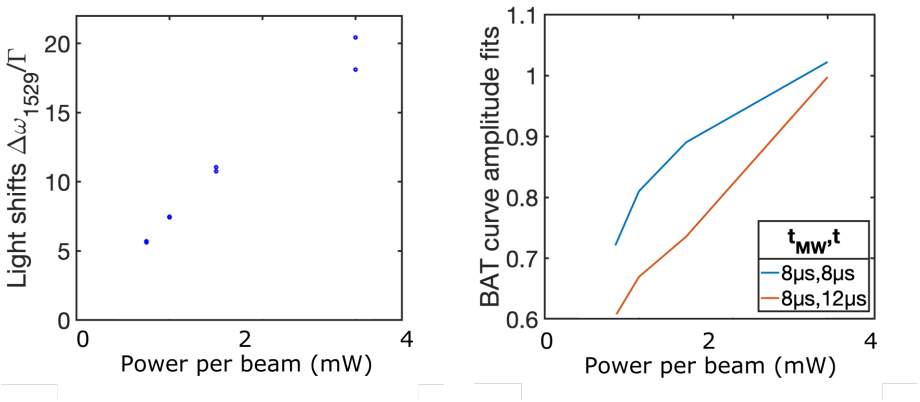

Figure E.21: The 2 fit parameters from the BAT curves in the counter-propagating case with $i_{1529} = 8.3$ µm. Left: total light shift amplitude extracted from the fit (blue circles). Right: atom number scaling factor.

limitation of this method is the atom number detection limit of our imaging system. We plotted the experimental atom number corrected from the cross-section reduction using Eq. (E.32) to compute the in situ optical density. Similarly to the co-propagating case, the experimental data are getting much closer to the time-of-flight expectations of the 5LS model.

As a conclusion, we saw that the full-width at half maximum is scalable with both co- and counter-propagating beam configurations and agrees quantitatively with the 3LS/5LS theoretical models for the case of a repumper transition.

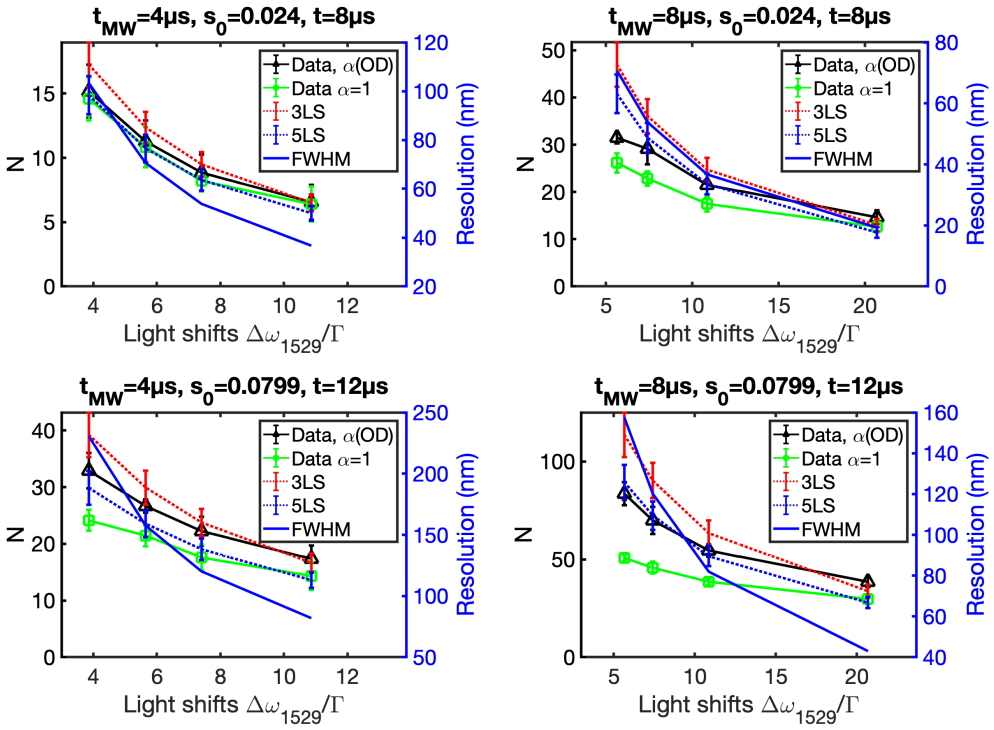

Figure E.22: Number of atoms at the middle of the modulation integrated in 1 interfringe in the counter-propagating 1529 configuration: experimental data measured with the high NA imaging axis and 3LS and 5LS expectations for the total number of atoms in the cloud based on the total atom number measured by TOF. Error bars for each data point correspond to the average atom number over 10 realizations and error bars for TOF are from 12 realizations.

E.4 Conclusion

In this chapter, in section E.1 we presented a new imaging technique for subwavelength imaging based on excited state dressing. It consists in using the optical transition at 1529 nm between the two first excited states of ^{87}Rb. The created light shift makes the transition at 780 nm between the ground state and the first excited spatially varying. In the region of strong light shift variations, the atom-light interaction is resonant in a subwavelength volume. Subwavelength widths directly link to the light shift amplitude. Light shifts have been computed in the perturbation theory and using a diagonalization to compute the exact shifts. The resulting subwavelength volumes have been theoretically computed from the three and five-level model given in Chapter C.

In section E.2, the optical setup for the 780 nm and 1529 nm lasers have been presented with their characterization. We gave the two geometries available on the experiment which are co- and counter-propagating 1529 nm beams. Finally, we showed that in situ images of an optical lattice with absorption imaging strongly depend on a fine alignment of our high numerical aperture microscope due to the Talbot effect.

In section E.3, we showed that on the repumper transition, expected subwavelength volumes match with experimental data by measuring atom numbers over a large range of parameters (saturation, duration, light shift). The limitations are mainly due to the atom number sensitivity, about 50 atoms, which prevents us to use very large light shifts. We saw that the method is scalable with both co- and counter-propagating 1529 nm geometries, where we measured respectively full-width at half maximum down to 100 nm and 20 nm. Our setup enables fast in situ absorption imaging in a few microseconds with subwavelength resolutions. To refine the analysis, level mixing due to large light shifts could be included in the repumper fraction model based on the eigenstates from the light shift diagonalization method. The use of the cross-section calibration of Chapter D lead to accurate atom number measurements in optically dense regions and quantitatively compare to the expected numbers.

Additional preliminary results have been obtained on the imaging transition. They are presented in Appendix III.ii. Subwavelength imaging is also possible but it is more complicated to analyze quantitatively for absorption imaging. Alternative imaging methods proportional to the scattering rates are a perspective towards quantitative imaging on a cycling transition with subwavelength resolutions. This method is particularly relevant to study the dynamics in an optical lattice in $|F_g = 1\rangle$. It can be used to transfer only a fraction of the population, with a microwave transition, into $|F_g = 2\rangle$ where subwavelength imaging can be performed.

Chapter F

Subwavelength imaging applied to the super-resolution of the sites of a trapping lattice

In this Chapter, we use the imaging method presented in Chapter E to image the sites of a trapping lattice with a period of 532 nm initially loaded with a BEC. First, in section F.1 we give an introduction on imaging methods with subwavelength resolutions in the field of biology where the demand is very high to study the dynamics of biological processes below the diffraction limit of standard microscopes. We then focus on the field of cold atoms in optical lattices, and finish by applying the formalism of our method to a trapping lattice. In section F.2, we give the experimental setup with its characterization, and focuses on the trapping lattice at 1064 nm. In section F.3 we present experimental data showing lattice site imaging when the relative phase between both lattices is varied. In section F.4 we use our method to best prepare a single wavefunction in a lattice site and image with a subwavelength resolution the corresponding on-site atomic density. Finally, in section F.5 we give the limitations of our setup that are contributing to the observed broadening of the atomic density width.

F.1 Introduction on subwavelength imaging

In this section, we review subwavelength imaging methods discussed in the literature with a specific focus on the field of cold atoms in optical lattices, then we present our imaging method to image lattice sites in a ground state lattice with a period of 532 nm.

F.1.1 Review of subwavelength imaging methods

In biology, many techniques have been developed to get subwavelength resolutions of biological samples to go beyond the optical limit of imaging systems. They can be classified into two categories: super-localization where the center of individual particles are pointed, and super-resolutions where subwavelength spatial areas are excited. We will mainly focus on the second kind of method. For instance, STimulated Emission Depletion (STED) (Vicidomini, Bianchini, and Diaspro, 2018) reduces the fluorescence volume using stimulated depletion. It consists in using a doughnut-shape beam that makes stimulated emission stronger than spontaneous emission in the wings. A homogenous excitation beam trans-

fers all molecule states to their excited states. As a result, due to a non-linear response of the sample to the excitation, at the center of the doughnut-shape beam, spontaneous emission dominates in a subwavelength volume. Stimulated and fluorescent lights can be separated to get super-resolution images from the fluorescence. A fluorescent image then consists of an Airy pattern with a center corresponding to a single molecule for instance.

Another method is the Super-Resolution Structured Illumination Microscopy (SR-SIM) (Heintzmann and Huser, 2017). Here, by structuring the illumination, high frequency patterns of the samples are encoded on lower frequencies thanks to Moiré magnification. By varying the periodicity of the structured light and rotating it across the sample, subwavelength details can be obtained via image reconstruction algorithms.

In the field of cold atoms, to overcome the diffraction limit in subwavelength optical lattices, many imaging techniques and instruments have been recently developed. Quantum gas microscopes have been a crucial element for quantum simulations using cold atoms in optical lattices (Schäfer et al., 2020). For instance, anti-ferromagnetic long-range order has been measured in a standard optical lattice (Mazurenko et al., 2017; Koepsell et al., 2020) by measuring spin-correlations between lattice sites with a microscopy that can resolve both the atomic density and spin. In this context, subwavelength lattices have emerged as a possibility to go towards strongly correlated systems as mentioned in Chapter A. An obvious consequence is that they require subwavelength imaging techniques to perform the same experiments as in quantum gas microscopes.

For example, (Weitenberg et al., 2011) use a super-localization method where a tightly focused beam onto a single lattice site creates a differential light shift that makes the atoms in this particular site resonant with an external micro-wave radiation. The spin internal degree of freedom between two hyperfine manifolds can then be controlled with this position-dependent microwave transfer. The drawback of this method is that it needs a focused beam with a diameter smaller than the lattice period. Also, the choice of its wavelength has to match a magic wavelength in order to shift the level of the upper hyperfine manifold and letting the lower one unchanged.

Another technique in (McDonald et al., 2019) consists in using an optical lattice on a repumper transition providing bright field absorption images to locally not repump atoms in a subwavelength volume. In this paper, they also used an alternative for subwavelength imaging which is based on the Moiré effect. They can tune the periodicity of the repumper lattice that is closed to the trapping lattice. As a result, a Moiré magnification enables them to measure subwavelength details at the micrometer scale which is within standard numerical aperture microscopes. Therefore (McDonald et al., 2019) shows both SR-SIM and STED methods applied to optical lattices.

In (Subhankar et al., 2019), they use an electromagnetically-induced-transparency scheme with an optical lattice for the control beam intensity which coherently transfers atoms in a subwavelength volume to a bright state that is imaged with a standard imaging system. This is a very interesting method as the transfer is coherent and fast which enables them to study timescale dynamics on the order of the lattice trap frequency.

Super-resolution microscopy of single-atoms per site in optical lattices can be done with the prior knowledge of the optical transfer function, noise properties, and discreteness of the lattice (Alberti et al., 2016). This relies then on the knowledge of the single-atom scattering function. It allows them to recover the initial atomic distribution using

deconvolution algorithms. However, as soon as the lattice filling factor increases and for more than 1 atom per site, such a deconvolution procedure has a reduced reliability.

On parallel tracks to subwavelength imaging techniques, electron (Santra and Ott, 2015) and ion (Stecker et al., 2017; Veit et al., 2021) microscopes have been developed. For instance, resolutions down to 200 nm (Veit et al., 2021) or 100 nm (Stecker et al., 2017) where neutral atoms are ionized and imaged with electrostatic lenses with large depth-of-fields on the order of 50 µm. They provide a way to measure bulk properties at the healing length scale or Fermi wavelength.

F.1.2 Our method using a dressed excited state

Our method is similar to (McDonald et al., 2019) except that first we transfer subwavelength volumes towards a bright state and secondly we take advantage of a dressed excited state with a transition between two excited states.

We want to image atoms in an optical lattice with a lattice period of 532 nm which is smaller than the measured resolution of our microscope objective $d_R = 1.3$ µm. Therefore to image in situ the lattice sites, we perform the method presented in section E.1. Similarly to Chapter E, we can tune the position of a lattice site such that a 780 nm repumper beam is resonant with either the bottom or the middle of the 1529 nm modulation.

F.1.2.1 Repumped population with a double lattice

Below we remind the formalism of Chapter E in the case of a double lattice at 1064 nm and 1529 nm. The light shifts due to both lattices at 1064 nm and 1529 nm for respectively the ground and the excited states are given by:

$$U_{5S}(x) = \frac{V_0}{2}\left(1 + \cos\left(2\pi\frac{x}{i_{1064}}\right)\right), \tag{F.1}$$

$$U_{5P}(x) = \frac{\Delta\omega_{1529}}{2}\left(1 - \cos\left(2\pi\frac{x}{i_{1529}} + \Phi_0\right)\right), \tag{F.2}$$

where $\Delta\omega_{1529}$ is the excited state modulation amplitude and Φ_0 is the relative phase between the lattices.

The ground state trap depth is as usual given by:

$$V_0 = sE_r, \tag{F.3}$$

where $E_r = \hbar \times 2\pi \times 2.028$ kHz is the recoil energy at 1064 nm. Note that we define the adimensional parameter $s < 0$ for a red-detuned laser.

The global detuning from the bare transition is:

$$\Delta(x) = \Delta_{780} - \frac{U_{5P}(x) - U_{5S}(x)}{\hbar}, \tag{F.4}$$

where $\Delta_{780} = \omega - \omega_0$, $U_{5P}(x)$ and $U_{5S}(x)$ are the ground and excited state potentials generated by the 1064 nm or 1529 nm laser beams. For all experimental situations described in this chapter, the 1529 nm beam dresses only the excited state upwards and we neglect

its effect on the ground state (see section E.1.2.3). The 1064 nm dresses the ground state downwards (red-detuned trapping lattice) and the excited state upwards.

In this chapter, the subwavelength method is applied on the repumper transition where the repumped population $\rho_{22}(x)$ is given either by Eq. (C.61) or Eq. (C.65). At large trap depths, the initial atomic density $n_0(x)$ in the trapping lattice can be considered as spatially equidistant wavepackets given by the harmonic oscillator ground state (section A.3.2). The spatially repumped population $g(x)$ is:

$$g(x) = \rho_{22}(x).n_0(x). \tag{F.5}$$

Experimentally, we do not measure directly $g(x)$ but the convolution of $g(x)$ with the point spread function of our imaging system: $g(x) * PSF(x)$.

The repumped fraction f is finally computed as:

$$f = \int_{-\infty}^{+\infty} g(x)dx. \tag{F.6}$$

Using this formalism to compute the repumped fraction, we are going to give the periodicities for both lattices that are available in our experiment due to mechanical constraints.

F.1.2.2 Commensurability of the double lattice

Due to the different 1064 nm and 1529 nm lattice periodicities, a perfect commensurability can be obtained for a given number of sites n_{1064} at 1064 nm for the ground state and to which corresponds several sites n_{1529} at 1529.366 nm for the excited state. The commensurability is obtained for a set of angles and number of sites n_{1064}, n_{1529}:

$$n_{1529} i_{1529} = n_{1064} i_{1064}, \tag{F.7}$$

where the lattice periods are $i_{1529} = \lambda_{1529}/2\cos(\theta)$ (Eq. (E.29)) and $i_{1064} = \lambda_{1064}/2$.

This gives sets of angles for θ for which the commensurability is obtained:

$$\theta = \text{acos}\left(\frac{n_{1529}\lambda_{1529}}{n_{1064}\lambda_{1064}}\right). \tag{F.8}$$

Due to mechanical constraints, our setup can reach angles from 3.5° to 8° (see Fig. E.14). The available angles in that range verifying Eq. (F.8) are resumed in Table F.1. As a result, we chose the angle $\theta = 5.67°$ as it corresponds to the lower commensurability with $n_{1064} = 13$ and $n_{1529} = 9$. It means that every 13 interfringes of the 1064 nm lattice, atoms will see exactly the same modulation of the 1529 nm lattice in the excited state. It corresponds to 6.9 µm which is well resolved by our microscope objective.

We stress that Eq. (F.8) is correct and differs from theoretical studies given in previous PhD thesis (Salvador Vasquez Bullon, 2016; Busquet, 2017) where wrong formulas for interfringes below the diffraction limit with standard optical lattices have been used.

As detailed in Chapter E, two 1529 nm beam configurations can be realized (Fig. E.12): co-propagating and counter-propagating.

n_{1064}	n_{1529}	θ (°)
26	16	0.758
13	9	5.67
29	20	7.57
16	11	8.81
19	13	10.4
22	15	11.5

Table F.1: Sets of angle θ for the commensurability of the lattices at 1529 nm and 1064 nm.

Using the notations of Fig. E.12, let us evaluate the angle sensitivity in the co-propagating configuration. It will help us evaluating to which precision we can tune the interfringe in the counter-propagating case.

For the co-propagating lattice period $i_{1529} = \lambda_{1529}/(2\sin(\alpha))$, the angle sensitivity is given by $di_{1529}/d\alpha = \lambda_{1529}/2 \times \cos(\alpha)/\sin^2(\alpha)$. For $\alpha = 5.7°$ we have $di_{1529}/d\alpha = 1346$ nm/deg. Given our experimental signal-to-noise, we can measure the lattice period in the co-propagating case with an error of 0.1 µm. It corresponds to a precision of 0.074° on the angle.

For the counter-propagating lattice period, we have $i_{1529} = \lambda_{1529}/(2\cos(\theta))$ and $di_{1529}/d\theta = -\lambda_{1529}/2 \times \sin(\theta)/\cos^2(\theta)$. The corresponding angle sensitivity for $\theta = 5.7°$ is 1.34 nm/deg. Tuning the angle in the co-propagating configuration, we know the angle with a precision of 0.074°. We therefore know the interfringe with a precision of 0.1 nm. Over a large periodicity of $13i_{1064} = 6916$ nm, the precision is 1.3 nm which is much smaller than the ground state harmonic oscillator length. The lattice commensurability can then be finely tuned to avoid or induce Moiré patterns.

F.1.2.3 Examples: initial alignment at the middle or bottom

In this part, we give typical experimental configurations of the two lattices. The objective is to be able to measure a single site, named as site n°0, in the 1064 nm lattice while minimizing the coupling to other sites.

We consider cases where the 780 nm repumper is tuned either at the bottom of the modulation where site n°0 coincides with the bottom of the 1529 modulation ($\Phi_0 = 0°$ and $\Delta_{780} = 0$) or at the middle where site n°0 coincides with the middle of the 1529 modulation ($\Phi_0 = 90°$ and $\Delta_{780} \approx \Delta\omega_{1529}/2$).

First let us consider a ground state in a trap depth $s = -40$. As expected from commensurability, Fig. F.1 shows that sites 0 and ±13 are simultaneously resonant. Nevertheless, they are not the only ones and many other peaks are close to resonance: $\pm 3, \pm 6, \pm 7$, etc. These residual peaks are mainly due to the choice of wavelengths and angles. Indeed, for ±3, $(3i_{1064} - 2i_{1529}) = 59$ nm and for ±6, $(6i_{1064} - 4i_{1529}) = 118$ nm. This means that to resolve independently site 0 and 3, the ground state width a_{OH} has to be small compared to 59 nm. Thus it is not the case at $s = -40$ as the harmonic oscillator length $a_{OH} = 67$ nm.

As we compress the 1064 nm lattice up to $s = -1000$, Fig. F.2 shows that residual peaks decrease in amplitude. This is due to the reduction of the harmonic oscillator length down

to $a_{OH} = 30$ nm. Even at such a trap depth, sites ± 3 stay 'resonant' but the visibility goes up to 1 between sites the $0, \pm 3$ and the residuals sites $\pm 6, \pm 7$.

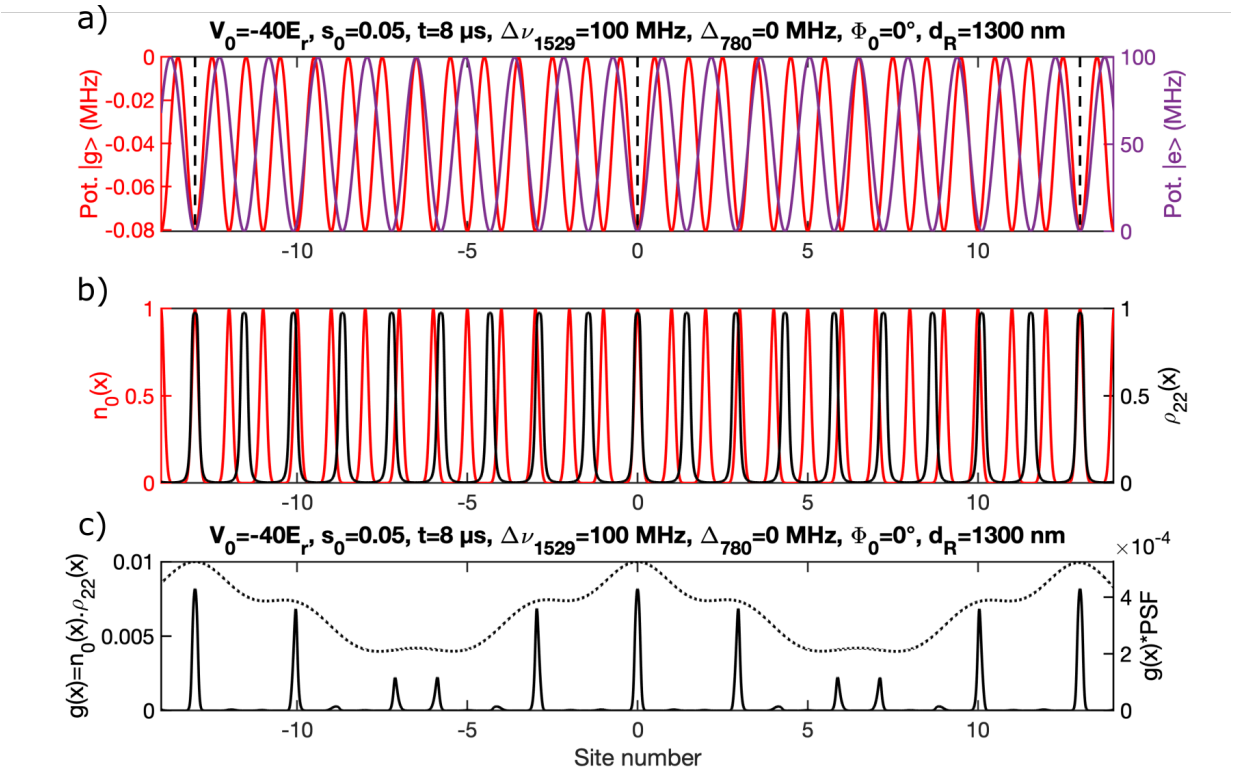

Figure F.1: a) Ground and excited state lattice potentials for $\theta = 5.7°$, b) periodic lattice atomic density $n_0(x)$, repumped population $\rho_{22}(x)$ and c) $g(x)$ (black solid line) and image after applying the microscope point spread function $g(x) * PSF(x)$ (black dashed line) for $s = -40$ and $\Phi_0 = 0°$.

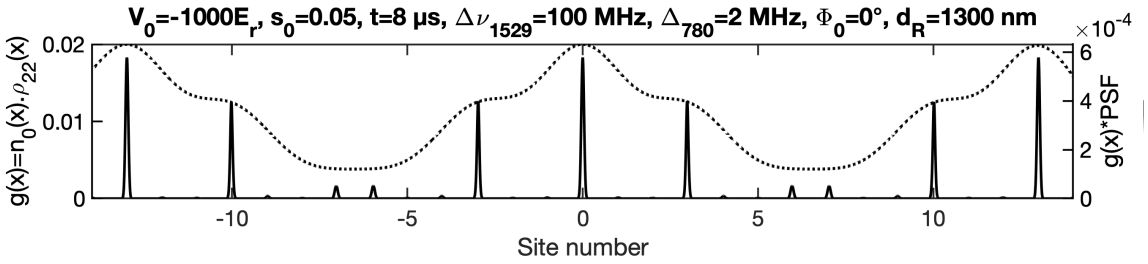

Figure F.2: Repumped population $g(x)$ (black solid line) and image after applying the microscope point spread function $g(x) * PSF(x)$ (black dashed line) for $s = -1000$ and $\Phi_0 = 0°$. It compares to Fig. F.1.

Now, in the case of the middle of the modulation, the repumped population is more complex and it is difficult to resolve the sites at $s = -40$ (Fig. F.3) or $s = -1000$ (Fig. F.4).

In the next parts, we will see that it is more appropriate to use the bottom configuration for lattice site imaging (section F.3) and the middle configuration to super-resolve a single site in an almost empty lattice (section F.4). Before entering into the detail of the results, we will describe the experimental setup generating the lattices.

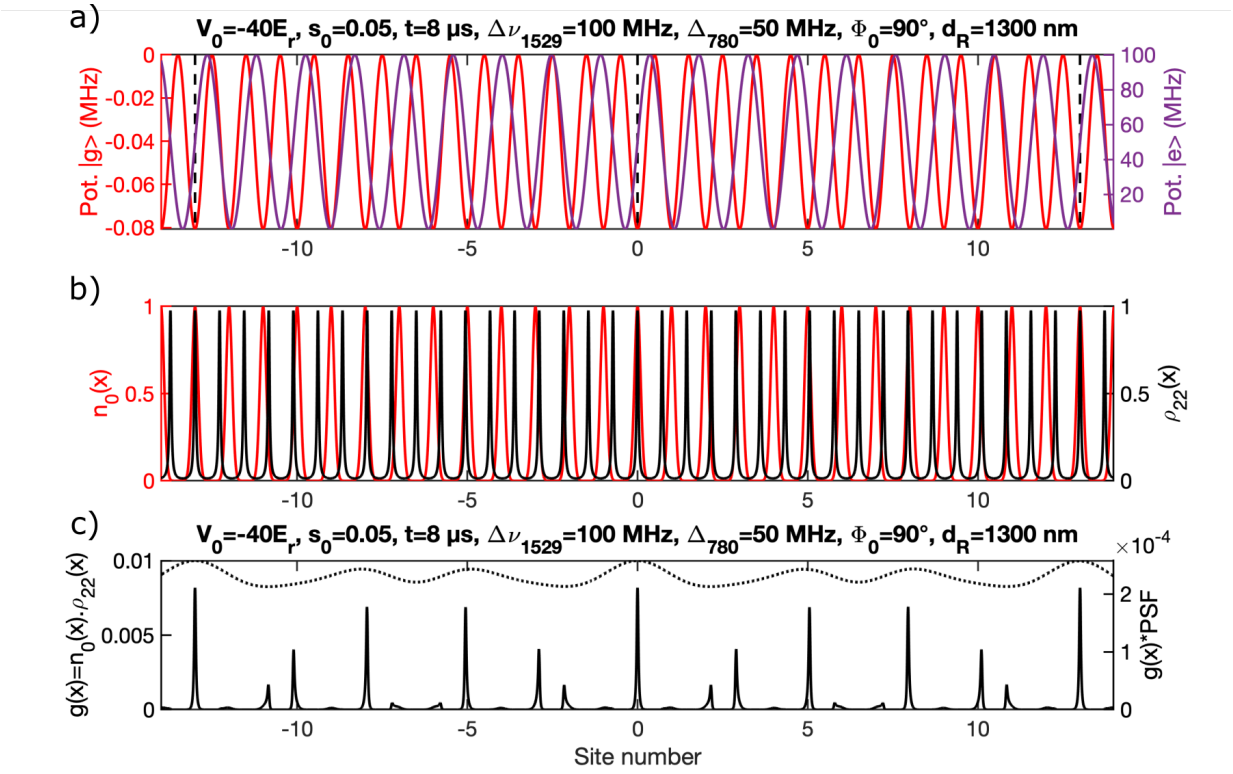

Figure F.3: a) Ground and excited state lattice potentials for $\theta = 5.7°$, b) periodic lattice atomic density $n_0(x)$, repumped population $\rho_{22}(x)$ and c) $g(x)$ (black solid line) and image after applying the microscope point spread function $g(x) * PSF(x)$ (black dashed line) for $s = -40$ and $\Phi_0 = 90°$.

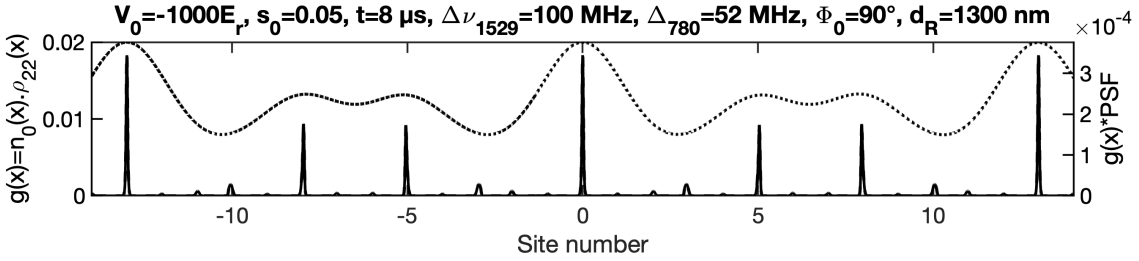

Figure F.4: Repumped population $g(x)$ (black solid line) and image after applying the microscope point spread function $g(x) * PSF(x)$ (black dashed line) for $s = -1000$ and $\Phi_0 = 90°$. It compares to Fig. F.3.

F.2 Optical setup for the 1064 and 1529 lattices

The optical setup for generating the lattice at 1529 nm is exactly the same as in Chapter E where its characterization was given. The 1064 nm lattice setup was also shown on the main experimental setup in Fig. B.2. The 1064 nm lattice beam is controlled by a dedicated AOM that has a fast rise time of 20 ns.

The key elements are resumed in Fig. F.5. We name as 'lattice 1' the beam that propagates in the same direction as DT1 (upwards on Fig. F.5) and 'lattice 2' the beam that propagates in the opposite direction than DT1 (downwards on Fig. F.5).

'Lattice 1' is aligned to spatially overlap with DT1 using a beam profiler such that they follow exactly the same path. After the second 150 mm aspheric lens, 'lattice 1' (polarized along x) is transmitted through a PBS and DT1 (polarized along z) is reflected towards a beam dump. 'Lattice 1' is then reflected by a mirror to form now 'lattice 2'. This mirror is controllable with a Newport actuator mirror mount as described in section B.4.2.2. The mirror angle is optimized by maximizing the retro-injected power into the lattice fiber[1]. The mirror is glued on a piezoelectric Thorlabs PK44RB5P2. It is controlled with a Cicero analog channel which is amplified by a factor of 2[2]. With a piezo voltage from 0V to 20V, it enables us to move the mirror by 1 µm which corresponds to almost $2i_{1064}$. Piezoelectric actuators show hysteresis. Before any change, the voltage value is reset to 0V.

The lattice potential is directly given by two-counter propagating beams forming a periodic intensity profile with a period of $i_{1064} = 532$ nm. The ground state lattice potential is given by:

$$V(\mathbf{r}) = 2V_0(\mathbf{r}) \left(1 + \cos\left(\frac{2\pi x}{i_{1064}}\right)\right). \tag{F.9}$$

For this lattice potential, we recall the trap frequencies in a site with maximum trap depth $V_0 = sE_r$ that are given by:

$$\begin{aligned} \omega_x &= \frac{2E_r}{\hbar}\sqrt{|s|}, \\ \omega_{y,z} &= \sqrt{\frac{4|s|E_r}{mw_0^2}}. \end{aligned} \tag{F.10}$$

The adiabaticity of the loading of the BEC into the 1D 1064 nm lattice has been characterized and described in Appendix IV.i, and its trap depth using Kapitza-Dirac scattering in Appendix IV.ii. The induced light shifts by the 1064 nm beams on the atomic states have been quantified in Appendix IV.iii. All these calibrations were necessary to perform the quantitative analysis of the next sections.

[1] 'Lattice 1' has to be well-aligned onto DT1 first, then retro-injecting the lattice can be done with a $\lambda/4$ waveplate at the collimator input. At the fiber output of the retro-reflected beam, a PBS separates the reflection from the main lattice beam. If 'lattice 1' is not well-aligned, we noticed that 'lattice 2' gives a higher trap depth when 'lattice 2' is not maximally retro-injected in the fiber.

[2] We remind that Cicero analog channels range from -10V to 10V. According to the datasheet, at maximum the piezo can be displaced by 9.5 µm for 150 V.

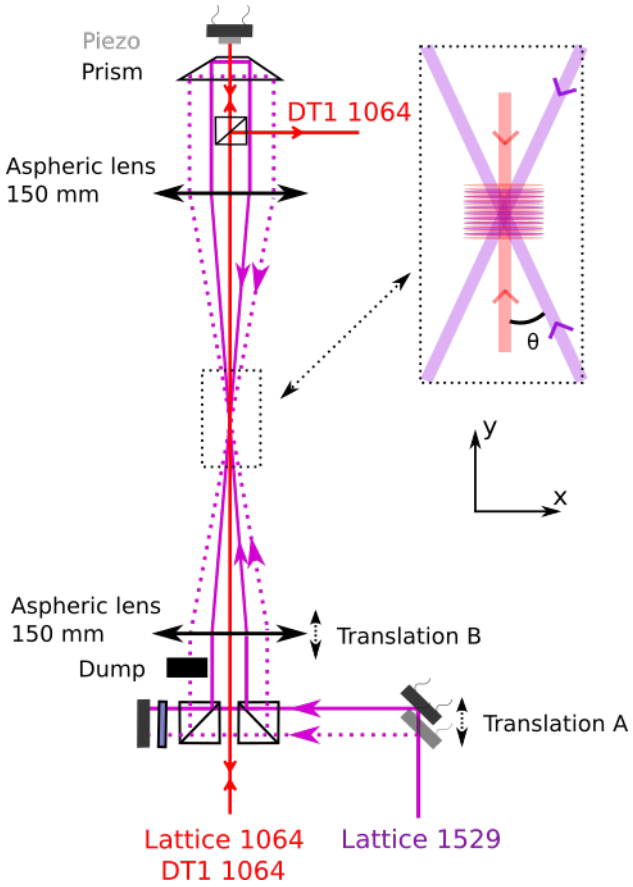

Figure F.5: Double lattice at 1064 and 1529 that can be realized on the experiment. All beams can be seen on the main experimental setup of Fig. B.2.

F.3 Results on lattice site imaging

In section F.1.2.2, we have seen that $\theta = 5.67°$ gives a perfect commensurability with $n_{1064} = 13$ ($i_{1064} = 532$ nm) and $n_{1529} = 9$ ($i_{1529} = 768.4$ nm) which can be resolved with our high NA imaging system.

The following measurements are performed on a BEC initially prepared in a hybrid trap involving DT1. The lattice is then adiabatically increased up to $40E_r$. The magnetic gradient is decreased to zero and a magnetic bias of about 280 mG is set along z. We use a double MW transfer to prepare a fraction of the atoms in the lattice (the second MW pulse being 12 µs so the fraction is 39%). The atoms are transferred into $|F_g = 2\rangle$ with $s_0 = 0.020$, $t = 8$ µs, $\Delta\nu_{1529} = 96$ MHz, $\Delta_{780} = 0$. The imaging beam is tuned on resonance with a saturation of 3 and duration of 10 µs. At the beginning of the sequence, the piezo is set to a variable value Φ_{1064} which moves the 1064 nm lattice with respect to the 1529 nm lattice.

On Fig. F.6, the left plot shows the integrated atom number along the 1064 nm lattice directions vs. the piezo displacement. Yellow lines are not perfectly straight as the piezo itself has a small nonlinearity (and an hysteresis). The right plot shows the expected results simulated by varying the phase Φ_{1064}, and using a 3LS model to evaluate the repumped population and a PSF of 1.3 µm. It shows that site 0 is resonant at $\Phi_{1064} = 0$ and also at $\Phi_{1064} = 532$ nm which is the ground state lattice period. From site 0 and $\Phi_{1064} = 0$, moving along a yellow fringe corresponds in cases where sites $+3$, $+6$ etc.

are successively resonant. From site 0 and increasing Φ_{1064}, around 300 nm the 1064 lattice has moved such that sites $+2$ and -1 are resonant. As a result, 2 'full' yellow fringes correspond to 532 nm which calibrates the experimental piezo displacement to 100 nm/V. The fringe contrast on the experimental data reaches 0.22 while the model predicts 0.48. The discrepancy could come from the pixelization of the image which has not been taken into account to compute the simulated contrast and it also strongly depends on the PSF so it would be hard to be quantitative. A PSF radius of 1.3 µm does not render the periodicity along a yellow fringe (*i.e.* the colormap intensity oscillation along a yellow fringe on the right plot is not observable on the left plot) so in practice the spatial resolution was probably a bit larger than 1.3 µm.

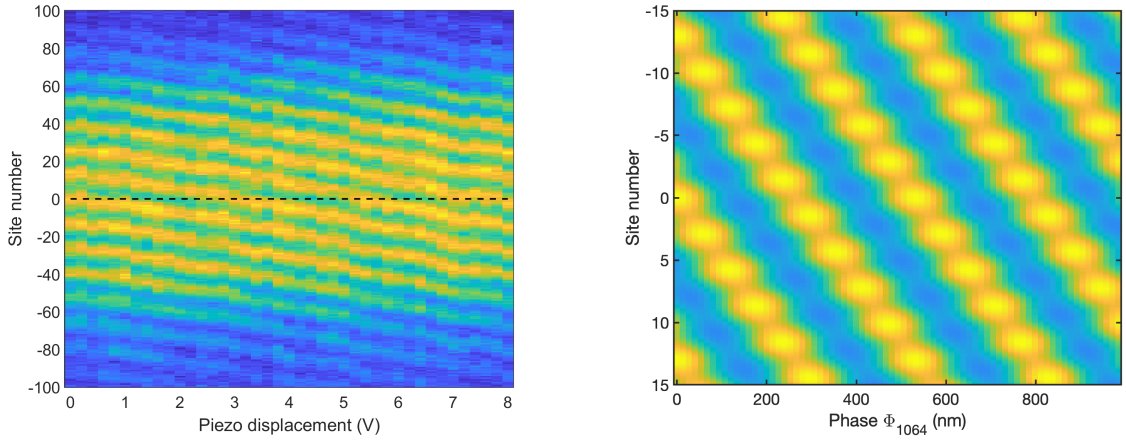

Figure F.6: Integrated repumped atom numbers vs. piezo displacement: experiment (left) and theory (right). The horizontal black dashed line is a guide for the eye to follow site 0. We use the right plot to calibrate the piezo displacement of the left plot.

So far, we demonstrated that our method can be used to image different sites in an optical lattice by varying the relative phase between both lattices. To be more quantitative in terms of atom numbers and resolution, we are going to use the dressed excited state to prepare a wavefunction in a single site and image it.

F.4 Results on on-site atomic density imaging

In this section, we use repumper pulses to clean the residual sites that are responsible for the reduction of the contrast. We therefore take advantage of our method to 'clean' the lattice to prepare at our best a single wavefunction with the perfect commensurability periodicity. We will then image it with our best resolution which is obtained at the middle of the 1529 modulation.

The initial BEC of 2.10^5 atoms is obtained in a hybrid trap involving DT1. A compression up to a trap depth of $70E_r$ is then performed to avoid gravitational sag effects. The corresponding trap frequencies are 160 Hz for the transverse directions of the dipole trap and 15 Hz along the magnetic trap direction. The corresponding averaged trap frequency is 73 Hz and the chemical potential is 1.5 kHz (using equations in section A.2.2). This gives a peak atomic density of $n_0 = 2.10^{20}$ at/m^3.

The cleaning sequence consists in 5 steps which are depicted on Fig. F.7. We first detail the coarse cleaning steps (steps 1, 2 and 4) which clean all sites except 0, $+3$ and -3:

- t_1: Site 0 is at the bottom of the 1529 modulation where $\Phi_0 = 0$. 5 repumper pulses tuned at the top of the modulation clean the sites $-2, -5, -8, -11$ as shown on Fig. F.9.

- 100 ms: The 1064 lattice is moved by a phase shift corresponding to $i_{1529}/4 = 192$ nm[3].

- t_2: Site 0 is tuned at the middle of the modulation (which is the best situation for protection) where $\Phi_0 = \pi/2$. 5 pulses at the top of the modulation clean the sites $-1, -4, -7$ as shown on Fig. F.9.

- t_4: 5 pulses at the bottom of the modulation clean the sites $-6, -9, -12$ as shown on Fig. F.9.

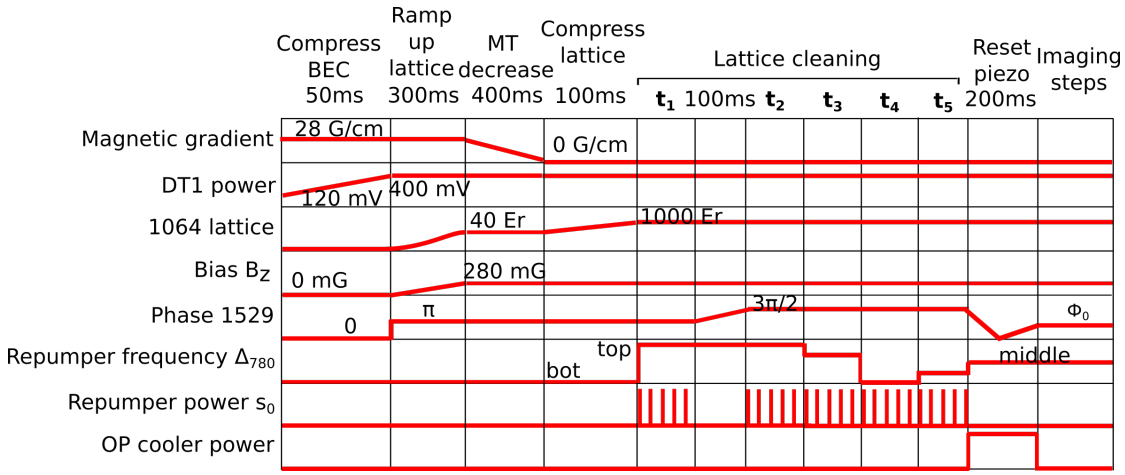

Figure F.7: Experimental sequence for the cleaning stage in the 1064 lattice.

Fig. F.8 shows raw images obtained only with the coarse cleaning steps. The first image is with only DT1. There is no longitudinal confinement as there is no magnetic trapping and no lattice. The second image is when the 1064 lattice has been turned on up to $40E_r$. The longitudinal confinement is due to the presence of the lattice. In this case, lattice sites are not resolved. In the third image, we used coarse cleaning steps and imaged the remaining atoms with homogeneous resonant repumper and imaging beams. A single fringe corresponds then to sites 0 and ± 3.

The hardest sites to clean are ± 3. Given the periodicity of our system, their respective frequencies are very close (equiv. 59 nm). We take advantage of the light shift to address independently sites 0, -3 and +3 as shown on Fig. F.10. The equivalent system due to the lattice periodicity is to have site 0 at the middle of the 1529 nm modulation ($\Delta\omega_{1529}/2$) and sites +3/-3 shifted by $\pm n\Gamma$. Due to the harmonic oscillator width which is 30 nm at $1000E_r$, it is difficult to repump ± 3 without affecting the site 0. As shown on Fig. F.10, one way is to repump the side of the density of $|\Psi_{\pm 3}|^2(x)$ and let a time for thermalization. At $1000E_r$ the trap frequency is 128 kHz *i.e.* an oscillation period of 7.8 µs.

On the experiment, we pulsed the repumper laser with a series of N and M pulses to clean sites ± 3. These steps correspond to t_3 and t_5 on Fig. F.7 and correspond to:

[3]For the particular dataset in this section, the piezo started at 2V and increased to 4V. It is a bit larger than the piezo calibration which is 100 nm/V.

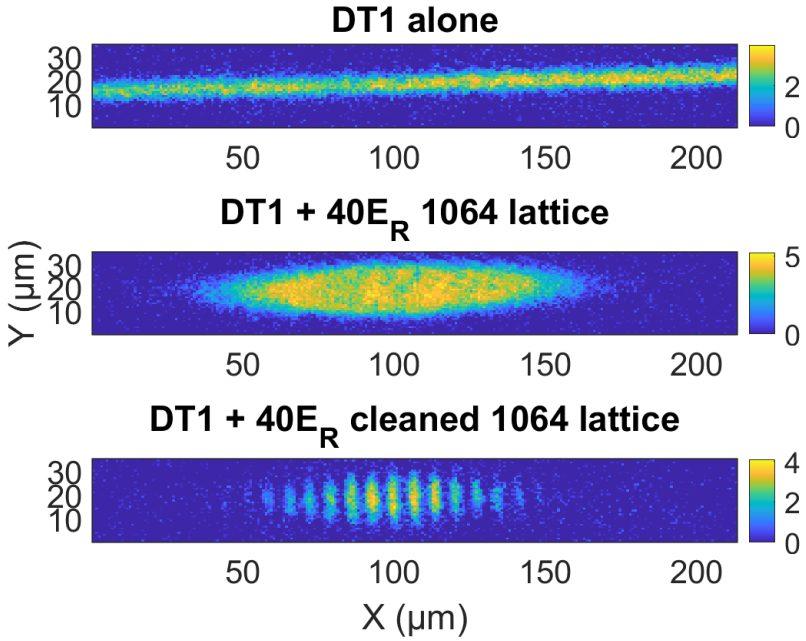

Figure F.8: Raw images of in situ optical densities for DT1 alone with no trapping along the longitudinal axis, DT1+$40E_r$ 1064 lattice imaging on resonance and DT1+$40E_r$ 1064 lattice which has been cleaned (steps t_1, t_2, t_4) using the 1529 lattice then imaged on resonance on the cycling transition without 1529 nm beams.

- t_3: The phase is $\Phi_0 = \pi/2$. Site 0 is at the middle of the modulation. M pulses of duration 16 µs with a dead time of 100 µs in-between are used at a detuning of -2Γ below the top of the modulation. It cleans site +3.
- t_5: The phase is $\Phi_0 = \pi/2$. Site 0 is still at the middle of the modulation. N pulses of duration 16 µs with a dead time of 100 µs in-between are used at a detuning of $+2\Gamma$ from the modulation bottom. It cleans site −3.

After the full cleaning sequence, we reset the piezo to 0V and move it to a variable quantity to scan the atomic density using a repumper tuned at the middle of the modulation. We measure the total atom number on the image and plot it vs. the piezo displacement for many pulse numbers N, M. Finally, we fit this atom number with the following Gaussian function:

$$N = N_0 e^{-\frac{(x-x_0)^2}{2\sigma^2}} + N_{offset}, \tag{F.11}$$

where we are mainly interested in the width σ that we want to compare to our sub-wavelength spatial resolution and the ground state lattice depth, and to the position offset.

For the cleaning cases of Fig. F.11 and F.12, we see that the center of the wavefunction moves due to the fact that we empty only either site +3 or −3. In theory it should shift at maximum by $59/2 = 29.5$ nm in the case where either site 0 and site 3 or site 0 and site -3 are populated. Experimentally, we see that the central position x_0 moves by 15 nm which could be explained by the fact that the sites ±3 have been partially cleaned during the coarse cleaning stage.

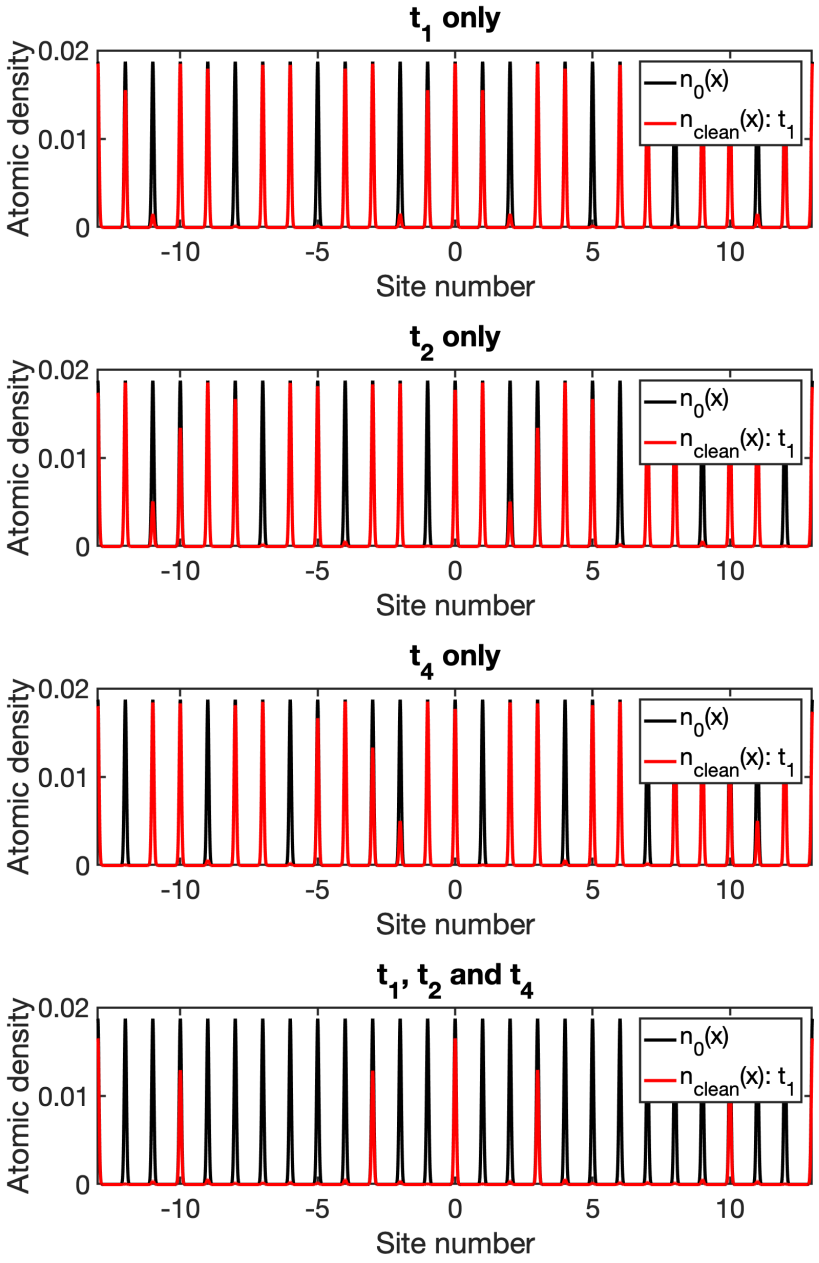

Figure F.9: Independent coarse cleaning steps corresponding to t_1, t_2 and t_4. In black is the lattice with equal initial population for all sites and red is the remaining population after a given cleaning step indicated in each subplot title.

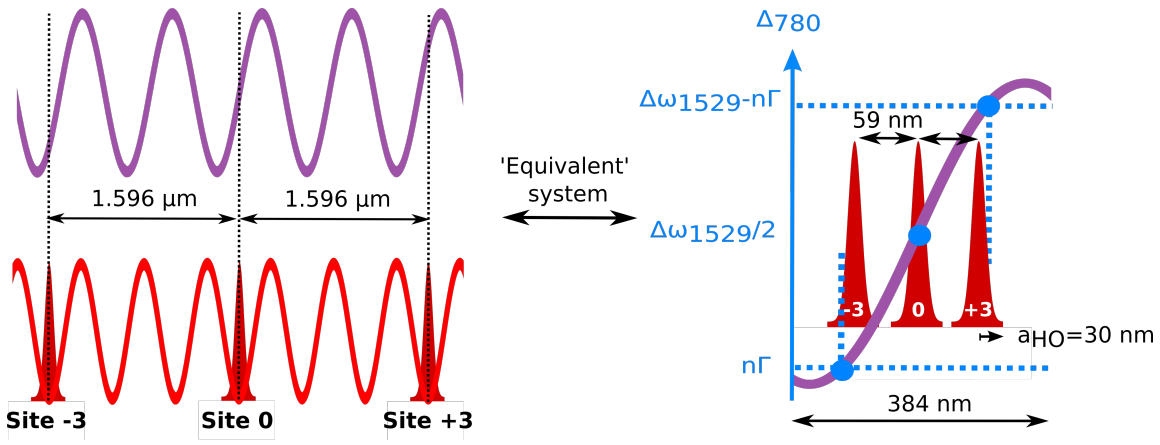

Figure F.10: Atomic densities in sites 0, ±3 which are 1.596 µm apart from each other and the equivalent system where two sites would be at 59 nm from each other.

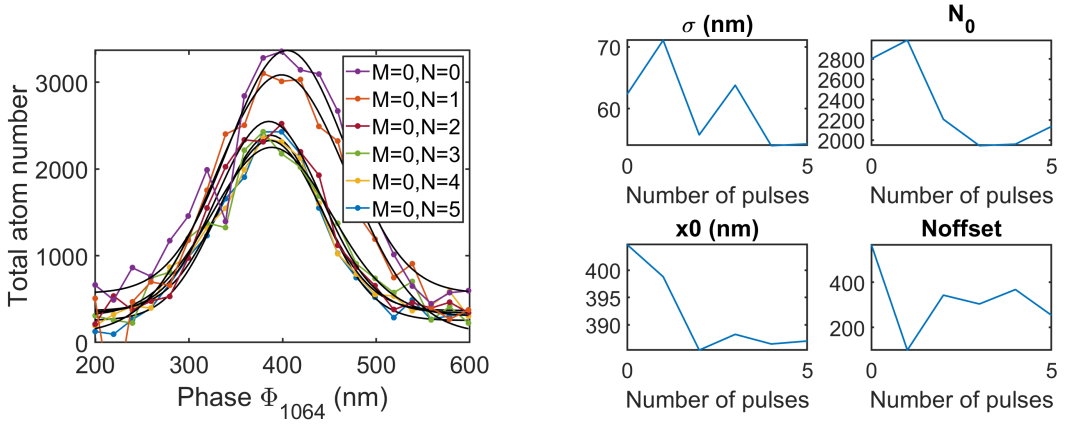

Figure F.11: Total atom number after lattice cleaning with $M = 0$ and N repumper pulses vs. the piezo displacement. Lattice depth is $1000E_r$ and the light shift is 106 MHz. Black solid lines are fits with Eq. (F.11).

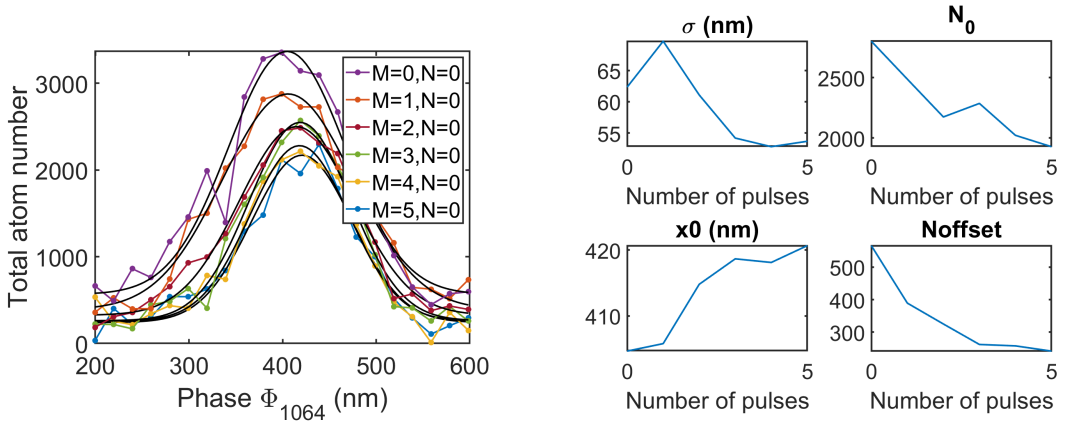

Figure F.12: Total atom number after lattice cleaning with $N = 0$ and M repumper pulses vs. the piezo displacement. Lattice depth is $1000E_r$ and the light shift is 106 MHz. Black solid lines are fits with Eq. (F.11).

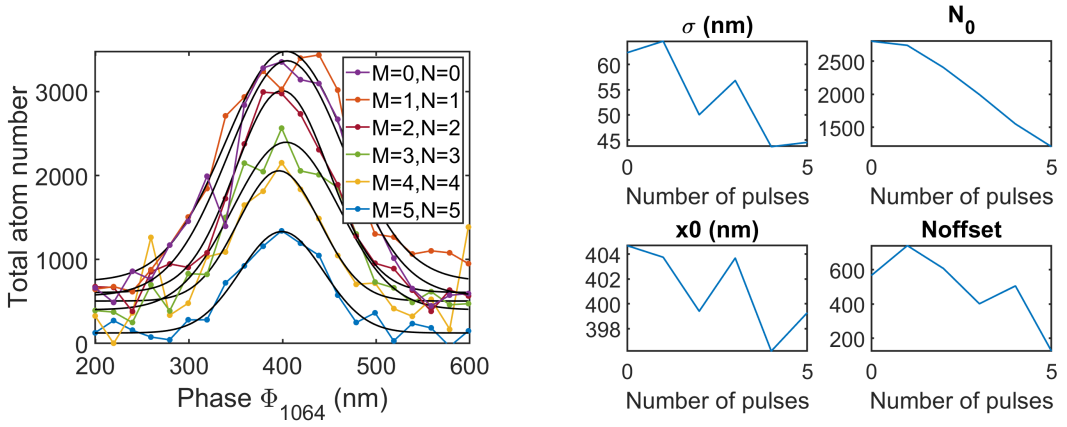

Figure F.13: Total atom number after lattice cleaning with $N = M$ repumper pulses vs. the piezo displacement. Lattice depth is $1000E_r$ and the light shift is 106 MHz. Black solid lines are fits with Eq. (F.11).

Fig. F.13 shows that after cleaning both ±3 sites the width of the Gaussian function goes down to 45 nm. In theory, we expect a slightly smaller value. At high lattice power, the ground state along the lattice direction is the harmonic oscillator ground state. The chemical potential is indeed much smaller than the HO energy spacing given by the lattice trap frequency of 128 kHz. We have $a_{OH} = 30$ nm for the ground state site wavefunction so $30/\sqrt{2} = 21.3$ nm for the atomic density. For our subwavelength imaging method, with a 1529 nm modulation amplitude of 106 MHz, a repumper duration of 16 µs and saturation 0.020, we expect a FWHM at the middle of the modulation of 27 nm (Eq. (E.24)) *i.e.* an equivalent Gaussian standard deviation of 11.5 nm. Assuming a convolution of 11.5 nm and 21.3 nm, the expected width is 24 nm which is lower than the measured width of 45 µm.

To conclude, we found that the width is $45/24 = 1.9$ times larger than the expected harmonic oscillator ground state at $1000E_r$. As the trap oscillation period is smaller than the repumper duration, the atomic motion might be the reason for the broadened spatial width. Other effects could come into play that we are going to list and evaluate in the last following section.

F.5 Width broadening effects

A few effects could come into play to explain the broadening of the width. In the following, we will detail the role of an imperfect cleaning sequence. We will then discuss the role of a remaining thermal fraction in the lattice, non-adiabatic effects like transient heating in a spatially strongly varying excited state, density effects such that dipole-dipole interactions which would create a repulsive force, and three-body losses. In this section, we will give some insights for each of them and evaluate their effects on our measurements.

F.5.1 Imperfect cleaning and initial relative phase

The first broadening could simply come from an imperfect lattice cleaning stage of sites ±3. In this section, we assume that only sites 0 and ±3 remain with equal population after coarse cleaning.

We now vary the population ratio in those sites for different cases and look at the remaining atomic density distribution. To that purpose, we compute the width that we would measure if we scan the 1529 slope across site 0 by varying the phase of the 1064 nm lattice. Numerically it is the convolution of the subwavelength response function with the atomic density followed by a Gaussian fit. The simulations are performed with the same parameter as on the experiment: a light shift of 106 MHz, a repumper saturation of 0.016, and duration of 16 µs under the 3LS repumper model.

Let's consider the case where site +3 is empty and we vary the population ratio between site -3 and site 0. Fig. F.14 shows the width and position of a Gaussian fit at the middle of the modulation. The normalized atomic density profile (dashed line) is shown and the Gaussian fit (solid line). The width starts around 47 nm and goes down to 27 nm. The position shifts at maximum by 30 nm. This was expected as the distance between 0 and -3 is 59/2.

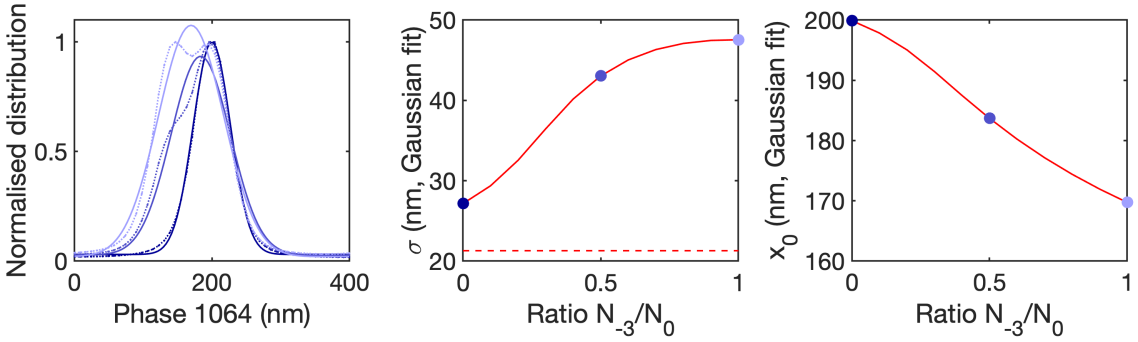

Figure F.14: (left) Dashed lines are the expected repumped population and solid lines are Gaussian fits; Gaussian (middle) width σ and (right) central position x_0 of the Gaussian fits for different initial population ratio (0, 0.5 and 1) in sites 0 and -3. Population in site +3 is always 0. The red dashed line is the harmonic oscillator atomic density width σ_0.

Let's now vary the population ratio between site ±3 and site 0 keeping the population in -3 equal to +3. The normalized atomic density profile (dashed line) is shown and the Gaussian fit (solid line). Fig. F.15 shows the width and position of a Gaussian fit of the repumped fraction at the middle of the modulation. Without cleaning, the width starts around 71 nm and goes down to the theoretical limit of 27 nm.

As a result, an imperfect cleaning definitely broadens the observable width. However for these extreme cases, atom number offsets for phases of 0 remains small contrary to experimental data of Fig. F.11 and Fig. F.13. Other sites are pretty easy to clean so there are probably other effects that are responsible for width broadening.

Such an imperfect cleaning could occur due to the initial relative lattice phase. So far, for the analysis, we assumed that there is always a 1064 nm site that is aligned with a 1529 nm site. However, the relative phase was not locked. The initial phase could vary with temperature fluctuations of the lab. To evaluate the effect of the initial phase, we assume a random 1064 nm lattice phase ϕ_{1064} such that the ground state lattice is $\frac{1}{2}(1-\cos(2\pi x/i_{1064}+\phi_{1064}))$ and a fixed 1529 nm lattice such that $\frac{1}{2}(1-\cos(2\pi x/i_{1529}))$. Two 'bottom' sites are considered aligned if derivatives of these functions are zero at the same position. Computing these derivatives gives the following criterion on the position of the bottom sites $dx = x_{1064} - x_{1529}$:

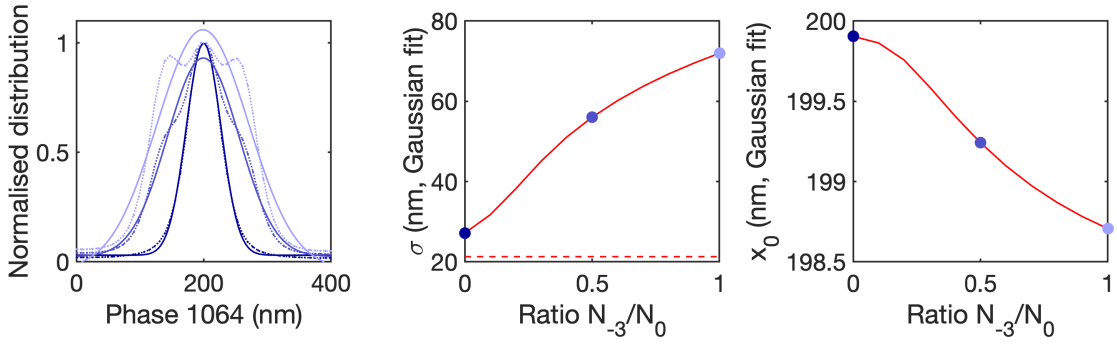

Figure F.15: (left) Dashed lines are the expected repumped population and solid lines are Gaussian fits; Gaussian (middle) width σ and (right) central position x_0 of the Gaussian fits for different initial population ratio (0, 0.5 and 1) in sites 0 and ± 3. Population in site $+3$ is equal to the one in -3. The red dashed line is the harmonic oscillator atomic density width σ_0.

$$dx = i_{1064}k - i_{1529}m - i_{1064}\phi_{1064}/2\pi, \tag{F.12}$$

where k, m are integers.

We compute $\min(dx)$ for any k, m which is the shortest distance between a bottom site of the excited state and a bottom site of the ground state. Fig. F.16 shows that every 59 nm a different site is resonant. The worst-case corresponds to a 1064 nm lattice phase shift of about 30 nm which also gives $\min(dx) \approx 30$ nm. We show the remaining population in each site after the full cleaning sequence of F.4. For a phase shift of 30 nm, sites 0 and $+3$ remain with equal population. According to Fig. F.14 it would give a measurable width of 47 nm. This could also explain large atom number offsets at the border of the Gaussian as observed in section F.4 and position displacements smaller than expected.

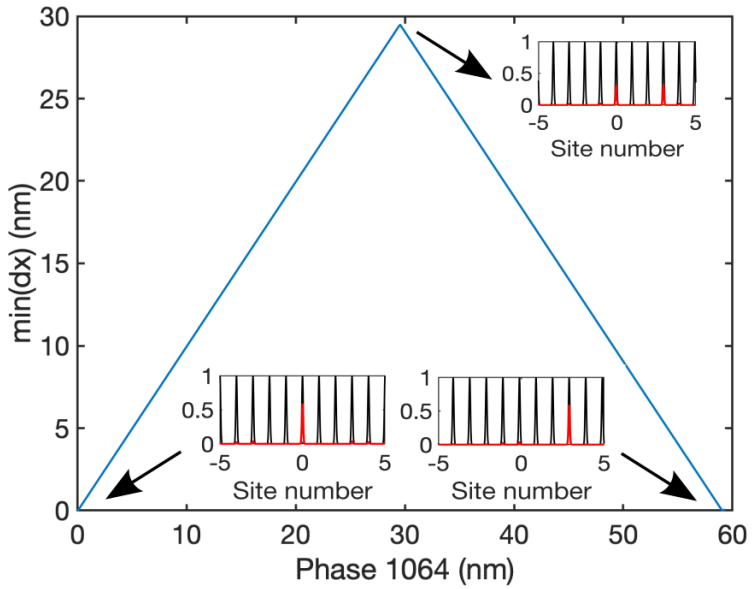

Figure F.16: Minimum distance between a bottom 1064 site and a bottom 1529 site vs. the initial relative phase between both lattices. We show normalized lattice site populations before cleaning (black) and after cleaning (red).

For further experimental studies, it would be interesting to do exactly the same cleaning sequence as presented here, but vary the initial phase and measure the Gaussian width. As soon as the width decreases, other effects will be on the same order of magnitude, one of them being the initial cloud temperature at loading.

F.5.2 Lattice loading with a thermal part in a QHO

In this section we consider the case where the initial cloud has a thermal part with temperature T_i in an initial trap with mean frequency $\tilde{\omega}_i = (\omega_{x,i}\omega_{y,i}\omega_{z,i})^{1/3}$. We consider that some atoms are captured in a lattice site in a low lattice depth $s_i = 1$. We ignore the tunneling and interaction inside the thermal part for which the dynamics is assumed to be slow compared to the adiabatic duration.

We consider an adiabatic compression of the lattice site up to $s_f = 1000$. At constant atom number in the lattice site, the temperature evolves linearly with the trap depth as given in Table A.1: $T_f = T_i\tilde{\omega}_f/\tilde{\omega}_i$. The final trap frequency is $\tilde{\omega}_f = (\omega_{x,f}\omega_{y,f}\omega_{z,f})^{1/3}$. Trap frequencies for the 1064 nm lattice (waist w_l) are given by Eq. (F.10) and for the initial hybrid trap with DT1 (waist w_1 and 20 Hz trap frequency for the MT) by Eq. (B.23). For $s = 40E_r$, the lattice trap frequency is 25.6 kHz (equiv. 1.2 µK) and at $1000E_r$ it is 128 kHz (equiv. 6.1 µK).

The mean trap frequency for the total trap is given by:

$$\tilde{\omega}^3 = \left(\frac{4U_1}{mw_1^2} + \frac{4sE_r}{mw_l^2}\right)^{\frac{1}{2}} \left(\frac{4U_1}{mw_1^2} + \frac{4sE_r}{mw_l^2}\right)^{\frac{1}{2}} \left(4s\frac{E_r^2}{\hbar^2} + \omega_{MT}^2\right)^{\frac{1}{2}}. \tag{F.13}$$

Using Eq. (F.13) and the sequence given in Fig. F.7, we compute $\tilde{\omega}_i$ and $\tilde{\omega}_f$ yielding at $1000E_r$ a temperature increase of $T_f \approx 8T_i$. With an initial temperature of $T_i = 200$ nK, we get $T_f = 1.6$ µK[4].

Fig. F.17 shows the width of a thermal cloud in a quantum harmonic oscillator given by Eq. (A.42) as a function of temperature. We also plot the corresponding populations of the longitudinally excited levels using Eq. (A.41). At $T = 1.6$ µK, the width of the distribution is almost unchanged $\sigma(T) \approx \sigma_0$. As a conclusion, a thermal part of 200 nK should not affect significantly the width of the measured atomic distribution.

F.5.3 Transient heating in the lattice and GPE simulations

As described above, the presence of a thermal part could come from the initial temperature of the BEC, but it could also arise from non-adiabatic manipulations.

We consider the total potential composed of a 1064 nm HO in the ground state and a 1529 nm slope for the excited state (middle of the modulation). Using Eq. (A.62) with populations $\rho_{5S} \approx 1$ and $\rho_{5P} \approx 0$, the total potential U_{tot} coming from the total dipole force is given by:

$$U_{tot} = \frac{1}{2}m\omega^2x^2 + \rho_{5P}\frac{\pi\Delta\omega_{1529}}{i_{1529}}x, \tag{F.14}$$

[4]If we start at $s_i = 0$, we would end up with $T_f \approx 45T_i$ and $T_f = 9$ µK. But in this case, the adiabaticity is not a good approximation as the temperature should depend on the atom number. Moreover, experimentally, the lattice is always turned on at a low trap depth around $s_i = 1$ at the beginning of the loading to be sure that the power lock is working and ready to go up to $1000E_r$.

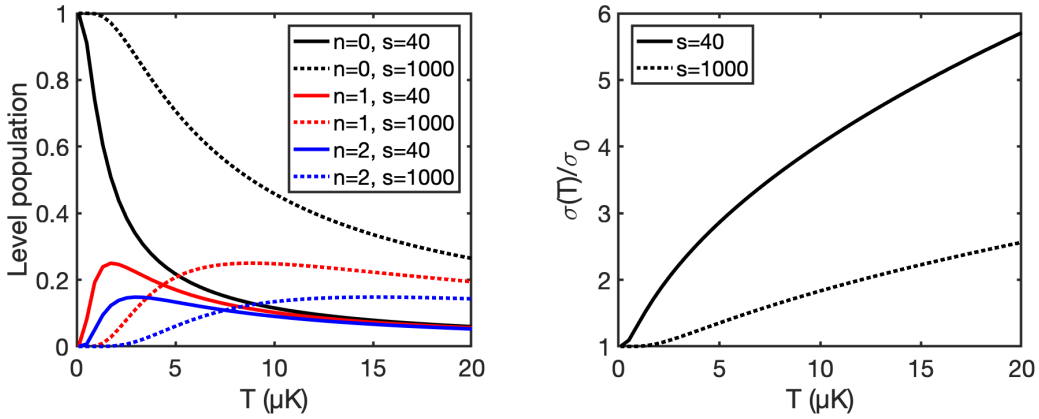

Figure F.17: Population of the longitudinal excited state $n = 0, 1, 2$ and their corresponding Gaussian widths for a thermal state of temperature T in a single lattice site in the quantum harmonic oscillator approximation for lattice depth of $40E_r$ and $1000E_r$.

where $\rho_{5P} = \frac{s_0/2}{1+s_0+4\Delta^2}$ with $\Delta = n\Gamma$ the detuning between site 0 and a 780 laser.

The derivative of Eq. (F.14) leads to

$$\Delta x = -\frac{\rho_{5P}}{m\omega^2}\frac{\pi\Delta\omega_{1529}}{i_{1529}}. \tag{F.15}$$

On the repumper transition, during a time of $1/\Gamma$ in the excited state the wavefunction is shifted by Δx which can be responsible for non-zero longitudinal excited state populations in the harmonic oscillator.

For $s_0 = 0.1$, a light shift of 100 MHz and a 1064 nm trap frequency of 128 kHz (at $1000E_r$), Eq. (F.15) evaluated for $n = 1$, $n = 3$ and $n = 5$ reads respectively -0.7 nm, -1.3 nm and -3.4 nm. Compared to the harmonic oscillator length $a_0 = 30$ nm, the displacement of the minimum of potential energy is quite small. However, this has also to be compared to the time spent in the excited state *i.e.* the number of repumper pulses. In order to evaluate the heating of site 0 during the cleaning stage, we use the DDS potential in the Gross-Pitaevskii equation to compute the excited population.

The doubly dressed state potential was given by Eq. (A.66). As the chemical potential is smaller than the HO level spacing in the lattice direction, we use the GPE equation of Eq. (A.24) in the weak interaction regime, corresponding to solving the usual Schrödinger equation.. To simulate the dynamics of an initial ground state wavefunction in a single quantum harmonic oscillator, we use a GPElab library in Matlab widely described in (Antoine and Duboscq, 2014; Antoine and Duboscq, 2015).

As the 1529 dipole force is directional, parametric heating due to the DDS force occurs at a frequency equal to twice the harmonic oscillator trapping frequency. We simulate[5] the effect of the 1529 nm DDS force onto site 0 with a 780 nm laser tuned at $\Delta_{780} = 3\Gamma$ for a 1529 nm light shift of 17Γ. The middle of its modulation is aligned onto site 0. The ground state is an harmonic oscillator with a trap depth corresponding to a lattice at $1000E_r$ (so a trapping frequency of $\nu_{1064} = 128$ kHz). The saturation parameter as a

[5]For the GPElab simulations: gpe1D function: Computation = 'Dynamic'; Ncomponents = 1; Type = 'Relaxation'; xmin = -10; xmax = 10; Nx = $2^1$1+1;

function of time has 5 pulses of durations Δt and dead time t_{dead} between consecutive pulses.

On Fig. F.18 we show the worst-case scenario where the pulse duration is half the trap frequency followed by another half duration for the dead time. This leads to parametric oscillations where some excitations are introduced onto site 0. To evaluate the amount of excitation, we projected the state at the end of the 5 pulse train onto the harmonic oscillator basis given by Eq. (A.39). We see that the norm of the wavefunction has about $0.9^2 \approx 0.8$ population in the ground state.

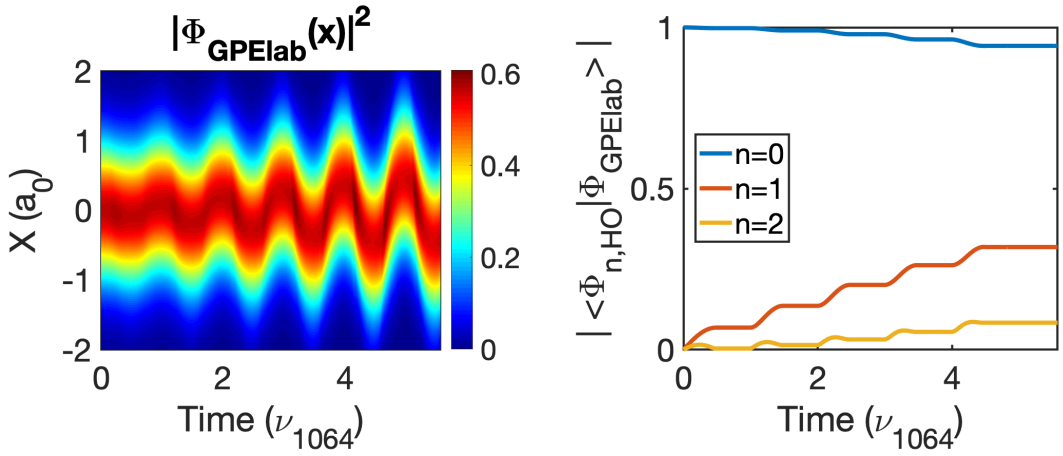

Figure F.18: 1D GPElab time evolution with $\nu_{1064}\Delta t = 0.5$ and $\nu_{1064}t_{dead} = 0.5$ of an initial ground state wavefunction is an harmonic oscillator with a trap depth of $1000E_r$ and using a DDS dipole force corresponding to site 0 when cleaning at $\Delta_{780} = 3\Gamma$.

On Fig. F.19, we used experimental conditions $\Delta t = 16$ µs *i.e.* $\nu_{1064}\Delta t = 2.043$ and a dead time of $\nu_{1064}t_{dead} = 0.769$ where we removed unnecessary full oscillations. We see that we still have some excitations but most of the population is still in the ground state.

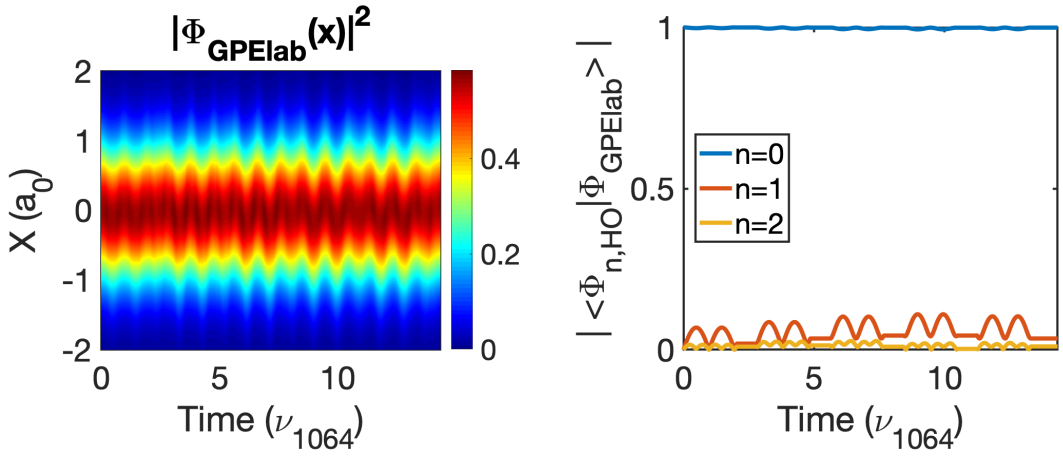

Figure F.19: 1D GPElab time evolution with $\nu_{1064}\Delta t = 2.043$ and $\nu_{1064}t_{dead} = 0.769$ of an initial ground state wavefunction is an harmonic oscillator with a trap depth of $1000E_r$ and using a DDS dipole force corresponding to site 0 when cleaning at $\Delta_{780} = 3\Gamma$.

We point out that the simulations used steady-state solutions of a two-level atom which would be the case for a cycling transition. For a repumper transition, the excited state

population should be obtained from time-dependent expressions. In addition, the saturation is experimentally smaller by a factor of 5 so the effect of the DDS force should be negligible.

To conclude, repumper durations have to be different to the parametric heating cases (half of the trap period) to minimize excitations. From the above simulations, the DDS heating force is expected to be negligible.

To go further in the simulations, a damping of excitations in the BEC part due to thermalization processes with a reservoir (Solnyshkov et al., 2014) could be added as a loss term in the GPE equation. Such an open driven-dissipative system can be used to model the pumping with the repumper.

F.5.4 High atomic density effects

Dipole-dipole interactions : For high atomic densities where the distance between two atoms is $kr \leq 1$, short range interaction via resonant dipole-dipole coupling leads to collective effects (Chomaz et al., 2012; Corman, 2016; Chomaz, 2014).

Let's consider a pair of 2 atoms separated by a distance $\mathbf{r}$ with atomic transition frequency ω_0. One of them is in the excited state such that the bare states are $|eg\rangle$ or $|ge\rangle$ and have the same energies. They interact with a light beam with a polarization perpendicular to $\mathbf{r}$. For $k|\mathbf{r}| \leq 1$, the interaction leading term scales as $1/|\mathbf{r}|^3$. The dressed states are a super-radiant state $|+\rangle$ and sub-radiant state $|-\rangle$. Their corresponding eigenenergies $\Delta E_\pm$ (real part of eigenvalues) and radiative lifetimes $\Gamma_\pm$ (imaginary part of eigenvalues) are given by (Corman, 2016):

$$\begin{aligned} \Delta E_\pm &\propto \hbar\omega_0 \pm \frac{\hbar\Gamma}{(kr)^3}, \\ \Gamma_+ &\xrightarrow[kr\to 0]{} 2\Gamma, \\ \Gamma_- &\xrightarrow[kr\to 0]{} 0. \end{aligned} \tag{F.16}$$

We verify that at large distances *i.e.* $kr \gg 1$, $|+\rangle$ and $|-\rangle$ tend to the bare states $|eg\rangle$ and $|ge\rangle$.

One can compute the corresponding dipole force from the potential given by $\Delta E_\pm$ for an excited atom :

$$|\mathbf{F}| \propto -3\frac{\hbar\Gamma}{r(kr)^3}. \tag{F.17}$$

The velocity associated with the force $|\mathbf{F}|$ with an averaged time in the excited state of Γ^{-1} is:

$$v \propto 3\frac{v_{rec}}{(kr)^4}. \tag{F.18}$$

For $\lambda = 780$ nm, the mean distance is $r_0 = n_0^{-1/3}$. In our case, before the lattice loading step, the peak atomic density is $n_0 = 2 \times 10^{20}$ at/m^3 when DT1 is compressed (equiv. $70E_r$, see sec. IV.iii) as shown on Fig. F.7. Here we have $kr_0 = 1.4$ so we are close to the limit where resonant dipole-dipole effects are expected. It has an impact for sites that are resonant with the repumper beam. For imaging purposes, repumper and imaging

durations have to be small compared to the acquired velocity given by Eq. (F.18) to resolve lattice fringes. This strongly depends on the actual atomic density in the lattice.

Three-body losses : The atomic density depends on three-body losses. The corresponding loss rate is $\Gamma_{3b} = K_{3B} n_0^2$ with $K_{3b} = 5.8.10^{-30}$ s^{-1}cm^6. For the above parameters in the hybrid trap, we have $\Gamma_{3b} = 0.23$ s^{-1} which is not negligible compared to experimental step durations (Fig. F.7).

When we load the 1064 nm lattice, these atoms are redistributed over the lattice sites. In a lattice site, the volume of atoms over one period i_{1064} is put in a lattice site which has a length given by the harmonic oscillator length $a_0 = \sqrt{\hbar/m\omega}$ where the trap frequency is $\omega = \frac{2E_r}{\hbar}\sqrt{s}$. The new density after ramping up the lattice up to $40E_r$ and decreasing DT1 to zero, is then approximately given by $n_{0,site} = n_0 i_{1064}/\sqrt{2\pi}\sigma_0$ where $\sigma_0 = a_0/\sqrt{2}$. We have $a_0 = 67$ nm for $s = 40$ so the on-site density is $n_{0,site} \approx 4.5 n_0 \approx 9.10^{20}$ at/m^3. The local density in the condensate decreases as $\frac{dn(\mathbf{r})}{dt} = -K_{3b} n^3(\mathbf{r})$ (Brantut, 2009). In this situation, after 0.5 s at $40E_r$, the density is 3.8×10^{20} at/m^3.

Then, the compression of the lattice up to $1000E_r$ will also reduce to the density due to three-body losses. We can assume that the density will remain around 4×10^{20} at/m^3 due to three-body losses. These collisions lead to atom losses and heating where atoms could also populate higher HO levels.

Experimentally, on Fig. F.13, we ended up with about 1000 atoms for about 10 sites meaning that we have about 100 atoms per site. For 100 atoms per sites, at $1000E_r$, transverse directions have trap frequencies of 680 Hz (waist of 45 µm) and 408 Hz (waist of 75 µm). The longitudinal lattice trap frequency is 128 kHz. The mean trap frequency is then 3.3 kHz and the chemical potential 7.2 kHz. Assuming a Thomas-Fermi distribution in the transverse direction where the radii are 1.9 µm and 3.2 µm, and a Gaussian density in the lattice direction with 21 nm width, we have a peak density of $n_0 = 2.2.10^{20}$ at/m^3. This density confirms the presence of three-body losses.

In order to avoid high density effects or at least be at the limit of them, we should start with lower atom numbers at the beginning in the compressed hybrid trap. At $1000E_r$ we have $n_{0,site} \approx 70 n_0$ where n_0 is the initial peak density in the hybrid trap. Starting with 10^4 atoms in total at the beginning would be enough to go up to $1000E_r$ without losing or heating the atoms.

F.6 Conclusion

In this chapter, in section F.2 we have set up and characterized a 1D trapping lattice at 1064 nm which we initially loaded with a BEC. Especially, we characterized the trap depth from a robust method using the diffraction of the BEC onto a 1D grating and we finely calibrated the differential light shifts on the 780 nm transition coming from the high power lattice.

In sections F.3 and F.4, using our high NA imaging system with the subwavelength imaging method, we have shown that using a dressed excited state is a versatile tool as it provides an additional degree of freedom to manipulate atoms in an optical lattice and image them with a subwavelength resolution. We experimentally demonstrated that these spatial resolutions (on-site density widths of 45 nm have been measured) can be much smaller than the diffraction limit and provide a way to measure on-site atomic densities.

In theory, it would be possible to increase the excited state modulation amplitude but it requires being able to detect very small atom numbers.

Finally, in section F.5, we listed effects that could explain the measured width of the on-site atomic density. We found that the initial relative phase between the lattices can be responsible for most of the broadening. The second source of broadening would be the cloud temperature of the thermal part with a large initial temperature. After that, we found with Gross-Pitaevskii simulations that the dipole force coming from the strong variation of the excited state is important only in a regime of parametric oscillations and becomes negligible otherwise. Finally, we pointed out that we were at the edge of density effects. The influence of on-site dipole-dipole interactions and three-body losses will have to be evaluated.

To go down to the sensitivity of single-atoms, absorption imaging could have to be replaced with either dark ground imaging or fluorescence imaging (Reinhard et al., 2014; Pappa et al., 2011). So far our absorption imaging system has a detection limit of about 10 atoms in a single fringe and needs averaging with our best imaging system (Princeton camera, no residual light).

The simplest way to avoid residual sites would be to have $n_{1064} i_{1064} \gg d_R$ where d_R is the resolution of the imaging system *i.e.* $n_{1064} \gg 2$ and $n_{1529} = 1$. In such a situation, it would be impossible to have residual sites between two consecutive 1529 sites. Angles for this case are given in Table F.2. Note that in the case where n_{1064} is an even number, for $n_{1529} = 1$ there is a commensurability at the middle of the 1529 modulation. For $n_{1529} > 1$, wavefunction widths and subwavelength resolution have to be taken into account which limits the experimental parameters ranges (trap depths, light shifts).

n_{1064}	n_{1529}	θ (°)
6	1	76.14
11	1	82.50
12	1	83.12

Table F.2: Sets of angle θ for the commensurability of the lattices at 1529 nm and 1064 nm with $n_{1529} = 1$.

To go further, it would be interesting to change the 1529 nm polarization from linear to circular. It would create a spin-dependent excited state light shift that will allow us to super-resolve spins in lattice sites.

Finally, one of the challenges to realize subwavelength lattices to model new Hamiltonians is to better understand the influence of collective effects for high atomic densities. Indeed, in subwavelength lattices, atoms would be very close to each other and the condition $kr \leq 1$ is easily fulfilled. Standard optical lattices with subwavelength imaging methods will be a good experimental platform to study such effects (Glicenstein et al., 2021) which have a key role in atomic clocks based on optical lattices (Chang, Ye, and Lukin, 2004) and single-atomic layers for optical mirrors (Rui et al., 2020; Shahmoon et al., 2017).

Conclusion (EN/FR)

English version

The initial motivation of this PhD thesis has been to explore a new subwavelength imaging technique based on a dressed excited state using an optical transition at 1529 nm between two excited states of ^{87}Rb. For that purpose, to evaluate the spatial resolutions of the method, we used in situ absorption imaging which lead to a re-interpretation of a calibration method of atom numbers widely used in the cold atom community.

In the first Chapter A, we reminded the relevant elements of theory of ultra-cold atoms from evaporative cooling to Bose-Einstein Condensation and optical lattices. We detailed the long-term motivation for this PhD work which is to interface ultra-cold atoms with a nanostructured surface in subwavelength potentials.

Experimentally, the first task of the PhD has been to produce Bose-Einstein condensates using evaporative cooling. In Chapter B we experimentally produced Bose-Einstein condensates of ^{87}Rb from an existing setup that has been completely revisited, from the evaporative stage towards the BEC in a hybrid trap or crossed dipole trap. In addition, we implemented and characterized different tools like the microwave manipulation of the BEC and ex vacuo in situ imaging with a high numerical aperture microscope. This PhD thesis contrasts with the previous PhD thesis as BECs can now be realized on a daily basis and many tools have been implemented and characterized for long-term use.

Chapter C gives a theoretical background on the density matrix evolution of a single atom in a complex environment composed of a coherent driving field for a given polarization at any saturation, magnetic field biases, and an incoherent background field. Simulations using a master equation for the full multi-level system showed that the scattering cross-section of a single quantum system is particularly robust to an imperfect coherent probe polarization or stray magnetic fields. It is mainly due to optical pumping mechanisms. By contrast, the presence of an incoherent pumping would strongly reduce the scattering cross-section by an additional factor without dramatically changing the scattering rates dependency on the probe saturation.

In Chapter D, we studied the propagation of a coherent probe through an atomic ensemble in a well-controlled environment. We showed that in such well-controlled conditions, the scattering cross-section can be strongly reduced. We measured that the reduction factor α depends linearly on the optical density b and seems to be universal, at least for the case of a σ probe polarization. We proposed a model including an incoherent pumping to simulate the propagation of a coherent probe in an atomic ensemble. The origin of this incoherent pumping links to multiple scattering *i.e.* re-diffusion of photons in an optically dense medium scaling usually with the optical density. We proposed a modified

Beer-Lambert law including an incoherent pumping that would emerge from temporally and spatially incoherent scattering rates. The self-consistent numerical solution from the proposed 1D model renders the linear dependence on the optical density. The reduction of the apparent absorption cross-section is connected, in the diffusive regime ($b \gg s_c$), to the residual diffuse transmission, and, in the saturating regime, to the ambient electromagnetic background originating from multiple incoherent scattering in the cloud (s_i). A similar calibration could certainly be performed for other typical configurations such as linear π probes.

Chapter E gives a theoretical model for the subwavelength imaging method by computing the light shifts and expected resolutions using a 1529 nm optical lattice to dress the first excited state. We experimentally showed on a repumper transition that subwavelength volumes can be transferred in a few microseconds to a bright state where standard imaging can be done. Spatial resolutions down to 100 nm to 20 nm have been measured for different 1529 nm beam geometries. We have seen that the light shift of the excited state can be calibrated using a spectroscopy method. The width of the resulting 'BAT' curves directly gives the light shift amplitude and matches with theoretical expectations. To refine the analysis, level mixing due to large light shifts could be included in the repumper fraction model based on the eigenstates from the diagonalization method of the full Hamiltonian. The cross-section reduction of Chapter D could also be included in the data analysis. Also, the absorption imaging method would have to be replaced with either dark ground imaging or fluorescence imaging to get a deeper insight into the results on the cycling transition.

Chapter F is a direct application of the subwavelength imaging method on a trapping lattice. A BEC has been adiabatically loaded into a 1D lattice made by counter-propagating 1064 nm beams. The trap depth of the trapping lattice has been finely characterized using Kapitza-Dirac scattering. We performed in situ subwavelength imaging of the 1064 lattice sites using the 1529 nm lattice dressing the excited state. We experimentally demonstrated that lattice sites can be excited with a subwavelength resolution. Also, the method provides a way to measure on-site atomic densities by scanning the relative phase between both lattices. We used the method to clean the lattice sites and prepare at our best a single wavefunction. In the particular studied beam geometry, the commensurability of the lattices made it difficult to interact with a single site without affecting sites at the edges of the high numerical aperture microscope point spread function. This can be overcome using an appropriate lattice period for the excited state. It has then to be considered at the very beginning of an experiment in construction. To go further, on-site width broadening effects have been listed. We gave orders of magnitudes of the following effects: the initial relative phase between the two lattices, the initial temperature of the residual thermal part of the BEC, the dipole force of the excited state, and effects occurring at high atomic density like dipole-dipole interactions and three-body losses.

The experimental study of the dressed excited state using a radiation at 1529 nm showed that this method allows to manipulate atoms in a reliable and well-understood way. The dressed state can be spatially resonant with a 780 nm radiation which changes the populations in the ground and excited states. This is due to the atomic coherences coming with the 1529 nm radiation happening on a much faster timescale than the atomic coherences coming with the 780 nm radiation. It remains a good approximation if the detuning between the 1529 nm laser and the $5P_{3/2}$ to $4D_{5/2}$ transition is much larger than the light

shifts.

The 1D setup presented in Chapter A with a 1D beam at 1529 nm can be used to study the lifetimes of these doubly dressed states. This will test the trap properties in real experimental conditions and the comparison with theoretical lifetimes in (Bellouvet et al., 2018) will be possible. After that, such states could be reliably used as near-field traps. They will have to be used to probe Casimir-Polder forces on a planar surface. To study such effects, transport procedures of atoms towards a surface down to a hundred nanometers will have to be realized experimentally. Theoretical studies have been done in a previous PhD thesis (Busquet, 2017) by using an on-chip magnetic trap to bring atoms from 500 µm down to 5 µm. These atoms are then loaded in a fringe of an optical lattice. Finally, changing the angle between the surface and the beams, atoms will be transferred down to 250 nm from the surface (Busquet, 2017).

Experiments modeling Bose-Hubbard or Fermi-Hubbard Hamiltonians have taken advantage of the diluteness of cold atoms where collective effects can be neglected. By diluteness we mean the mean inter-particle distance ($n_{3D}k^3 \ll 1$) rather than beyond mean-field corrections ($n_{3D}a^3 \ll 1$). The internal degrees of freedom of atoms are manipulated in optical lattices having periodicities higher than the diffraction limit established by the atomic transition ($\lambda_0/2$). To realize systems as in (Bellouvet et al., 2018) with a periodicity of 100 nm ($< \lambda_0/2$), the effects of external degrees of freedom via short-range dipole-dipole interactions will have to be included in the models. Indeed the regime $n_{3D}k^3 \geq 1$ will be intrinsically fulfilled for such systems. Probing atoms with quantum gas microscopes and manipulating them in subwavelength lattices will require new techniques. Strong couplings via dipole-dipole interactions are studied with dedicated setups (Glicenstein et al., 2021) and have a key role in atomic clocks based on optical lattices (Chang, Ye, and Lukin, 2004), in optical mirrors based on single atomic layers (Shahmoon et al., 2017; Rui et al., 2020) or on photon blockade in subwavelength lattices (Cidrim et al., 2020).

French version

La motivation initiale de ce travail de thèse a été d'explorer une nouvelle technique d'imagerie basée sur des états excités habillés en utilisant une transition optique à 1529 nm entre deux états excités du ^{87}Rb. Dans ce but, pour évaluer les résolutions spatiales, nous avons utilisé une imagerie par absorption in situ qui a conduit à une ré-interprétation d'une méthode de calibration de nombre d'atomes largement utilisée dans la communauté atomes froids.

Dans le premier chapitre A, nous avons rappelé les éléments de théorie pertinents pour les atomes ultra-froids, du refroidissement par évaporation à la Condensation de Bose-Einstein jusqu'aux réseaux optiques. Nous avons détaillé la motivation long terme de ce travail de thèse qui est d'amener des atomes ultra-froids proches d'une surface nanostructurée avec des potentiels sub-longueur d'onde.

Expérimentalement, la première tâche de cette thèse a été de produire des condensats de Bose-Einstein en utilisant le refroidissement par évaporation. Dans le chapitre B nous avons expérimentalement produit des condensats de Bose-Einstein de ^{87}Rb à partir d'un montage existant qui a été complètement revisité, du refroidissement par évaporation

jusqu'au condensat dans un piège hybride ou croisé. De plus, nous avons implémenté et caractérisé différents outils comme la manipulation du condensat avec des micro-ondes et un objectif de microscope à forte ouverture numérique pour de l'imagerie in situ ex vacuo. Ce travail de thèse contraste avec les thèses précédentes car des condensats peuvent être réalisés au quotidien et plusieurs outils ont été implémentés et caractérisés pour des utilisations longs termes.

Le chapitre C donne une base théorique sur l'évolution de la densité de matrice pour un atome dans un environnement complexe composé d'un champ cohérent de polarisation donnée pour tout régime de saturation, des champs magnétiques de biais et un champ incohérent de fond. Des simulations utilisant une équation maîtresse du système multi-niveaux ont montré que la section efficace d'un seul système quantique est particulièrement robuste à une polarisation imparfaite de la sonde cohérente ou des champs magnétiques de biais. Ceci est principalement dû aux mécanismes de pompage optique. En revanche, la présence d'un pompage incohérent réduirait fortement la section efficace par un facteur supplémentaire sans changer drastiquement la variation des taux de diffusion vis-à-vis de la saturation de la sonde.

Dans le chapitre D, nous avons étudié la propagation d'une sonde cohérente à travers un ensemble atomique dans un environnement très contrôlé. Nous avons montré que même avec un tel contrôle des paramètres, la section efficace peut être fortement réduite. Nous avons mesuré que le facteur de réduction α dépend linéairement de la densité atomique et semble être universel, au moins pour le cas d'une polarisation σ. Nous avons proposé un modèle incluant un pompage incohérent pour simuler la propagation d'une sonde cohérente dans un ensemble atomique. La loi de Beer-Lambert en saturation usuelle est modifiée incluant un pompage incohérent qui s'alimenterait par des diffusions incohérentes spatiales et temporelles. La solution auto-consistante numérique de ce modèle rend la dépendance linéaire en densité optique. La réduction apparente de la section efficace est connectée, dans le régime diffusif ($b \gg s_c$), à une transmission diffuse résiduelle, et, dans le régime saturant, au champ électromagnétique de fond venant de diffusions multiples incohérentes dans le nuage (s_i). Une calibration similaire pourrait être réalisée pour d'autres configurations typiques comme des sondes de polarisation π.

Le chapitre E développe un modèle théorique pour la méthode d'imagerie sub-longueur d'onde en calculant les déplacements lumineux et les résolutions attendues avec un réseau optique à 1529 nm pour habiller le premier état excité. Nous montrons expérimentalement sur une transition repompeur (transition ouverte) que des volumes sub-longueur d'onde peuvent être transférés en quelques microsecondes vers un état de la transition cyclante où une imagerie standard peut être effectuée. Des résolutions spatiales de 100 nm à 20 nm ont été mesurées pour différentes géométries de faisceaux à 1529 nm (co- ou contre-propageants). Nous avons vu que le déplacement lumineux des états excités peut être calibré en utilisant une méthode spectroscopique. La largeur des courbes 'BAT' obtenues donne directement l'amplitude du déplacement lumineux et est en accord avec les calculs théoriques. Pour aller plus loin, le mixage des états dû aux forts déplacements lumineux pourraient être inclus dans le calcul de la fraction repompée en se basant sur les états propres de la méthode de diagonalisation de l'hamiltonien total. La réduction de la section efficace du chapitre D pourrait aussi être incluse dans l'analyse des données. De même, la méthode d'imagerie par absorption pourrait être remplacée avec une imagerie de champ diffusé ou de fluorescence pour avoir une analyse quantitative des résultats sur une transition cyclante (transition fermée).

Le chapitre F est une application directe de la méthode d'imagerie sub-longueur d'onde sur un réseau piégeant. Un condensat a été adiabatiquement chargé dans un réseau 1D créé par deux faisceaux à 1064 nm contre-propageants. La profondeur de piège du réseau piégeant a été précisément calibrée en utilisant la diffusion de Kapitza-Dirac. Nous avons réalisé l'imagerie sub-longueur d'onde des sites du réseau à 1064 nm en utilisant le réseau à 1529 nm habillant l'état excité. Nous avons expérimentalement démontré que les sites du réseau peuvent être excités avec une résolution sub-longueur d'onde. De même, la méthode fournit un moyen de mesurer la densité atomique dans un site en scannant la phase relative entre les deux réseaux. Nous avons utilisé la méthode pour nettoyer les sites du réseau et préparer au mieux une unique fonction d'onde. Dans la géométrie des faisceaux étudiée, la commensurabilité des réseaux permet difficilement d'interagir avec un seul site sans affecter les sites aux bords de la fonction d'étalement du point du microscope à forte ouverture numérique. Ce problème pourrait être résolu en utilisant un pas de réseau approprié pour l'état excité. Cela doit être pensé au début de la construction d'une expérience. Pour aller plus loin, les effets d'élargissement de la taille mesurée des densité atomiques d'un site ont été listés. Nous avons donnée des ordres de grandeurs des effets suivants: la phase relative initiale entre les deux réseaux, la température résiduelle initiale de la partie thermique du condensat, la force dipolaire de l'état excité et les effets apparaissant aux fortes densités atomiques comme les effets dipole-dipole et les pertes à trois corps.

L'étude expérimentale sur l'état excité habillé par un champ laser à 1529 nm a montré que les atomes peuvent être manipulés avec prédiction. L'état habillé peut être spatialement résonant avec un champ laser à 780 nm ce qui change les populations dans les états fondamental et excité. Cela est dû à l'établissement des cohérences atomiques venant du champ à 1529 nm se produisant sur une échelle de temps beaucoup plus rapide que les cohérences atomiques venant du champ à 780 nm. Cela reste une bonne approximation dès lors que le désaccord entre le laser à 1529 nm et la transition entre $5P_{3/2}$ à $4D_{5/2}$ est grand devant le déplacement lumineux.

Le montage 1D présenté dans le chapitre A avec un faisceau 1D à 1529 nm pourrait être utilisé pour étudier les temps de vie de ces états doublement habillés. Leurs propriétés de piège seraient testées dans des conditions expérimentales réelles et la comparaison avec les temps de vie théoriques de (Bellouvet et al., 2018) serait possible. Ensuite, de tels états pourront être utilisés dans des pièges en champ proche de façon fiable. Ils devront être utilisés pour sonder les forces de Casimir-Polder en premier lieu sur une surface plane. Pour étudier de tels effets, les procédures de transport des atomes vers une surface jusqu'à des distances d'une centaine de nanomètres devront être mises en place expérimentalement. Des études théoriques ont été réalisés dans les thèses précédentes (Busquet, 2017) en utilisant un piège magnétique sur puce pour amener les atomes de 500 µm à 5 µm de la surface. Ces atomes sont ensuite chargés dans une frange d'un réseau optique. Enfin, en changeant l'angle entre la surface et les faisceaux, les atomes seront transférés à 250 nm de la surface (Busquet, 2017).

Les expériences modélisant les hamiltoniens de Bose-Hubbard ou de Fermi-Hubbard ont tiré parti de la propriété diluée des gaz d'atomes froids où les effets collectifs peuvent être négligés. Par dilué, on signifie la distance moyenne inter-particules ($n_{3D}k^3 \ll 1$) plutôt que les corrections au-delà du champ moyen ($n_{3D}a^3 \ll 1$). Les degrés de liberté internes sont manipulés dans les réseaux optiques ayant des périodicités plus grande que la limite de diffraction établie par la transition atomique ($\lambda_0/2$). Pour réaliser des systèmes

tels que dans (Bellouvet et al., 2018) avec une périodicité de 100 nm ($< \lambda/2$), les effets des degrés de liberté externes via des interactions courtes portées de type dipole-dipole devront être inclus dans les modèles. En effet, le régime $n_{3D}k^3 \geq 1$ sera intrinsèquement vérifié pour de tels systèmes. Sonder des atomes avec des microscopes à gaz quantique et les manipuler dans des réseaux sub-longueur d'onde requerra de nouvelles techniques. Des couplages forts via des interactions dipole-dipole sont déjà à l'étude avec des montages dédiés (Glicenstein et al., 2021) et ont un rôle clé dans les horloges atomiques à base de réseaux optiques (Chang, Ye, and Lukin, 2004), dans les miroirs optiques basés sur des couches d'atomes structurées (Shahmoon et al., 2017; Rui et al., 2020) ou sur le blocage de photon dans des réseaux sub-longueur d'onde (Cidrim et al., 2020).

Detailed outline (FR)

Chacun des chapitres de ce manuscrit de thèse est résumé en français en rappelant les principaux résultats théoriques et expérimentaux. L'ensemble du manuscrit concerne l'atome de Rubidium 87 qui est une espèce bosonique. Les transitions optiques importantes sont celles entre l'état $5^2S_{1/2}$ vers $5^2P_{3/2}$ à 780.241 nm et l'état $5^2P_{3/2}$ vers $4^2D_{5/2}$ à 1529.366 nm (voir Annexe I.i).

Chapitre A: éléments de théorie sur les atomes ultrafroids et les réseaux optiques

Nous avons rappelé les éléments de théorie sur le refroidissement d'atomes neutres par évaporation qui permettent d'entrer dans le régime de dégénérescence quantique. En particulier, nous avons rappeler les lois d'échelle sur la densité dans l'espace des phases en fonction du nombre d'atomes pour la dynamique d'évaporation dans différentes géométries de pièges telles que linéaires et harmoniques.

Ensuite, nous avons rappelé comment caractériser un Condensat de Bose-Einstein (CBE) avec une équation de champ moyen. Les cas limites de forte et faible interactions ont été donnés à travers l'équation de Gross-Pitaevskii. Le CBE est une onde de matière et constitue un état quantique macroscopique qui est le point de départ pour étudier des systèmes complexes à plusieurs corps. L'un d'entre eux consiste à charger un CBE dans des réseaux optiques et d'étudier sa dynamique dans différents régimes d'interactions. Nous avons détaillé le cas du réseau optique 1D en donnant la structure de bande. Nous avons discuté de la limite des réseaux profonds très bien approximés par des oscillateurs harmoniques sur chacun des sites du réseau.

La dynamique du CBE se fait communément à travers l'Hamiltonien de Bose-Hubbard qui a été rappelé pour des réseaux optiques standards limités par la diffraction ($\lambda/2$). Il introduit des échelles d'énergie telles que l'énergie d'interaction sur site U et l'énergie d'effet tunnel t. La transition de phase d'un état superfluide à un état d'isolant de Mott peut être obtenue en variant le ratio t/U. L'étude des régimes fortement corrélés avec des fermions avec des interactions spin-spin sont caractérisées par une énergie de superéchange $J \propto t^2/U$. L'ordre de grandeur des fréquences caractéristiques est de 0.04Hz ce qui est très lent par rapport aux temps de cohérence et temps de vie des systèmes d'atomes froids. Il est nécessaire d'accélérer la dynamique du système en réduisant le pas du réseau ($\ll \lambda/2$) pour augmenter toutes les échelles d'énergie.

Le projet long terme de cette thèse, issu d'une étude théorique présentée en Fig. A.4, est de réaliser des réseaux sub-longueur d'onde en piégeant les atomes en champ proche d'une surface nanostructurée. La méthode de piégeage consiste à utiliser des états dou-

blement habillés (Bellouvet et al., 2018) dont nous avons montré le principe à travers la présentation de données expérimentales en espace libre en Fig. A.3. Dans un cas 1D, nous avons montré la force dipolaire générée par l'état excité qui a été habillé par un potentiel dipolaire entre deux états excités. Une barrière de potentiel permet de créer un confinement des atomes dans la direction de la force. La position de cette barrière est contrôlée simplement par la fréquence de couplage à 780 nm entre l'état fondamental et le premier état excité. Cette dépendance spatial du couplage est utilisée dans les chapitres E et F pour réaliser une méthode d'imagerie sub-longueur d'onde.

Chapitre B: Montage expérimental pour le Condensat de Bose-Einstein

Nous avons décrit les modifications effectuées sur le montage expérimental pour réaliser des Condensats de Bose-Einstein. Parmi eux figurent la stabilisation de la pression de la chambre ultra-vide, l'installation d'une étape de pompage optique pour le chargement du piège magnétique, l'automatisation des positionnements des faisceaux avec des platines micrométriques, des miroirs montés sur piézo-électrique et l'installation d'un axe d'imagerie en temps de vol avec un grandissement $\times 2$.

Ces modifications ont permis de réaliser et caractériser des condensats polarisés dans l'état Zeeman $|F_g = 1, m_F = -1\rangle$ avec un piège hybride combinant un piège magnétique et un piège dipolaire. Le condensat est typiquement constitué de 2.10^5 atomes à une température inférieure à 200 nK. En utilisant les éléments de théorie du chapitre A sur l'évaporation, nous avons caractérisé l'efficacité de l'évaporation jusqu'au régime de dégénérescence quantique où la densité dans l'espace des phases devient plus grande que 1 (Fig. B.30). Nous avons observé la double structure caractéristique d'un CBE (Fig. B.31).

Des implémentations ont permis de manipuler et d'imager les atomes. Le CBE peut être transféré dans un piège dipolaire croisé avant d'éteindre le gradient magnétique. Cela permet d'établir un champ magnétique homogène afin de pouvoir réaliser des transitions micro-ondes entre des états hyperfins avec des oscillations de Rabi de fréquences typiques de 20 kHz. L'ensemble de la chaîne micro-onde a été caractérisé (sec. B.2.3). Les contrôles en courants des bobines de compensation ont été changés afin de réduire les bruits de courant. Le bruit de champ magnétique est ainsi inférieur à 1 mG. L'axe de quantification pour les processus d'imagerie est ainsi bien déterminé. Un axe d'imagerie a été mis en place pour l'imagerie in situ des atomes (sec. B.3.4). Il est caractérisé par une ouverture numérique mesurée de 0.3, ce qui correspond à une résolution spatiale de 1.3 µm.

Ce chapitre sert de base expérimentale pour toutes les expériences présentées dans les prochains chapitres. Le schéma complet avec l'ensemble des faisceaux optiques est donné en Fig. B.2 et l'axe d'imagerie à forte ouverture numérique en Fig. B.18.

Chapitre C: Équations de Bloch optiques pour un système multi-niveaux

Ce chapitre sert de base théorique pour modéliser l'interaction d'un atome multi-niveaux en présence d'un champ cohérent de polarisation donnée, d'un biais magnétique constant et d'un pompage incohérent externe. Pour cela, le formalisme des équations maîtresses est utilisé. Ce chapitre permet d'identifier les mécanismes réduisant la section efficace d'absorption d'un seul système multi-niveaux.

Nous avons dérivé les équations de Bloch optiques pour un système à deux niveaux (S2N) incluant un pompage incohérent. Ce dernier est défini comme temporellement incohérent si le temps de cohérence associé est court devant la période d'une oscillation de Rabi. L'origine physique peut être une source de lumière large bande ou bien un bain de photons provenant des diffusions des atomes environnants (chapitre D). Les solutions analytiques sont données pour ce cas S2N. Le modèle est ensuite généralisé pour un système multi-niveaux (SMN) d'une transition fermée qui nécessite une résolution numérique.

Afin de réduire la complexité d'un système multi-niveaux, nous avons défini un système à effectif deux niveaux qui décrit au mieux la réponse d'un SMN. L'idée est de faire correspondre dans le modèle effectif la variation des taux de diffusion cohérents et incohérents pour tout régime de saturation au modèle complet SMN à l'état d'équilibre.

Sans champ incohérent et sans champ magnétique, le SMN se réduit exactement à un modèle effectif à deux niveaux avec une réduction de la section efficace d'un facteur α et une modification du champ diffusé cohérent β pour n'importe quelle polarisation du champ cohérent (Fig. C.4). Pour les cas limites de polarisation π et σ, $\beta = 1$ et α vaut respectivement 1.829 et 1. Dans le cas σ, ces facteurs sont particulièrement robustes à une polarisation imparfaite en raison du pompage optique qui tend à polariser le champ émis.

En présence d'un biais magnétique petit devant la largeur naturelle, les amplitudes des taux de diffusion se décrivent très bien par un modèle effectif et sont robustes à des imperfections de polarisation. Dans le cas circulaire, le modèle est même très robuste à de telles polarisations imparfaites. Ils correspondent exactement dans des cas particuliers où le champ magnétique est aligné pour des transitions soit π (Fig. C.6 à $\zeta = 0$) ou σ (Fig. C.5 à $\zeta = 1$). La modèle effectif étant scalaire, il ne rend pas les effets magnéto-optiques tels que des rotations de polarisation. Cependant les cas π et σ correspondent à la majorité des expériences.

En présence d'un champ incohérent de saturation s_i et du champ cohérent circulaire de saturation s_c, la réponse du système multi-niveaux est complexe (Fig. C.8). Le modèle effectif rend les tendances générales des taux de diffusions. La réduction de la section efficace d'un facteur α est tout de même proche de 1. La réduction totale de la section efficace est alors donnée par $\alpha_{eff} = \alpha(1+s_i)$. Le modèle effectif sert de base pour analyser les résultats du chapitre D.

Le formalisme a aussi été utilisé pour étudier la réduction de la section efficace sur des temps d'interaction courts. Elle dépend à la fois de la population initiale et de la polarisation du faisceau cohérent. La dynamique la plus longue est atteinte lorsque plusieurs diffusions sont nécessaires pour atteindre l'état d'équilibre lorsque des diffusions ont lieux pendant le régime transitoire sur les transitions optiques les plus faiblement couplées à la

lumière.

Enfin, la solution d'évolution des populations pour le cas d'une transition ouverte (une transition repompeur) a été donnée pour des systèmes à trois et cinq niveaux pour les chapitres E et F pour calculer le volume d'atomes de taille sub-longueur d'onde.

Chapitre D: Calibration de nombre d'atomes en imagerie par absorption saturante

Ce chapitre correspond à des mesures de section efficace d'absorption par imagerie d'absorption en régime de saturation.

Pour cela la loi de Beer-Lambert en saturation a été dérivée à partir d'une équation en champ. La polarisation étant circulaire, le facteur α a été introduit pour calibrer la section efficace de la même façon que (Reinaudi et al., 2007) et correspond aussi au facteur introduit dans le chapitre C.

Les effets de la sonde cohérente ont été discutés afin de minimiser les erreurs systématiques. Le paramètre de saturation et sa durée ont été bornés (Fig. D.4) afin de s'affranchir de plusieurs effets: le déplacement transverse des atomes sous l'effet d'une marche aléatoire par des diffusions de photon; le déplacement longitudinal le long de la sonde pour rester dans la profondeur de champ du microscope et le shift Doppler acquis par les atomes lors de diffusions. Le signal-sur-bruit sur la densité optique doit aussi être supérieur à 1 et maximisé pour ne pas être limité par le bruit de photon ou le bruit de caméra.

Ensuite, le montage expérimental pour mesurer la transmission de la sonde cohérente à travers un nuage d'atomes thermiques a été présenté. Le nombre d'atomes total et la température ont été calibrés par temps de vol pour donner une estimation des tailles du nuage et de la densité optique b in situ. Le paramètre de saturation a été calibré en mesurant la puissance pour chaque point expérimental avec une photodiode rapide, la taille du faisceau a été mesurée et la position du faisceau par rapport aux atomes mesurée. Le champ magnétique est aligné avec la direction du faisceau incident afin d'initialement bien définir l'axe de quantification. Le nombre d'atomes peut être varié avec un tranfert micro-onde. L'oscillation de Rabi entre l'état fondamental $|F_g = 1, m_F = -1\rangle$ et l'état de la transition cyclante $|F_g = 2, m_F = -2\rangle$ permet de contrôler le nombre d'atomes à imager avec une sonde circulaire. Avec toutes ces calibrations, le facteur de correction α devrait être égal à 1 pour la réponse d'un atome unique.

En suivant (Reinaudi et al., 2007), nous avons mesuré le paramètre α pour plusieurs nombres d'atomes contrôlés avec la micro-onde (Fig. D.12). Une forte dépendance de α avec la densité optique apparaît. Avec un modèle de propagation 1D des champs cohérents et incohérents, nous avons montré que (Fig. D.15) la réduction de la section efficace d'absorption est connectée, dans le régime diffusif ($b \gg s_c$), à la transmission diffuse résiduelle, et, dans le régime saturant, au champ résiduel de fond venant de diffusions multiples incohérentes dans le nuage. Dans les deux cas, la correction est linéaire avec la densité optique et reproduit bien les dépendances expérimentales de α. Nous montrons que ce facteur n'est pas unique pour un nuage donné car la densité optique varie spatialement. Pour une polarisation circulaire, la facteur de correction que nous mesurons est $\alpha = 1.17(9) + 0.255(2)b$ et semble être universel. L'incertitude sur l'ordonnée à l'origine est dominée par l'incertitude sur le paramètre de saturation. Le cas limite de faible densité

optique converge vers la réponse d'un atome unique.

Pour aller plus loin, le modèle pourrait être généralisé à 3D et intégrer les modifications de ré-absorption des photons du spectre de Mollow. Une calibration similaire pourrait aussi être faite pour une polarisation π.

Chapitre E: Imagerie par absorption in situ avec une résolution sub-longueur d'onde en utilisant un état excité habillé

Ce chapitre présente la méthode d'imagerie sub-longueur d'onde utilisant l'habillage de l'état excité $5P_{3/2}$. La transition optique à 1529 nm entre les états excités $5P_{3/2}$ et $4D_{5/2}$ permet de réaliser un habillage de l'état $5P_{3/2}$. La transition atomique à 780 nm est ainsi modulée spatialement. Dans des zones de fortes variations du déplacement lumineux, l'interaction avec un faisceau homogène à 780 nm est résonante dans un volume de taille sub-longueur d'onde (Fig. E.6). Ces tailles dépendent directement de l'amplitude des déplacements lumineux de l'état excité. Ces derniers ont été calculés numériquement afin de les comparer aux expériences à l'aide des modèles trois et cinq niveaux donnés dans le chapitre C.

Nous avons donné des formules analytiques pour les largeurs à mi-hauteurs pour les cas où le faisceau à 780 nm est résonant en bas ou au milieu de la modulation à 1529 nm. Pour une transition repompeur avec un modèle à trois niveaux: Eq. (E.23) est la largeur à mi-hauteur en bas de modulation et Eq. (E.24) celle au milieu de modulation.

Nous avons présenté les montages optiques pour les faisceaux à 780 nm et 1529 nm. Des géométries de faisceaux co-propageants et contra-propageants à 1529 nm peuvent être réalisées (Fig. E.12). Nous avons rappelé que l'alignement du microscope par rapport au réseau est critique pour de l'imagerie par absorption en raison de l'effet Talbot qui est la diffraction de l'onde incidente sur un réseau de diffraction (Fig. E.15).

Sur une transition repompeur, nous avons montré que mesurer des nombres d'atomes permet d'être quantitatif sur les résolutions spatiales de la méthode. La mesure quantitative de nombre d'atomes est limitée, à bas nombre d'atomes, par le niveau de sensibilité en nombre d'atomes par l'imagerie par absorption (10 atomes), et à grand nombre d'atomes, par la calibration de la section efficace d'absorption. Entre ces deux cas limites, sans paramètre ajustable, les nombres d'atomes mesurés in situ en milieu de modulation sont en accord avec une estimation théorique basée sur des mesures par temps de vol. Pour les cas co-propageant et contra-propageant, les meilleures résolutions mesurées sont respectivement de 100 nm (Fig. E.19) et 20 nm (Fig. E.22) pour des saturations de repompeur de l'ordre de 0.02 et des temps de 10 µs.

Sur une transition d'imagerie, la méthode s'applique mais une analyse quantitative par imagerie d'absorption est plus difficile. En effet, l'analyse est faite avec une loi de Beer-Lambert avec un désaccord qui dépend de l'espace. Le taux de diffusion varie en raison du désaccord alors que la densité optique est homogène. Il faudrait alors être quantitatif plutôt sur le nombre de photons diffusés ce qui nécessite la mesure de fluorescence ou de champ diffusé.

Chapitre F: Imagerie sub-longueur d'onde appliquée à la super-résolution des sites d'un réseau piégeant

Dans ce chapitre, nous avons appliqué la méthode d'imagerie sub-longueur d'onde du chapitre E sur un réseau piégeant 1D avec une période de 532 nm (piège dipolaire à 1064 nm). Pour cela, un condensat est initialement chargé adiabatiquement dans le réseau 1D. La profondeur du réseau (Fig. IV.7) est calibrée avec la méthode de diffusion Kapitza-Dirac. La profondeur maximale disponible sur l'expérience est de 1000 énergies de recul. Pour de telles profondeurs, les déplacements lumineux liés au piégeage sont de l'ordre de la largeur naturelle de la transition à 780 nm (Fig. IV.8).

Le double réseau (Fig. F.5) à 1064 nm et 1529 nm a une commensurabilité de 13 interfranges à 1064 nm pour un angle entre les faisceaux à 1529 nm de $2\theta = 2 \times 5.7°$. Ceci signifie que des atomes séparés de 13 interfranges voient exactement le même potentiel dans l'état excité. Ils sont séparés de 6.9 µm, ce qui est bien résolu par notre objectif de microscope.

À partir de ces calibrations, nous avons imagé in situ les sites du réseau avec le réseau à 1529 nm dans l'état excité. Le réseau à 1529 nm permet de contrôler sélectivement les sites résonants en variant la phase relative des deux réseaux et la fréquence à 780 nm (Fig. F.6). Cela nous permet de calibrer le déplacement du piézo-électrique qui contrôle la position du réseau à 1064 nm par rapport au réseau à 1529 nm.

En imageant en milieu de modulation à 1529 nm, nous mesurons la densité atomique dans les sites avec des résolutions typiques de 20 nm en largeur à mi-hauteur. Pour cela, nous utilisons le réseau à 1529 nm pour préparer au mieux un seul site dans le réseau à 1064 nm avant de l'imager. En pulsant un laser de repompeur, nous nettoyons le réseau en variant la fréquence du laser à 780 nm et la phase relative entre les réseaux (Fig. F.7). À la fin du nettoyage, nous mesurons expérimentalement une taille 1.9 fois plus grande que la valeur attnedue en théorie. Cette dernière étant connue par la résolution sub-longueur d'onde et la taille de la densité atomique dans l'état fondamental du piège à 1064 nm (Fig. F.13).

Nous avons donné des ordres de grandeurs sur les effets qui pourraient élargir la taille mesurée. Parmi eux, des fluctuations (long termes par la température) de la phase initiale entre les réseaux pourrait expliquer en grande partie la différence observée. L'hypothèse de l'occupation de la bande fondamentale peut être aussi remise en question. La température initiale de la partie thermique permettrait l'occupation de niveaux d'énergie excités longitudinaux dans le réseau à 1064 nm. De même, des effets non-adiabatiques dus à la force dipolaire de l'état excité par effet de double habillage peut conduire à du chauffage transitoire amplifié dans le régime d'oscillations paramétriques. Hors de ce régime, l'effet du double habillage reste négligeable. Enfin, nous avons donné les densités atomiques dans le réseau à 1064 nm. Des effets dipole-dipole à résonance peuvent conduire à du chauffage car les densités atomiques sont de l'ordre de $kr \approx 1$ où r est la distance moyenne inter-particules et k le vecteur d'onde à 780 nm. Cependant, hors résonance l'effet serait moindre. En revanche, avec 2.10^5 atomes dans le condensat initial, en chargeant le réseau, des pertes par recombinaison à trois corps réduisent le nombre d'atomes et peuvent conduire à du chauffage sur un site.

Appendix I

I.i Atomic structure of Rubidium 87

This Appendix shows the atomic structure of ^{87}Rb for the relevant levels used in this thesis. Fig. I.1 shows a few fine states with their corresponding hyperfine states. The D_2-line is from $5S_{1/2}$ to $5P_{3/2}$, more detail can be found in (Steck, 2001). Another transition used for this atom by other groups is the D_1-line which is from $5S_{1/2}$ to $5P_{1/2}$ (Steck, 2001).

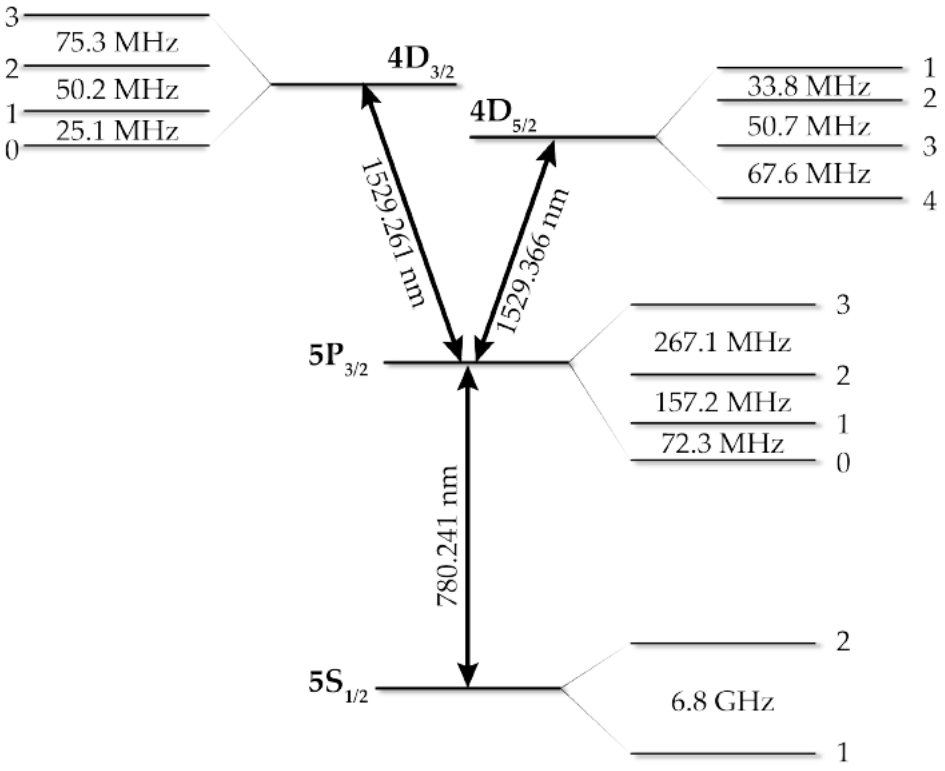

Figure I.1: Atomic structure of a few levels of ^{87}Rb from (Bellouvet, 2018).

Appendix II

This Appendix describes the electronic control of the experiment with a specific focus on the modifications performed during the thesis. We first describe the computer control with Cicero/Atticus softwares, then the implementation of output buffer circuits. After that, we describe the current control of the main quadrupole coils. Finally, we list all analog circuits that are used through the entire thesis.

II.i Computer control

The experiment is controlled and sequenced with the software Cicero Word Generator where analog/digital voltages, frequencies, and timings are defined. The time resolution can be tuned for each step to optimize the number of points in the buffers. Cicero (client) communicates on a local network with Atticus (server) software which sends all voltages to the experiments via analog and digital National Instrument cards. An FPGA clocks Atticus which enables the control of the time resolutions. All the information about the sequence is contained in Cicero that creates a .txt file at the beginning of each run which is read by all slave softwares.

Cicero and Atticus are our 'master' programs and in parallel to them, different 'slave' programs are running:

- MTPutty: used to communicate with direct digital synthesizers (DDS). It sends the laser detunings and RF frequencies for the experiment. It runs a script to read the .txt directly on Atticus via a local network connection. Then the frequencies are sent to the DDS using a RaspBerry Pi. This DDS is trigged at different times during the sequence to set/sweep the frequencies previously loaded into the DDS. There are 4 outputs for the DDS given in Table II.1. The current implementation of the frequencies has one issue: each time a frequency is added to the DDS list, the register of the DDS has to be updated with the new frequencies such that everytime a trigger is coming, a frequency is effectively changed at the right time. As a result, the DDS are fully operational after launching two runs.
- Camera's softwares waiting for external triggers will save the images in a local folder.
- A Matlab program treats in real time the acquired images.

In Appendix II.ii, we present the implementations of output buffers placed after the analog/digital National Instruments cards that reduce technical noises, avoid channel cross-talk and enable high driving power.

OUT	MTPutty channel name	Frequency for ...
1	mot2d	2DMOT cooler beatnote
2	mot3d	3DMOT cooler beatnote
3	RF	GHz transitions (hyperfine)
4	RF_F1	MHz transitions (Zeeman)

Table II.1: Frequency outputs of the DDS rack front panel.

II.ii Reducing the National Instrument card noises

The computer control widely described in the thesis (Salvador Vasquez Bullon, 2016) is composed of the following National Instrument cards:

- 1 TTL card PXIe-6536 which is device 1. It has 32 channels connected to a connector block NI CB-68LPR.
- 3 analog cards NI PXI-6733 which are devices 2 and 3 (16-bits) and NI PXI-6713 which is device 4 (12-bits). Each of them has 8 output channels. They are connected to BNC2110 connector blocks from National Instruments.

We noticed that the BNC2110 blocks were adding a lot of voltage noise on analog channels as seen for instance for the channel Dev3 ao3 in Fig. II.1 where the rms noise is reduced by more than a factor of 2 if the BNC2110 is by-passed. It was not a common noise as channels had different noises.

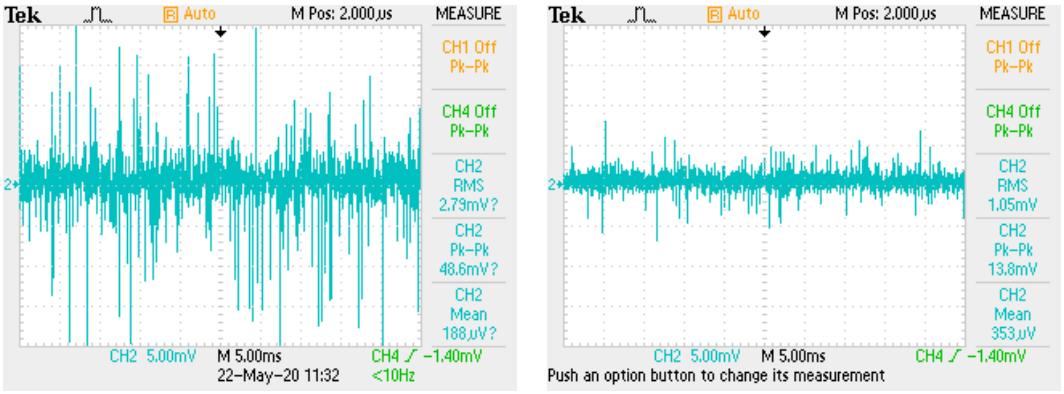

Figure II.1: Voltage noise from the Dev3 ao3 passing through the BNC2110 connector block (left) or by-passing it (right). It is measured with an oscilloscope TBS1064 (DC-60 MHz).

We decided to replace the connector blocks with 'buffer card' circuits developed by the electronics workshop to reduce voltage noises. It also offers the possibility to drive power up to 250 mA thanks to output buffers (Texas Instruments BUF634). It replaces the old system as shown on Fig. II.2. Power supplies of +24V are for fans, and ±15V are for the buffers[1].

Compared to the previous PhD thesis, the buffer circuits slightly change the offset (~ 20 mV) and slope (~ 0.98) of all the calibrations. The offset depends on the buffer and in general it is in-between 20 mV to 30 mV and the gain is about 0.98. This means that the voltage defined in Cicero V_{cicero} passes through a buffer and sends to the experiment the

[1]The power supply should be replaced by a high power one if many buffers are delivering high powers.

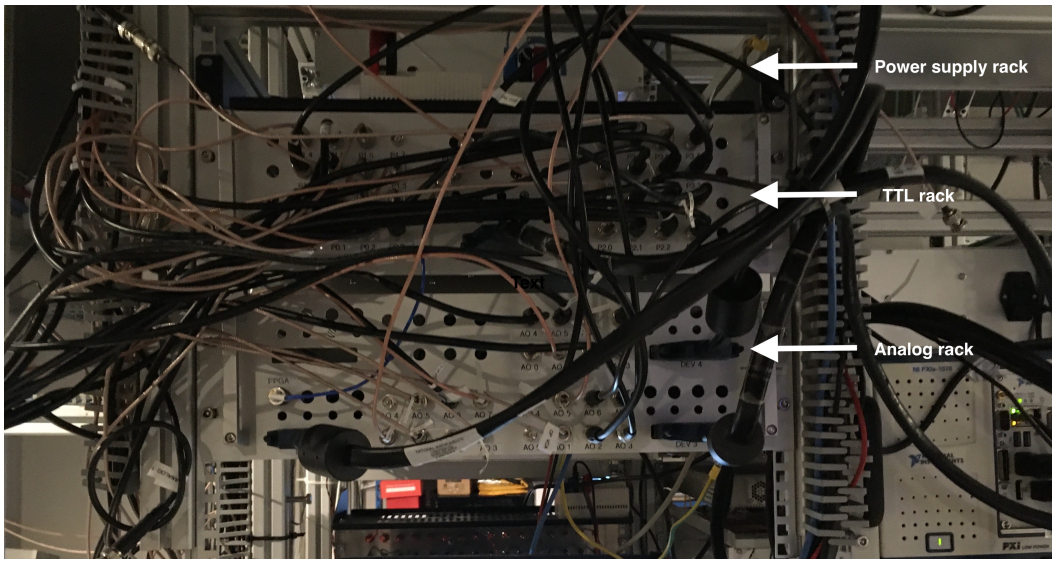

Figure II.2: Picture of the new system with buffers for distributing the voltages on the experiment.

voltage $V_{out} = aV_{cicero} + b$ where a and b depend on the buffer. In Fig. II.3 we show these coefficients for the output 0 of the device 2.

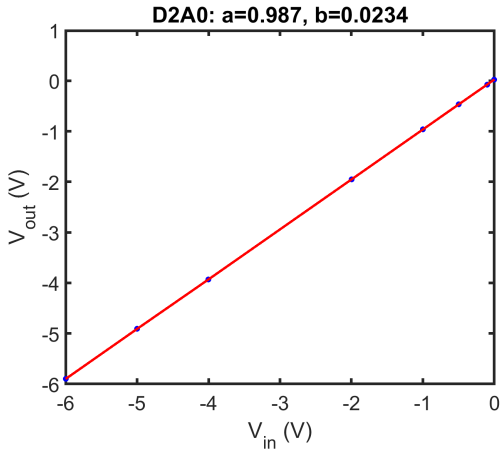

Figure II.3: Characterization data (points) of the buffer output V_{out} as a function of the input voltage from Cicero V_{cicero} and linear fit (red) with the slope a and the offset b (in V).

In practice, it is not useful to know these coefficients as calibrations can be done directly using V_{cicero} voltage[2].

II.iii High current control electronics for the magnetic trap coils

In our experiment, the stabilization of the high current flowing in the MOT and magnetic trapping coils is realized using a homemade control electronics. The coils are driven in

[2]If needed, these coefficients can be computed for all channels with data on 10/2020.

series so a single locking circuit is needed. The circuit of Fig. II.4 is composed of the following components:

- A power supply Delta Elektronika SM66-AR-110: it is the main coils power supply. The compliance voltage of the supply is externally controlled by the voltage $V_{c,PS}$ which is generated through Cicero by the NI cards[3]. The time response of the supply is slow (≈ 50 ms).
- A MOSFET IXFN200N10P: it is the transistor for the current feedback. It has $R_{DS(ON)} < 7.5m\Omega$ and dissipates $P = R_{DS}I^2$. A varistor S20K250 is mounted across GS to prevent MOSFET failures induced by AC spikes.
- A resistor TGHGCR0200FE $R_{RES} = 20m\Omega$, which is temperature stabilized with a PTC2.5K-CH temperature controller (wavelength electronics), gives the voltage measurement V_{RES} to be compared to the Cicero setpoint in the locking circuit.
- Locking circuit (Appendix II.iv): it takes V_{RES} and the Cicero voltage setpoint as inputs, integrates and feedbacks V_{fb} thanks to a differential operational amplifier across the MOSFET's GS. We noticed that INA128-amplifiers were sensitive to the MHz-scale evaporation frequencies (small bumps in the current due to the antenna radiation) which causes a voltage offset in this component. The differential amplifier THS4131 does not have this issue, it is implemented on the circuit.
- IGBT VS-GA200SA60UP (or IXFN200N10P): its voltage drop saturation is $V_{CE(ON)} = 1.92V$ which makes it convenient for switching off the current with low dissipation $P = V_{CE(ON)}I$. A varistor S20K250 is mounted across the IGBT's GE to dissipate AC spikes.

During the sequence, the compliance voltage of the supply is constantly adapted to be large enough for the current to be delivered and low enough to minimize the voltage drop across the MOSFET's DS that is responsible for heat dissipation in the MOSFET.

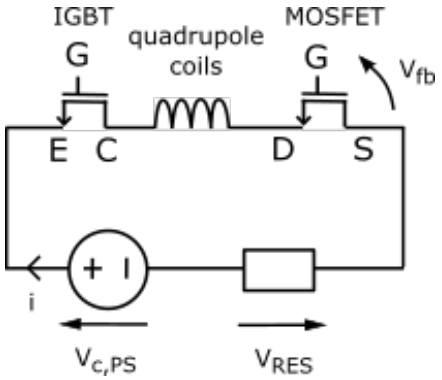

Figure II.4: Electronic circuit for quadrupole coils current feedback.

Calibration I(V): The voltage drop in the circuit is: $V_{c,PS} = (R_{DS(ON)} + R_{RES} + R_{coils})I + V_{CE(ON)}$ where we neglect the resistance of the cable. The position of the coils in the circuits is important for filtering voltage spikes when the IGBT is turned off. The calibration of the current I versus Cicero setpoint V_{lock}[4] is done by measuring the

[3] Additionally amplified by 13.2.

[4] Including the buffer card calibration (channel D2A0) in II.ii, $V_{lock} = 0.9873V_{NI} + 0.0234$ where V_{NI} is the voltage given by Cicero.

current with a Hall probe (Chauvin Arnoux P01120043A) as a function of the Cicero voltage setpoint. The $V_{c,PS}$ is calibrated[5] by increasing the compliance voltage until the current is locked. From the maximum current of 55 A, the current drops in 100 µs. The conversion to the total maximum magnetic gradient onto the atoms is (Busquet, 2017; Meyrath, 2004) $B^{'} = 2.94$ (G/cm/A). Table[6] II.2 gives the typical experimental current setpoints.

Sequence step	$B^{'}$ (G/cm)	I (A)	V_{lock} (V)	$V_{c,PS}$ (V) (no gain)
MOT	11.8	4.01	-0.336	0.27
CMOT	23.5	7.99	-0.661	0.41
Molasses	0	0	-0.008	0.12
MT abrupt	50	17.01	-1.396	0.74
MT final	161.7	55	-4.496	2.11
DT loading	28.8	9.8	-0.808	0.48
DT exp evap	25	8.5	-0.7	0.43

Table II.2: MT gradients: typical optimized setpoints for the experiment.

Remarks

- To do TOF measurements, the MT gradient is linearly swept to zero by sweeping the current to zero during 200 µs at the beginning of the TOF. This ensures that the atoms are adiabatically following the local quantization axis towards the one given by compensation coils when the MT gradient is zero. Due to coil inductance and Eddy currents, the quadrupole magnetic field tends to zero with a decay time of about 5 ms.
- The MT gradient calibration can be precisely done with a TOF in a nonzero magnetic gradient lower than the gravity gradient, as their acceleration gives access to the magnetic gradient along z.
- Experimentally, it is possible to control the coils independently from each other with two identical current locking circuits and two MOSFETs (called circuits 'up' and 'down'). It will enable to tune the potential minimum position. The 2nd MOSFET channel is ready to be used but still needs to be calibrated.
- As detailed in (Busquet, 2017), there is an Arduino that prevents the coils from overheating by setting the TTL to 0 above a coil temperature of 30°C.

II.iv Analog circuits for amplifiers, PIDs, etc.

In this PhD, we widely used analog cards that have previously made by S. Bernon and previous members:

- '2 fast amplifiers' circuits: used for amplifying RF signals or for transimpedance amplifiers for homemade photodiodes (power locks mainly).

[5]Calibration of the MT coils current and MT power supply versus the lock setpoint: $I(A) = -12.255V_{lock}(V) - 0.10165$ and $V_{c,PS} = -5.8396V_{lock}(V) + 0.57302 + 1$. The last +1V guarantees that the power supply does not limit the current at any moment.

[6]Tab 18/03/2019 in file 'calibration_voltage_cicero_experiment.xlsx'.

- '2 integrators' circuits: used for integration (integrator only) and feedback of error signals like power locks taking reference setpoints from Cicero. An external feed-forward voltage can be summed up with the integrated error to feedback the signal around the desired setpoint which is useful to be faster than the integrator time.
- 'Differential locking amplifier' circuits: used for the current lock of the main quadrupole coils which has 1 differential input (measurement), 1 input setpoint (Cicero) and 1 differential output (feedback).

Other cards developed by the electronics workshop have been used:

- 'Frequency to voltage converter': a frequency to voltage converter is done with a fixed '/8' divider HMC434 (0.2-8 GHz, minimum input 0 dBm) followed by a tunable '/N' divider UXN6M9P (DC-9 GHz) where N can be tuned from 8 to 511 with internal switches. Then, the frequency/voltage divider AD650 can divide up to 1 MHz. After that, an error signal is obtained by a summing amplifier summing the converted voltage, a reference Cicero analog voltage, and an internal offset (to lock around a given frequency). Finally, a PID where both P and I can be externally controlled with trimmers is used to generate the feedback voltage. Refer to the electronics workshop datasheet for more detail. This circuit has been used to frequency lock the Sacher laser for the frequency tunable repumper laser in the subwavelength imaging chapters.
- 'Voltage reference': used to drive VCOs with stable voltages. It is described below as it has been developed during this PhD.

Below, we give the details of the 'voltage reference' circuits. VCOs were originally driven by analogs channels from the NI cards, but they are constant values that do not change during the experiment. In order to have more analog channels available on the NI cards, the VCOs are now driven by reference voltage racks composed of an adjustable low noise voltage reference. The circuit developed by J.H. Codarbox from the electronics workshop is given in figures II.5, II.6 and II.7.

We decided to have 3 identical channels with the following characteristics: a low noise adjustable voltage reference MAX6160 followed by a voltage follower for impedance separation, a summing amplifier which sums this constant voltage with an external RF voltage (molex In BNC FAV), then a switch which can change the sign with another amplifier if needed and finally a current follower (BUF634).

For the MAX6160, the internal R_3, R_4 resistors and external *trimmer* set the voltage values. IMPORTANT: the implemented circuits on the experiment have a mistake: the MAX6160 output pin is connected to the molex input 1 instead of being connected to the voltage follower input 3. It is solved by hand by putting a 0 Ω resistor on R_3 and a resistor of the same value as R_3 but between the cables coming from output 1 of MAX6160 and input 3 of the voltage follower. This mistake isn't in figures II.5, II.6 and II.7 as the connections have been corrected.

The resistors of the voltage reference stage are $R_3 = 150\ k\Omega$, $R_4 = 270\ k\Omega$ and a trimmer of 20 or 50 $k\Omega$ to tune the voltage. The next amplifier stage has a fixed gain about 4. The rack output voltages are resumed in Table II.3.

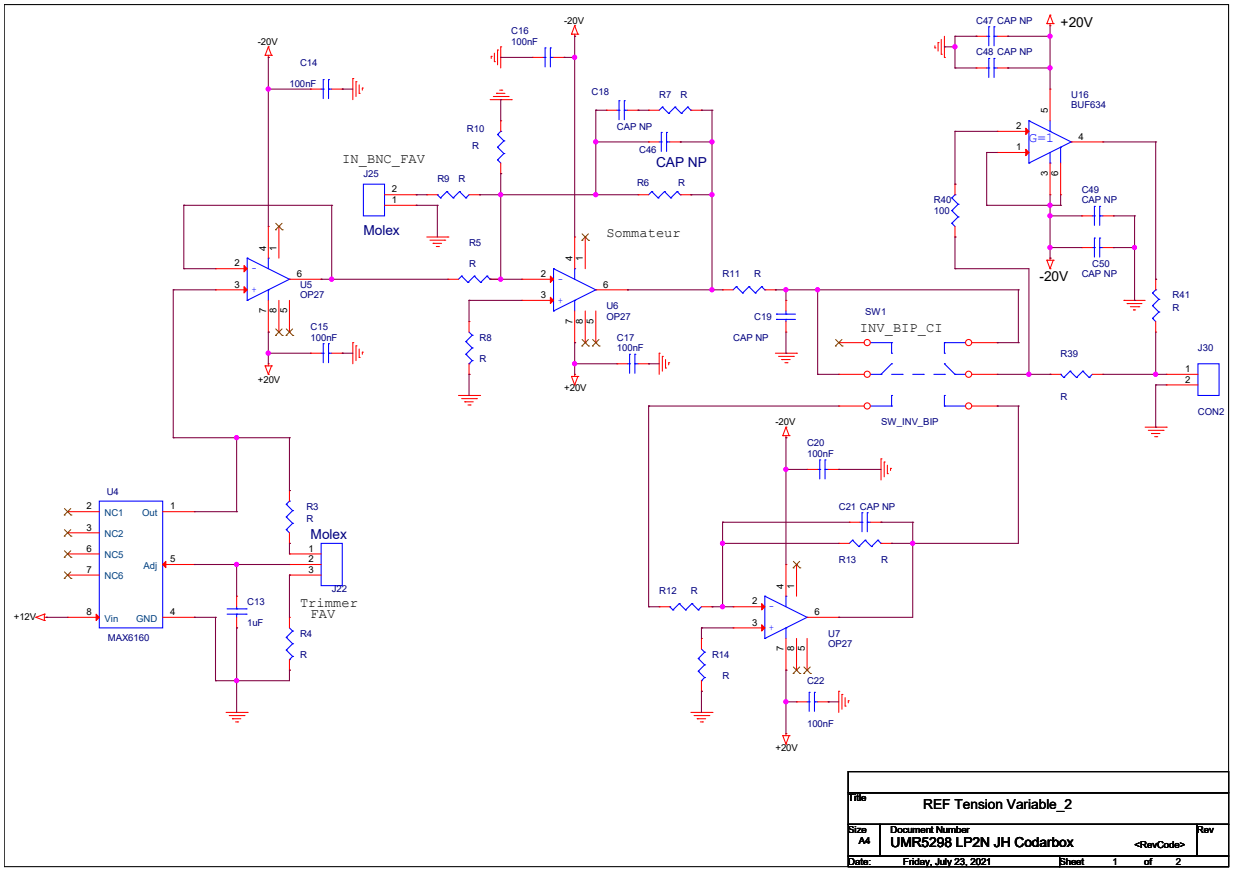

Figure II.5: Main electronics circuit for the reference voltage racks.

VCO name	VCO input voltage (V)
3DMOT R	8.807
3DMOT C	9.162
Im	1.545
OP C	-7.6
OP R	8.9

Table II.3: Voltage outputs from the reference voltage circuits for all VCOs of the 780 nm optical bench.

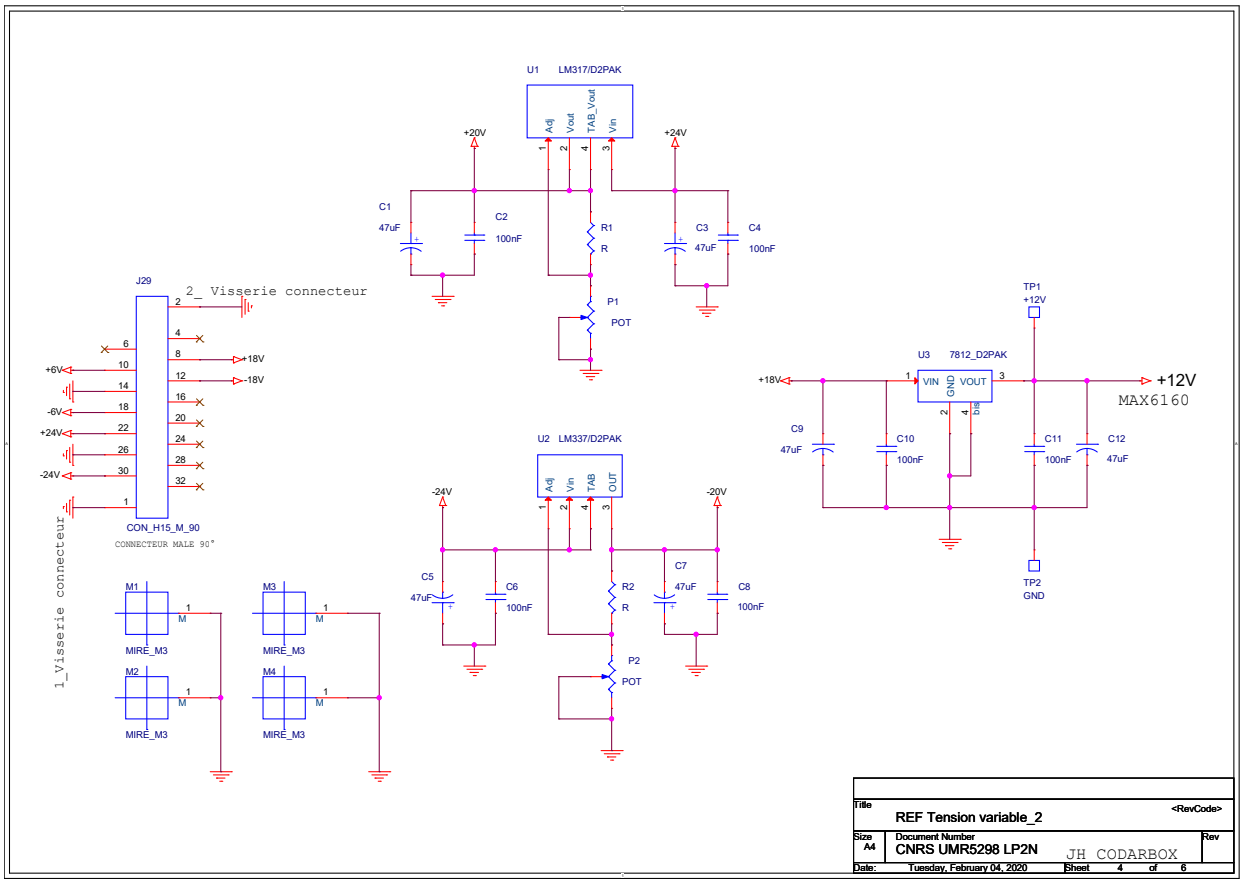

Figure II.6: Electrical connectors and internal regulators of the main electronics circuit for the reference voltage racks.

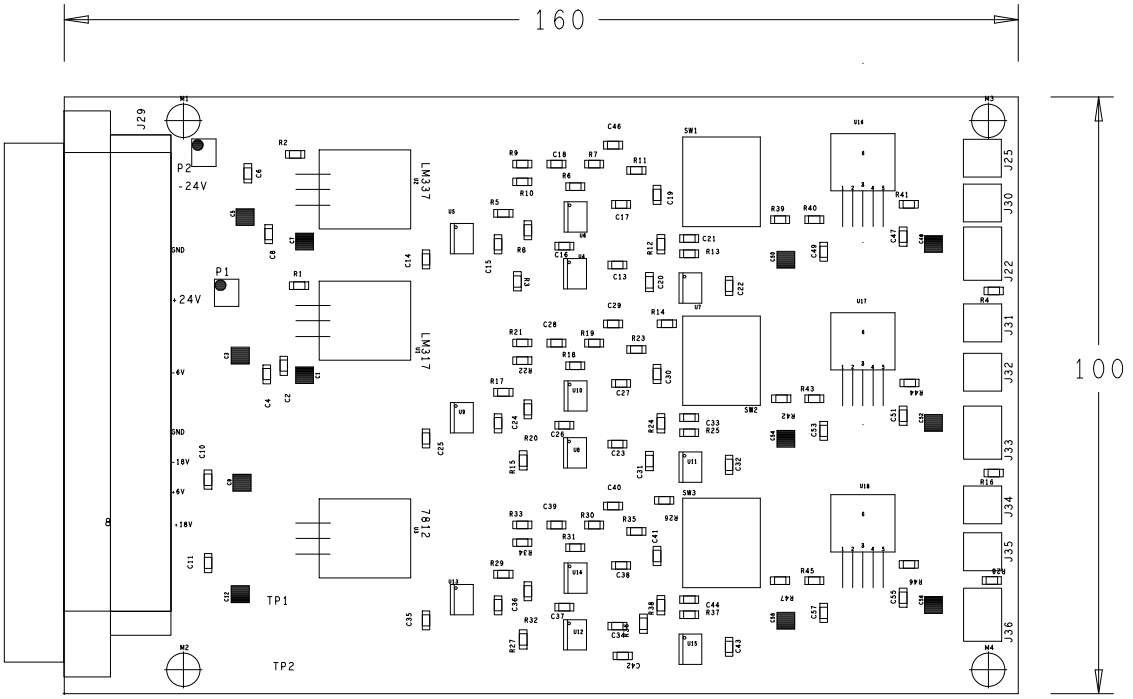

Figure II.7: Top view of the reference voltage cards showing the 3 horizontal channels.

Appendix III

III.i Talbot effect

In this Appendix, we discuss the Talbot effect occurring when we get in situ images of a lattice using absorption imaging. A plane wave with a wavelength λ will diffract on a grating with period d. It results in an intensity pattern which varies along the propagation due to interferences of waves coming from each slit. After the Talbot (Wen, Zhang, and Xiao, 2013) length z_T, the intensity pattern is exactly the one of the grating. It is called a Talbot image. At the distance $z_T/2$, a Talbot subimage appears and the intensity profile is shifted by a phase of π in the transverse direction.

In our experiment, in order to appropriately image in situ the fringes with our microscope objective, which has a narrow depth-of-field, the focus needs to be well-positioned and we should make sure we do not image a Talbot image.

The Talbot equation is derived following (Wen et al., 2011). The Fresnel-Kirchhoff diffraction integral is used to compute the diffraction of a plane wave onto a grating after a distance Z for a grating at position $z = 0$. Under the paraxial approximation such that $\lambda \ll d$, *i.e.* small diffraction angles, the field is given by:

$$E(X, Z) = B \int_{-\infty}^{+\infty} A(x, 0) e^{ik(Z + \frac{x^2}{2Z} - \frac{xX}{Z} + \frac{X^2}{2Z})} dx, \tag{III.1}$$

where B is a global prefactor, X a coordinate is the observation plane and x a coordinate in the object plane.

The transmitted field right after the grating is decomposed onto the Fourier basis:

$$A(x, 0) = \sum_{n=-\infty}^{n=+\infty} c_n e^{i2\pi n \frac{x}{d}}. \tag{III.2}$$

The Talbot effect is obtained by combining Eq. (III.1) and Eq. (III.2) and performing the integral:

$$E(X, Z) = B \sum_{n=-\infty}^{n=+\infty} c_n e^{-i2\pi n^2 \frac{Z}{z_T}} e^{i2\pi n \frac{X}{d}}, \tag{III.3}$$

where the Talbot length is defined as $z_T \equiv 2d^2/\lambda$.

The intensity at position (X, Z) is then computed as:

$$I(X,Z) = \frac{1}{2} C\epsilon_0 |E(X,Z)|^2. \tag{III.4}$$

First, let us consider the case of a pure sinusoidal grating with period d such as $A(x, L) = (1 + \cos(2\pi x/d))$. The Talbot effect arises from a three-beam interference:

$$E(X,Z) = B\left(\frac{1}{2} + \frac{1}{4} e^{-i\pi\lambda Z/d^2} e^{-i2\pi X/d} + \frac{1}{4} e^{-i\pi\lambda Z/d^2} e^{+i2\pi X/d}\right). \tag{III.5}$$

The 2D plot of the intensity versus the propagation Z and transverse distance X is called a Talbot carpet. Fig. III.1 shows the intensity profile for the sinusoidal case of Eq. (III.5). As mentioned before, the plane $Z = 0$ is the image of the grating, $Z/z_T = 1$ is a Talbot image and $Z/z_T = 0.5$ is a Talbot subimage[1].

Another example is a square grating (Case et al., 2009) that is similar to Young's slits. It has more Fourier components as depicted on Fig. III.1 leading to a more complicated diffraction pattern.

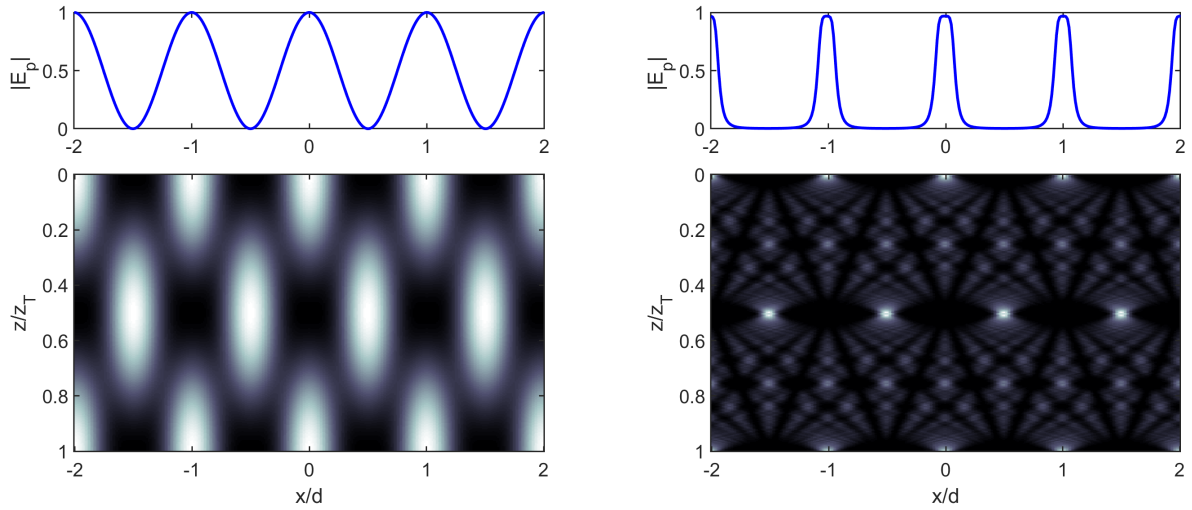

Figure III.1: 1D plots of the probe transmission ($|E_p| = |A|$) for a sinusoidal (left) and square (right) grating at $z = 0$ and 2D plots of the Talbot carpets.

Now, we consider the case of a 1529 nm lattice on the repumper transition. After being repumped, atoms are similar to a grating as they modulate the amplitude of the transmission. On resonance and in the low saturation regime, the transmitted field is given by the Beer-Lambert's law $T(x, L) = e^{-n_{2D}(x)\sigma_0/2}$. The atomic column density $n_{2D}(x)$ is proportional to the repumped fraction ρ_{22} given by Eq. (C.62). Therefore the fringe pattern obtained after repumping at a given repumper detuning gives Fourier components that will contribute to the diffraction of the resonant imaging beam. Numerically we decompose the previous transmission onto Fourier components in order to compute the intensity of Eq. (III.4) which leads to the optical density $b(Z) = n_{2D}\sigma_0 = -\ln(I(Z)/I_0)$ that one can measure. Fig. III.2 shows tomographic images of $b(Z)$ that can be used as an abacus to estimate the out-of-focus length of the image plane for any given Talbot length.

[1]More detail for this case can be found in (Zhou and Burge, 2010), and (Goodman, 1996) to go beyond the paraxial limit.

For the co-propagating 1529 nm beam configuration that can be resolved by our imaging system, the interfringe ranges from 6 to 12 µm which verifies the paraxial condition $\lambda \ll d$. For λ =780 nm, it gives z_T ranging from 92 to 370 µm, meaning that if the lattice period changes, then the Talbot length changes a lot compared to the microscope depth-of-field. Any focus misalignment is dramatic for measuring the transmission. In the main text we showed out-of-focus and on-focus experimental images in Fig. E.15. Based on Fig. III.2 the out-of-focus situation might correspond to the case $Z/z_T = 0.2$ or 0.3. For $d = 8$ µm, it is a defocus of 32 to 50 µm.

The counter-propagating 1529 beams where the interfringe is about 765 nm corresponds to larger diffraction angles so the paraxial approximation does not hold anymore. The diffraction equations are more complicated. In any case, as these fringes are not resolved by our imaging system, we would not see a difference while moving the microscope focus.

Microscope alignment: to avoid Talbot images, we first image a compressed dipole trap (DT1). First, we scan the focus by imaging a compressed DT1 and measure the cloud width. The minimum width gives the best focus aligned onto the atoms. It avoids diffraction effects coming from a grating in the object plane. A fine scan of the focus is then performed using the co-propagating 1529 beams and repumping on resonance the atoms. Again the minimum fringe width will give the focus. From here, the microscope is considered aligned and the counter-propagating 1529 beams can be used.

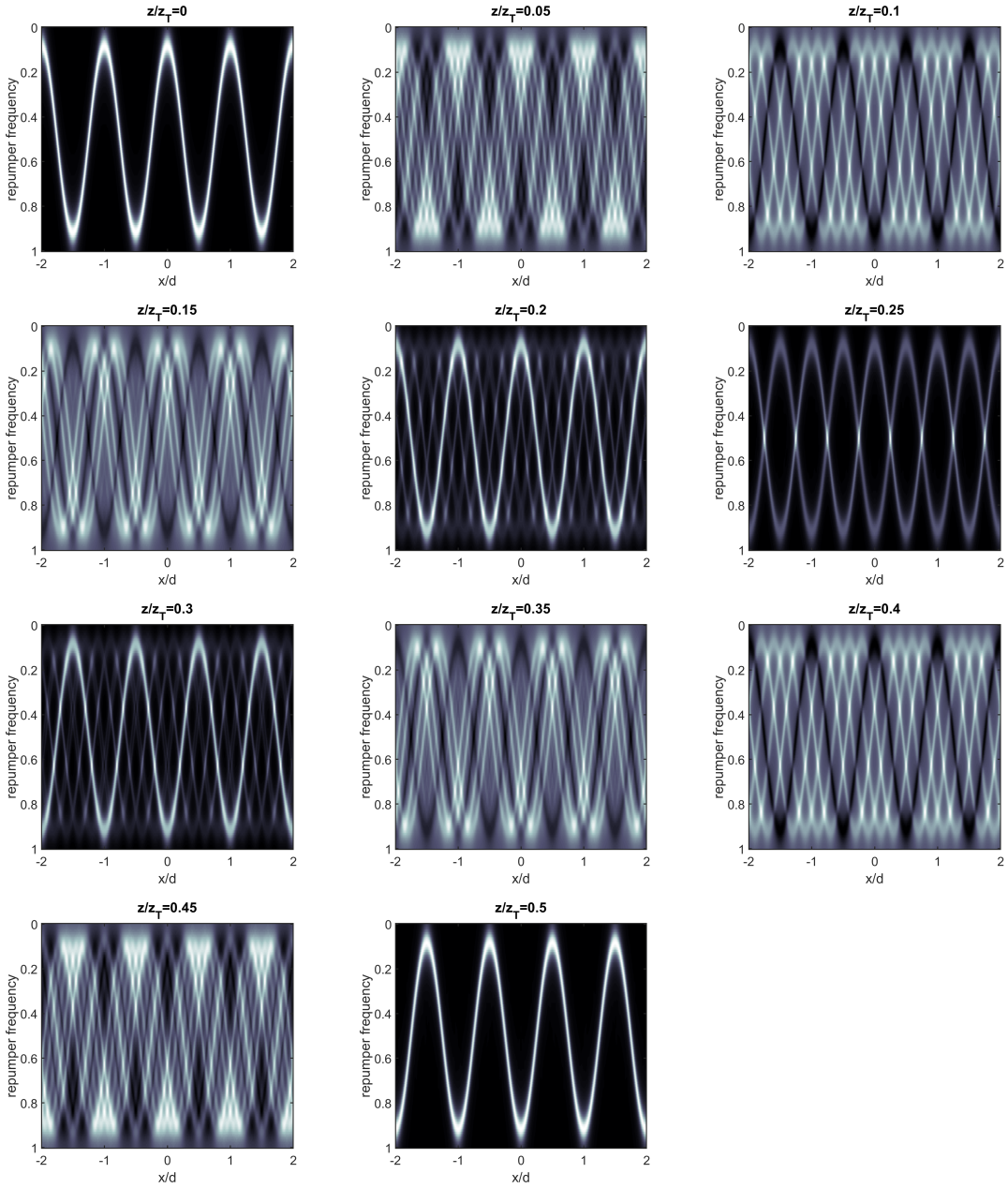

Figure III.2: Simulations of the tomography images at different propagation distances for the co-propagating 1529 nm beams with d=8 µm, t=10 µs, s_0=0.15 and a light shift of 17Γ.

III.ii Results on the imaging transition

In this section, we show results that have been obtained in the case where a 1529 nm co-propagating lattice is used while imaging the atoms on the cycling transition. First we propose a simple model based on Beer-Lambert's law to evaluate the absorption signal and then we compare it to experimental data.

C.2.1 Model with the Beer-lambert law

During the imaging process on a cycling transition with a 1529 nm lattice, the detuning is periodically varying due to the light shift with $\delta(x) = \Delta(x)/\Gamma$. The optical density is then given by:

$$b(x) = -\alpha\left(1+4\delta(x)^2\right)\ln T(x) + s_0(1-T(x)), \tag{III.6}$$

where s_0 is the saturation parameter for the imaging beam.

In the case of an elongated cloud along the lattice direction, the atomic density is homogeneous over an interfringe width. For a far-off-resonance probe in regions of strong light shifts, the transmission signal is very close to 1, therefore it is not possible to reconstruct the optical density in these regions. The optical density can be recovered using Eq. (III.6) only near resonant regions.

Experimentally, to evaluate the effect of subwavelength imaging, we analyze the experimental data by integrating the transmission peak over a width of one interfringe:

$$I = \int_0^{i_{1529}} (1-T(x))dx, \tag{III.7}$$

where the transmission can be written using the Lambert W function based on Eq. (III.6):

$$T(x) = \frac{\alpha(1+4\delta(x)^2)}{s_0} W\left(\frac{s_0}{\alpha(1+4\delta(x)^2)} e^{\frac{s_0-b}{\alpha(1+4\delta(x)^2)}}\right). \tag{III.8}$$

If the light shift amplitude $\Delta\omega_{1529}$ increases, then the transmission peak will be narrower. In the following, we integrate the area below the transmission peak to compare experiment and theory.

C.2.2 BAT curves and resolution

The experimental sequence is similar to Fig. E.16 except that we use only a single MW transfer of duration t_{MW} and we image the atoms with the 1529 beams that are turned ON during the imaging pulse of duration t and saturation s_0. As the imaging is done on the cycling transition with a σ-polarized beam, the system stays theoretically closed and equivalent to a TLS with a spatially varying detuning. The theoretical resolutions are then the ones given in section E.1.3.1 by Eq. (E.20).

Fig. III.3 shows a BAT curve for a dataset where the transmission is measured after averaging the integrated transmission over a width of 3 interfringes. It shows BAT curves on the cycling transition similar to the ones obtained in section E.3 for a repumper transition.

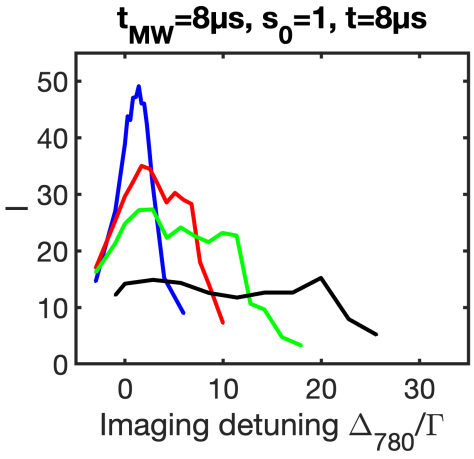

Figure III.3: BAT curve example of a dataset showing the integrated transmission as a function of the imaging beam detuning for different light shifts on $|F_e = 3, m_F = -3\rangle$. Each point has been average over 2 runs. The curves from top to bottom correspond to powers per beam of: 0.58, 1.74, 2.9 and 5.8 mW.

Finally, we plot on Fig. III.4 the integrated transmission vs. the light shifts for a 780 imaging beam tuned at the middle of the modulation (solid black curve). The expected integrated transmission I given by Eq. (III.8) is plotted using an estimation of the optical density from time-of-flight measurements (dashed black curve). This estimation is sensitive to the calibration of the atom number but also to the calibration of the cloud width along the propagation direction. Errorbars for the model only include the uncertainty on the atom number. The cloud width along the propagation direction has not been measured for this set of data, so we used the same value as the transverse direction along y which is $\sigma_y = 2.4$ µm. From the in situ widths and atom number from time-of-flight, we can compute the expected optical density. For instance, a peak optical density of $OD_0 \approx 1.99$ corresponds to a transfer of $t_{MW} = 4$ µs.

We see that the agreement is good and the same systematic errors appear as in section E.3.1.2 for low light shifts (high optical densities). In Fig. III.4, the right scale gives the expected full-width at half maximum (blue solid curve) at the middle of the modulation given by Eq. (E.20). It shows that resolutions of about 300 nm have been reached for light shifts of 12Γ.

As a conclusion, this subwavelength imaging method has the main advantage to be fast compared to any atomic motion during the pulse duration. So atomic motion during the imaging can be neglected. The main drawback of this method on the cycling transition is that the integrated transmission I is not easily connected to a physical quantity. To give a better quantitative analysis for this subwavelength imaging method, other imaging techniques such as fluorescence or dark ground imaging would be more appropriate as they are directly proportional to the total scattering rate.

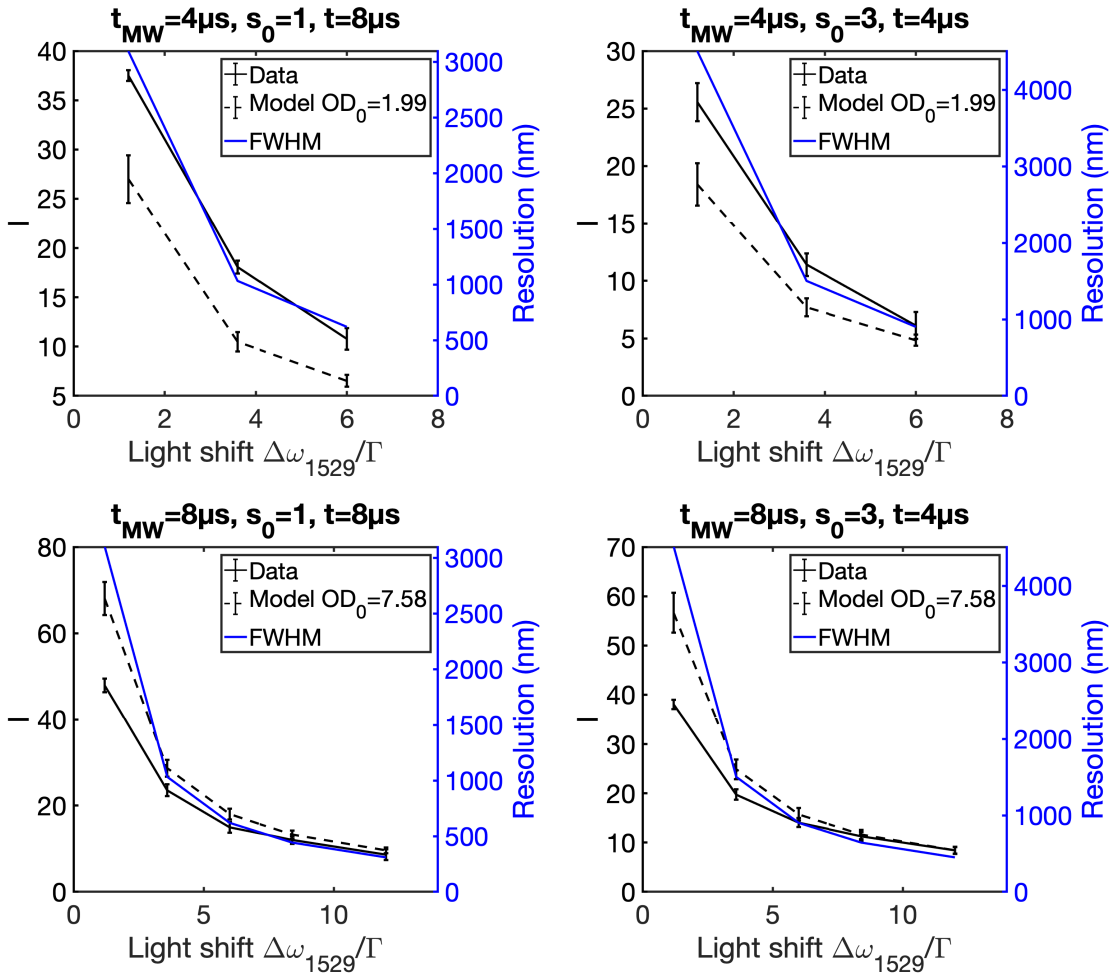

Figure III.4: Integrated experimental transmission vs. the light shift on the cycling transition. Error bars for each data point correspond to the averaged transmission over 10 realizations and error bars for the model are from 8 realizations.

Appendix IV

This Appendix describes calibrations for Chapter F. First, the adiabaticity of the loading of a BEC into a 1064 nm optical lattice is discussed. Then, we calibrate the lattice trap depth using Kapitza-Dirac scattering. Finally, we quantify the induced light shifts at 1064 nm on the ground $5S_{1/2}$ and excited $5P_{3/2}$ states.

IV.i Adiabatic loading of the BEC in the 1064 nm lattice

Experimentally, to adiabatically load a BEC into an optical lattice, at least two timescales are relevant. The first one corresponds to the single-particle band structure. To avoid excitations to higher-order bands, and verify the adiabaticity criteria, the rising time of the lattice depth V_0 has to be smaller than the gap energy between Bloch bands. For $q = 0$, the energy gap between band $n = 0$ and the first band $n = 1$ verifies $E_1 - E_0 \geq 4E_r$ for any trap depth, the right-hand side being given by the low trap depth limit where the band structure is directly given by the kinetic energy of a free particle. The first criterion is then given by (Denschlag et al., 2002):

$$\frac{d|V_0|}{dt} \ll \frac{16E_r^2}{\hbar}. \tag{IV.1}$$

To go up to a lattice depth of $V_0(t) = sE_r f(t)$ where $f(t)$ is a temporal variation of the lattice depth, the condition becomes $df/dt \ll 16E_r/|s|\hbar$ so $(df/dt)^{-1} \gg 5s$ µs. This criterion is experimentally easily fulfilled for low lattice depths. For larger trap depths the gap increases and the criterion is even more easily fulfilled.

The second adiabaticity criterion is due to the dynamics within the lowest band where the atoms redistribute over the lattice sites to maintain a constant chemical potential through the cloud (Greiner, 2003). In (Gericke et al., 2007), for a 3D optical lattice with $s = 10$ and a period of 425 nm, a ramp time of 100 ms is necessary to be adiabatic. In our experiment with a 1D lattice, we use the S-shape-like time dependence of (Gericke et al., 2007) to increase the trap depth:

$$V_0(t) = \frac{V_1}{1 + e^{-\alpha(t-t_0)}} + V_2, \tag{IV.2}$$

where $V_0(t = 0) = V_i$ (experimentally we lock the power at a very low trap depth) and $V_0(t = t_{max}) = V_f$ (the target trap depth). The end point constraints the parameters of

Eq. (IV.2) to:

$$\begin{aligned} V_1 =& \frac{V_i - V_f}{(1+e^{\alpha t_0})^{-1} - (1+e^{-\alpha(t_{max}-t_0)})^{-1}}, \\ V_2 =& V_i - \frac{V_1}{1+e^{\alpha t_0}}. \end{aligned} \tag{IV.3}$$

We optimized the loading by doing an S-shape to go up to $40E_r$ and another one to return to the initial trap depth. Then, with time-of-flight measurements, we measured the BEC fraction for different sets of t_{max} and α. We found that the thermal fraction was the same when loading with $t_{max} \gg 200$ ms, $\alpha = 9/t_{max}$ and $t_0 = t_{max}/2$. Above these parameters, it is quite insensitive and we could recover the initial BEC with the same BEC fraction.

To test the first type of adiabaticity (band structure), we used another way to be more quantitative which is to measure the momentum components of the state in the lattice after an S-shape. Indeed, for a lattice ground state Φ_0^0, after a sudden turn off of the potential, the projection of the ground state onto plane waves predicts that the percentage of the momentum populations are 65% of $0\hbar k$-component and 17% of $\pm 2\hbar k$-component (Denschlag et al., 2002). Testing the adiabaticity of the loading can be done by measuring these components in TOF after ramping up and suddenly switching off the lattice light.

We performed measurements with the following initial cloud: a crossed dipole trap where the magnetic gradient has been decreased to zero, followed by an S-shape loading in the lattice with $t_{max} = 50$ ms and a variable maximum trap depth up to $s = 5E_r$ as shown on Fig. IV.1.

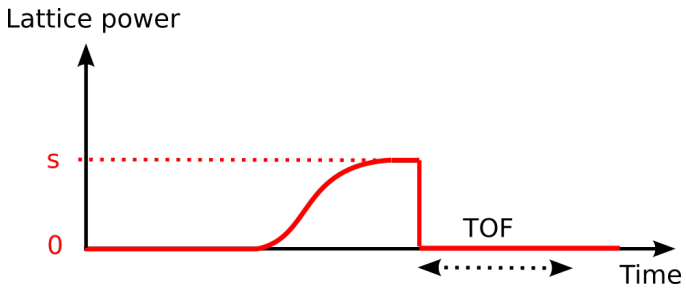

Figure IV.1: Ramp diagram of the adiabatic loading of the BEC in the 1D lattice followed by a time-of-flight after suddenly switching off the lattice light.

After a TOF of 5.9 ms, we measure the momentum population as a function of the lattice depth in order to compare with the single-particle band structure expectations of 67% and 17% mentioned above. Fig. IV.2 shows that as the trap depth increases, $\pm 2\hbar k$ momenta are populated up to a trap depth where we get speckle-like images.

We plotted the ratio of the population in $0\hbar k$, $\pm 2\hbar k$ over the total population on Fig. IV.3. It shows that the ratios are around the expected values of 67% and 17% at trap depths below $4E_r$. Above that, the images are blurred preventing the computation of the momentum populations. In other words, the visibility goes down to zero.

This blurring effect has also been observed in (Sapiro, Zhang, and Raithel, 2009) where they use a lattice with a wavelength of 852 nm ($E_r = \hbar \times 2\pi.3.16$ kHz). In this reference,

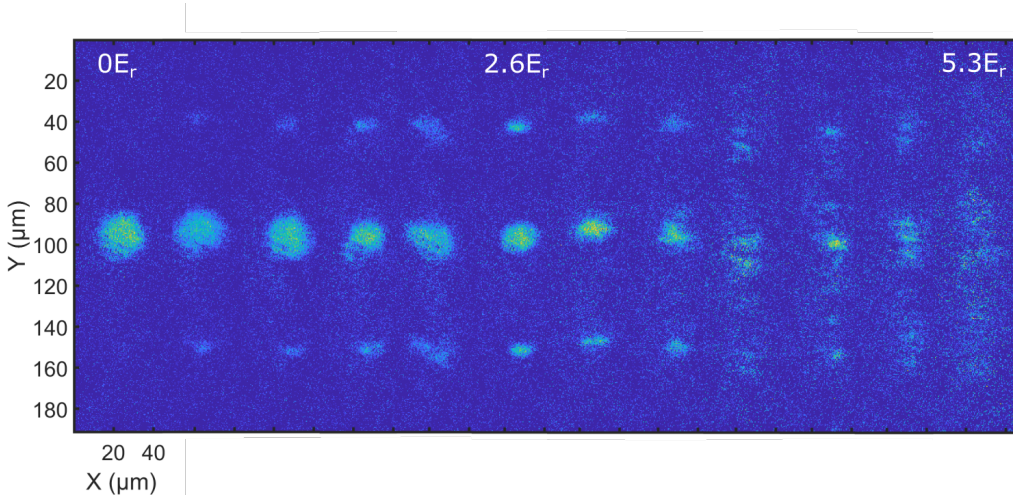

Figure IV.2: Raw images with a TOF of 5.9 ms after adiabatic loading of the BEC into the lattice initially in a crossed dipole trap without magnetic gradient for different lattice depths.

they could recover a BEC phase even after losing phase coherence in a 1D optical lattice. It can be interpreted either as a 1D Mott-superfluid transition or a lack of adiabaticity of the lattice ramp time compared to the many-body dynamics (tunneling, insulator energy gap). They lose the phase coherence at $30E_r$ with a linear ramp of 10 ms and were able to come back to the initial BEC after ramping down in 10 ms the lattice. They studied the effect of the holding time for a trap depth of $23E_r$ and saw that it takes a few milliseconds for the sites of different pancakes to dephase leading to blurred images after a time-of-flight. In our case, we probably observed a lack of adiabaticity as the interaction energy per particle is comparable to the external envelop of potential energy between two lattice sites. This means that the interactions are not high enough for the Mott insulator to be realised.

Ref. (Sapiro, Zhang, and Raithel, 2009) differs from us in the order of magnitude of the observable trap depths by a factor of 2 where the loss of coherence occurs. We stress that data of Fig. IV.2 and IV.3 have been taken before removing residuals interferences between DT1 and the 1064 nm lattice. It could lead to some additional dephasing between lattice sites and incorrect trap depths. In the next section, the trap depth is more reliably calibrated using Kapitza-Dirac scattering.

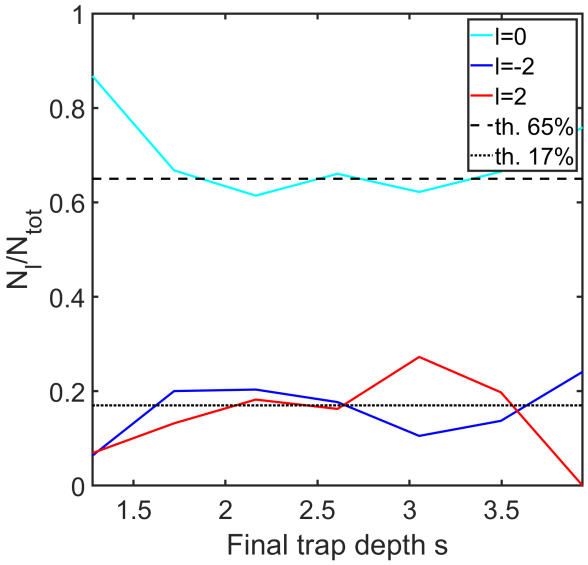

Figure IV.3: Atom numbers in the momentum components of Fig. IV.2 after a time-of-flight as a function of the end trap depths.

IV.ii Lattice depth calibration using Kapitza-Dirac scattering

It is important to know precisely the trap depth of the lattice at 1064 nm. However, experimentally it is not trivial to know exactly the trap depth. Waists and beam positions are difficult to measure.

The optical system was aligned at 1529 nm. Therefore, chromatic aberrations of the 150 mm lenses make it difficult to trap the atoms exactly at the focus of both 1064 nm lattice beams. In other words, we cannot change the divergence of the input beam to get the focus at the same position for both beams. For instance, after measuring the 'lattice 1' waist of 45 µm with trap oscillations, we estimated, using ABCD matrix formalism (Bernon, 2011), that the waist of the 'lattice 2' beam was 75 µm. This difference was mostly due to lens defocus.

To precisely calibrate the trap depth, we measure oscillation frequencies in-between the lattice bands using Kapitza-Dirac scattering (Denschlag et al., 2002; Andersen, 2008).

After preparing a BEC, the method consists in 3 steps depicted on Fig. IV.4: 1) Lattice beams are suddenly turned on, 2) At constant power the state freely evolves for a time duration τ, 3) Lattice beams are suddenly turned off. It can be interpreted as a Mach-Zehnder interferometer where steps 1) and 3) would be the splitter and the combiner and step 2) the propagation in the arms of the interferometer.

From Chapter A, we recall that a Bloch vector $\left|\Phi_q^n\right\rangle$ can be expressed in the plane wave basis $|\phi_{2l\hbar k+q}\rangle$ using Eq. (A.36) that we recall here using bra-ket notation:

$$\left|\Phi_q^n\right\rangle = \sum_l c_l^{(n,q)} \left|\phi_{2l\hbar k+q}\right\rangle , \tag{IV.4}$$

where the projection of the position verifies $\langle x|\phi_{2l\hbar k+q}\rangle = e^{i(2l\hbar k+q)x/\hbar}$.

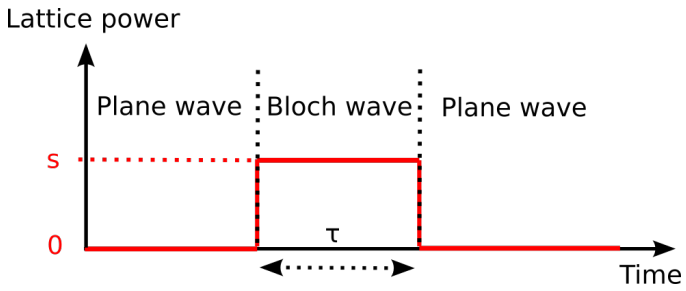

Figure IV.4: Kapitza-Dirac scattering for the calibration of the trap depth: the lattice power is abruptly turned on followed by a free evolution time τ and a sudden turn off of the power.

First, we consider that a BEC is well-described by a plane wave $|\phi_q\rangle$ with momentum q which is justified as the initial BEC width is larger than the lattice period.

Then, step 1) consists in projecting the initial state onto the Bloch basis:

$$|\Psi(t=0)\rangle = \sum_n \left|\Phi^n_{q'}\right\rangle \left\langle \Phi^n_{q'}\middle|\phi_q\right\rangle = \sum_{n,l} c_l^{(n,q)^*} \left\langle \phi_{2l\hbar k+q}|\phi_q\right\rangle \left|\Phi^n_{q'}\right\rangle = \sum_n c_0^{(n,q)^*} \left|\Phi^n_q\right\rangle . \quad \text{(IV.5)}$$

After that step 2) consists in applying the free evolution operator using eigenvalues and eigenvectors of a 1D lattice given in section A.3.5:

$$|\Psi(\tau)\rangle = \sum_n c_0^{(n,q)^*} e^{-iE_q^{(n)}\tau/\hbar} \left|\Phi^n_q\right\rangle . \quad \text{(IV.6)}$$

And finally step 3) consists in projecting the state after the time evolution onto the plane wave basis *i.e.* $\left|\Phi^n_q\right\rangle = \sum_l c_l^{(n,q)} |\phi_{2l\hbar k+q}\rangle$:

$$|\Psi(t=\tau)\rangle = \sum_{n,l} b_l^{(n,q)}(\tau) |\phi_{2l\hbar k+q}\rangle , \quad \text{(IV.7)}$$

where the complex number coefficient $b_l^{(n,q)}(\tau)$ evolves as follows:

$$b_l^{(n,q)}(\tau) = c_0^{(n,q)^*} c_l^{(n,q)} e^{-iE_q^{(n)}\tau/\hbar} . \quad \text{(IV.8)}$$

Eq. (IV.8) means that for the BEC initial momentum q, the momentum population l in the band n has the probability $|b_l^{(n,q)}|^2$ to be occupied and is then time-independent[1]. As a result, we compute the total population per momentum l by summing over all bands n:

[1]For a symmetric initial wavefunction, only symmetric Bloch wavefunctions are populated *i.e.* even bands. For an asymmetric initial wavefunction, for instance with an initial momentum kick, any parity band can be populated. Also, by quasi-momentum conservation only multiples of $2\hbar k[q]$ are populated. It can be seen as resulting from the absorption of a photon from the first beam and the stimulated emission of a photon into the second beam.

$$P_l^{(q)}(\tau) = \left| \sum_{n=0}^{\infty} b_l^{(n,q)}(\tau) \right|^2 . \tag{IV.9}$$

Eq. (IV.9) shows that the coherent sum of the population now depends on time as many bands can contribute to the same momentum. Experimentally[2], we use those population oscillations in the momentum components to precisely calibrate the lattice depth s as a function of the lattice power which is the unique free parameter. We stress that the only assumptions in the above theory are neglecting interactions, assuming an infinite 1D lattice in addition to the knowledge of the initial state.

Experimentally, we prepare a BEC at rest such that $q = 0$, with a Thomas-Fermi radius of 30 µm so $\Delta q \approx 0.003\hbar k$, and the chemical potential is $\mu = h \times 500$ Hz in a hybrid trap with DT1. The plane wave approximation is then justified and we can neglect the role of interactions as the dynamics is long compared to the pulses that we consider.

The lattice power is pulsed for a duration τ as shown on Fig. IV.4. Our power lock (single integrator, Appendix II.iv) has a 10%-90% rising time of 3 µs which is faster than the oscillation frequencies. Moreover, we also use a feed-forward drive which enables us to directly drive the AOM around the lock setpoint such that the optical power is directly around the target value[3].

We measure the momentum distributions for different durations τ after a short time-of-flight[4] TOF of 5.9 ms which corresponds to moving both the telescope and camera of our high NA imaging setup by 15 mm ($\frac{1}{2} M g \mathrm{TOF}^2$ with a magnification of 500/53). The time-of-flight is high enough to spatially resolve the momentum peaks. Indeed, an atom acquires multiples of $2v_{rec}$ recoil velocities along the lattice direction with $v_{rec} = 2\pi\hbar/\lambda m$. After the time-of-flight, it corresponds to displacements about 50 µm between two consecutive peaks which is what we see on the raw image in Fig. IV.6.

On Fig. IV.6 the populations are projected to get a 1D profile of the peaks. We fit, as a function of time, the momentum populations of $0\hbar k$, $-2\hbar k$ and $2\hbar k$ all together with the function $N_1 P_l^{(q)}(\tau) + N_0$ which has 3 free parameters: the lattice depth s from Eq. (IV.9), the total atom number N_0 and an offset N_1. The left plot is when DT1 and lattice have the same frequency and shows that for some durations, populations in $+2\hbar k$ and $-2\hbar k$ are anti-correlated. This effect can occur during Bloch oscillations in the case where a force is applied along the lattice direction. However here the anti-correlation was not reproducible from run to run. It turns out that DT1 and lattice at 1064 nm were not perfectly crossed in polarization and had exactly the same frequency. On the main experimental setup of Fig. B.2 a PBS combines DT1 and 'lattice 1' but are followed by a few mirrors before interacting with the atoms. This leads to residual interferences with a random phase between DT1 and 'lattice 2' (no phase relation). Using different diffraction orders of the AOMs (+80 MHz for DT1 and −80 MHz for lattice) sets a beating frequency

[2] Another possibility for simplifying the model is to consider lattice pulse durations shorter than the lattice trap frequencies which enables one to neglect kinetic energy such that the phase evolution is only given by the external potential: this is the Raman-Nath regime (Gadway et al., 2009; Cabrera-Gutiérrez et al., 2018). In this section, we keep the full expression as it is easy to use and valid for any lattice depth.

[3] 1 Cicero channel for the lock setpoint and 1 Cicero channel for the feed-forward. Both the integrator feedback voltage and the feed-forward voltages are summed up and sent onto the AOM.

[4] We neglect the blurring coming from our microscope depth-of-field which could lead to wrong atom number measurements.

between the beams at 160 MHz, faster than any dynamics in our system. We therefore obtained the curve on the right on Fig. IV.6 showing smooth oscillations.

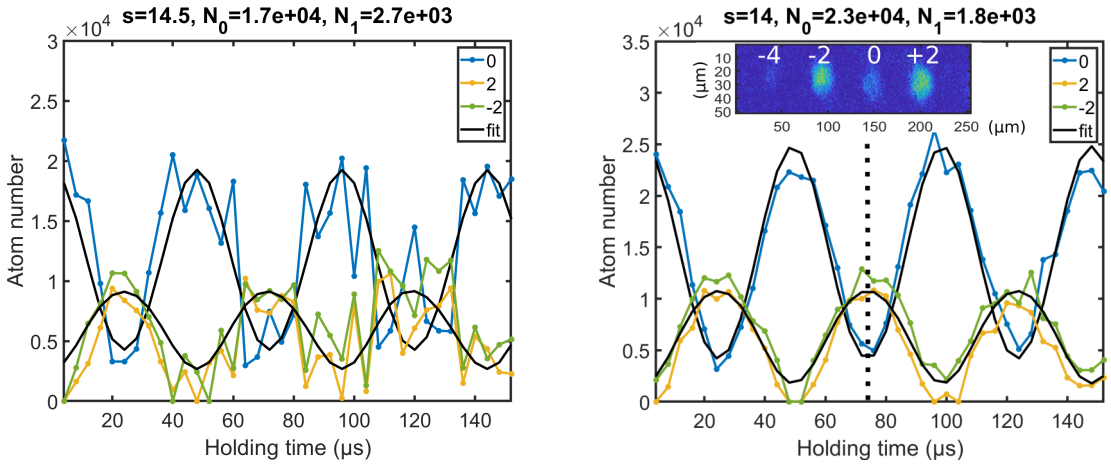

Figure IV.5: Kapitza-Dirac oscillations after an expansion of 5.9 ms for the same power setpoint but with the same diffraction order for DT1 and lattice AOMs (left), or different AOM diffraction orders (right) . The solid black line is a global fit on momentums $0, \pm 2\hbar k$. Each data point is a single run.

So far we ignored momentum higher than $\pm 2\hbar k$. This is expected as we can see on Fig. A.1 where the lattice depth $s = 14$ is just enough to populate the second band $n = 2$. This means that below this lattice depth, the oscillation is a pure sine function.

For trap depths larger than $s > 14$, more than 2 bands are populated leading to a more complex time evolution involving many frequency components. On Fig IV.6 we show momentum population oscillations in the case of $s = 33.6$. It matches pretty well with the theoretical model from which we extract the trap depth.

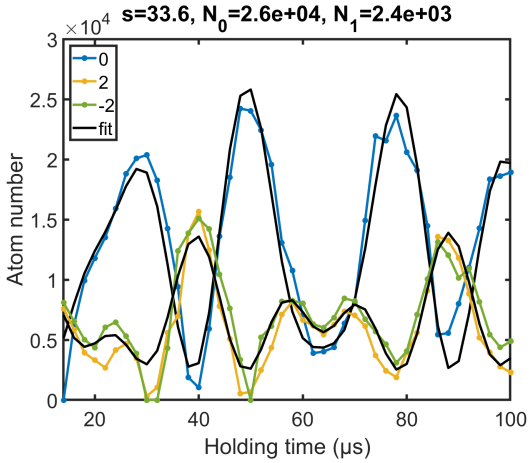

Figure IV.6: Kapitza-Dirac oscillations after an expansion of 5.9 ms for a trap depth of 33.6. The solid black line is a global fit on momentums $0, \pm 2\hbar k$. Each data point is a single run.

In Fig. IV.7 we show the trap depth s vs. the Cicero voltage setpoint V_{cicero} after measuring Kapitza-Dirac oscillations to extract the trap depth which experimentally calibrates the effective trap depth seen by the atoms. The trap depth is then given by

$s = -126.78V_{cicero}(V) - 6.114$. The maximum trap depth $s = 1000$ is reached for about -8V[5].

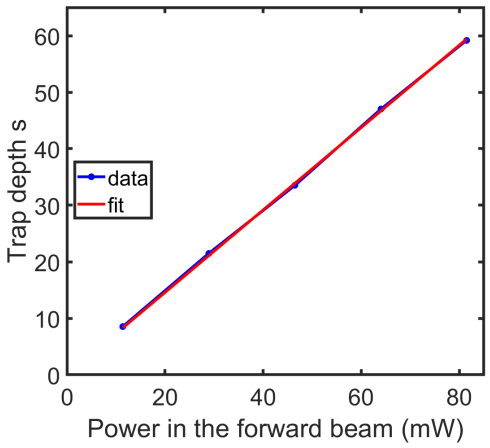

Figure IV.7: Calibration of the trap depth vs. the optical power in the forward beam using Kapitza-Dirac calibration.

IV.iii Light shifts due to high dipole trap powers

For high dipole trap powers, light shifts of the ground and excited state at 1064 nm are not negligible. When an atom is interacting with a repumper or a cooler beam at 780 nm, a small detuning has to be corrected to compensate for the 1064 nm light shift.

In this section, we give the light shifts induced by the 1064 nm radiation for all states that we are interested in. They are expressed in units of recoil energy at 1064 nm to directly compare with lattice physics. We remind that for ^{87}Rb the recoil energy at 1064 nm is $E_r = 2.028$ kHz. As the light is very far-detuned from atomic transitions, the rotating wave approximation cannot be applied. The rotating terms are far from each other, such that the light shifts for each independent rotating term can be summed up.

We compute the light shifts using Eq. (E.2) for π, σ^- and σ^+ polarizations of the 1064 nm and we use a peak intensity of 6393.2428 mW/cm^2 which gives a ground state shift of $V_0 = -1000E_r$. We resume all shifts in Tables IV.1, IV.2, IV.3 and IV.4.

	$\|1,-1\rangle$	$\|1,0\rangle$	$\|1,+1\rangle$
π	-2.0280799	-2.0280787	-2.0280799
σ^-	-2.0054399	2.0280799	-2.0507187
σ^+	-2.0507187	–2.0280799	-2.0054399

Table IV.1: Light shifts at 1064 nm of ^{87}Rb at an intensity of 6393.2428 mW/cm^2 in unit of MHz for $5S_{1/2}$, $F = 1$ for $V_0 = -1000E_r$.

Using the above light shifts, we can compute the total shift of any repumper or cooler transitions. We give shifts of the principal transitions that are driven during our experiments in Table IV.5. We consider the case where the polarization is either linear along

[5]It corresponds to about 1.4 W of optical power for the 'lattice 1' beam.

	$\|2,-2\rangle$	$\|2,-1\rangle$	$\|2,0\rangle$	$\|2,+1\rangle$	$\|2,+2\rangle$
π	-2.0281992	-2.0282025	-2.0282036	-2.0282025	-2.0281992
σ^-	-2.0734974	-2.0508483	-2.0508483	-2.0055534	-1.9829076
σ^+	-1.9829076	-2.0055534	-2.0282003	-2.0282003	-2.0734974

Table IV.2: Light shifts at 1064 nm of ^{87}Rb at an intensity of 6393.2428 mW/cm^2 in unit of MHz for $5S_{1/2}$, $F = 2$ for $V_0 = -1000E_r$.

	$\|2,-2\rangle$	$\|2,-1\rangle$	$\|2,0\rangle$	$\|2,+1\rangle$	$\|2,+2\rangle$
π	3.43852	3.43847	3.43845	3.43847	3.43852
σ^-	3.92186	3.68019	3.43850	3.19680	2.95507
σ^+	2.95507	3.19680	3.43850	3.68019	3.92186

Table IV.3: Light shifts at 1064 nm of ^{87}Rb at an intensity of 6393.2428 mW/cm^2 in unit of MHz for $5P_{3/2}$, $F = 2$.

the quantization axis (z) which makes it a π polarization; or linear along a direction perpendicular to the quantization axis such that the shift is the sum of half the one of a σ^- plus half the one of a σ^+. These total shifts have to be compared to the natural linewidth frequency which is $\Gamma/2\pi = 6.065$ MHz.

In our experiment the quantization axis is usually set by a magnetic bias along z of about 300 to 500 mG, so the case 'linear along z' corresponds to DT1 (polarization along z) and the case 'Linear perp. to z' corresponds to DT2 (polarization along y) and lattice (polarization along x). We see that transitions are shifted by about $\Gamma/2$ to Γ due to the light shift induced by the dipole trap.

At full optical powers, DT1 and DT2 have respectively a trap depth for the ground state of about 120 µK (Cicero setpoint at 7.2V) and 90 µK (Cicero setpoint at 8.5V) which correspond respectively to about $1250E_r$ and $920E_r$.

During the compression step, when DT1 compensates for the gravity sag, it reaches a trap depth of $70E_r$ (Cicero voltage of 0.4V). It corresponds to a shift of 0.04Γ according to Table IV.5

Experimentally, we varied the imaging beam detuning and measured the atom number as shown on Fig. IV.8. The initial cloud is in a hybrid trap with DT1 and a magnetic quadrupole at 30 G/cm. The lattice is linearly ramped up in 300 ms up to $40E_r$ and the magnetic trap is decreased to 0 in 400 ms. A homogeneous magnetic field bias of 280 mG along z is applied at the same time. Finally, the lattice is compressed to the desired value s. After that, a double MW transfer is used to prepare an atom number equivalent to a 4 µs transfer. It avoids optical density effects (see section E.16 for details of the double MW transfer).

The measurements were done with the high NA imaging axis, a saturation parameter for the imaging beam of 2, and a duration of 20 µs. We see on Fig. IV.8 that at 40 E_r the resonance is effectively around 0 as the light shift of DT1 (0.044Γ) and lattice (0.042Γ) are small compared to Γ.

This reference of shift is actually within the frequency calibration uncertainty which is set by long-term drifts of our Muquans laser system (temperature drifts). At 997.5 E_r we observe a positive shift about 1Γ as expected from Table IV.5 where the shift is computed

	$\|3,-3\rangle$	$\|3,-2\rangle$	$\|3,-1\rangle$	$\|3,0\rangle$	$\|3,+1\rangle$	$\|3,+2\rangle$	$\|3,+3\rangle$
π	1.77560	1.77560	4.43625	4.43625	4.43625	1.77560	1.77560
σ^-	4.99513	3.92195	3.18136	2.77334	2.69791	2.95506	3.54479
σ^+	3.54479	2.95506	2.69791	2.77334	3.18136	3.92195	4.99513

Table IV.4: Light shifts at 1064 nm of ^{87}Rb at an intensity of 6393.2428 mW/cm^2 in unit of MHz for $5P_{3/2}$, $F = 3$ for $V_0 = -1000E_r$.

	Repumper	Cooler
Linear along z	5,466551927	3,80
Linear perp. to z	5,466577717	6,30

Table IV.5: Total light shifts at 1064 nm of ^{87}Rb at an intensity of 6393.2428 mW/cm^2 in unit of MHz for the repumper transition $|F_g = 1, m_F = -1\rangle$ to $|F_e = 2, m_F = -1\rangle$ and cooler transition $|F_g = 2, m_F = -2\rangle$ to $|F_e = 3, m_F = -3\rangle$ for $V_0 = -1000E_r$.

to be $6.30/6.065 = 1.04\Gamma$.

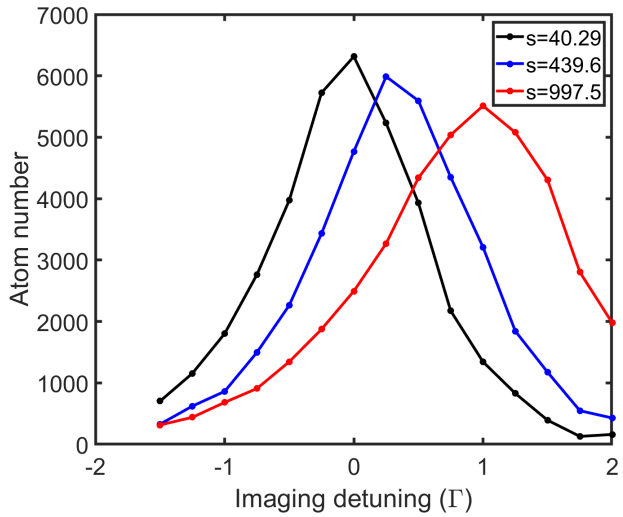

Figure IV.8: Atom number as a function of the imaging detuning (cooler transition) for different lattice trap depths measured in situ.

In addition to the imaging transition, we have also characterized the repumper transition $|F_g = 1, m_F = -1\rangle$ to $|F_e = 2, m_F = -1\rangle$ by scanning the repumper frequency. We give the setpoints in voltage which is easier to compare to the experiment. At $40E_r$, the resonance was at -2.03V and at $1000E_r$ the resonance was at -2.09V. Using the calibration given in section E.2.1 -108.12 MHz/V, we have an experimental line shift of 5.4 MHz i.e. 0.9Γ which is also in good agreement with Table IV.5.

In conclusion, the light shifts due to the 1064 nm lattice at high power can create light shifts of about Γ. They have to be taken into account to properly compute atom numbers or manipulate the atoms for large trap depths.

Bibliography

[1] A. Alberti et al. "Super-resolution microscopy of single atoms in optical lattices". In: New J. Phys. 18.5 (2016). ISSN: 1367-2630. DOI: 10.1088/1367-2630/18/5/053010.

[2] E. Altman et al. "Quantum Simulators: Architectures and Opportunities". In: PRX Quantum 2.1 (2021), p. 017003. ISSN: 2691-3399. DOI: 10.1103/PRXQuantum.2.017003. URL: https://link.aps.org/doi/10.1103/PRXQuantum.2.017003.

[3] H. K. Andersen. "Bose-Einstein condensates in optical lattices, PhD thesis". In: Aarhus Universitetsforlag (2008).

[4] M. H. Anderson et al. "Observation of Bose-Einstein Condensation in a Dilute Atomic Vapor". In: Science 269.5221 (1995). ISSN: 0036-8075. DOI: 10.1126/science.269.5221.198.

[5] X. Antoine and R. Duboscq. "GPELab, a Matlab toolbox to solve Gross–Pitaevskii equations I: Computation of stationary solutions". In: Comput. Phys. Commun. 185.11 (2014). ISSN: 00104655. DOI: 10.1016/j.cpc.2014.06.026.

[6] X. Antoine and R. Duboscq. "GPELab, a Matlab toolbox to solve Gross–Pitaevskii equations II: Dynamics and stochastic simulations". In: Comput. Phys. Commun. 193 (2015). ISSN: 00104655. DOI: 10.1016/j.cpc.2015.03.012.

[7] B. Arora, M. S. Safronova, and C. W. Clark. "Magic wavelengths for the np-ns transitions in alkali-metal atoms". In: Phys. Rev. A 76.5 (2007). ISSN: 1050-2947. DOI: 10.1103/PhysRevA.76.052509.

[8] B. Arora and B. K. Sahoo. "State-insensitive trapping of Rb atoms: Linearly versus circularly polarized light". In: Phys. Rev. A 99.4 (2019). ISSN: 2469-9926. DOI: 10.1103/PhysRevA.99.049901.

[9] V. Bagnato, D. E. Pritchard, and D. Kleppner. "Bose-Einstein condensation in an external potential". In: Physical Review A 35.10 (1987), pp. 4354–4358. ISSN: 0556-2791. DOI: 10.1103/PhysRevA.35.4354. URL: https://link.aps.org/doi/10.1103/PhysRevA.35.4354.

[10] P. Barthelemy and L. M. K. Vandersypen. "Quantum Dot Systems: a versatile platform for quantum simulations". In: Ann. Phys. 525.10-11 (2013), pp. 808–826. ISSN: 0003-3804. DOI: 10.1002/andp.201300124. URL: https://onlinelibrary.wiley.com/doi/10.1002/andp.201300124.

[11] M. Bellouvet. "Condensation de Bose-Einstein et simulation d'une méthode de piégeage d'atomes froids dans des potentiels sublongueur d'onde en champ proche d'une surface nanostructurée, PhD thesis". In: Université de Bordeaux (2018).

[12] M. Bellouvet et al. "Doubly dressed states for near-field trapping and subwavelength lattice structuring". In: Phys. Rev. A 98.2 (2018). ISSN: 2469-9926. DOI: 10.1103/PhysRevA.98.023429.

[13] L. M. Bennie et al. "A versatile high resolution objective for imaging quantum gases". In: Opt. Express 21.7 (2013). ISSN: 1094-4087. DOI: 10.1364/OE.21.009011.

[14] S. Bernon. "Piégeage et mesure non-destructive d'atomes froids dans une cavité en anneau de haute finesse, PhD thesis". In: École Polytechnique (2011).

[15] S. Bernon et al. "Manipulation and coherence of ultra-cold atoms on a superconducting atom chip". In: Nat. Commun. 4.1 (2013), p. 2380. ISSN: 2041-1723. DOI: 10.1038/ncomms3380. URL: http://www.nature.com/articles/ncomms3380.

[16] A. Bertoldi et al. "In situ characterization of an optical cavity using atomic light shift". In: Opt. Lett. 35.22 (2010). ISSN: 0146-9592. DOI: 10.1364/OL.35.003769.

[17] V. Bose. "Plancks Gesetz und Lichtquantenhypothese". In: Zeitschrift für Phys. 26.1 (1924). ISSN: 1434-6001. DOI: 10.1007/BF01327326.

[18] J.-P. Brantut. "Manipulation d'atomes froids dans des potentiels lumineux, PhD thesis". In: Université Paris XI (2009).

[19] C. D. Bruzewicz et al. "Trapped-ion quantum computing: Progress and challenges". In: Appl. Phys. Rev. 6.2 (2019), p. 021314. ISSN: 1931-9401. DOI: 10.1063/1.5088164. URL: http://aip.scitation.org/doi/10.1063/1.5088164.

[20] D. Budker et al. "Resonant nonlinear magneto-optical effects in atoms". In: Rev. Mod. Phys. 74.4 (2002). ISSN: 0034-6861. DOI: 10.1103/RevModPhys.74.1153.

[21] E. A. Burt et al. "Coherence, Correlations, and Collisions: What One Learns about Bose-Einstein Condensates from Their Decay". In: Phys. Rev. Lett. 79.3 (1997). ISSN: 0031-9007. DOI: 10.1103/PhysRevLett.79.337.

[22] C. Busquet. "Développement d'un système d'imagerie superrésolue d'un gaz d'atomes ultrafroids piégés dans des réseaux, PhD thesis". In: Université de Bordeaux (2017).

[23] C. Cabrera-Gutiérrez et al. "Robust calibration of an optical-lattice depth based on a phase shift". In: Phys. Rev. A 97.4 (2018). ISSN: 2469-9926. DOI: 10.1103/PhysRevA.97.043617.

[24] A. Camara, R. Kaiser, and G. Labeyrie. "Scaling behavior of a very large magneto-optical trap". In: Physical Review A 90.6 (2014), p. 063404. ISSN: 1050-2947. DOI: 10.1103/PhysRevA.90.063404. URL: https://link.aps.org/doi/10.1103/PhysRevA.90.063404.

[25] G. K. Campbell and W. D. Phillips. "Ultracold atoms and precise time standards". In: Philos. Trans. R. Soc. A Math. Phys. Eng. Sci. 369.1953 (2011). ISSN: 1364-503X. DOI: 10.1098/rsta.2011.0229.

[26] W. B. Case et al. "Realization of optical carpets in the Talbot and Talbot-Lau configurations". In: Opt. Express 17.23 (2009). ISSN: 1094-4087. DOI: 10.1364/OE.17.020966.

[27] J. Chabé et al. "Coherent and incoherent multiple scattering". In: Phys. Rev. A 89.4 (2014). ISSN: 1050-2947. DOI: 10.1103/PhysRevA.89.043833.

[28] D. E. Chang, Jun Ye, and M. D. Lukin. "Controlling dipole-dipole frequency shifts in a lattice-based optical atomic clock". In: Phys. Rev. A 69.2 (2004). ISSN: 1050-2947. DOI: 10.1103/PhysRevA.69.023810.

[29] D. E. Chang et al. "Trapping atoms using nanoscale quantum vacuum forces". In: Nat. Commun. 5.1 (2014). ISSN: 2041-1723. DOI: 10.1038/ncomms5343.

[30] L. Chomaz. "Coherence and superfluidity of Bose gases in reduced dimensions : from harmonic traps to uniform fluids, PhD thesis". In: École Normale Supérieure (2014).

[31] L. Chomaz et al. "Absorption imaging of a quasi-two-dimensional gas: a multiple scattering analysis". In: New J. Phys. 14.5 (2012). ISSN: 1367-2630. DOI: 10.1088/1367-2630/14/5/055001.

[32] A. Cidrim et al. "Photon Blockade with Ground-State Neutral Atoms". In: Phys. Rev. Lett. 125.7 (2020), p. 073601. ISSN: 0031-9007. DOI: 10.1103/PhysRevLett.125.073601. URL: https://link.aps.org/doi/10.1103/PhysRevLett.125.073601.

[33] C. Cohen-Tannoudji. "Condensation de Bose-Einstein : gaz sans interactions, Leçons du Collège de France, Chaire de physique atomique et moléculaire". In: (1997). URL: http://www.phys.ens.fr/$\sim$cct/college-de-france/1997-98/1997-98.htm.

[34] G. Condon. "Bose-Einstein condensation: from finite size periodic potentials to phase space manipulations, PhD thesis". In: Université Toulouse 3 Paul Sabatier (2015).

[35] R. Corgier et al. "Fast manipulation of Bose–Einstein condensates with an atom chip". In: New J. Phys. 20.5 (2018). ISSN: 1367-2630. DOI: 10.1088/1367-2630/aabdfc.

[36] L. Corman. "The two-dimensional Bose Gas in box potentials, PhD thesis". In: PSL Research University (2016).

[37] L. Corman et al. "Transmission of near-resonant light through a dense slab of cold atoms". In: Phys. Rev. A 96.5 (2017). ISSN: 2469-9926. DOI: 10.1103/PhysRevA.96.053629.

[38] F. Cottier, R. Kaiser, and R. Bachelard. "Role of disorder in super- and subradiance of cold atomic clouds". In: Phys. Rev. A 98.1 (2018). ISSN: 2469-9926. DOI: 10.1103/PhysRevA.98.013622.

[39] F. Cottier et al. "Microscopic and Macroscopic Signatures of 3D Anderson Localization of Light". In: Phys. Rev. Lett. 123.8 (2019). ISSN: 0031-9007. DOI: 10.1103/PhysRevLett.123.083401.

[40] F. Dalfovo et al. "Theory of Bose-Einstein condensation in trapped gases". In: Rev. Mod. Phys. 71.3 (1999). ISSN: 0034-6861. DOI: 10.1103/RevModPhys.71.463.

[41] J. Dalibard. "Collisional dynamics of ultra-cold atomic gases, Proceedings of the International School of Physics - Enrico Fermi". In: (1999).

[42] J. Dalibard. "Cours atomes ultra-froids, Enseignement à l'Ecole normale supérieure". In: (1999). URL: http://pro.college-de-france.fr/jean.dalibard/.

[43] J. Dalibard and C. Cohen-Tannoudji. "Dressed-atom approach to atomic motion in laser light: the dipole force revisited". In: J. Opt. Soc. Am. B 2.11 (1985). ISSN: 0740-3224. DOI: 10.1364/JOSAB.2.001707.

[44] J. E. Debs et al. "Cold-atom gravimetry with a Bose-Einstein condensate". In: Phys. Rev. A 84.3 (2011). ISSN: 1050-2947. DOI: 10.1103/PhysRevA.84.033610.

[45] C. L. Degen, F. Reinhard, and P. Cappellaro. "Quantum sensing". In: Rev. Mod. Phys. 89.3 (2017), p. 035002. ISSN: 0034-6861. DOI: 10.1103/RevModPhys.89.035002. URL: http://link.aps.org/doi/10.1103/RevModPhys.89.035002.

[46] B. DeMarco and D. S. Jin. "Onset of Fermi Degeneracy in a Trapped Atomic Gas". In: Science 285.5434 (1999). ISSN: 0036-8075. DOI: 10.1126/science.285.5434.1703.

[47] D. DeMille. "Quantum Computation with Trapped Polar Molecules". In: Phys. Rev. Lett. 88.6 (2002), p. 067901. ISSN: 0031-9007. DOI: 10.1103/PhysRevLett.88.067901. URL: https://link.aps.org/doi/10.1103/PhysRevLett.88.067901.

[48] J H. Denschlag et al. "A Bose-Einstein condensate in an optical lattice". In: J. Phys. B 35.14 (2002). ISSN: 09534075. DOI: 10.1088/0953-4075/35/14/307.

[49] A. Dodin, T. V. Tscherbul, and P. Brumer. "Quantum dynamics of incoherently driven V-type systems: Analytic solutions beyond the secular approximation". In: J. Chem. Phys. 144.24 (2016). ISSN: 0021-9606. DOI: 10.1063/1.4954243.

[50] A. Dodin et al. "Secular versus nonsecular Redfield dynamics and Fano coherences in incoherent excitation: An experimental proposal". In: Phys. Rev. A 97.1 (2018). ISSN: 2469-9926. DOI: 10.1103/PhysRevA.97.013421.

[51] A. Einstein. "Quantentheorie des einatomigen idealen Gases". In: Akademie-Vorträge. Wiley, 1924. DOI: 10.1002/3527608958.ch27.

[52] C. J. Foot. "Atomic physics". In: (2005).

[53] B. Gadway et al. "Analysis of Kapitza-Dirac diffraction patterns beyond the Raman-Nath regime". In: Opt. Express 17.21 (2009). ISSN: 1094-4087. DOI: 10.1364/OE.17.019173.

[54] B. Gao. "Effects of Zeeman degeneracy on the steady-state properties of an atom interacting with a near-resonant laser field: Analytic results". In: Phys. Rev. A 48.3 (1993). ISSN: 1050-2947. DOI: 10.1103/PhysRevA.48.2443.

[55] N. Garcia, A. Z. Genack, and A. A. Lisyansky. "Measurement of the transport mean free path of diffusing photons". In: Phys. Rev. B 46.22 (1992), pp. 14475–14479. ISSN: 0163-1829. DOI: 10.1103/PhysRevB.46.14475. URL: https://link.aps.org/doi/10.1103/PhysRevB.46.14475.

[56] I. M. Georgescu, S. Ashhab, and F. Nori. "Quantum simulation". In: Rev. Mod. Phys. 86.1 (2014), pp. 153–185. ISSN: 0034-6861. DOI: 10.1103/RevModPhys.86.153. URL: https://link.aps.org/doi/10.1103/RevModPhys.86.153.

[57] F. Gerbier and Y. Castin. "Heating rates for an atom in a far-detuned optical lattice". In: Phys. Rev. A 82.1 (2010), p. 013615. ISSN: 1050-2947. DOI: 10.1103/PhysRevA.82.013615. URL: https://link.aps.org/doi/10.1103/PhysRevA.82.013615.

[58] T. Gericke et al. "Adiabatic loading of a Bose–Einstein condensate in a 3D optical lattice". In: J. Mod. Opt. 54.5 (2007). ISSN: 0950-0340. DOI: 10.1080/09500340600777730.

[59] N. Gisin et al. "Quantum cryptography". In: Rev. Mod. Phys. 74.1 (2002), pp. 145–195. ISSN: 0034-6861. DOI: 10.1103/RevModPhys.74.145. URL: https://link.aps.org/doi/10.1103/RevModPhys.74.145.

[60] A. Glicenstein et al. "Collective Shift in Resonant Light Scattering by a One-Dimensional Atomic Chain". In: Phys. Rev. Lett. 124.25 (2020). ISSN: 0031-9007. DOI: 10.1103/PhysRevLett.124.253602.

[61] A. Glicenstein et al. "Preparation of one-dimensional chains and dense cold atomic clouds with a high numerical aperture four-lens system". In: Phys. Rev. A 103.4 (2021). ISSN: 2469-9926. DOI: 10.1103/PhysRevA.103.043301.

[62] J. W. Goodman. "Introduction to Fourier Optics, 2nd edition". In: (1996).

[63] M. Greiner. "Ultracold quantum gases in three-dimensional optical lattice potentials, PhD thesis". In: Universität München (2003).

[64] M. Greiner, C. A. Regal, and D. S. Jin. "Emergence of a molecular Bose–Einstein condensate from a Fermi gas". In: Nature 426.6966 (2003). ISSN: 0028-0836. DOI: 10.1038/nature02199.

[65] M. Greiner et al. "Quantum phase transition from a superfluid to a Mott insulator in a gas of ultracold atoms". In: Nature 415.6867 (2002). ISSN: 0028-0836. DOI: 10.1038/415039a.

[66] R. Grimm, M. Weidemüller, and Y. B. Ovchinnikov. "Optical Dipole Traps for Neutral Atoms". In: (2000). DOI: 10.1016/S1049-250X(08)60186-X.

[67] W. Guerin, M. O. Araújo, and R. Kaiser. "Subradiance in a Large Cloud of Cold Atoms". In: Phys. Rev. Lett. 116.8 (2016). ISSN: 0031-9007. DOI: 10.1103/PhysRevLett.116.083601.

[68] W. Guerin, M.T. Rouabah, and R. Kaiser. "Light interacting with atomic ensembles: collective, cooperative and mesoscopic effects". In: J. Mod. Opt. 64.9 (2017). ISSN: 0950-0340. DOI: 10.1080/09500340.2016.1215564.

[69] Z. Hadzibabic et al. "Berezinskii–Kosterlitz–Thouless crossover in a trapped atomic gas". In: Nature 441.7097 (2006). ISSN: 0028-0836. DOI: 10.1038/nature04851.

[70] R. Heintzmann and T. Huser. "Super-Resolution Structured Illumination Microscopy". In: Chem. Rev. 117.23 (2017). ISSN: 0009-2665. DOI: 10.1021/acs.chemrev.7b00218.

[71] M. Horikoshi et al. "Appropriate Probe Condition for Absorption Imaging of Ultracold 6 Li Atoms". In: J. Phys. Soc. Japan 86.10 (2017). ISSN: 0031-9015. DOI: 10.7566/JPSJ.86.104301.

[72] R. Howl, R. Penrose, and I. Fuentes. "Exploring the unification of quantum theory and general relativity with a Bose–Einstein condensate". In: New J. Phys. 21.4 (2019). ISSN: 1367-2630. DOI: 10.1088/1367-2630/ab104a.

[73] R. Howl et al. "Non-Gaussianity as a Signature of a Quantum Theory of Gravity". In: PRX Quantum 2.1 (2021). ISSN: 2691-3399. DOI: 10.1103/PRXQuantum.2.010325.

[74] K. Hueck et al. "Calibrating high intensity absorption imaging of ultracold atoms". In: Opt. Express 25.8 (2017). ISSN: 1094-4087. DOI: 10.1364/OE.25.008670.

[75] S. Inouye et al. "Observation of Feshbach resonances in a Bose–Einstein condensate". In: Nature 392.6672 (1998). ISSN: 0028-0836. DOI: 10.1038/32354.

[76] S. D. Jenkins and J. Ruostekoski. "Controlled manipulation of light by cooperative response of atoms in an optical lattice". In: Phys. Rev. A 86.3 (2012). ISSN: 1050-2947. DOI: 10.1103/PhysRevA.86.031602.

[77] S. Jennewein et al. "Coherent scattering of near-resonant light by a dense, microscopic cloud of cold two-level atoms: Experiment versus theory". In: Phys. Rev. A 97.5 (2018). ISSN: 2469-9926. DOI: 10.1103/PhysRevA.97.053816.

[78] H. Kadau et al. "Observing the Rosensweig instability of a quantum ferrofluid". In: Nature 530.7589 (2016). ISSN: 0028-0836. DOI: 10.1038/nature16485.

[79] W. Ketterle and N.J. V. Druten. "Evaporative Cooling of Trapped Atoms". In: (1996). DOI: 10.1016/S1049-250X(08)60101-9.

[80] W. Ketterle, D. S. Durfee, and D. M. Stamper-Kurn. "Making, probing and understanding Bose-Einstein condensates". In: (1999). arXiv: 9904034 [cond-mat].

[81] I. H. A. Knottnerus et al. "Microscope objective for imaging atomic strontium with 063 micrometer resolution". In: Opt. Express 28.8 (2020). ISSN: 1094-4087. DOI: 10.1364/OE.388809.

[82] J. Koepsell et al. "Robust Bilayer Charge Pumping for Spin- and Density-Resolved Quantum Gas Microscopy". In: Phys. Rev. Lett. 125.1 (2020). ISSN: 0031-9007. DOI: 10.1103/PhysRevLett.125.010403.

[83] G. Labeyrie et al. "Coherent backscattering of light by an inhomogeneous cloud of cold atoms". In: Phys. Rev. A 67.3 (2003). ISSN: 1050-2947. DOI: 10.1103/PhysRevA.67.033814.

[84] G. Labeyrie et al. "Observation of coherent backscattering of light by cold atoms". In: J. Opt. B Quantum Semiclassical Opt. 2.5 (2000). ISSN: 1464-4266. DOI: 10.1088/1464-4266/2/5/316.

[85] T. D. Ladd et al. "Quantum computers". In: Nature 464.7285 (2010), pp. 45–53. ISSN: 0028-0836. DOI: 10.1038/nature08812. URL: http://www.nature.com/articles/nature08812.

[86] A. E. Leanhardt et al. "Cooling Bose-Einstein Condensates Below 500 Picokelvin". In: Science 301.5639 (2003), pp. 1513–1515. ISSN: 0036-8075. DOI: 10.1126/science.1088827. URL: https://www.science.org/doi/10.1126/science.1088827.

[87] P. A. Lee, N. Nagaosa, and X.-G. Wen. "Doping a Mott insulator: Physics of high-temperature superconductivity". In: Rev. Mod. Phys. 78.1 (2006), pp. 17–85. ISSN: 0034-6861. DOI: 10.1103/RevModPhys.78.17. URL: https://link.aps.org/doi/10.1103/RevModPhys.78.17.

[88] X. Li et al. "High-resolution ex vacuo objective for cold atom experiments". In: Appl. Opt. 57.26 (2018). ISSN: 1559-128X. DOI: 10.1364/AO.57.007584.

[89] Y.-J. Lin et al. "Rapid production of ^{87}Rb Bose-Einstein condensates in a combined magnetic and optical potential". In: Phys. Rev. A 79.6 (2009). ISSN: 1050-2947. DOI: 10.1103/PhysRevA.79.063631.

[90] O. J. Luiten, M. W. Reynolds, and J. T. M. Walraven. "Kinetic theory of the evaporative cooling of a trapped gas". In: Phys. Rev. A 53.1 (1996). ISSN: 1050-2947. DOI: 10.1103/PhysRevA.53.381.

[91] A. Mazurenko et al. "A cold-atom Fermi–Hubbard antiferromagnet". In: Nature 545.7655 (2017). ISSN: 0028-0836. DOI: 10.1038/nature22362.

[92] M. McDonald et al. "Superresolution Microscopy of Cold Atoms in an Optical Lattice". In: Phys. Rev. X 9.2 (2019). ISSN: 2160-3308. DOI: 10.1103/PhysRevX.9.021001.

[93] D. C. McKay and B. DeMarco. "Cooling in strongly correlated optical lattices: prospects and challenges". In: Reports Prog. Phys. 74.5 (2011), p. 054401. ISSN: 0034-4885. DOI: 10.1088/0034-4885/74/5/054401. URL: https://iopscience.iop.org/article/10.1088/0034-4885/74/5/054401.

[94] T. Meyrath. "Electromagnet design basics for cold atom experiments". In: (2004).

[95] B. R. Mollow. "Absorption and Emission Line-Shape Functions for Driven Atoms". In: Physical Review A 5.3 (1972), pp. 1522–1527. ISSN: 0556-2791. DOI: 10.1103/PhysRevA.5.1522. URL: https://link.aps.org/doi/10.1103/PhysRevA.5.1522.

[96] B. R. Mollow. "Power Spectrum of Light Scattered by Two-Level Systems". In: Physical Review 188.5 (1969), pp. 1969–1975. ISSN: 0031-899X. DOI: 10.1103/PhysRev.188.1969. URL: https://link.aps.org/doi/10.1103/PhysRev.188.1969.

[97] B. R. Mollow. "Stimulated Emission and Absorption near Resonance for Driven Systems". In: Phys. Rev. A 5.5 (1972). ISSN: 0556-2791. DOI: 10.1103/PhysRevA.5.2217.

[98] C. Mordini et al. "Single-shot reconstruction of the density profile of a dense atomic gas". In: Opt. Express 28.20 (2020). ISSN: 1094-4087. DOI: 10.1364/OE.397567.

[99] T. Moriya and K. Ueda. "Antiferromagnetic spin fluctuation and superconductivity". In: Reports Prog. Phys. 66.8 (2003), pp. 1299–1341. ISSN: 0034-4885. DOI: 10.1088/0034-4885/66/8/202. URL: https://iopscience.iop.org/article/10.1088/0034-4885/66/8/202.

[100] O. Morizot et al. "Trapping and cooling of rf-dressed atoms in a quadrupole magnetic field". In: J. Phys. B At. Mol. Opt. Phys. 40.20 (2007). ISSN: 0953-4075. DOI: 10.1088/0953-4075/40/20/004.

[101] J. L. O'Brien, A. Furusawa, and J. Vučković. "Photonic quantum technologies". In: Nat. Photonics 3.12 (2009). ISSN: 1749-4885. DOI: 10.1038/nphoton.2009.229.

[102] K. M. O'Hara et al. "Scaling laws for evaporative cooling in time-dependent optical traps". In: Phys. Rev. A 64.5 (2001). ISSN: 1050-2947. DOI: 10.1103/PhysRevA.64.051403.

[103] M. Pappa et al. "Ultra-sensitive atom imaging for matter-wave optics". In: New J. Phys. 13.11 (2011). ISSN: 1367-2630. DOI: 10.1088/1367-2630/13/11/115012.

[104] J. Pellegrino et al. "Observation of Suppression of Light Scattering Induced by Dipole-Dipole Interactions in a Cold-Atom Ensemble". In: Phys. Rev. Lett. 113.13 (2014). ISSN: 0031-9007. DOI: 10.1103/PhysRevLett.113.133602.

[105] J.-P. Perez. "Optique fondements et applications". In: (2004).

[106] W. D. Phillips. "Nobel Lecture: Laser cooling and trapping of neutral atoms". In: Rev. Mod. Phys. 70.3 (1998). ISSN: 0034-6861. DOI: 10.1103/RevModPhys.70.721.

[107] W. D. Phillips, J. V. Prodan, and H. J. Metcalf. "Laser cooling and electromagnetic trapping of neutral atoms". In: J. Opt. Soc. Am. B 2.11 (1985). ISSN: 0740-3224. DOI: 10.1364/JOSAB.2.001751.

[108] L. Pitaevskii and S. Stringari. "Elementary Excitations in Trapped Bose-Einstein Condensed Gases Beyond the Mean-Field Approximation". In: Phys. Rev. Lett. 81.21 (1998). ISSN: 0031-9007. DOI: 10.1103/PhysRevLett.81.4541.

[109] G. Reinaudi. "Manipulation et refroidissement par évaporation forcée d'ensembles atomiques ultra-froids pour la production d'un jet intense dans le régime de dégénérescence quantique : vers l'obtention d'un laser à atomes continu, PhD thesis". In: Université Paris 6 (2008).

[110] G. Reinaudi et al. "Strong saturation absorption imaging of dense clouds of ultracold atoms". In: Opt. Lett. 32.21 (2007). ISSN: 0146-9592. DOI: 10.1364/OL.32.003143.

[111] A. Reinhard et al. "Dark-ground imaging of high optical thickness atom clouds". In: Opt. Commun. 324 (2014). ISSN: 00304018. DOI: 10.1016/j.optcom.2014.02.070.

[112] Max F. Riedel et al. "Atom-chip-based generation of entanglement for quantum metrology". In: Nature 464.7292 (2010), pp. 1170–1173. ISSN: 00280836. DOI: 10.1038/nature08988. arXiv: 1003.1651.

[113] C. Rigetti et al. "Superconducting qubit in a waveguide cavity with a coherence time approaching 0.1 ms". In: Phys. Rev. B 86.10 (2012), p. 100506. ISSN: 1098-0121. DOI: 10.1103/PhysRevB.86.100506. URL: https://link.aps.org/doi/10.1103/PhysRevB.86.100506.

[114] M.S. Robbins and B.J. Hadwen. "The noise performance of electron multiplying charge-coupled devices". In: IEEE Trans. Electron Devices 50.5 (2003). ISSN: 0018-9383. DOI: 10.1109/TED.2003.813462.

[115] J. Rui et al. "A subradiant optical mirror formed by a single structured atomic layer". In: Nature 583.7816 (2020). ISSN: 0028-0836. DOI: 10.1038/s41586-020-2463-x.

[116] H. Salvador Vasquez Bullon. "Construction d'une nouvelle expérience pour l'étude degaz quantiques dégénérés des réseaux optiques, et étuded'un système d'imagerie super-résolution, PhD thesis". In: Université de Bordeaux (2016).

[117] B. Santra and H. Ott. "Scanning electron microscopy of cold gases". In: J. Phys. B-At. Mol. Opt. 48.12 (2015), p. 122001. ISSN: 0953-4075. DOI: 10.1088/0953-4075/48/12/122001. URL: https://iopscience.iop.org/article/10.1088/0953-4075/48/12/122001.

[118] R. E. Sapiro, R. Zhang, and G. Raithel. "Reversible loss of superfluidity of a Bose–Einstein condensate in a 1D optical lattice". In: New J. Phys. 11.1 (2009). ISSN: 1367-2630. DOI: 10.1088/1367-2630/11/1/013013.

[119] F. Schäfer et al. "Tools for quantum simulation with ultracold atoms in optical lattices". In: Nat. Rev. Phys. 2.8 (2020). ISSN: 2522-5820. DOI: 10.1038/s42254-020-0195-3.

[120] J. Scherschligt et al. "Development of a new UHV/XHV pressure standard (cold atom vacuum standard)". In: Metrologia 54.6 (2017). ISSN: 0026-1394. DOI: 10.1088/1681-7575/aa8a7b.

[121] E. M. Seroka et al. "Repeated measurements with minimally destructive partial-transfer absorption imaging". In: Opt. Express 27.25 (2019). ISSN: 1094-4087. DOI: 10.1364/OE.27.036611.

[122] E. Shahmoon et al. "Cooperative Resonances in Light Scattering from Two-Dimensional Atomic Arrays". In: Phys. Rev. Lett. 118.11 (2017). ISSN: 0031-9007. DOI: 10.1103/PhysRevLett.118.113601.

[123] S. Slussarenko and G. J. Pryde. "Photonic quantum information processing: A concise review". In: Appl. Phys. Rev. 6.4 (2019), p. 041303. ISSN: 1931-9401. DOI: 10.1063/1.5115814. URL: http://aip.scitation.org/doi/10.1063/1.5115814.

[124] J. Söding et al. "Three-body decay of a rubidium Bose–Einstein condensate". In: Appl. Phys. B 69.4 (1999). ISSN: 0946-2171. DOI: 10.1007/s003400050805.

[125] I. M. Sokolov and W. Guerin. "Comparison of three approaches to light scattering by dilute cold atomic ensembles". In: J. Opt. Soc. Am. B 36.8 (2019). ISSN: 0740-3224. DOI: 10.1364/JOSAB.36.002030.

[126] D. D. Solnyshkov et al. "Hybrid Boltzmann–Gross-Pitaevskii theory of Bose-Einstein condensation and superfluidity in open driven-dissipative systems". In: Phys. Rev. A 89.3 (2014). ISSN: 1050-2947. DOI: 10.1103/PhysRevA.89.033626.

[127] R. Stassi, M. Cirio, and F. Nori. "Scalable quantum computer with superconducting circuits in the ultrastrong coupling regime". In: npj Quantum Inf. 6.1 (2020), p. 67. ISSN: 2056-6387. DOI: 10.1038/s41534-020-00294-x. URL: https://www.nature.com/articles/s41534-020-00294-x.

[128] D. A. Steck. "Quantum and atom optics". In: (2019). URL: http://steck.us/teaching.

[129] D. A. Steck. "Rubidium 87 D line data". In: (2001).

[130] M. Stecker et al. "A high resolution ion microscope for cold atoms". In: New J. Phys. 19.4 (2017). ISSN: 1367-2630. DOI: 10.1088/1367-2630/aa6741.

[131] S. Subhankar et al. "Nanoscale Atomic Density Microscopy". In: Phys. Rev. X 9.2 (2019). ISSN: 2160-3308. DOI: 10.1103/PhysRevX.9.021002.

[132] M. K. Tey et al. "Interfacing light and single atoms with a lens". In: New J. Phys. 11.4 (2009). ISSN: 1367-2630. DOI: 10.1088/1367-2630/11/4/043011.

[133] P. Treutlein. "Coherent manipulation of ultracold atoms on atom chips, PhD thesis". In: Universität München (2008).

[134] T. V. Tscherbul and P. Brumer. "Partial secular Bloch-Redfield master equation for incoherent excitation of multilevel quantum systems". In: J. Chem. Phys. 142.10 (2015). ISSN: 0021-9606. DOI: 10.1063/1.4908130.

[135] R. Tyson. "Principles and Applications of Fourier Optics". In: (2014). DOI: 10.1088/978-0-750-31056-7.

[136] J.A. Vaumoron and M.P. De Biasio. "Argon and rare gas instability with heavy metal cathode penning pumps". In: Vacuum 20.3 (1970). ISSN: 0042207X. DOI: 10.1016/S0042-207X(70)80335-9.

[137] C. Veit et al. "Pulsed Ion Microscope to Probe Quantum Gases". In: Phys. Rev. X 11.1 (2021). ISSN: 2160-3308. DOI: 10.1103/PhysRevX.11.011036.

[138] R. Veyron et al. "Effective two-level approximation of a multi-level system driven by coherent and incoherent fields". In: (2021). arXiv: 2110.08894.

[139] R. Veyron et al. "Quantitative absorption imaging of optically dense effective two-level systems". In: (2021). arXiv: 2110.12505.

[140] G. Vicidomini, P. Bianchini, and A. Diaspro. "STED super-resolved microscopy". In: Nat. Methods 15.3 (2018). ISSN: 1548-7091. DOI: 10.1038/nmeth.4593.

[141] J.-L. Ville. "Quantum gases in box potentials : sound and light inbosonic Flatland, PhD thesis". In: PSL Research University (2019).

[142] J. L. Ville et al. "Loading and compression of a single two-dimensional Bose gas in an optical accordion". In: Phys. Rev. A 95.1 (2017). ISSN: 2469-9926. DOI: 10.1103/PhysRevA.95.013632.

[143] P. Wang et al. "Single ion qubit with estimated coherence time exceeding one hour". In: Nat. Commun. 12.1 (2021), p. 233. ISSN: 2041-1723. DOI: 10.1038/s41467-020-20330-w. URL: http://www.nature.com/articles/s41467-020-20330-w.

[144] C. Weitenberg et al. "Single-spin addressing in an atomic Mott insulator". In: Nature 471.7338 (2011). ISSN: 0028-0836. DOI: 10.1038/nature09827.

[145] J. Wen, Y. Zhang, and M. Xiao. "The Talbot effect: recent advances in classical optics, nonlinear optics, and quantum optics". In: Adv. Opt. Photonics 5.1 (2013). ISSN: 1943-8206. DOI: 10.1364/AOP.5.000083.

[146] J. Wen et al. "Electromagnetically induced Talbot effect". In: Appl. Phys. Lett. 98.8 (2011). ISSN: 0003-6951. DOI: 10.1063/1.3559610.

[147] D. S. Wiersma et al. "Localization of light in a disordered medium". In: Nature 390.6661 (1997). ISSN: 0028-0836. DOI: 10.1038/37757.

[148] T. Yefsah et al. "Exploring the Thermodynamics of a Two-Dimensional Bose Gas". In: Phys. Rev. Lett. 107.13 (2011). ISSN: 0031-9007. DOI: 10.1103/PhysRevLett.107.130401.

[149] J. Yoshida et al. "Scaling Law for Three-Body Collisions of Identical Fermions with p-Wave Interactions". In: Phys. Rev. Lett. 120.13 (2018), p. 133401. ISSN: 0031-9007. DOI: 10.1103/PhysRevLett.120.133401. URL: https://link.aps.org/doi/10.1103/PhysRevLett.120.133401.

[150] R. Zamora-Zamora et al. "Validity of Gross–Pitaevskii solutions of harmonically confined BEC gases in reduced dimensions". In: J. Phys. Commun. 3.8 (2019). ISSN: 2399-6528. DOI: 10.1088/2399-6528/ab360f.

[151] P. Zhou and J. H. Burge. "Analysis of wavefront propagation using the Talbot effect". In: Appl. Opt. 49.28 (2010). ISSN: 0003-6935. DOI: 10.1364/AO.49.005351.

Abstract
Cold atoms are a quantum system well-isolated from the environment. Since the 80s, they have been used to make high-sensitivity atomic sensors and to deepen the understanding of quantum physics phenomena. At low temperatures, degenerate atomic gas regimes can be reached. They are characterized by a macroscopic quantum state that can be manipulated and controlled by lasers. Placing such atomic wavefunction in optical lattices provides a way to study the dynamics of complex many-body systems. In this context, diffraction-limited quantum gas microscopes have emerged as standard tools to probe such complex systems and to measure atomic density correlations between lattice sites. By further reducing the optical lattice dimensions, the energy scales are strongly enhanced and favor novel quantum phases. Such reductions of optical lattice dimensions requires novel trapping and imaging techniques to manipulate cold atoms with subwavelength spatial resolutions.

In this PhD thesis, we experimentally perform subwavelength imaging of ultra-cold atoms of Rubidium 87 using a dressed excited state method, initially proposed for generating subwavelength trapping potentials. The measurements are performed using in situ absorption imaging. A quantitative comparison of data and theory lead us to reinterpret and modify a method for atom number calibrations that is commonly used in the community. This reinterpretation requires a fine understanding of the interaction of a single quantum multi-level system and a coherent saturating field. The measurement of the in situ transmission of a coherent probe shows a linear reduction of the single-atom scattering cross-section with the optical density for which we propose a physical interpretation and a model. Once calibrated, we use our subwavelength imaging method that reaches down to 20 nm resolution in a few microseconds to super-resolve a tiny quantum object: the longitudinal wavefunction of a BEC in a very tight lattice.

Résumé
Les atomes froids sont un système quantique très bien isolé de l'environnement. Depuis les années 80, ils sont utilisés pour faire des capteurs atomiques très sensibles et pour approfondir la compréhension des phénomènes de la physique quantique. À de très basses températures, des régimes de gaz atomiques dégénérés peuvent être atteints. Ils sont caractérisés par un état quantique macroscopique qui peut être manipulé et contrôlé par lasers. En chargeant ces états quantiques bien déterminés dans des réseaux optiques il est possible détudier la dynamique de systèmes complexes à N corps qui ne peuvent pas être simulés numériquement. Les microscopes à gaz quantique limités par la diffraction ont ensuite émergé pour sonder de tels systèmes en mesurant des corrélations de densité atomique entre les sites du réseau. En réduisant la taille des réseaux optiques jusqu'à des dimensions sub-longueur d'onde, il devrait être possible d'atteindre de nouvelles transitions de phase quantiques. De tels réseaux nécessitent le développement de techniques de piégeage et d'imagerie permettant de manipuler les atomes froids avec des résolutions spatiales sub-longueur d'onde.

Dans ce travail de thèse, nous démontrons expérimentalement une imagerie sub-longueur d'onde d'atomes ultra-froids de Rubidium 87 dont nous expliquons la production expérimentale. Cette imagerie utilise une méthode d'état excité habillé, initialement proposée pour générer des potentiels de piégeage sub-longueur d'onde. Pour être quantitatif sur notre imagerie par absorption de volumes sub-longueur d'onde, nous avons ré-interprété et modifié une méthode de calibration des nombres d'atomes communément utilisée dans la communauté. Cette ré-interprétation repose sur une compréhension fine de l'interaction d'un atome multi-niveaux avec un champ cohérent saturant dans des conditions perturbées. En mesurant in situ la transmission avec un champ cohérent, nous montrons alors que la section efficace de diffusion à un seul atome diminue linéairement avec la densité optique et nous proposons une interprétation et un model pour cette dépendance. Après avoir calibré notre méthode d'imagerie sub-longueur d'onde qui permet d'atteindre des résolutions spatiales de 20 nm en quelques microsecondes, nous l'appliquons à la mesure super-résolue des sites d'un réseau très fortement compressé.